On the evolution of and the deposition from an evaporating sessile droplet

PhD Thesis

Hannah-May D'Ambrosio
Department of Mathematics and Statistics
University of Strathclyde, Glasgow

July 27, 2022

This thesis is the result of the author's original research. It has been composed by the author and has not been previously submitted for examination which has led to the award of a degree.

Abstract

This thesis concerns the theoretical modelling and analysis of the evolution of, and the deposition from, an evaporating sessile droplet. In particular, the thesis focuses on the diffusion-limited situation in which the diffusive transport of vapour away from the droplet in the atmosphere is the rate-limiting mechanism for evaporation.

First, the evolution of a thin droplet in a shallow well of rather general shape is described both before and after the free surface of the droplet touches down on the well. In particular, it is shown that, depending on the shape of the well, touchdown can occur at the lip of the well, everywhere within the well simultaneously, or at the centre of the well. The mathematical model is validated by finding good agreement between the theoretical predictions and the results of physical experiments performed by collaborators at Durham University for the special case of a cylindrical well.

Second, the effect of gravity on the shape, evolution, and lifetime of thin sessile and pendant droplets is studied for four different modes of evaporation. Droplets of arbitrary volume are investigated and the limiting behaviours for small and large droplet volumes are determined. In particular, the mathematical model confirms that the contact radius of, and the total evaporative flux from, a sessile droplet is always larger than that for a pendant droplet of the same volume. It is also shown that the lifetime of a pendant droplet is always greater than that of a sessile droplet of the same initial volume for all four modes of evaporation studied.

Finally, the effect of spatial variation in the local evaporative flux on the deposition of particles from an evaporating sessile droplet is considered. A one-parameter family of spatially-varying local evaporative fluxes that captures a wide range of qualitatively different behaviours is investigated. It is shown that the flow within, and the deposition

from, an evaporating droplet depends strongly on the local evaporative flux profile. In particular, the mathematical model predicts three qualitatively different deposit types depending on the spatial variation in the local evaporative flux, namely, a ring deposit, a paraboloidal deposit, and a deposit at the centre of the droplet.

Contents

Acknowledgements

Firstly, I am indebted to my supervisors Professor Stephen Wilson and Dr Brian Duffy for their invaluable expertise, time, and guidance over the last 4 and a half years. To Stephen, thank you for all of the opportunities that you have provided me with. To Brian, thank you for always being there to answer any of my questions. I am also grateful to Dr Alexander Wray who, despite not being an official supervisor on this project, contributed a great deal to this work.

I would like to acknowledge the financial support of the United Kingdom Engineering and Physical Sciences Research Council (EPSRC), the University of Strathclyde, and Merck Chemicals Ltd. In particular, thank you to my industrial supervisor at Merck Chemicals Ltd, Dr Daniel Walker, for your guidance in the first two years of my PhD. Additionally, thank you to Teresa Colosimo, Dr Lisong Yang, and Professor Colin Bain at Durham University for your contribution towards the work in Chapter 3.

I am extremely grateful to my family and friends for their support and kindness. Thank you all for your encouragement.

Finally, to Angelo, thank you for everything. I simply could not have done this without your constant support, motivation, self-sacrifice, love, patience, and, most importantly, your jokes. You convinced me that I could do it and I will be forever grateful.

Chapter 1

Introduction

1.1 Droplets

A droplet (or drop) is a small volume of fluid which, as illustrated in Figure 1.1, can occur in several different forms, for example, on a substrate (*i.e.* a sessile or a pendant droplet), free-falling (*e.g.* a rain droplet or a droplet ejected from the nozzle of an inkjet printhead), or in the air (*e.g.* in aerosols or sprays). The dynamics of droplets have been of scientific interest for more than 200 years because of their widespread relevance in nature, biology and industry. In particular, various aspects of droplet behaviour have been investigated, including the impact, wetting and spreading of droplets on substrates (see, for example, the review articles by Hardt and McHale [107], Khojasteh *et al.* [137], and Tadmor [278, 279]), the falling of droplets in air under gravity (Szakáll *et al.* [276]), the inkjet printing of droplets (Hoath [114], Wijshoff [299]), the collision and coalescence of droplets (Kamp *et al.* [131]), the transport of respiratory droplets and aerosols in the atmosphere (Jayaweera *et al.* [123], Sun *et al.* [274]), as well as drop-wise condensation (El Fil *et al.* [76]) and icing phenomena (Zhoa *et al.* [319]).

This thesis concerns the evaporation of droplets that are on a substrate (*i.e.* sessile or pendant droplets, as shown in Figures 1.1a,b). In this Chapter we discuss the importance of droplet evaporation, and describe how various properties of the system, such as droplet size and the nature of the substrate, affect the evaporation process. We also describe the deposition of particles from an evaporating droplet and discuss the

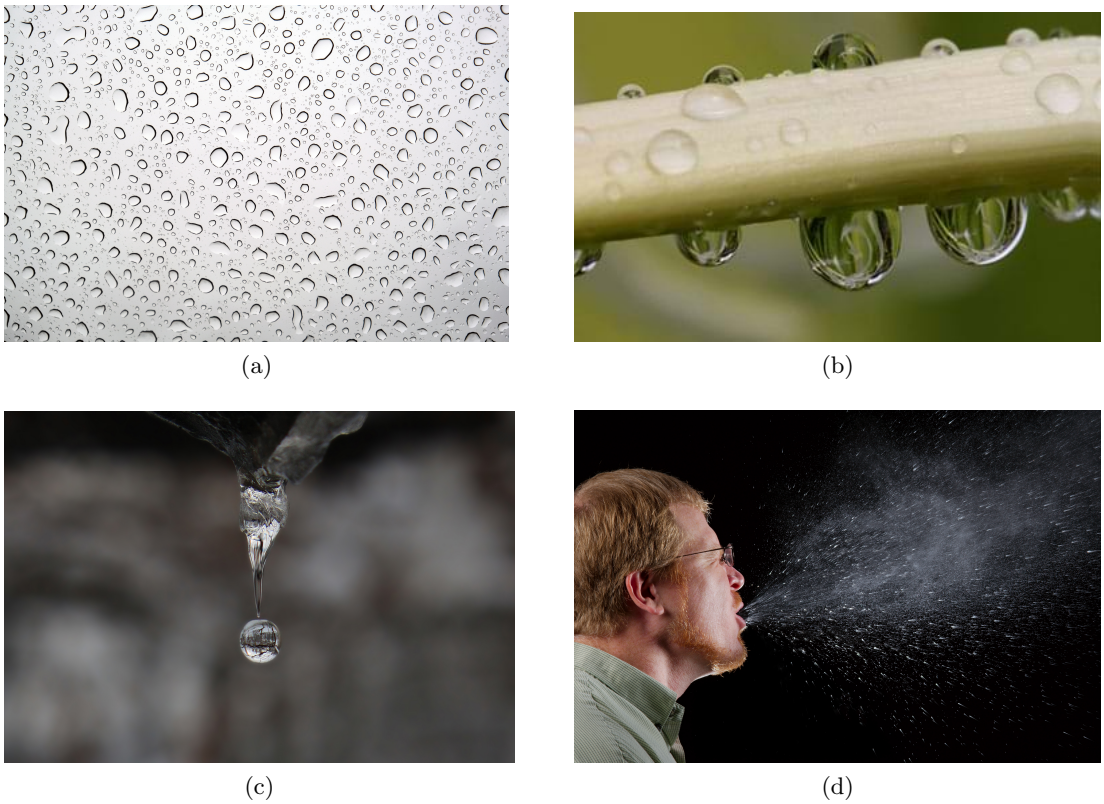

(a) (b)

(c) (d)

Figure 1.1: Examples of droplets occuring in several different forms: (a) Sessile droplets on a car. Reproduced from Kallerna [130]. (b) Sessile and pendant rain droplets on a plant stem. Reproduced from Karim [136]. (c) A falling droplet. Reproduced from Traianou [286]. (d) A spray of saliva droplets expelled during a sneeze. Reproduced from Gathany [97].

large body of ongoing research that investigates the mechanisms that can influence and control particle deposition.

1.2 Droplet evaporation

When a droplet is deposited onto a substrate, the fluid is in contact with the atmosphere along the droplet–atmosphere interface, hereafter referred to as the free surface of the droplet. The curve along which the droplet, substrate, and atmosphere meet is termed the contact line of the droplet (sometimes referred to as the three-phase line), and the angle that the free surface of the droplet makes with the substrate is termed the contact angle of the droplet. In general, the contact angle may vary along the contact

line, such as for asymmetric droplets; however, in this thesis we are only concerned with axisymmetric droplets in which the contact angle is the same all the way along the contact line. Additionally, for axisymmetric droplets the distance between the centre of the droplet and the contact line is termed the contact radius of the droplet. As the droplet evaporates, there is a net loss of fluid molecules from the free surface of the droplet in the form of vapour, the mass of vapour in the atmosphere increases, and the volume of the droplet decreases. The evaporation is characterised by the local evaporative mass flux, *i.e.* the mass of fluid escaping into the atmosphere per unit area per unit time, and the total evaporative mass flux, *i.e.* the total mass of fluid escaping into the atmosphere per unit time, from the droplet. The droplet evaporates completely in what we term the lifetime of the droplet, after which time all of the fluid initially contained within the droplet has been converted into vapour.

The process of droplet evaporation occurs in a wide variety of physical contexts, with practical applications in agricultural spraying (Taylor [285], Tredenick *et al.* [288]), chemical and biological assays (Garcia-Cordero and Fan [94]), and inkjet printing (Kuang *et al.* [146]). There have therefore been extensive experimental, numerical, and theoretical investigations on the evaporation of a droplet in recent years (see, for example, the review articles by Brutin and Starov [35], Cazabat and Guéna [40], Erbil [79], Giorgiutti-Dauphiné and Pauchard [101], Kovalchuk *et al.* [144], Lohse and Zhang [166], Routh [229], Talbot *et al.* [280], Wilson and D'Ambrosio [302], Zang *et al.* [317], and Zhong *et al.* [321], and the many references therein).

The importance of the deposition of particles from an evaporating droplet will be discussed in the next Section.

1.3 The deposition of particles from an evaporating droplet

In practice, droplets often contain non-volatile solutes and/or particles in suspension (hereafter, referred to simply as "particles"). In many industrial and scientific processes a primary concern is the spatial distribution of the particles left behind on the substrate after the droplet has completely evaporated, hereafter referred to as the final deposit. In particular, the ability to control the distribution of particles within the droplet during

the drying process is key, often with the aim of obtaining uniform deposits for numerous applications such as inkjet printing (Lim *et al.* [162], Park and Moon [209]) and DNA chip manufacturing (Dugas *et al.* [69]). However, other deposit types are also of interest, such as rings in disease diagnostics (Trantum *et al.* [287]) or for conductive coatings (Layani *et al.* [151]), multiple or concentric rings in the production of resonators in optical communications (Hong *et al.* [115]), or small concentrated deposits in mass spectrometry (Kudina *et al.* [147]) with applications in drug testing and carbon dating. Figure 1.2 shows examples of different deposition patterns that may be observed after the complete evaporation of a droplet, such as single, multiple or concentric rings, uniform deposits, small concentrated or "inner" deposits, "spoke-like" deposits, and patterned deposits.

As a consequence of the wide variety of practical applications, the deposition from an evaporating droplet has been subject to extensive investigation in recent years (see, for example, the review articles by Al-Milaji and Zhoa [6], Anyfantakis and Baigl [9], Giorgiutti-Dauphiné and Pauchard [101], Kolegov and Barash [142], Kuang *et al.* [146], Larson [150], Mampallil and Eral [176], Parsa *et al.* [212], Shao *et al.* [251], Sefiane [242], Yang *et al.* [311], Zang *et al.* [317], and Zhong *et al.* [321], and the many references therein), much of it building upon the pioneering work of Deegan *et al.* [63, 64] and Deegan [62]. There has been particular attention paid to the well-known "coffee-ring effect" (sometimes also called the "coffee-stain effect") described by Deegan *et al.* [64], in which a ring deposit is formed near the contact line of a pinned evaporating droplet (*i.e.* a droplet in which the contact line remains fixed in position). The dynamics of the coffee-ring effect and the mechanisms that control particle deposition from an evaporating droplet will be discussed further in Sections 1.9 and 1.10, respectively.

1.4 Mathematical modelling of droplet evaporation

A key ingredient to understanding droplet evaporation is, of course, to capture the appropriate physical mechanism(s) controlling the evaporation from the free surface of the droplet into the surrounding atmosphere. Depending on the physical situation, different physical mechanisms can control the evaporation. In particular, as Murisic

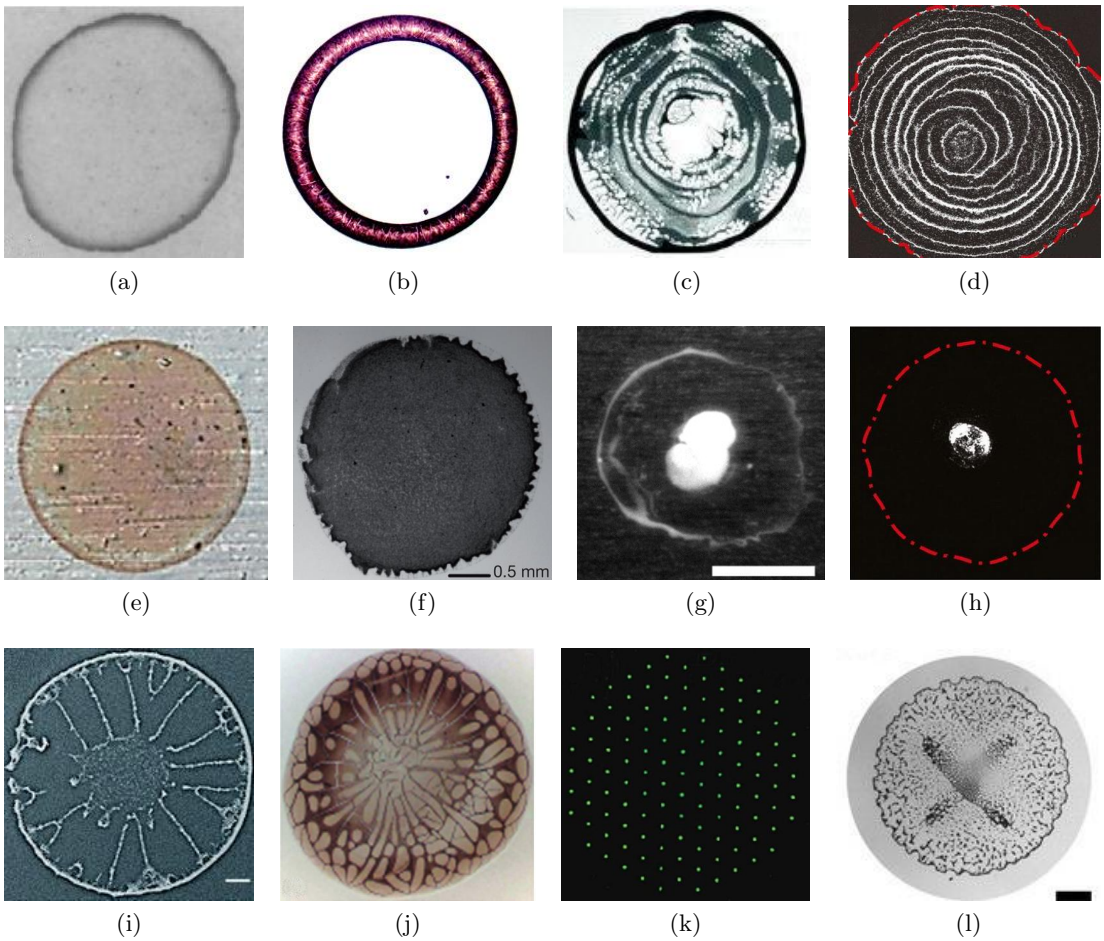

Figure 1.2: Examples of different deposition patterns after the complete evaporation of a droplet: (a)–(b) Ring deposits, (c)–(d) multiple or concentric ring deposits, (e)–(f) uniform deposits, (g)–(h) small concentrated or "inner" deposits, (i)–(j) "spoke-like" deposits, and (k)–(l) patterned deposits. (a) Reprinted figure with permission from Deegan *et al.* [64]. Copyright 2000 by the American Physical Society. (b) Reprinted with permission from Sommer [265]. Copyright 2004 American Chemical Society. (c) Reprinted with permission from Bhardwaj *et al.* [23]. Copyright 2010 American Chemical Society. (d) Reprinted with permission from Li *et al.* [158]. (e) Reprinted from Cho *et al.* [50], Copyright (2020), with permission from Elsevier. (f) Reprinted by permission from Springer Nature: Yunker *et al.* [316], Copyright (2011). (g) Reproduced from Ta *et al.* [277] with permission from the Royal Society of Chemistry. (h) Reprinted with permission from Li *et al.* [158]. (i) Republished with permission of the Royal Society of Chemistry, from Yang *et al.* [312]; permission conveyed through Copyright Clearance Center, Inc. (j) Reprinted by permission from Springer Nature: Sefiane [241], Copyright (2010). (k) Republished with permission of the Royal Society, from Harris *et al.* [108]; permission conveyed through Copyright Clearance Center, Inc. (l) Reprinted with permission from Malinowski *et al.* [173] (https://doi.org/10.1021/acs.jpclett.7b02831). Further permissions related to the material excerpted should be directed to the ACS.

and Kondic [193] discuss, the rate-limiting mechanism may be the transport of vapour away from the droplet in the atmosphere, the phase transition at the free surface of the droplet, the transport of heat through the droplet, the conduction of heat through the substrate, or a combination thereof.

1.4.1 The diffusion-limited model

For a droplet evaporating in a quiescent atmosphere, it can be shown that the transfer of molecules from the fluid into the vapour across the free surface is typically much faster than the transport of vapour away from the droplet in the atmosphere (see, for example, Popov [220]). In this case, the gradient from the high (saturated) concentration of vapour at the free surface to the low (ambient) concentration of vapour in the atmosphere drives a diffusive flux of vapour away from the free surface of the droplet. Models that describe the evaporation of a droplet in a quiescent atmosphere are therefore called "diffusion-limited" models, as the diffusive transport of vapour away from the droplet in the atmosphere is the rate-limiting mechanism for the evaporation. Additionally, it can be shown that the diffusion of vapour in the atmosphere is typically on a much shorter timescale than that of the timescale for the free surface of the droplet to adjust due to evaporation (see, for example, Popov [220]). Therefore, the evaporation process may be considered to be quasi-steady.

Picknett and Bexon [217] pioneered the modelling of droplets evaporating in a quiescent atmosphere, obtaining expressions for the evolution, and hence the lifetime, of a droplet undergoing diffusion-limited evaporation for the full range of initial contact angles. Following Picknett and Bexon [217], many subsequent authors, including Birdi *et al.* [24], Bourgès-Monnier and Shanahan [33], Dash and Garimella [57], Deegan [62], Deegan *et al.* [63, 64], Dunn *et al.* [71, 72], Hu and Larson [116, 117, 119], Masoud *et al.* [182], McHale *et al.* [184,185], Nguyen and Nguyen [196], Nguyen *et al.* [194,197], Popov [220], Sáenz *et al.* [232], Schofield *et al.* [238–240], Stauber *et al.* [267–270], Wray *et al.* [305,306], and Zigelman and Manor [324] have obtained exact, asymptotic, approximate, and numerical descriptions of the evolution, and hence the lifetime, of a droplet undergoing diffusion-limited evaporation in a wide range of situations.

We give a full description of a theoretical model for the diffusion-limited evaporation of a sessile droplet in Chapter 2. In particular, for the model described in Chapter 2, the evaporation of the droplet is controlled by the diffusion of vapour from its constant saturated value, denoted by $\hat{c}_{\rm sat}$, on the free surface of the droplet to its constant ambient value, denoted by $\hat{c}_{\infty}$. In this situation the evaporative problem for the concentration of vapour in the atmosphere is decoupled from the thermal problem for the temperature distribution in the system.

1.4.2 Generalisations of the diffusion-limited model

The evaporation of a droplet requires latent heat, and so, in general, evaporative cooling occurs as the droplet evaporates. For situations in which significant evaporative cooling occurs, the diffusion-limited model may need to be extended to include coupling between the evaporative and thermal problems. In particular, various models have been proposed that couple the evaporative and thermal problems by acknowledging that the local value of the surface tension (see, for example, Hu and Larson [117] and Ristenpart *et al.* [227]) and/or the saturation concentration (see, for example, Ait Saada *et al.* [3], Dunn *et al.* [71, 72], Nguyen *et al.* [194], Schofield *et al.* [238], and Sefiane *et al.* [243]) will, in general, depend on the local temperature of the free surface. Furthermore, when the substrate has a very high thermal resistance and/or the saturation concentration depends very strongly on temperature, the rate-limiting mechanism controlling evaporation is the conduction of heat through the droplet and the substrate rather than the diffusion of vapour in the atmosphere (see, for example, Dunn *et al.* [73] and Schofield *et al.* [239]). We note that when the local value of the surface tension of the free surface depends on the local temperature the (in general, spatially non-uniform) evaporative cooling of the free surface of the droplet will give rise to a thermocapillary-driven (*i.e.* a Marangoni) flow, which is of particular interest because of the role it can play in the deposition from an evaporating droplet; this will be discussed further in Section 1.10.

There can also be situations in which the effects of buoyancy-driven convection in the atmosphere play a significant role (see, for example, Carle *et al.* [37], Dunn *et al.* [72], and Shahidzadeh-Bonn *et al.* [247]). Numerical solutions of a generalised

version of the diffusion-limited model for a droplet of water including both evaporative cooling and buoyancy-driven convection in both the droplet and the atmosphere by Pan *et al.* [205, 206] have clarified the influence of these effects and the limitations of the diffusion-limited model.

1.4.3 The one-sided model

For the case when the rate of transfer of fluid molecules into vapour across the free surface of the droplet is the rate-limiting mechanism, the evaporation may be described by the so-called "one-sided" model (see, for example, Ajaev [4,5], Anderson and Davis [8], Burelbach *et al.* [36], Cazabat and Guéna [40], Craster and Matar [52], Espin and Kumar [82], Haut and Colinet [111], Murisic and Kondic [193], and Sodtke *et al.* [263,264]). This model assumes that the density, dynamic viscosity, and thermal conductivity of the vapour in the atmosphere are small compared to those in the fluid (see, for example Burelbach *et al.* [36]), and may be expected to apply for situations in which a droplet with a contaminated free surface evaporates very slowly, for the forced evaporation of a droplet on a significantly heated substrate, and for a droplet evaporating in an atmosphere of its pure vapour (see, for example, Cazabat and Guéna [40]). In addition, generalised models that include both the diffusion-limited model and the one-sided model as limiting cases have also been developed by, for example, Sultan *et al.* [273]. However, this thesis concerns droplets undergoing diffusion-limited evaporation, and so the one-sided model will not be discussed further in this work.

1.5 Modes of evaporation

The evolution, and hence the lifetime, of an evaporating droplet depends on the manner in which it evaporates. As a droplet evaporates its volume will decrease and therefore the contact radius $\hat{R} = \hat{R}(\hat{t})$ and/or the contact angle $\hat{\theta} = \hat{\theta}(\hat{t})$ of the droplet change with time $\hat{t}$. The manner in which the geometry of the droplet changes as it evaporates is called its mode of evaporation. Four different modes of evaporation will be described in this Section.

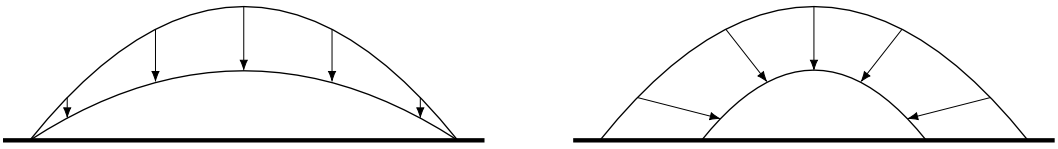

(a) (b)

Figure 1.3: Sketch of a sessile droplet evaporating in the (a) constant contact radius (CR) mode and (b) constant contact angle (CA) mode.

1.5.1 The extreme modes of evaporation

In their pioneering work, Picknett and Bexon [217] identified two "extreme" modes of evaporation for a droplet, namely, the constant contact radius (CR) mode and the constant contact angle (CA) mode, which are sketched in Figure 1.3. For a droplet evaporating in the CR mode, the contact line of the droplet is pinned to the substrate (*i.e.* it remains fixed in position) due to surface roughness and/or chemical heterogeneities. Therefore, the contact radius remains constant at its initial value $\hat{R} = \hat{R}(0) \equiv \hat{R}_0$ throughout evaporation and the contact angle $\hat{\theta}$ decreases in time from its initial value $\hat{\theta}(0) \equiv \hat{\theta}_0$ to zero, at which time the droplet has completely evaporated. On an ideal substrate, *i.e.* a perfectly smooth, chemically homogeneous, rigid, impermeable, and insoluble substrate, a droplet evaporates in the CA mode, and the contact line is unpinned (*i.e.* it is free to move). Therefore, the contact angle $\hat{\theta}$ of the droplet remains constant at its initial value $\hat{\theta}_0$, and the contact line de-pins and recedes, the contact radius $\hat{R}$ decreasing from its initial value $\hat{R}_0$ to zero, at which time the droplet has completely evaporated. Table 1.1 provides examples of experimental investigations that observed droplets evaporating in the extreme modes of evaporation for most or all of their lifetime.

In practice, the mode in which a droplet evaporates will depend on the properties of the substrate, including surface structure and roughness, chemical heterogeneities, permeability, and porosity, with droplets often evaporating in mixed modes (*i.e.* modes in which both the contact radius $\hat{R}$ and contact angle $\hat{\theta}$ decrease). We will now describe

Mode of evaporation	References
CR and CA modes	[12, 13], [16], [80], [93], [95], [98], [102], [103], [152], [163], [208], [261, 262], [250], [254, 255], [281], [289]
SS mode	[7], [33], [45], [46], [57], [58], [81], [90], [112], [121], [140], [152], [163], [190], [191], [196, 197], [218], [245], [266], [289], [308]
SJ mode	[1], [7], [14–16], [26], [28], [61], [67], [103], [112], [155], [171], [184], [188, 189], [200], [213], [224], [249], [257], [307]

Table 1.1: Examples of experimental investigations that observed droplets evaporating in the CR, CA, SS, and SJ modes.

two commonly-reported mixed modes of evaporation in the two subsequent Subsections. The effect of the substrate on the evaporation of a droplet will be discussed further in Sections 1.6 and 1.7.

1.5.2 The stick–slide (SS) mode of evaporation

Bourgès-Monnier and Shanahan [33] described a mixed mode of evaporation for the case of an evaporating water droplet on a polished epoxy substrate, identifying four stages in the evolution of the geometry; their results are reproduced in Figure 1.4. In their experiments the droplet is initially surrounded by a saturated atmosphere and so, in stage I, evaporation is negligible. In stage II the droplet evaporates in a CR phase, in which the contact line is pinned and the contact angle decreases, in stage III the droplet evaporates in a CA phase, in which the contact line recedes and the contact angle is constant, and in stage IV the contact radius and the contact angle of the droplet decrease simultaneously, as shown in Figure 1.4. We note that the simultaneous decrease of the contact radius and the contact angle of a droplet, as described in stage IV by Bourgès-Monnier and Shanahan [33], is typically observed for a short time (relative to the lifetime of the droplet) in the final stage of droplet evaporation (see, for example, Gao *et al.* [93], Gatapova *et al.* [96], Semenov *et al.* [245], and Xu *et al.* [308]) and so is often neglected when modelling the evolution of an evaporating droplet.

Stages II and III in the work of Bourgès-Monnier and Shanahan [33] correspond to one of the most commonly reported mixed modes of evaporation, namely the stick–

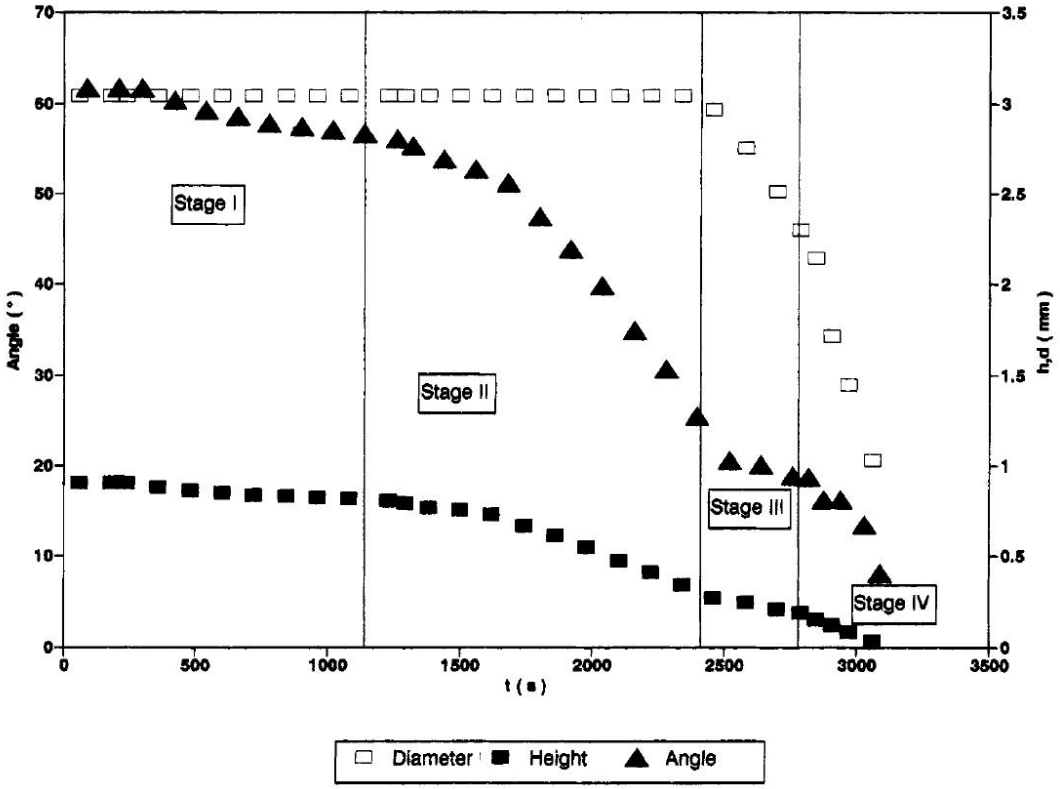

Figure 1.4: Evolutions of the contact diameter ($2\hat{R}$), height, and contact angle $\hat{\theta}$ of an evaporating $4\,\mu$L sessile water droplet on a polished epoxy substrate. Reprinted with permission from Bourgès-Monnier and Shanahan [33]. Copyright 1995 American Chemical Society.

slide (SS) mode. In the SS mode the droplet initially evaporates in a CR (*i.e.* "stick") phase with $\hat{R} \equiv \hat{R}_0$, $\hat{\theta} = \hat{\theta}(\hat{t})$ until a time $\hat{t} = \hat{t}^*$ at which a critical receding angle $\hat{\theta}^*$ ($0 \leq \hat{\theta}^* \leq \hat{\theta}_0$) is reached, after which the droplet evaporates in a CA (*i.e.* "slide") phase with $\hat{R} = \hat{R}(\hat{t})$, $\hat{\theta} \equiv \hat{\theta}^*$. Table 1.1 also provides examples of experimental investigations that observed droplets evaporating in the SS mode in various contexts. In particular, the SS mode has been reported by authors investigating the effect of initial droplet volume (Dash and Garimella [57], Erbil *et al.* [81], Fukai *et al.* [90], Kim *et al.* [140]), substrate wettability (Anantharaju *et al.* [7], Bourgès-Monnier and Shanahan [33], Chen *et al.* [46], Dash *et al.* [58], Erbil *et al.* [81], He *et al.* [112], Kim *et al.* [140], Lee *et al.* [152], Moore *et al.* [191], Nguyen *et al.* [197], Pittoni *et al.* [218], Soolaman and Yu [266], Trybala *et al.* [289], Xu *et al.* [308]), substrate temperature (Mollaret *et al.* [190]), droplet orientation (Moore *et al.* [191]), polymers (Hwang *et al.* [121]), surfactants (Semenov *et al.* [245]), and nanoparticle suspensions (Fukai *et al.* [90], Nguyen and Nguyen [195], Trybala *et al.* [289]) on the evolution of an evaporating droplet.

The evolution of a droplet evaporating in the SS mode has been theoretically investigated by many authors (see, for example, Dash and Garimella [57], Nguyen and Nguyen [195, 196], Nguyen *et al.* [197], Semenov *et al.* [244], and Stauber *et al.* [268, 270]). In particular, Stauber *et al.* [268] analysed the evolution of a droplet evaporating in the CR, CA, and SS modes, and analytically determined the evaporation rate (*i.e.* the total evaporative flux) and the lifetime of the droplet in each of these modes. They identified six possible orderings of the lifetimes of initially identical droplets evaporating in the CR, CA, and SS modes depending on the values of the initial $\hat{\theta}_0$ and critical receding $\hat{\theta}^*$ contact angles of the droplets, and verified the model by comparing their results with experimental data in the literature. Stauber *et al.* [270] then went on to describe the evolution, and hence the lifetime, of a droplet evaporating in the SS mode taking into account a physically-plausible relationship between the initial $\hat{\theta}_0$ and critical receding $\hat{\theta}^*$ contact angles of the droplet based on the pinning/de-pinning force at the contact line of the droplet.

There are other situations in which the contact line of the droplet does not recede

continuously as observed in the SS mode. One of these is the stick–jump (SJ) mode described in the next Subsection.

1.5.3 The stick–jump (SJ) mode of evaporation

The SJ mode of evaporation consists of a number of CR (*i.e.* "stick") phases, in which the contact line is pinned and the contact angle of the droplet decreases, separated by a number of short "jump" phases, in which the contact line rapidly recedes and the contact angle rapidly increases. Table 1.1 also provides examples of experimental investigations that observed droplets evaporating in the SJ mode in various contexts. In particular, the SJ mode has been reported by authors investigating evaporating droplets containing suspended particles (Adachi *et al.* [1], Bodiguel *et al.* [26], Shmuylovich *et al.* [257]), including nanoparticles (Askounis *et al.* [14–16], Li *et al.* [155], Moffat *et al.* [188, 189], Orejon *et al.* [200]) and DNA (Maheshwari *et al.* [171]), droplets containing suspended particles evaporating on heated substrates (Parsa *et al.* [213]), as well as pure droplets evaporating on pillared (Anantharaju *et al.* [7], Guan *et al.* [103], McHale *et al.* [184], Xu *et al.* [307]), micro-patterned (Debuisson *et al.* [61], He *et al.* [112]), heated (Putnam *et al.* [224]), and rough polymer (Bormashenko *et al.* [28], Shanahan and Sefiane [249]) substrates. Additionally, Dietrich *et al.* [67] studied the dissolution of alcohol droplets in water, observing the SJ mode for microscale droplets. In particular, they showed that if the potential-energy barrier overcome in each jump is the same then the relative change in the contact radius of a droplet after a jump phase is proportional to $1/\hat{R}^{1/2}$, which therefore increases as the size of the droplet decreases, making the SJ mode easier to observe for small droplets. Figure 1.5 shows examples of droplets evaporating in the SJ mode in the experiments by (a) Xu *et al.* [307] in which a water droplet evaporates on a substrate with non-uniform micro-pillar arrays with gradient spacings varying from $10\,\mu$m to $70\,\mu$m, (b) Debussion *et al.* [61] in which a deionized water droplet evaporates on a micro-patterned SU-8 substrate that contains concentric circular troughs every $50\,\mu$m, and (c) Orejon *et al.* [200] in which water droplets containing different concentrations of TiO_2 nanoparticles evaporate on a CYTOP substrate. In particular, Figure 1.5 shows that the number of jump phases

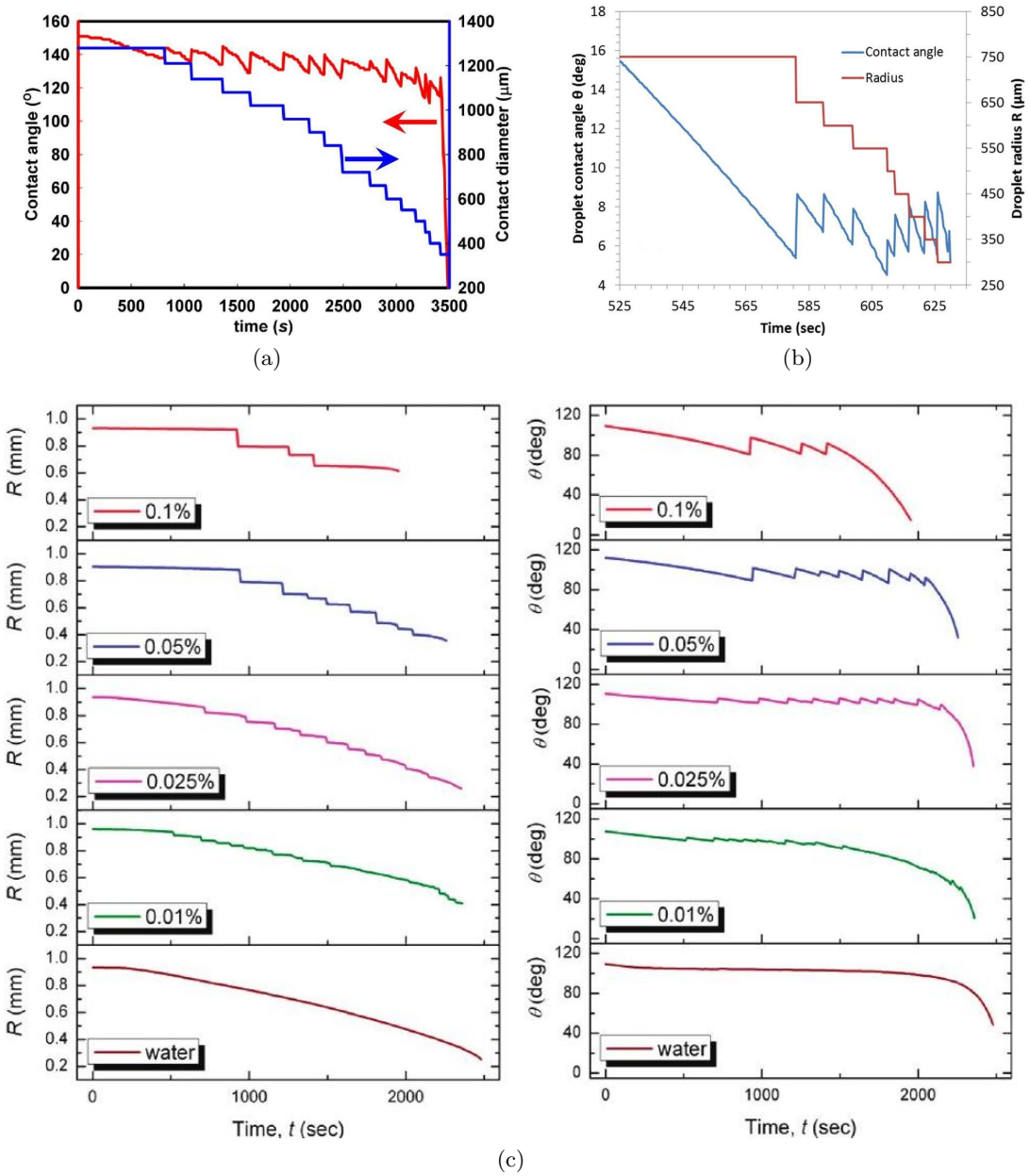

Figure 1.5: Examples of experimental observations of droplets evaporating in the SJ mode. Evolution of the contact radius $\hat{R}$ and the contact angle $\hat{\theta}$ of: (a) A water droplet on a substrate with non-uniform micro-pillar arrays with gradient spacings varying from 10 μm to 70 μm. Reprinted from Xu *et al.* [307], with the permission of AIP Publishing. (b) A deionized water droplet evaporating on a micro-patterned SU-8 substrate that contains concentric circular troughs every 50 μm. Reprinted with permission from Debussion *et al.* [61]. Copyright 2016 American Chemical Society. (c) Water droplets containing different concentrations of TiO_2 nanoparticles evaporating on a CYTOP substrate. Reprinted with permission from Orejon *et al.* [200]. Copyright 2011 American Chemical Society.

and the duration of each stick phase is dependent on the properties of the substrate and the concentration of the particle suspension within the droplet. It also shows that the contact angle of the droplet jumps approximately between two critical values and that a jump phase is of very short duration compared to the stick phases. Therefore this rapid jump is often considered instantaneous when modelling the evolution of an evaporating droplet in the SJ mode.

The SJ mode was first described theoretically by Shanahan [248], who used an argument based on the Gibbs free energy to describe the pinning and de-pinning of the contact line of the droplet. This theory was the basis for subsequent energy-barrier equations describing the evolution of evaporating droplets containing a suspension of nanoparticles (see, for example, Askounis *et al.* [14–16], Oksuz and Erbil [198], Orejon *et al.* [200], and Shanahan and Sefiane [249]). Further theoretical and numerical studies have investigated the pinning and de-pinning of the contact line of an evaporating droplet containing a suspension of particles (Adachi *et al.* [1]), and on a chemically patterned substrate (Kusumaatmaja and Yeomans [148]). Dietrich *et al.* [67] modelled the dissolution of sessile alcohol droplets in water by considering the mathematically equivalent problem of the evaporation of a water droplet. They developed a model in which the contact line of the droplet de-pins once a critical contact angle is reached, and instantaneously jumps inwards and re-pins with the contact angle then taking the value of the (larger) initial contact angle of the droplet. Stauber [267] derived a mathematical model that is similar to, but more general than, that of Dietrich *et al.* [67]. In this model for the SJ mode the droplet initially evaporates in a CR phase with $\hat{R} \equiv \hat{R}_0$ and a contact angle $\hat{\theta}$ that decreases from $\hat{\theta}_0$ to a critical minimum angle $\hat{\theta}_{\min}$ ($0 \leq \hat{\theta}_{\min} \leq \hat{\theta}_0$), at which time the contact angle jumps instantaneously from $\hat{\theta}_{\min}$ to a critical maximum angle $\hat{\theta}_{\max}$ ($0 \leq \hat{\theta}_{\min} \leq \hat{\theta}_{\max} \leq \hat{\theta}_0$) and the contact radius jumps instantaneously to a lower value $\hat{R} = \hat{R}_1$. Since $\hat{\theta}$ is bounded below by $\hat{\theta}_{\min}$ in this model, the process of a CR phase followed by an instantaneous jump phase then repeats an infinite number of times until the droplet completely evaporates in a finite time.

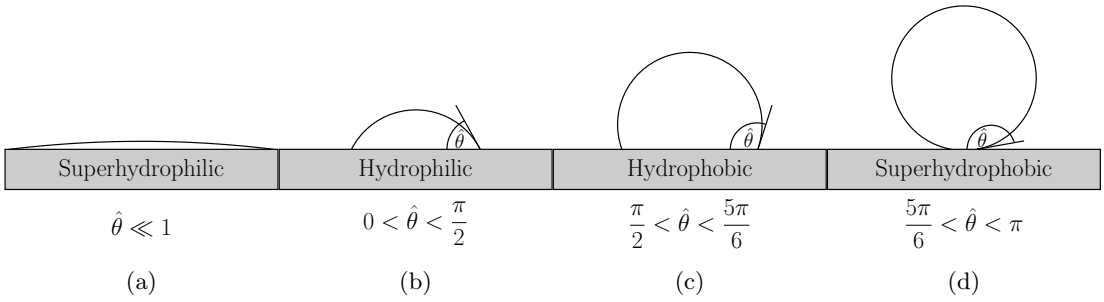

Figure 1.6: Sketch of droplets in different wetting states on different types of substrates.

1.6 The importance of the substrate

In this Section we will describe various aspects of the substrate that can affect the dynamics of an evaporating droplet.

How a droplet sits on a substrate is dependent upon, among other things, the substrate chemistry, roughness, and topography. In particular, substrates are often classified into four different types depending on their affinity to be wetted by the fluid, namely, superhydrophilic (sometimes also referred to as super-wetting or super-wettable), hydrophilic, hydrophobic, and superhydrophobic (sometimes also referred to as ultrahydrophobic) substrates, corresponding to a substrate on which a droplet forms a contact angle $\hat{\theta}$ that is small $\hat{\theta} \ll 1$, between 0 and $\pi/2$, between $\pi/2$ and $5\pi/6$, and between $5\pi/6$ and π, respectively (see, for example, the review articles by Drelich *et al.* [68], Roach *et al.* [228], and Shirtcliffe *et al.* [256]), as sketched in Figure 1.6.

Previous experimental, numerical, and theoretical studies have shown that the evolution, and hence the lifetime, of a droplet will depend on the size of its initial contact angle, and therefore the wettability of the substrate (see, for example, Nguyen and Nguyen [196], Nguyen *et al.* [197], Picknett and Bexon [217], Shin *et al.* [255], Sobac and Brutin [261], and Stauber *et al.* [268,269]). In particular, Stauber *et al.* [269] showed that the local evaporative flux from a droplet undergoing diffusion-limited evaporation is qualitatively different depending on the value of the contact angle. Specifically, Stauber *et al.* [269] showed that the local evaporative flux is largest (theoretically singular) at the contact line and smallest at the apex of the droplet when $0 \leq \hat{\theta} < \pi/2$,

uniform when $\hat{\theta} = \pi/2$, and largest at the apex of the droplet and zero at the contact line when $\pi/2 < \hat{\theta} \leq \pi$; their results are reproduced in Figure 1.7. Additionally, they obtained asymptotic expressions for the evolutions and lifetimes of droplets evaporating in the CR and CA modes on hydrophobic substrates, and described the manner in which the extreme modes of evaporation become indistinguishable on superhydrophobic substrates. Furthermore, it has been shown that the size of the contact angle can affect the flow within the droplet (see, for example, Chen *et al.* [47] and Pan *et al.* [205,207]), as well as the evaporative cooling of the system (see, for example, Pan *et al.* [205,207]).

In addition, the thermal properties of the substrate, as well as those of the fluid of the droplet and the atmosphere, can affect the evolution, and hence the lifetime, of an evaporating droplet. In particular, as discussed in Section 1.4, there are situations for which the rate-limiting mechanism controlling evaporation is the conduction of heat through the droplet and the substrate. In general, the evaporation rate of a droplet on a poorly-conducting substrate, such as a plastic, can be significantly less than that of the same droplet on a highly-conducting substrate, such as a metal (see, for example, David *et al.* [59], Dunn *et al.* [72], Schofield *et al.* [238,239], and Sobac and Brutin [262]). Schofield *et al.* [238] used a fully coupled model for the evaporative and thermal problems to analyse the evolution of a sessile droplet evaporating in the CR, CA, SS, and SJ modes, and showed that the lifetimes of a droplet of water evaporating in one of the extreme modes on a poorly-conducting substrate made of PTFE can be significantly longer than that of the same droplet on a highly-conducting substrate made of aluminium, as well as that predicted by the diffusion-limited model, with a greater difference for droplets with large initial contact angles; their results are reproduced in Figure 1.8.

Moreover, it has been shown both experimentally (see, for example, Lopes and Bonaccurso [167,168]) and theoretically (see, for example, Charitatos and Kumar [41]) that a droplet evaporating on a soft substrate will have a shorter lifetime than the same droplet evaporating on a hard substrate since the deformation of the soft substrate at the contact line promotes contact-line pinning which increases the evaporation rate from the droplet. On the other hand, a lubricated substrate promotes contact-line

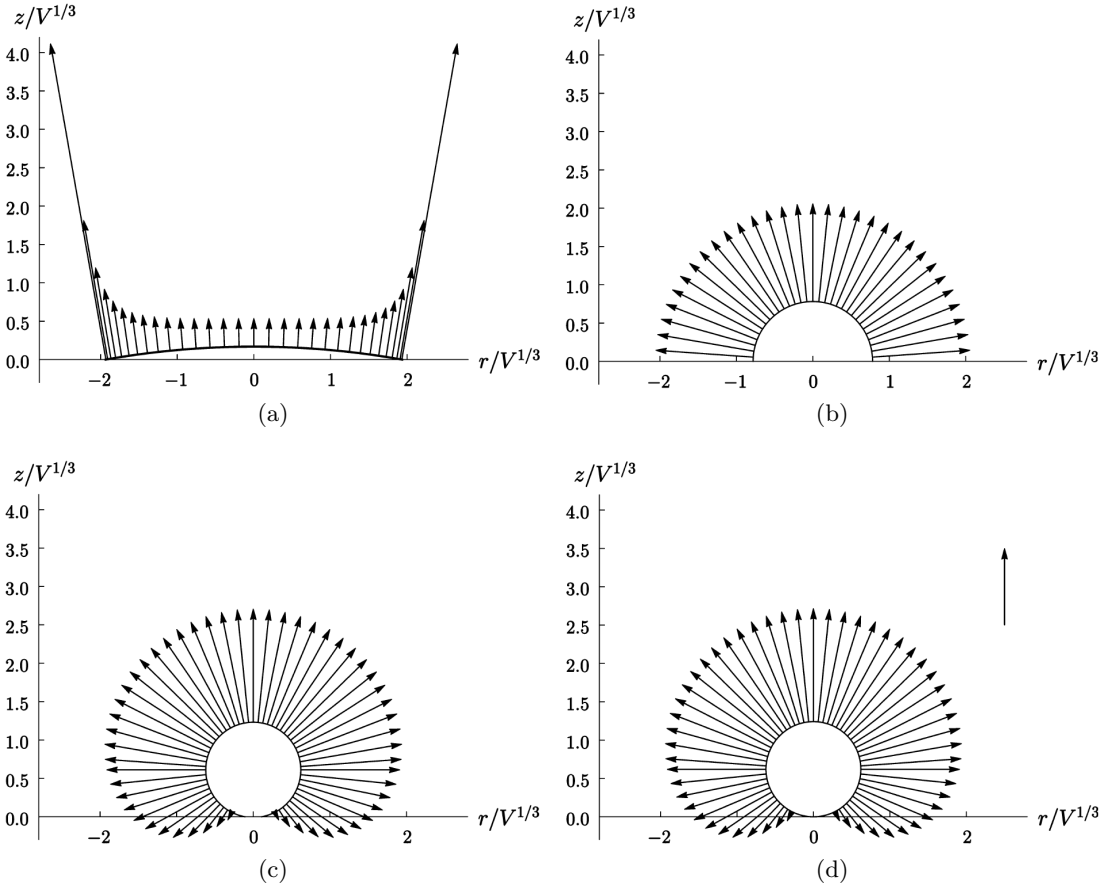

Figure 1.7: Plots of four droplets, each with the same volume, but different contact angles, namely, (a) $\hat{\theta} = \pi/18$, (b) $\hat{\theta} = \pi/2$, (c) $\hat{\theta} = 17\pi/18$, and (d) $\hat{\theta} = \pi$, together with the corresponding local evaporative flux from the free surface, shown by the arrows. Reprinted with permission from Stauber *et al.* [269] (https://pubs.acs.org/doi/10.1021/acs.langmuir.5b00286). Further permissions related to the material excerpted should be directed to the ACS.

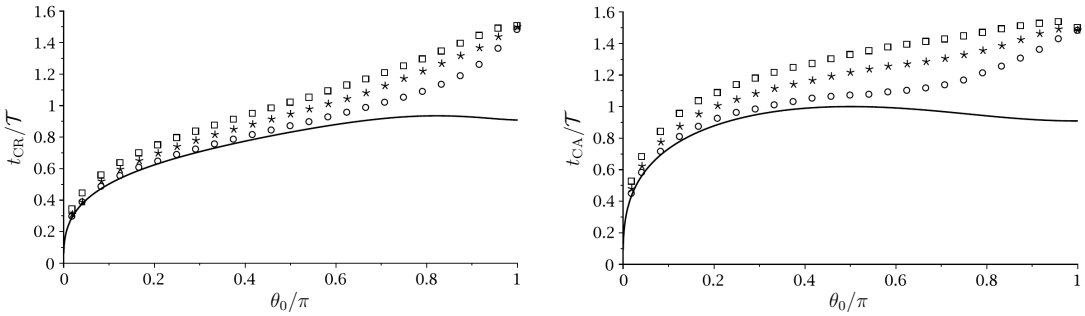

(a) (b)

Figure 1.8: Scaled lifetimes of droplets of water with initial contact radius $\hat{R}_0 = 1$ mm evaporating in (a) the CR mode and (b) the CA mode into an atmosphere of air at an ambient temperature of 295 K on substrates of aluminium (circles), HDPE (stars) and PTFE (squares) plotted as functions of the scaled initial contact angle. The solid lines show the corresponding lifetimes predicted by the diffusion-limited model. Adapted with permission from Schofield *et al.* [238]. Copyright 2021.

de-pinning (see, for example, Armstrong *et al.* [12] and Guan *et al.* [103]) which will decrease the evaporation rate from the droplet.

1.7 Non-planar substrates

So far, we have discussed situations in which droplets evaporate on planar (*i.e.* flat) substrates. In this Section we will describe the effect that substrate geometry has on the evolution of an evaporating droplet.

Droplet evaporation on non-planar substrates is of interest in a variety of applications, such as on curved (*e.g.* concave or convex) substrates in the fabrication of flexible displays (Kuang *et al.* [145]), electrochemical sensors (Pu *et al.* [222, 223]), and microlenses (Bonaccurso *et al.* [27]). Additionally, in recent years, inkjet-printing of materials (dissolved in one or more carrier solvents) into small cavities, hereafter referred to as "wells", in the substrate, the solvent thereafter evaporating to leave the desired deposit of material in the well, has become of increasing interest in the manufacture of technological displays, such as Organic-Light-Emitting-Diode (OLED) displays (see, for example, Halls [104], Levermore *et al.* [154], Madigan *et al.* [170], Shimoda *et al.* [253], Singh *et al.* [259], and Walker *et al.* [294]). Figure 1.9 shows a sketch of the

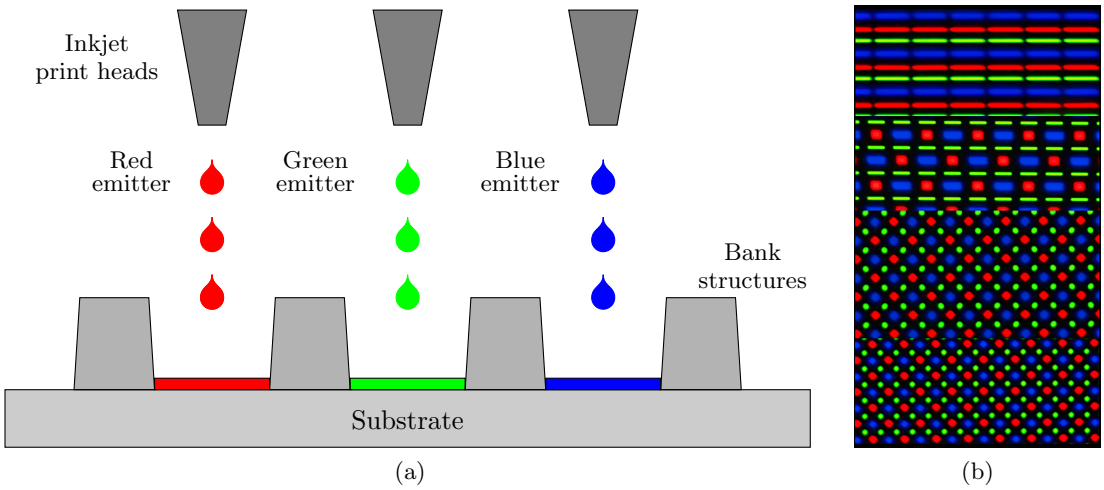

Figure 1.9: (a) A sketch of the inkjet-printing method that is used to create RGB pixels for technological displays, and (b) examples of different pixel patterns that are used in Active Matrix OLED (AMOLED) displays. Microscopic images of a Galaxy S2, S3, S4 and a Nexus 6 screen (from top to bottom). Reproduced from French [89].

inkjet-printing method that is used to create RGB pixels for technological displays, and examples of different pixel patterns that are used in Active Matrix OLED (AMOLED) displays. Inkjet printing of droplets into wells also arises in other contexts, such as, in biotechnology (see, for example, Jackman *et al.* [122] and Marizza *et al.* [180]) and the fabrication of organic transistors (see, for example, Kwak *et al.* [149]). Moreover, cylindrical wells have been used in experimental studies of the particle deposition from an evaporating droplet to ensure contact-line pinning at the lip of the well (see, for example, Jung *et al.* [126] and Kajiya *et al.* [129]). While there is a substantial body of work on the inkjet-printing process and, in particular, on the ejection of the droplets from the printheads and the subsequent dynamics of the detached droplets (see, for example, Hoath [114]), far less work has been done on the evolution of the droplets once they have been deposited into the wells.

Experimental studies have been undertaken to investigate the evolution of an evaporating droplet in a cuboidal well by van den Doel and van Vliet [290], and in a cylindrical well by Chen *et al.* [43, 45], Jung *et al.* [126], Kajiya *et al.* [129], Rieger *et al.* [226], and Vlasko-Vlasov *et al.* [291]. In particular, van den Doel and van Vliet [290] and Rieger *et al.* [226] studied the evolution of the free-surface profile of an ethylene glycol

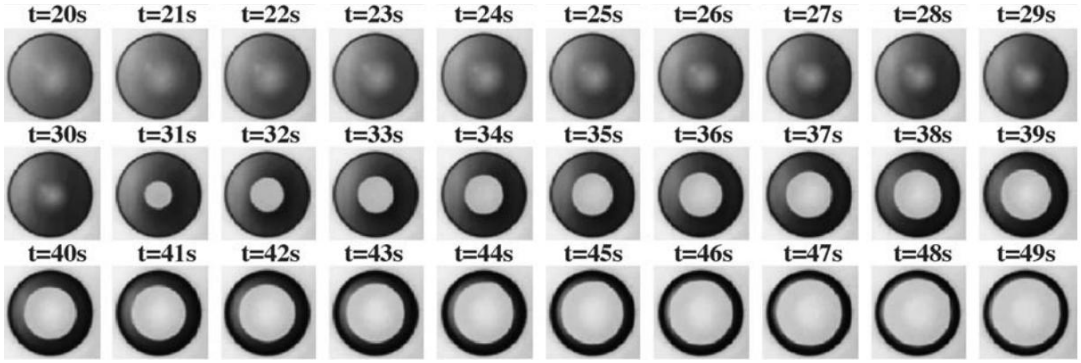

Figure 1.10: A series of top view images of a droplet evaporating in a cylindrical well of radius 250 μm and depth 65 μm. Reprinted from Chen *et al.* [45], Copyright (2006), with permission from Elsevier.

droplet before it touches the bottom of the well, hereafter referred to as "touchdown", and showed that the volume of the droplet decreases at a rate that is approximately constant in time and proportional to the length of the contact line (rather than the surface area) of the droplet (which is consistent with predictions of a diffusion-limited model). Chen *et al.* [45] investigated the evolution of a water droplet after touchdown and found that, at least for the situations they investigated, a new inner contact line appears at the centre of the well at touchdown which then recedes outwards towards the lip of the well at an approximately constant speed; their results are reproduced in Figure 1.10. Chen *et al.* [43] showed that the wettability properties of the well can have a strong effect on the evolution of the shape of the droplet, including the time of touchdown, and hence on the spatial distribution of the final deposit left in the well after a water droplet containing polystyrene particles has completely evaporated. Jung *et al.* [126] studied the evolution of, and the final deposit from, a droplet of a polymer solution whose contact line is pinned at the lip of the well, and Kajiya *et al.* [129] extended this work to investigate the effect of adding various surfactants to the droplet. More recently, Vlasko-Vlasov *et al.* [291] performed a detailed investigation of a final deposit in the form of concentric rings arising from a stick–slip motion of the receding inner contact line of a water droplet containing gold nanoparticles.

In addition to these primarily experimental studies, a number of theoretical investigations of the evaporation of a droplet in a well have also been performed. Okuzono

et al. [199] assumed the local evaporative flux from the droplet to be spatially uniform and used a thin-film approximation to analyse the evolution of, and the final deposit from, a two-dimensional droplet in a rectangular well. Subsequently, Eales *et al.* [74] used the same approach to investigate the final deposit from an axisymmetric droplet in an axisymmetric (but, in general, non-cylindrical) well. However, both of these works concern droplets of a polymer solution in which gelation (*i.e.* solidification) effects play a key role and so, unlike in the experimental observations by Rieger *et al.* [226] and Chen *et al.* [43, 45], touchdown never occurs. Ahn and Son [2] used a sharp-interface level-set method to simulate numerically the evolution of an evaporating water droplet in both cuboidal and cylindrical wells, respectively. They investigated the evolution of the shape of the droplet for situations in which both the contact line at the lip of the well and the new inner contact line at the centre of the well recede simultaneously after touchdown. They studied a range of non-zero receding contact angles $\hat{\theta}^*$ and observed an increase in the evaporation rate of the droplets as $\hat{\theta}^*$ decreases. Wang and Fukai [295] used a finite-element method to calculate numerically the local and total evaporative flux from a droplet in a cylindrical well before touchdown. They considered the situation in which the contact line is pinned at various points on the vertical side of the well (rather than at the lip of the well), and found that the confining effect of the side of the well can significantly suppress the evaporation in the vicinity of the contact line and lead to a substantial reduction in the total evaporative flux.

In related work on non-evaporating droplets, the impact and evolution of a droplet in a cuboidal well has been investigated experimentally and numerically (see, for example, Liou *et al.* [164, 165], Subramani *et al.* [272], Yang *et al.* [309], and Zhang *et al.* [318]), while Kant *et al.* [133, 134] used a combination of experimental and analytical methods to analyse the spreading of both a single droplet and a sequence of partially overlapping droplets in a "stadium-shaped" well.

Motivated by the increasing interest in inkjet-printing droplets directly into wells in the substrate during the manufacture of OLED displays, in Chapter 3 we formulate and analyse a mathematical model for the evolution of a thin droplet in a shallow axisymmetric well of rather general shape both before and after touchdown that accounts

for the spatially non-uniform evaporation of the fluid.

1.8 Gravity effects

So far, the majority of the studies discussed consider the evaporation of small (*i.e.* capillary-dominated) droplets in which gravitational effects are neglected. Specifically, they consider droplets where the appropriate characteristic length scale of the droplet $\hat{L}$ is much smaller than the capillary length $\hat{\ell} = \sqrt{\hat{\sigma}/\hat{\rho}\hat{g}}$, *i.e.* $\hat{L} \ll \hat{\ell}$, corresponding to a small Bond number $\mathrm{Bo} = (\hat{L}/\hat{\ell})^2 \ll 1$, where $\hat{\sigma}$ and $\hat{\rho}$ are the constant surface tension and fluid density, respectively, and $\hat{g}$ denotes the magnitude of acceleration due to gravity. In this case the free-surface profile of a droplet takes the form of a spherical cap, and the shapes of sessile and pendant droplets are identical. While in many cases this is the appropriate limit and this approach has given great insight into the evaporation of small droplets, there are situations in which gravitational effects are significant and it leaves the question of the effects of gravity on the evaporation of large (*i.e.* gravity-dominated) droplets unresolved.

In the following two Subsections we will discuss the effect of gravity on droplet shape and droplet evaporation in turn, with particular interest in the influence of droplet orientation, *i.e.* whether the droplet is sessile or pendant.

1.8.1 Droplet shape

The shape of static sessile and pendant droplets under the effect of gravity is a classical problem that has been studied for over 150 years (see, for example, Bashforth and Adams [21], Boucher and Evans [30], Boucher *et al.* [31], Fordham [85], Middleman [186], Padday [202, 203], Padday and Pitt [204], and Worthington [304]). Figure 1.11 shows a sketch of the static shapes of sessile and pendant droplets for increasing volume with small contact angle $\hat{\theta} \ll 1$.

Early numerical calculations of the static shapes of axisymmetric droplets by, for example, Boucher and Evans [30], Padday [202, 203], and Padday and Pitt [204] show that, for droplets on planar substrates, the volume of a sessile droplet may become

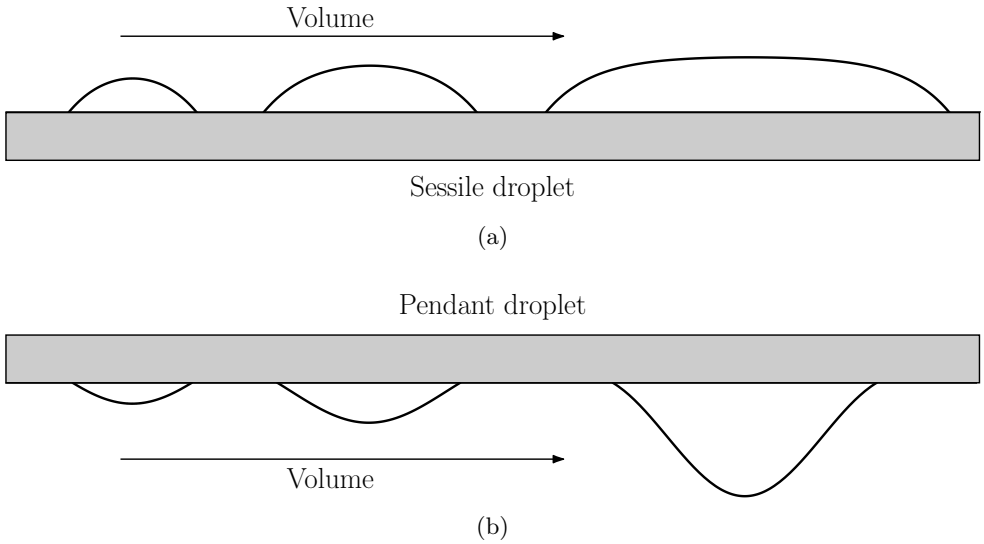

Figure 1.11: Sketch of the static shapes of (a) sessile and (b) pendant droplets for increasing volume with small contact angle $\hat{\theta} \ll 1$.

arbitrarily large, with the contact radius increasing and the free-surface profile flattening with increasing volume, whereas, there is a finite maximum volume of a pendant droplet (hereafter referred to as the detachment volume), at which the droplet will fall off the substrate. Padday [203] showed that, for any $0 < \hat{\theta} < \pi$, the height at the centre of a sessile droplet increases with volume until a maximum value is reached at an intermediate volume, and thereafter decreases to a limiting value as volume of the droplet becomes large. Wente [297] conducted a rigorous mathematical investigation of the stability of axisymmetric pendant droplets proving that, for any $0 < \hat{\theta} < \pi$, the free-surface profile of the droplet increases everywhere and the contact radius of the droplet increases with volume until a maximum contact radius is reached; thereafter the droplet becomes unstable, and the contact radius then decreases until the detachment volume is reached. Additionally, Wente [297] showed that, in general, a stable pendant droplet will not have more than one inflection point (sometimes also referred to as a "neck") in its free-surface profile and that for the case of thin droplets, *i.e.* for droplets with small contact angle $\hat{\theta} \ll 1$, the volume of the droplet will reach the detachment volume before the appearance of the inflection point in the free-surface profile. The stability of sessile and pendant droplets for situations in which the contact

radius of the droplet is limited by the radius of the substrate (sometimes referred to as the $\hat{R}$-limited case), *e.g.* for droplets on rods, in which both sessile and pendant droplets have a detachment volume, has also been investigated (see, for example, Padday and Pitt [204]).

More recently, in related work, the effect of gravity on the the spreading of non-evaporating droplets has been investigated theoretically and numerically (see, for example, Bartashevich *et al.* [20], Brochard-Wyart *et al.* [34], de Gennes [60], Lubarda and Talke [169], Mistry and Muralidhar [187], and Savva and Kalliadasis [236]). In particular, Brochard-Wyart *et al.* [34] analysed the spreading of sessile droplets on a planar substrate, quantifying three different regimes depending on the size of the contact radius $\hat{R}$ in which capillary forces, gravity forces, and viscous dissipation compete to determine the shape of the free surface.

1.8.2 Droplet evaporation

Experimental studies have been undertaken to investigate the effect of gravity on the evolution of evaporating sessile droplets by Kadhim *et al.* [127] and Carle *et al.* [37]. In particular, Kadhim *et al.* [127] studied the evaporation of small and large sessile water droplets on hydrophobic and hydrophilic heated substrates and compared the results with numerical solutions for the evolution based on the crude assumption that the droplet is a spherical cap. The numerical solutions are in agreement with the experimental results for a sessile droplet evaporating on hydrophilic substrate in which the droplet remains approximately spherical. However, the numerical results do not accurately predict the evaporation rate of large droplets evaporating on hydrophilic substrates, which they attribute to deviations of the droplet shape from a spherical cap. Carle *et al.* [37] investigated the evaporation of pinned sessile ethanol droplets in normal (terrestrial) and reduced gravity conditions on a heated aluminium substrate. Their study shows that the diffusion-limited model is appropriate for ethanol droplets evaporating in microgravity; however, in normal gravity, natural convection is enhanced and its effect on evaporation increases with substrate temperature.

The evaporation of sessile and pendant droplets has been compared experimentally

to determine the effect of droplet orientation on the evolution of an evaporating droplet (see, for example, Moore *et al.* [191]) and on the flow within an evaporating droplet (see, for example, Edwards *et al.* [75], Li *et al.* [157], Masoudi and Kuhlmann [183], and Prahdan and Panigrahi [221]). In particular, Moore *et al.* [191] experimentally studied the evaporation rates of sessile and pendant droplets of different fluids evaporating on substrates of varying wettability. They showed that the de-pinning time of a droplet evaporating in the SS mode depends on whether the droplet is sessile or pendant, and that sessile droplets evaporate approximately $16 - 35\%$ faster than pendant droplets, depending on the fluid and substrate used, even for relatively small droplets of volume 4–8 μL, corresponding to a Bond number of order between 10^{-2} and 10^{-1}. They attribute this difference to a combination of buoyancy effects in the atmosphere and gravitational effects on the shape and contact-line pinning of the droplet. Edwards *et al.* [75] and Li *et al.* [157] investigated the flow within small (microlitre-sized) evaporating binary sessile and pendant droplets. Both studies observed droplet orientation-dependent flow which they attribute to buoyancy effects from density gradients within the droplets that arise due to the different evaporation rates of the two components of the binary droplets. In addition, Edwards *et al.* [75] did not observe flow reversal in the later stages of evaporation (*i.e.* when the more volatile fluid has completely evaporated), showing that buoyancy-driven convection in the atmosphere does not influence the flow in this situation. In addition, the effect of droplet orientation on the deposition from evaporating droplets has also been investigated (see, for example, Devlin *et al.* [66], Hampton *et al.* [106], Li *et al.* [156], Sandu and Fleaca [234], Sandu *et al.* [233, 235], and Sommer [265]).

There have been a few theoretical investigations of the effect of gravity on the evolution of an evaporating sessile droplet. Barash *et al.* [19] numerically investigated the evaporation of a sessile toluene droplet undergoing diffusion-limited evaporation with a pinned contact line and contact radius $\hat{R}$ approximately equal to the capillary length $\hat{\ell}$. They showed that the local evaporative flux from the droplet under the effect of gravity is smaller near the apex of the droplet and larger near the contact line of the droplet in comparison with the solution when the droplet is assumed to take the

shape of a spherical cap (corresponding to a small droplet, as shown in Figure 1.7(a), or a droplet in a low-gravity environment), but that the total evaporative flux from the droplet agrees well with the spherical-cap approximation. Kolegov and Lobanov [143] modelled the evolution of a thin pinned sessile evaporating droplet under the effect of gravity. They proposed an idealised expression for the local evaporative flux to mimic diffusion-limited evaporation and performed numerical calculations to determine the behaviour of the flow within the droplet. The study shows that while for a droplet with large Bo, *i.e.* $\mathrm{Bo} \gg 1$, the free surface of the droplet is far from the typical spherical-cap shape, the qualitative behaviour of the radially-outward flow within the droplet does not change. As far as we are aware, there have been no theoretical studies that investigate the effect of gravity on the evolution of a droplet evaporating in other modes of evaporation.

In Chapter 4 we formulate and analyse a mathematical model for the shape, evolution, and lifetime of thin sessile and pendant droplets evaporating in the CR, CA, SS, and SJ modes under the effect of gravity.

1.9 The coffee-ring effect

As previously discussed in Section 1.3, the coffee-ring effect is the formation of a ring deposit near the contact line after the complete evaporation of a pinned droplet containing suspended particles. As explained by Deegan *et al.* [64] for the case of a thin pinned droplet evaporating according to the diffusion-limited model, the ring deposit is a consequence of radially outward capillarity-driven flow inside the droplet that advects particles towards its pinned contact line. In particular, as the fluid evaporates, the free-surface profile of the droplet diminishes and fluid that has evaporated near the contact line must be replenished by fluid from the bulk of the droplet. Thus, there is an outward flow that carries the particles to the contact line. Boulogne *et al.* [32] obtained the exact solution for the flow within a thin pinned droplet evaporating according to the diffusion-limited model; typical instantaneous streamlines of the flow are shown in Figure 1.12. In addition, the solutions for the flow within a non-thin pinned

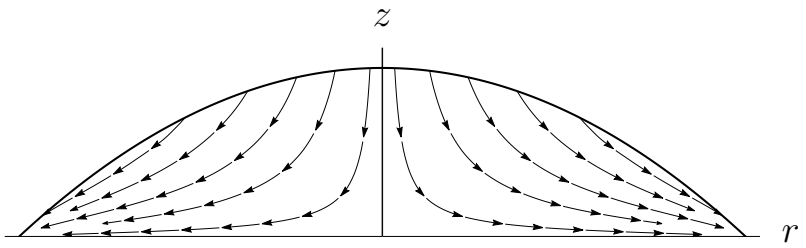

Figure 1.12: Instantaneous streamlines of the flow within a thin pinned droplet evaporating according to the diffusion-limited model.

droplet evaporating according to approximate and modified versions of the diffusion-limited model have been obtained by, for example, Hu and Larson [118] and Masoud and Felske [181].

Previous studies have quantified the growth of the ring deposit analytically for diffusion-limited evaporation (Deegan *et al.* [64], Boulogne *et al.* [32]) and for spatially-uniform evaporation (Boulogne *et al.* [32]), under the assumption that the particles are passive and are simply advected by the flow (sometimes referred to as "tracer particles"). In addition, Boulogne *et al.* [32] compared the theoretical predictions for the growth of the ring deposit with experimental observations for both diffusion-limited and spatially-uniform evaporation, finding good agreement. The geometry and density of the ring deposit have also been investigated. Popov [220] modelled the width and height of the deposit for diffusion-limited evaporation by considering an incompressible "deposit phase" in which the concentration of deposited particles remains constant after reaching some maximum packing value, resulting in a ring deposit whose inner boundary moves radially inwards. Zheng [320] extended the work of Popov [220] by considering a deposit phase in which the deposit that is formed assumes the same shape as the droplet, compressing vertically as the droplet evaporates, such that the concentration of deposited particles varies in both space and time. Zheng [320] obtained an analytical expression for the radially-varying density of the ring deposit, and compared the results for diffusion-limited and spatially-uniform evaporation. Kajiya *et al.* [128] conducted experiments to visualize the concentration profile inside an evaporating droplet and showed that the thickness of the ring deposit is dependent on the qualitative form of the local evaporative flux, with a broader ring and larger film thick-

ness at the centre of the droplet for nearly spatially-uniform evaporation in comparison with diffusion-limited evaporation. Berteloot *et al.* [22] experimentally studied the different growth phases of the ring, including the initial growth of the deposit near the contact line, the motion of the deposition front that moves inwards from the contact line to the centre of the droplet, and the cracks and delamination that were observed to occur at the inner boundary of the ring deposit towards the end of evaporation. Marin *et al.* [178, 179] conducted experiments to investigate the final structure of the ring, concluding that the rapid acceleration of particles towards the contact line during the final stages of evaporation, which they termed "the rush-hour effect" due to an increase in the magnitude of flow towards the contact line (see, for example, Hamamoto *et al.* [105]), results in a lack of order of the particles at the inner boundary of the ring deposit.

As discussed in Section 1.3, a wide variety of other types of deposit have been observed and so before discussing the deposition further we seek to clarify the terminology regarding these different deposit types. Figure 1.13 shows a sketch of the different deposit types described in the literature and the terminology that will be used to describe them throughout the remainder of this thesis.

There have been several extensions to the model proposed by Deegan *et al.* [64] for the deposition from an evaporating droplet that have been used to investigate the dynamics of the evaporation and fluid flow near the contact line of the droplet when the concentration of particles becomes large. Tarasevich *et al.* [283] and Vodolazskaya and Tarasevich [292] modelled and numerically investigated an evaporating droplet on a planar substrate taking into account the gelation of solutions by proposing an expression for the local evaporative flux which decreases as the concentration of particles increases, and by considering the viscosity of the solution as a function of particle concentration. Their model predicts a transition from ring deposits to near-uniform deposits depending on the initial concentration of particles and the strength of capillary effects. Kaplan and Mahadevan [135] proposed a multiphase model that couples evaporation-driven flow in the bulk of the droplet, where the concentration of particles is relatively low, to a region of Darcy flow near the contact line, forming an effective porous medium, where

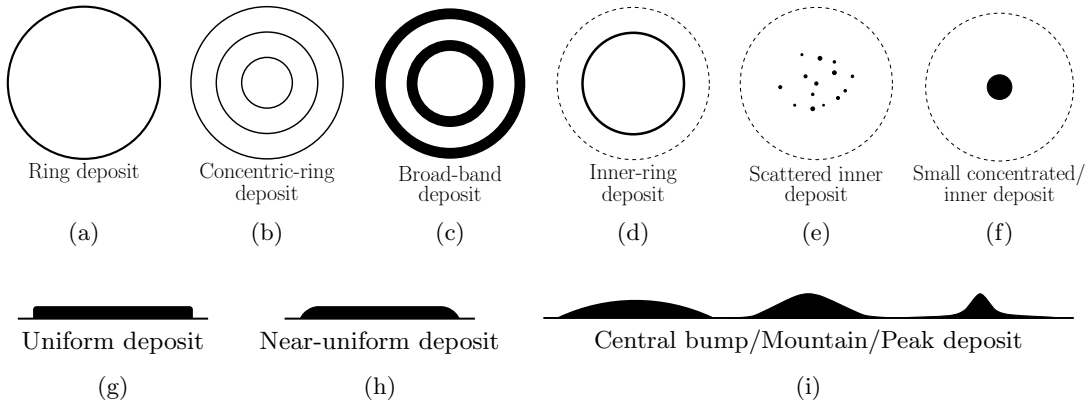

Figure 1.13: A sketch of different deposit types described in the literature: Top view schematic of (a) a ring deposit, (b) a concentric-ring deposit, (c) a broad-band deposit, (d) an inner-ring deposit, (e) a scattered inner deposit, and (f) a small concentrated or inner deposit, and cross-sectional views of (g) a uniform deposit, (h) a near-uniform deposit, and (i) three different deposit types that are more concentrated at the centre of the droplet than at the contact line, typically termed a central bump, mountain, or peak deposit. The dashed lines in (d)–(f) indicate the initial contact line of the droplet.

the concentration of particles is relatively high. This model predicts various deposit types, such as uniform deposits, single or concentric rings, and broad bands, depending upon the initial concentration of particles and the relative magnitude of viscous forces to capillary forces. Recently, Moore *et al.* [192] performed an asymptotic analysis for the concentration of particles in the limit of small particle diffusion, accounting for the effects of particle diffusion in a boundary layer near the contact line of the droplet in which the concentration of particles is large but not yet at its maximum packing value. Their study shows that particle diffusion drives the formation of the ring deposit and that a droplet undergoing diffusion-limited evaporation will produce a thinner ring shape in the concentration profile than for spatially-uniform evaporation.

In addition, whilst the majority of the literature focuses on single axisymmetric droplets, recently there have been advances in modelling the deposition from a non-axisymmetric droplet (see, for example, Sáenz *et al.* [232]) and from multiple droplets (see, for example, Hu *et al.* [120] and Wray *et al.* [306]).

The studies discussed in this Section show that factors such as the local evaporative flux and particle concentration can have an effect on the shape of the final deposit from

an evaporating droplet. In the next Section we will further discuss the mechanisms that control particle deposition.

1.10 Controlling particle deposition

As discussed in Section 1.3, the ability to control the shape of the final deposit from an evaporating droplet is key in numerous applications, and therefore a variety of methods of control have been explored in the literature (see, for example, the review articles by Al-Milaji and Zhao [6], Anyfantakis and Baigl [9], Kolegov and Barash [142], Kuang *et al.* [146], Larson [150], Mampallil and Eral [176], Parsa *et al.* [212], Sefiane [242], Shao *et al.* [251], Yang *et al.* [311], and Zhong *et al.* [321], and the many references therein). In general, control over deposition can be achieved by influencing the flow within the droplet through, for example, contact-line de-pinning, the presence of Marangoni flow, or manipulation of the vapour field, as well as by promoting particle trapping or gelation through, for example, particle–free-surface, particle–particle and particle–substrate interactions. Table 1.2 provides examples of different methods used in experimental investigations to control the deposition from an evaporating droplet. Four mechanisms that can be manipulated to change the shape of the final deposit from an evaporating droplet are discussed below.

1.10.1 Contact-line de-pinning

A pinned contact line is required for a ring deposit to form, and so, a simple and effective way of changing the shape of the final deposit is through controlling contact-line de-pinning. The final deposit observed after the complete evaporation of a droplet in the CR, CA, SS, and SJ modes is typically a ring deposit near the contact line of the droplet (see, for example, Deegan *et al.* [64]), a small concentrated deposit or a mountain deposit (see, for example, Patil *et al.* [214] and Willmer *et al.* [301]), an inner-ring or a small concentrated deposit (see, for example, Li *et al.* [160, 161]), and multiple ring deposits (see, for example, Askounis *et al.* [16] and Orejon *et al.* [200]), respectively. Table 1.2 includes examples of experimental investigations that use contact-line de-

Mechanism manipulated	Method	Example references
Contact line de-pinning	Electrowetting	[77]
	Particle properties	[25], [125], [312]
	Substrate coatings	[56], [92], [158]
	Substrate wettability	[25], [49], [153], [160], [158], [214]
Marangoni flow	Binary fluids	[139], [209], [282], [323]
	External vapour source	[113], [172], [173]
	Heating	[42], [159], [175], [211, 213], [214], [277], [313], [322]
	Surfactants	[129], [139], [246], [271]
Vapour field	Ambient pressure	[16]
	Controlled airflow	[310]
	Liquid bath	[64], [128]
	Masking/confinement	[64], [108–110], [230]
	Relative humidity	[29], [48]
Particle interactions	Base fluid composition	[11], [23], [54], [65], [70], [139], [231]
	Electrowetting	[201]
	Particle concentration	[10], [153], [174]
	Particle material	[10], [65]
	Particle shape	[70], [315, 316]
	Particle size	[18], [153], [174, 175], [231]

Table 1.2: Examples of different methods used in experimental investigations to control the deposition from an evaporating droplet.

pinning to control the deposition from an evaporating droplet. In particular, transitions from ring or concentric-ring deposits for droplets evaporating in the CR and the SJ modes of evaporation (*i.e.* when contact-line pinning occurs) to small concentrated deposits for droplets evaporating in the CA mode of evaporation (*i.e.* when no contact-line pinning occurs) have been reported by authors allowing droplets to evaporate on substrates of different wettability (see, for example, Biswas *et al.* [25], Chhasatia and Yun [49], Lee *et al.* [153], and Patil *et al.* [214]) or on oil-coated substrates (see, for example, Das *et al.* [56], Goa *et al.* [92] and Li *et al.* [158]), and by applying an electric field to an evaporating droplet, to induce electrowetting (see, for example, Eral *et al.* [77]). Additionally, it has been shown that particle properties such as size and concentration can have an effect on the motion of the contact line, and hence on the deposition from an evaporating droplet. Orejon *et al.* [200] showed that nanoparticles promote contact-line pinning, and therefore ring deposits, on hydrophilic substrates, and SJ contact-line motion, and therefore concentric-ring deposits, on hydrophobic substrates. Yang *et al.* [312] observed a transition from a ring deposit to a concentric-ring deposit from a droplet evaporating on a hydrophilic substrate by increasing the initial concentration of nanoparticles within the droplet. Yang *et al.* [312] also showed a transition from ring and concentric-ring deposits to spoke-like deposits by increasing the size of the particles from 20 nm to 200 nm, which they attribute to partial contact-line pinning when the particles are larger. On the other hand, a scattered inner deposit or an inner-ring deposit is typically observed after the complete evaporation of droplets containing microparticles due to an absence of contact-line pinning for most or all of the lifetime of the droplet (see, for example, Biswas *et al.* [25] and Jung *et al.* [125]).

In addition, the deposition from an evaporating droplet with a moving contact line has been studied theoretically and numerically (see, for example, Freed-Brown [88], Man and Doi [177], and Zigelman and Manor [324]). Freed-Brown [88] analysed a droplet undergoing spatially-uniform evaporation in the CA mode. As the droplet evaporates, the flow advects particles inwards towards the centre of the droplet. However, the receding contact line moves faster than the flow and so some particles are "caught" by the moving contact line at which point they are then deposited. Therefore deposi-

tion occurs gradually throughout evaporation, and the model predicts a peak deposit. Subsequently, Man and Doi [177] showed a transition from ring deposits to the peak deposits predicted by Freed-Brown [88] for a droplet undergoing spatially-uniform evaporation in the CA mode when the mobility of the contact line is increased. Zigelman and Manor [324] analysed the deposition from a droplet evaporating in the SJ mode, predicting concentric-ring deposits in which the spacing between the rings decreased logarithmically towards the centre of the droplet. In related work, Fraštia *et al.* [86,87] numerically investigated the deposition of line structures from an evaporating thin film with SJ contact-line motion and showed that the number and regularity of the deposited lines depend on the evaporation rate of the film and the initial concentration of particles within the film.

1.10.2 Marangoni flow

The coffee-ring effect is driven by radially-outward capillary flow, and so one natural way to change the shape of the final deposit is to induce a radially-inwards or a recirculating flow. Marangoni flow is driven by surface-tension gradients along the free surface of a droplet. This surface-tension gradient can be induced by either a temperature gradient or a concentration gradient at the free surface of the droplet, corresponding to thermal and solutal Marangoni flow, respectively. Hu and Larson [119] observed experimentally that, while the coffee-ring effect was present after the evaporation of a water droplet, some particles were deposited onto the substrate at the centre of the droplet after the evaporation of an octane droplet. They showed that a non-uniform distribution of the local temperature was present within the octane droplet due to strong evaporative cooling, which led to a recirculating thermal Marangoni flow that carried particles towards the centre of the droplet. They concluded that Marangoni flow must be suppressed in order to observe the coffee-ring effect after the complete evaporation of a pinned droplet. Following Hu and Larson [119], Ristenpart *et al.* [227] demonstrated experimentally and theoretically the effect of the thermal conductivity of the substrate and the fluid on the magnitude and circulation direction of the thermal flow, and hence on the deposition from an evaporating droplet. Table 1.2 includes

examples of experimental investigations that used Marangoni flow to control the deposition from an evaporating droplet. In particular, authors have reported transitions in the shape of the final deposit by inducing Marangoni flows through the addition of a more/less volatile fluid (see, for example, Kim *et al.* [139], Park and Moon [209], Talbot *et al.* [282], and Zhong and Duan [323]), the presence of an external vapour source (see, for example, Hedge *et al.* [113], Majumder *et al.* [172], and Malinowski *et al.* [173]), substrate heating (see, for example, Li *et al.* [159], Malla *et al.* [175], Parsa *et al.* [211, 213], Patil *et al.* [214], and Zhong and Duan [322]), heating the fluid prior to evaporation (see, for example, Chatterjee *et al.* [42]) or during evaporation via an external laser (see, for example, Ta *et al.* [277] and Yen *et al.* [313]), and the addition of surfactants (see, for example, Kajiya *et al.* [129], Kim *et al.* [139], Seo *et al.* [246], and Still *et al.* [271]).

1.10.3 Manipulation of the vapour field

Another method that can be used to disturb the radially-outward capillary flow within a pinned evaporating droplet is manipulation of the vapour field, and hence the local and total evaporative fluxes from the droplet. This method has the advantage that it does not require modification of the substrate or fluid composition. Table 1.2 includes examples of experimental investigations that manipulate the form of the vapour field to control the deposition from an evaporating droplet. In particular, authors have reported a change in the shape of the final deposit from an evaporating droplet by reducing the ambient pressure in the atmosphere to increase the evaporation rate from the droplet (see, for example, Askounis *et al.* [16]), using a controlled airflow above the droplet to enhance evaporation from its centre (see, for example, Yang *et al.* [310]), surrounding the droplet with a liquid bath and/or confining the droplet within a chamber to suppress evaporation near the contact line (see, for example, Deegan *et al.* [64] and Kajiya *et al.* [128]), placing the droplet underneath a mask in order to achieve a desired pattern of evaporation enhancement/suppression (see, for example, Harris *et al.* [108–110]), and increasing the relative humidity of the atmosphere to decrease the evaporation rate from the droplet (see, for example, Bou Zeid and Brutin [29]

and Chhasatia *et al.* [48]). Other studies have explored manipulating the form of the vapour field of an evaporating thin film through the use of a controlled airflow (see, for example, Wedershoven *et al.* [296]) and masking (see, for example, Cavadini [39], Parneix [210], and Routh and Russell [230]). Figure 1.14 shows examples of controlling the deposition from an evaporating droplet through manipulation of the form of the vapour field in experiments by (a) Askounis *et al.* [16] in which a water droplet containing SiO_2 nanoparticles evaporated under decreasing values of the atmospheric pressure, (b) Yang *et al.* [310] in which a water droplet containing polytetrafluoroethylene (PTFE) nanoparticles evaporated without and with a controlled airflow above the droplet, (c) Chhasatia *et al.* [48] in which a deionized water droplet evaporated under increasing values of the relative humidity, and (d) Deegan *et al.* [64] in which a water droplet containing polystyrene particles evaporated in a quiescent atmosphere, surrounded by a liquid bath, and confined by a chamber with a small hole above the centre of the droplet. In particular, Figure 1.14 shows that the shape and characteristics of the final deposit depend upon both the total evaporative flux from the droplet and the spatial variation of the local evaporative flux.

The concept of masking was first explored by Routh and Russell [230] for evaporating thin films, and subsequently by Deegan *et al.* [64] for evaporating droplets, as a simple way of controlling the deposition process. Deegan *et al.* [64] carried out three experiments involving a droplet evaporating under different conditions; their results are reproduced in Figure 1.14(d). They found that when the droplet evaporated in a quiescent atmosphere and surrounded by a liquid bath, corresponding to diffusion-limited and spatially-uniform evaporation, respectively, there is a radially-outward flow that causes a ring deposit to form near the contact line. However, when a droplet was confined by a chamber with a hole in the centre, producing a local evaporative flux profile that was proportional to the rate of decrease of the height of the droplet, the deposit shape was nearly uniform. Harris *et al.* [109] further investigated the effect of manipulating the spatial variation of the local evaporative flux by evaporating droplets under a mask with multiple holes. The mask induced periodic variations in the local evaporative flux profile and produced deposits that were concentrated below the holes in the

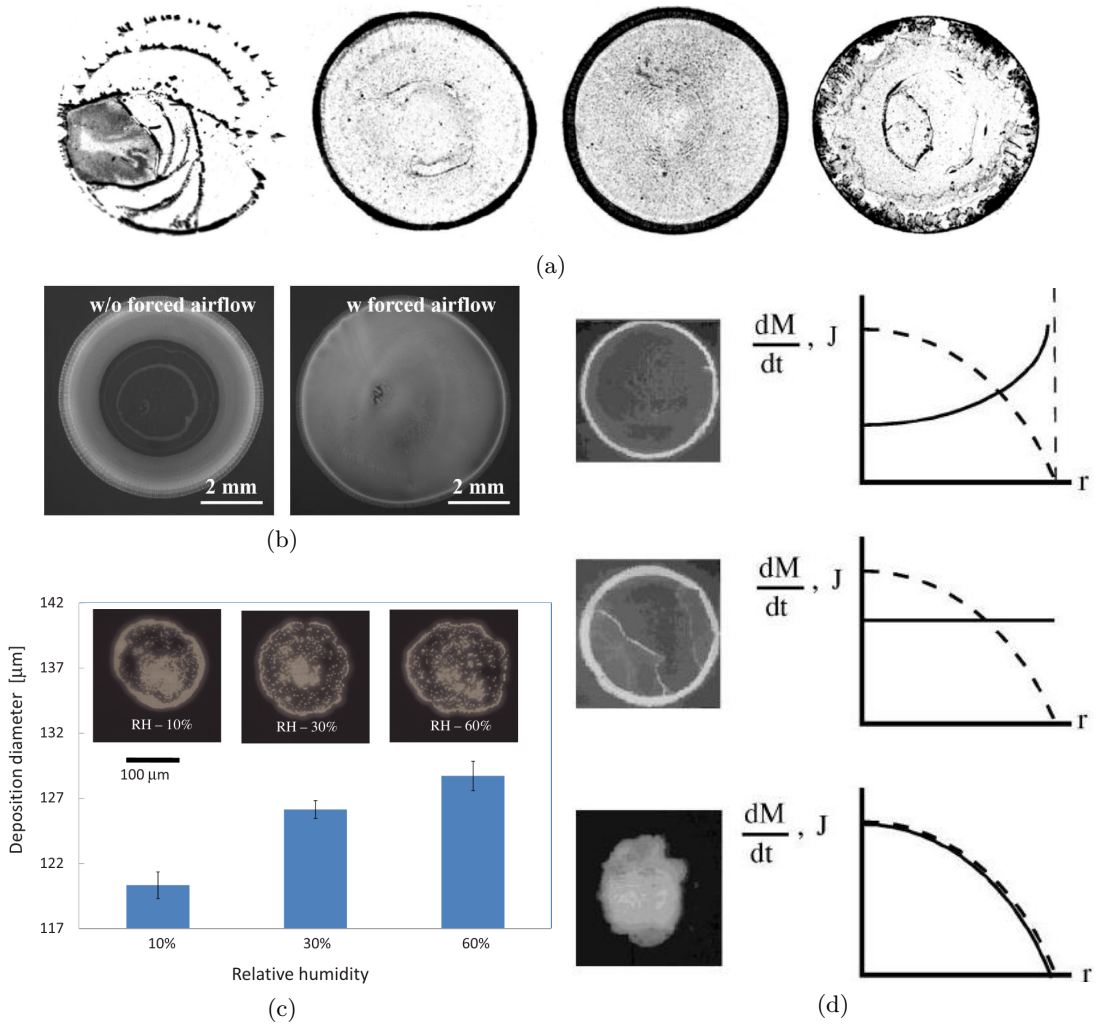

Figure 1.14: Examples of controlling the deposition from an evaporating droplet through manipulation of the form of the vapour field. Final deposit after the complete evaporation of: (a) A water droplet containing SiO_2 nanoparticles under 750, 500, 250 and 100 mbar atmospheric pressure (left to right). Reprinted from Askounis *et al.* [16], Copyright (2014), with permission from Elsevier. (b) A water droplet containing polytetrafluoroethylene (PTFE) nanoparticles without (left) and with (right) a controlled airflow above the droplet. Reprinted from Yang *et al.* [310], with the permission of AIP Publishing. (c) A deionized water droplet containing polystyrene particles for increasing values of the relative humidity. Reprinted from Chhasatia *et al.* [48], with the permission of AIP Publishing. (d) A water droplet containing polystyrene particles allowed to evaporate in a quiescent atmosphere, surrounded by a liquid bath, and confined by a chamber with a small hole above the centre of the droplet (top to bottom in the left column). A schematic plot of the local evaporative flux (solid lines) and the rate of decrease of the free surface of the droplet (dashed lines) is shown in the right column. Reprinted figure with permission from Deegan *et al.* [64]. Copyright 2000 by the American Physical Society.

mask, *i.e.* the mask provided a template for the shape of the final deposit. Tarasevich *et al.* [284] then developed a theoretical model using an idealised local evaporative flux to mimic the influence of a mask with three or four circular holes above the droplet to simulate the behaviour observed experimentally by Harris *et al.* [109]. Vodolazskaya and Tarasevich [293] generalised this model to account for the diffusion of vapour in the atmosphere, used this model to calculate the local evaporative flux numerically, and investigated the effects of the distance between the mask and the droplet, the radius of the holes in the mask, and the spacing between the holes, on the local evaporative flux and the shape of the final deposit. Parneix *et al.* [210] experimentally and numerically investigated the effect of placing an obstacle above an evaporating thin film and found that the evaporation, and therefore the deposition, was reduced under the masked region. One restriction on the practical uses of masking is that it reduces the evaporation rate from the droplets and therefore lengthens the total drying time. A combination of masking and heating via an infra-red lamp has been investigated experimentally by Georgiadis *et al.* [99, 100] and numerically by Kolegov [141] who confirmed that the heating increases the evaporation rate of the droplet.

In Chapter 5 we investigate the effect of spatial variation in the local evaporative flux on the deposition from an evaporating droplet. In particular, we identify when suppression of evaporation near the contact line of the droplet is sufficient to change the shape of the final deposit.

1.10.4 Particle interactions

So far, we have discussed control of the deposition from an evaporating droplet through manipulation of the flow within the droplet. In reality, the shape of the final deposit will be determined by both the flow within the droplet and the particle interactions present, with various forces, such as capillary, electrostatic, and van der Waals forces, contributing to the particle interactions. Table 1.2 includes examples of experimental investigations that control the deposition from an evaporating droplet by promoting particle–free-surface, particle–particle, and particle–substrate interactions. In particular, authors have reported a change in the shape of the final deposit from an evapo-

rating droplet through particle trapping and/or gelation by modifying the composition of the fluid through the addition of polymers (see, for example, Kim *et al.* [139] and Ryu *et al.* [231]), proteins (see, for example, Devineau *et al.* [65]), and surfactants (see, for example, Anyfantakis *et al.* [11] and Crivoi *et al.* [54]), or by changing the acidity/basicity (*i.e.* the pH) of the fluid (see, for example, Bhardwaj *et al.* [23] and Dugyala *et al.* [70]), and through the properties of the particles within the droplet such as particle concentration (see, for example, Anyfantakis *et al.* [10], Lee *et al.* [153], and Malla *et al.* [174]), material (see, for example, Anyfantakis *et al.* [10] and Devineau *et al.* [65]), shape (see, for example, Dugyala *et al.* [70] and Yunker *et al.* [315,316]), and size (see, for example, Bansal *et al.* [18], Lee *et al.* [153], Malla *et al.* [174,175], and Ryu *et al.* [231]). In addition, Orejon *et al.* [201] showed that electrowetting on dielectrics promotes particle–substrate interactions, termed electrophoresis. They observed transitions from concentric-ring deposits from droplets containing TiO_2 nanoparticles evaporating in the SJ mode of evaporation to uniform deposits from droplets evaporating in the CA mode under a direct current (DC) voltage. They attribute the uniform deposits to a shorter timescale for electrophoretic mobility of particles towards the substrate than the evaporation-driven particle advection towards the contact line. Figure 1.15 shows examples of controlling the deposition from an evaporating droplet through particle interactions in experiments by (a) Anyfantakis *et al.* [11] in which a water droplet containing anionic polystyrene particles (PS-AA) evaporated without and with the addition of a charged surfactant dodecyltrimethylammonium bromide (DTAB), (b) Yunker *et al.* [316] in which a water droplet containing spherical and ellipsoidal polystyrene particles evaporated, (c) Bhardwaj *et al.* [23] in which a water droplet containing titania particles of different pH values evaporated, and (d) Kim *et al.* [138] in which an ethanol and water droplet containing polystyrene particles evaporated without and with the addition of substrate-absorbent polymers. In particular, particle–free-surface, particle–particle, and particle–substrate interactions can promote transitions from ring or concentric-ring deposits to more uniform deposits, as illustrated in Figures 1.15(a), (b), and (c,d), respectively.

In addition, there have been various theoretical and numerical studies that investi-

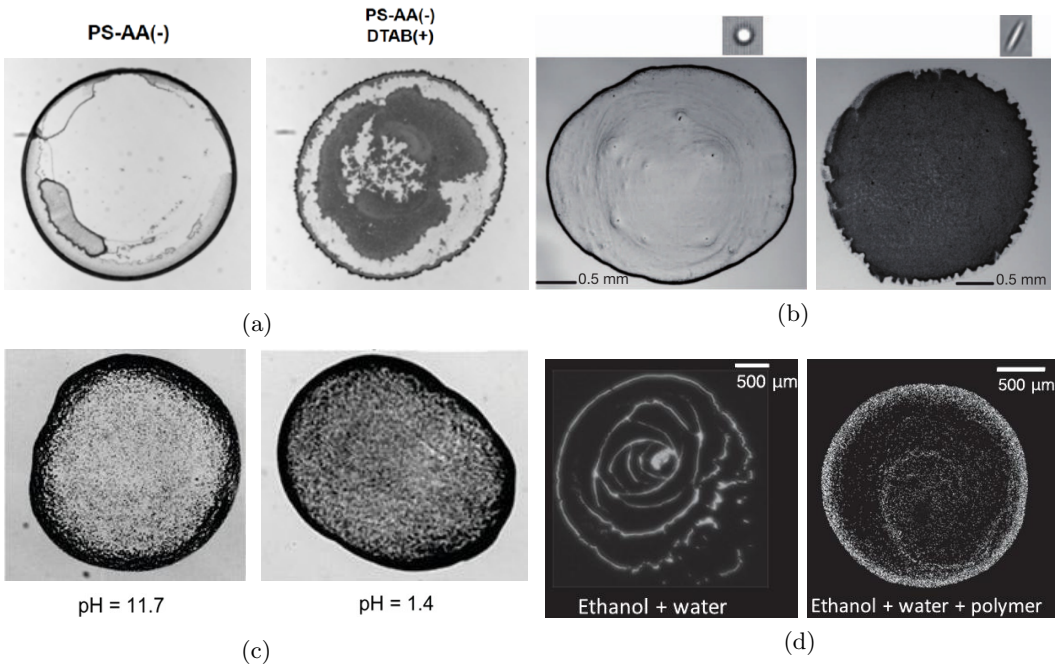

Figure 1.15: Examples of controlling the deposition from an evaporating droplet through the promotion of particle interactions. Final deposit after the complete evaporation of: (a) A water droplet containing anionic polystyrene particles (PS-AA) without (left) and with (right) the addition of a charged surfactant dodecyltrimethylammonium bromide (DTAB). Adapted with permission from Anyfantakis *et al.* [11]. Copyright 2015 American Chemical Society. (b) A water droplet containing spherical (left) and ellipsoidal (right) polystyrene particles. Reprinted by permission from Springer Nature: Yunker *et al.* [316], Copyright (2011). (c) A water droplet containing titania particles with pH values of 11.7 (left) and 1.4 (right). Reprinted with permission from Bhardwaj *et al.* [23]. Copyright 2010 American Chemical Society. (d) An ethanol and water droplet containing polystyrene particles without (left) and with (right) the addition of substrate-absorbent polymers. Reprinted figure with permission from Kim *et al.* [139]. Copyright 2016 by the American Physical Society.

gate the deposition from an evaporating droplet that incorporate particle interactions (see, for example, Crivoi and Duan [53], Crivoi *et al.* [54], Pham and Kumar [216], Ren *et al.* [225], Siregar *et al.* [260], Sung *et al.* [275], Widjaja and Harris [298], and Zigelman and Manor [325,326]). In particular, Zigelman and Manor [325,326] studied the effect of particle–substrate adsorption and particle–particle aggregation on the deposition from a pinned droplet undergoing spatially-uniform evaporation. They showed that, as the rate of particle–substrate adsorption increases, the shape of the final deposit transitions from a ring deposit to a deposit that is more concentrated at the centre of the droplet, termed a central bump deposit, and identified the special case in which the deposit is uniform.

In Section 6.2.3 we discuss preliminary work investigating the effect of particle–substrate adsorption on the deposition from an evaporating sessile droplet.

1.11 Overview of thesis

In this thesis we use a combination of analytical and numerical techniques to investigate the evolution of, and the deposition from, an evaporating sessile droplet.

In Chapter 2 we give a derivation of the diffusion-limited model for the evaporation of a sessile droplet.

In Chapter 3 we consider the evaporation of a thin droplet in a shallow well. We formulate and analyse a mathematical model for the evolution of a droplet in a well of rather general shape both before and after touchdown. We then validate the mathematical model by comparing the theoretical predictions with physical experiments for the special case of a cylindrical well.

In Chapter 4 we consider the evaporation of sessile and pendant droplets under the effect of gravity. We formulate and analyse a mathematical model for the shape, evolution, and lifetime of thin sessile and pendant droplets evaporating in the CR, CA, SS and SJ modes of evaporation.

In Chapter 5 we consider the effect of spatial variation in the local evaporative flux on the deposition of particles from an evaporating sessile droplet. We investigate the evaporation for a particular one-parameter family of spatially-varying local evaporative

fluxes that captures a wide range of qualitatively different behaviours. We show that the flow within, and deposition from, an evaporating droplet depends strongly on the local evaporative flux profile. In particular, the model predicts three qualitatively different deposit types depending on the spatial variation in the local evaporative flux, namely, a ring deposit, a paraboloidal deposit, and a deposit at the centre of the droplet.

In Chapter 6 we summarise the results obtained, draw conclusions, and discuss open questions and possible directions for future work.

1.12 Publications and presentations

The work in Chapter 3 has recently been published in the Journal of Fluid Mechanics (D'Ambrosio *et al.* [55]), as well as being presented as an oral presentation by my primary supervisor Prof. Stephen K. Wilson at the "Fundamental Fluid Dynamics Challenges in Inkjet Printing" Workshop, July 2019, Lorentz Center, Leiden; at the ICMS Continuum Mechanics Seminar Series, February 2021, Edinburgh (virtually); and at the American Physical Society Division of Fluid Dynamics 74th Annual Meeting, November 2021, Phoenix (virtually). Various aspects of this work have also been presented by me as a poster presentation at Droplets 2019, September 2019, Durham University, and as an oral presentation at the 24th Merck Annual Case Conference, April 2018, Southampton; at the UK Fluids Network Droplet Dynamics Special Interest Group Meeting, September 2018, Wadham College, Oxford; at the 61st British Applied Mathematics Colloquium, April 2019, University of Bath; and at the 32nd Scottish Fluid Mechanics Meeting, May 2019, Dundee University.

Aspects of the work in Chapter 4 are currently being prepared for publication and have been presented by myself at the UK Fluids Conference 2021, September 2021, University of Southampton (virtually).

The work in Chapter 5 is currently being prepared for publication and has also been presented as an oral presentation by myself at the American Physical Society Division of Fluid Dynamics 73rd Annual Meeting, November 2020, Chicago (virtually); at the 62nd British Applied Mathematical Colloquium, April 2021, University of Glasgow (virtually); at the 34th Scottish Fluid Mechanics Meeting, May 2021, Robert Gor-

don University (virtually); and at Droplets 2021, August 2021, Technische Universitat Darmstadt (virtually).

Furthermore, aspects of Chapters 1 and 5 will be published as part of a review article co-authored with my primary supervisor Prof. Stephen K. Wilson that is to appear in the Annual Review of Fluid Mechanics (Wilson and D'Ambrosio [302]).

Chapter 2

A Theoretical Model for the Diffusion-Limited Evaporation of a Sessile Droplet

2.1 Introduction

In this Chapter we outline a theoretical model of a sessile droplet undergoing quasi-static diffusion-limited evaporation. First we summarise the classical description of a small axisymmetric static sessile droplet, and the diffusion-limited model for the evaporation of such a droplet, and then we describe the special case of a thin droplet. For clarity we use hats to denote the dimensional quantities and unscaled angles, and a superscript "a" to denote quantities associated with the atmosphere; the absence of a superscript denotes quantities associated with the droplet.

2.2 The droplet geometry

We consider a sessile droplet of incompressible Newtonian fluid with known constant density $\hat{\rho}$, surface tension $\hat{\sigma}$, and viscosity $\hat{\mu}$. The droplet is deposited onto a substrate within an atmosphere with constant pressure $\hat{p}^{\mathrm{a}}$, and undergoes diffusion-limited evaporation; we denote the subsequent (unknown) concentration of vapour in the atmosphere

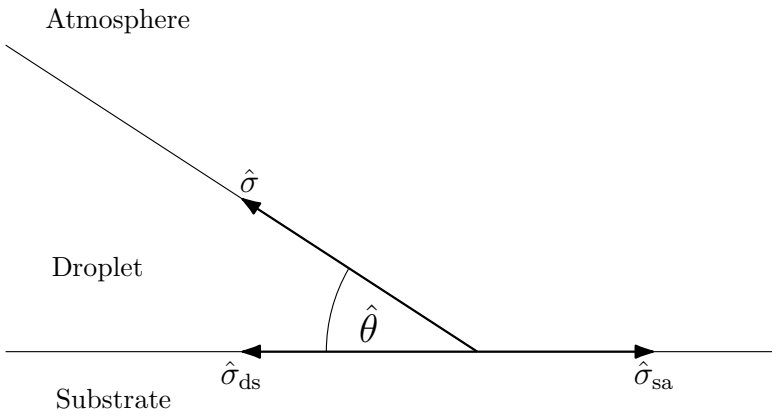

Figure 2.1: Sketch of the region near the contact line of a droplet on an ideal substrate with equilibrium contact angle $\hat{\theta} < \pi/2$.

by $\hat{c}$.

2.2.1 Wetting

After the droplet is deposited onto the substrate, the free surface of the droplet rapidly adopts a quasi-equilibrium shape with an equilibrium contact angle $\hat{\theta}$ ($0 \leq \hat{\theta} \leq \pi$). As discussed in Chapter 1, the value of the contact angle depends upon the properties of the system.

The equilibrium contact angle of a droplet on an ideal substrate is described by the Young equation [314]:

$$\hat{\sigma} \cos \hat{\theta} = \hat{\sigma}_{\mathrm{sa}} - \hat{\sigma}_{\mathrm{ds}} \tag{2.1}$$

where $\hat{\sigma}$, $\hat{\sigma}_{\mathrm{sa}}$, and $\hat{\sigma}_{\mathrm{ds}}$ denote the surface tensions at the droplet–atmosphere, substrate–atmosphere, and droplet–substrate interfaces, respectively, as sketched in Figure 2.1 for $\hat{\theta} < \pi/2$. In particular, equation (2.1) shows that a droplet on an ideal substrate has a unique equilibrium contact angle $\hat{\theta}$. However, in practice, substrates are not ideal, and the equilibrium contact angle can achieve a range of values due to contact-line pinning by substrate roughness and/or chemical heterogeneities. The difference between the largest and smallest possible equilibrium contact angles is called contact-angle hysteresis (see, for example, Eral *et al.* [78]).

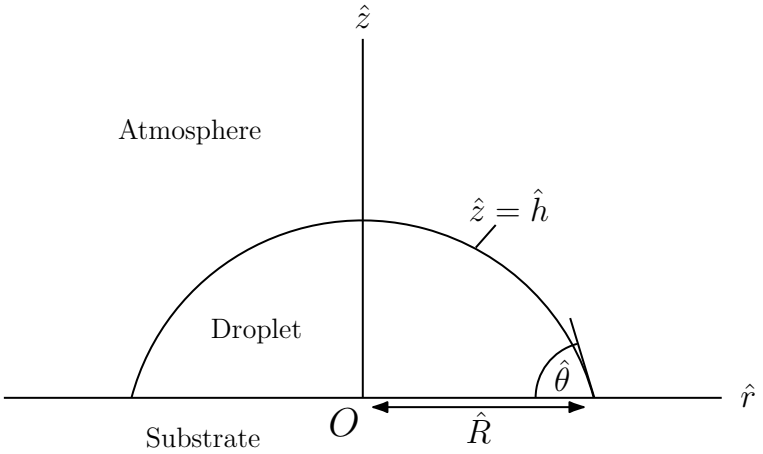

Figure 2.2: A cross-sectional view of an axisymmetric droplet with contact radius $\hat{R}$, contact angle $\hat{\theta}$, and free surface $\hat{h}$.

2.2.2 Determining the free surface

In this thesis we will consider the evaporation of axisymmetric droplets only, and so we work in cylindrical polar coordinates $(\hat{r}, \hat{\varphi}, \hat{z})$ with $O\hat{z}$ along the axis of the droplet, perpendicular to the substrate at $\hat{z} = 0$, as sketched in Figure 2.2. The contact radius, contact angle, volume, and free surface of the droplet are denoted by $\hat{R} = \hat{R}(\hat{t})$, $\hat{\theta} = \hat{\theta}(\hat{t})$, $\hat{V} = \hat{V}(\hat{t})$, and $\hat{h} = \hat{h}(\hat{r}, \hat{t})$, respectively, where $\hat{t}$ denotes time. The initial values of $\hat{R}$, $\hat{\theta}$, and $\hat{V}$ at $\hat{t} = 0$ are denoted by $\hat{R}(0) = \hat{R}_0$, $\hat{\theta}(0) = \hat{\theta}_0$, and $\hat{V}(0) = \hat{V}_0$, respectively.

We generally consider situations in which the droplet is sufficiently small that the effect of gravity is negligible, and the surface tension is sufficiently strong that the free surface of the droplet is quasi-static. More specifically, we consider situations in which the appropriately defined Bond number Bo, which characterises the ratio of gravitational and surface-tension effects, and capillary number Ca, which characterises the ratio of viscous and surface-tension effects, namely

$$\mathrm{Bo} = \left(\frac{\hat{L}}{\hat{\ell}}\right)^2 \ll 1 \quad \text{and} \quad \mathrm{Ca} = \frac{\hat{\mu}\hat{U}}{\hat{\sigma}} \ll 1, \tag{2.2}$$

are small, where $\hat{\ell} = \sqrt{\hat{\sigma}/\hat{\rho}\hat{g}}$ denotes the capillary length, $\hat{g}$ denotes the magnitude of acceleration due to gravity, $\hat{L}$ is an appropriate characteristic length scale of the droplet, and $\hat{U}$ is the appropriate characteristic velocity scale. We note that for diffusion-

limited evaporation the characteristic velocity scale is given by $\hat{U} = \hat{L}/\hat{\tau}$, where $\hat{\tau}$ is the appropriate characteristic time scale for evaporation, namely $\hat{\tau} = \big(\hat{\rho}/2\hat{D}(\hat{c}_{\rm sat} - \hat{c}_\infty)\big)(3\hat{V}_0/2\pi)^{2/3}$ (see, for example, Stauber *et al.* [267]).

For Bo $\ll 1$ and Ca $\ll 1$, the Stokes equations reduce to the statement that the pressure $\hat{p} = \hat{p}(\hat{r}, \hat{z}, \hat{t})$ within the droplet satisfies

$$\hat{\nabla}\hat{p} = \mathbf{0}, \tag{2.3}$$

subject to the Young–Laplace equation [314] at the free surface of the droplet, namely

$$\hat{p} - \hat{p}^{\rm a} = -\hat{\sigma}\hat{\nabla}\cdot\hat{\mathbf{n}} = \hat{\sigma}\hat{\kappa} \quad \text{on} \quad \hat{z} = \hat{h}, \tag{2.4}$$

where $\hat{p}^{\rm a}$ denotes the atmospheric pressure, $\hat{\mathbf{n}}$ is the unit outward normal to the free surface, and $\hat{\kappa}$ is the mean curvature of the free surface of the droplet. Equation (2.3) shows that the pressure $\hat{p}$ within the droplet is independent of $\hat{r}$ and $\hat{z}$, and therefore, from (2.4), the mean curvature of the droplet $\hat{\kappa}$ is spatially uniform.

We note that we will consider a small capillary number Ca $\ll 1$ throughout this thesis and a small Bond number Bo $\ll 1$ in Chapters 3 and 5. However, in Chapter 4 we consider the situation in which the droplet is sufficiently large that the effect of gravity is not negligible and so the Bond number is not small, *i.e.* Bo $= O(1)$.

2.3 The diffusion-limited model

As discussed in Chapter 1, the local and total evaporative fluxes from a sessile droplet depend on the rate-limiting mechanism(s) of evaporation. In this thesis we consider diffusion-limited evaporation, *i.e.* evaporation in which the rate-limiting mechanism is the diffusive transport of vapour in the atmosphere. More specifically, we consider situations in which the appropriately defined mass Péclet number $\mathrm{Pe_m}$, which characterises the ratio of diffusive and advective mass transport, and mass Fourier number $\mathrm{Fo_m}$,

which characterises the ratio of the evaporative and mass diffusion timescales, namely

$$\mathrm{Pe_m} = \frac{\hat{L}\hat{U}}{\hat{D}} \ll 1 \quad \text{and} \quad \mathrm{Fo_m} = \frac{\hat{\tau}\hat{D}}{\hat{L}^2} \gg 1, \tag{2.5}$$

are small and large, respectively, where $\hat{D}$ is the constant diffusivity of vapour in the atmosphere. We note that, as discussed in the previous Subsection, for diffusion-limited evaporation $\hat{U} = \hat{L}/\hat{\tau}$ and therefore $\mathrm{Pe_m} = 1/\mathrm{Fo_m}$ in this regime.

For $\mathrm{Pe_m} \ll 1$ and $\mathrm{Fo_m} \gg 1$, the concentration of vapour $\hat{c} = \hat{c}(\hat{r}, \hat{z}, \hat{t})$ in the atmosphere is governed by Laplace's equation

$$\hat{\nabla}^2 \hat{c} = 0 \quad \text{in the atmosphere,} \tag{2.6}$$

subject to

$$\hat{c} = \hat{c}_{\mathrm{sat}} \quad \text{on} \quad \hat{z} = \hat{h} \quad \text{for} \quad 0 \leq \hat{r} \leq \hat{R}, \tag{2.7}$$

$$\hat{c} \to \hat{c}_{\infty} \quad \text{as} \quad \hat{r}^2 + \hat{z}^2 \to \infty, \tag{2.8}$$

$$\frac{\partial \hat{c}}{\partial \hat{z}} = 0 \quad \text{on} \quad \hat{z} = 0 \quad \text{for} \quad \hat{r} > \hat{R}, \tag{2.9}$$

where $\hat{c}_{\mathrm{sat}}$ is the constant saturation concentration and $\hat{c}_{\infty} = \widehat{RH}\hat{c}_{\mathrm{sat}}$ is the constant ambient concentration, where $\widehat{RH}$ $(0 \leq \widehat{RH} \leq 1)$ is the relative humidity of the atmosphere (see, for example, Deegan *et al.* [64], Hu and Larson [116], and Popov [220]).

The local evaporative mass flux from the free surface of the droplet, denoted by $\hat{J} = \hat{J}(\hat{r}, \hat{t})$, is given by

$$\hat{J} = -\hat{\mathbf{n}} \cdot \hat{D}\hat{\nabla}\hat{c} \quad \text{on} \quad \hat{z} = \hat{h} \quad \text{for} \quad 0 \leq \hat{r} \leq \hat{R}, \tag{2.10}$$

and integrating $\hat{J}$ over the free surface of the droplet gives the total evaporative mass flux from the droplet, denoted by $\hat{F} = \hat{F}(\hat{t})$, namely

$$\hat{F} = \int \hat{J} \, \mathrm{d}\hat{S}. \tag{2.11}$$

The droplet evolves according to the global-mass conservation condition

$$-\hat{\rho}\frac{\mathrm{d}\hat{V}}{\mathrm{d}\hat{t}} = \hat{F} = \int \hat{J}\,\mathrm{d}\hat{S}. \tag{2.12}$$

We note that, as discussed in Chapter 1, for the diffusion-limited model described here, the evaporative problem for the concentration of vapour in the atmosphere is decoupled from the thermal problem for the temperature distribution in the system. Despite this, the evaporation of a droplet requires latent heat, and so, in general, evaporative cooling will occur. The, in general, non-uniform temperature within the droplet, substrate, and atmosphere can be determined once the evolution of the droplet has been determined (see, for example, Dunn *et al.* [71]); however, we do not explicitly consider the thermal problem in this thesis.

2.4 A thin droplet

Throughout this thesis we will consider the evaporation of thin droplets only, *i.e.* droplets with sufficiently small aspect ratio $\hat{h}/\hat{R} \ll 1$, corresponding to droplets with sufficiently small contact angle $\hat{\theta} \ll 1$. For this case we nondimensionalise and scale the variables according to

$$\begin{gathered}\hat{r} = \hat{L}r, \quad \hat{z} = \hat{\theta}_0\hat{L}z, \quad \hat{R} = \hat{L}R, \quad \hat{\theta} = \hat{\theta}_0\theta, \quad \hat{h} = \hat{\theta}_0\hat{L}h, \quad \hat{V} = \hat{\theta}_0\hat{L}^3V, \\ \Delta\hat{p} = \frac{\hat{\sigma}\hat{\theta}_0}{\hat{L}}p, \quad \hat{t} = \frac{\hat{\rho}\hat{\theta}_0\hat{L}^2}{\hat{D}(\hat{c}_{\mathrm{sat}} - \hat{c}_\infty)}t, \quad \hat{c} = \hat{c}_\infty + (\hat{c}_{\mathrm{sat}} - \hat{c}_\infty)c, \\ \hat{J} = \frac{\hat{D}(\hat{c}_{\mathrm{sat}} - \hat{c}_\infty)}{\hat{L}}J, \quad \hat{F} = \hat{D}(\hat{c}_{\mathrm{sat}} - \hat{c}_\infty)\hat{L}F,\end{gathered} \tag{2.13}$$

for the droplet, and similarly for the atmosphere except that

$$\hat{z} = \hat{L}z^{\mathrm{a}}. \tag{2.14}$$

In particular, we note that the appropriate characteristic time scale for diffusion-limited evaporation of a thin droplet is given by $\hat{\tau} = \hat{\rho}\hat{\theta}_0\hat{L}^2/\hat{D}(\hat{c}_{\mathrm{sat}} - \hat{c}_\infty)$ (see, for example, Wilson and Duffy [303]).

For sufficiently small droplets, as considered here and in Chapters 3 and 5, the appropriate characteristic length scale of the droplet $\hat{L}$ is the initial radius of the droplet, *i.e.* $\hat{L} = \hat{R}_0$, corresponding to Bond number $\mathrm{Bo} = (\hat{R}_0/\hat{\ell})^2 \ll 1$ from (2.2a). On the other hand, for sufficiently large droplets, as considered in Chapter 4, we take the appropriate length scale of the droplet to be the capillary length, *i.e.* $\hat{L} = \hat{\ell}$, corresponding to Bond number $\mathrm{Bo} = 1$ from (2.2a).

2.4.1 The droplet geometry

At leading order in the limit $\hat{\theta}_0 \to 0$, from equations (2.3) and (2.4), the spatially uniform pressure $p = p(t)$ within the droplet satisfies

$$p = \kappa = -\frac{1}{r}\frac{\partial}{\partial r}\left(r\frac{\partial h}{\partial r}\right), \tag{2.15}$$

and so using $\partial p/\partial r = 0$ from (2.3), the free-surface profile $h = h(r,t)$ of the droplet satisfies

$$\frac{\partial}{\partial r}\left(\frac{1}{r}\frac{\partial}{\partial r}\left(r\frac{\partial h}{\partial r}\right)\right) = 0. \tag{2.16}$$

The free-surface profile given by (2.16) must satisfy $h(R,t) = 0$ and $\partial h/\partial r = -\theta$ at $r = R$; in addition, h must be finite at $r = 0$, and is therefore given by the familiar paraboloidal form

$$h = \frac{\theta\big(R^2 - r^2\big)}{2R}, \tag{2.17}$$

or, equivalently,

$$h = h_{\mathrm{m}}\left(1 - \frac{r^2}{R^2}\right), \quad h_{\mathrm{m}} = \frac{\theta R}{2}, \tag{2.18}$$

where $h_{\mathrm{m}} = h(0,t)$ is the height of the free surface at the middle of the droplet. The volume $V = V(t)$ of the droplet is given by

$$V = 2\pi\int_0^R h\, r\, \mathrm{d}r = \frac{\pi\theta R^3}{4}. \tag{2.19}$$

2.4.2 The evaporative problem

At leading order in the limit $\hat{\theta}_0 \to 0$, from equations (2.6)–(2.9), the evaporative problem for the concentration of vapour $c = c(r, z^{\mathrm{a}}, t)$ in the atmosphere becomes

$$\nabla^2 c = 0 \quad \text{for} \quad z^{\mathrm{a}} > 0, \tag{2.20}$$

subject to

$$c = 1 \quad \text{on} \quad z^{\mathrm{a}} = 0 \quad \text{for} \quad 0 \le r \le R, \tag{2.21}$$

$$c \to 0 \quad \text{as} \quad r^2 + z^{\mathrm{a}2} \to \infty, \tag{2.22}$$

$$\frac{\partial c}{\partial z^{\mathrm{a}}} = 0 \quad \text{on} \quad z^{\mathrm{a}} = 0 \quad \text{for} \quad r > R. \tag{2.23}$$

The local evaporative flux $J = J(r, t)$ from (2.10) is given by

$$J = -\frac{\partial c}{\partial z^{\mathrm{a}}} \quad \text{on} \quad z^{\mathrm{a}} = 0 \quad \text{for} \quad 0 \le r \le R, \tag{2.24}$$

and the global mass-conservation condition (2.12) reduces to

$$\frac{\mathrm{d}V}{\mathrm{d}t} = -F \quad \text{where} \quad F = -2\pi \int_0^R J\, r \, \mathrm{d}r. \tag{2.25}$$

We note that (2.21) and (2.24) are applied on $z^{\mathrm{a}} = 0$ at leading order in $\hat{\theta}_0 \to 0$ rather than on the free surface for a thin droplet. The solution for the concentration c may be written in the form (see, for example, Carslaw and Jaeger [38])

$$c = \frac{2}{\pi} \sin^{-1} \frac{2R}{\left[(R+r)^2 + z^{\mathrm{a}2}\right]^{1/2} + \left[(R-r)^2 + z^{\mathrm{a}2}\right]^{1/2}}, \tag{2.26}$$

which, using (2.24), leads to the well-known expression for the local evaporative flux J, namely

$$J = \frac{2}{\pi (R^2 - r^2)^{1/2}}, \tag{2.27}$$

which is singular (but integrable) at the contact line of the droplet at $r = R$ (see, for example, Popov [220]).

Substituting the expression for V from (2.19) and the expression for J from (2.27) into (2.25) yields the following equation for the evolution of a thin evaporating droplet:

$$\frac{\mathrm{d}\left(\theta R^3\right)}{\mathrm{d}t} = -\frac{16R}{\pi}. \tag{2.28}$$

We note that equation (2.28) is not sufficient to determine how R and θ evolve and, in the absence of more detailed modelling of the physics in the vicinity of the contact line, appropriate idealised assumptions about the behaviour of R and/or θ must be made. As discussed in Chapter 1, a simple and common approach is to investigate the evolution of the droplet in different modes of evaporation.

Chapter 3

The Evaporation of a Thin Droplet in a Shallow Well

3.1 Introduction

In this Chapter, motivated by the increasing interest in inkjet printing droplets directly into wells in the substrate during the manufacturing of OLED displays, as discussed in Chapter 1, we consider the evaporation of a thin droplet in a shallow axisymmetric well of rather general shape. In Section 3.2 we formulate a mathematical model for the evolution, and hence the lifetime, of the droplet that accounts for the spatially non-uniform evaporation of the fluid. In Section 3.3 we analyse the evolution of the droplet before touchdown and in Section 3.4 we describe the subsequent evolution of the droplet after touchdown. We then describe physical experiments performed for the special case of a cylindrical well by T. Colosimo, L. Yang, and C. D. Bain at Durham University in Section 3.5, and compare the theoretical predictions with these experimental results in Section 3.6, as well as with experimental results obtained by previous authors in Section 3.7. All of the work described in this Chapter has recently been published in the Journal of Fluid Mechanics (D'Ambrosio *et al.* [55]).

3.2 Problem formulation

We consider a droplet of fluid in an axisymmetric well in the otherwise dry, planar surface of a substrate undergoing quasi-static diffusion-limited evaporation in a quiescent atmosphere. As in Chapter 2, we refer the description to cylindrical polar coordinates $(\hat{r}, \hat{\varphi}, \hat{z})$, with $O\hat{z}$ along the axis of the well, perpendicular to the surface of the substrate at $\hat{z} = 0$, as sketched in Figure 3.1. We denote the maximum depth of the well, which occurs at $\hat{r} = 0$, by $\hat{H}_0$, and the radius of its lip by $\hat{R}_0$, so that the lip is located at $\hat{r} = \hat{R}_0$, $\hat{z} = 0$. The droplet is deposited into the well at $\hat{t} = 0$, and thereafter its volume decreases due to evaporation until it has completely evaporated, which occurs at $\hat{t} = \hat{t}_{\text{lifetime}}$, where $\hat{t}_{\text{lifetime}}$ is the lifetime of the droplet.

We consider situations in which the droplet is thin and the well is shallow such that the aspect ratio of the droplet and the well, $\epsilon = \hat{H}_0/\hat{R}_0 \ll 1$, is small. Additionally, as in Chapter 2, we consider situations in which the droplet is sufficiently small that the effect of gravity is negligible, and the surface tension is sufficiently strong that the free surface of the droplet evolves quasi-statically. More specifically, we consider situations in which the appropriately defined Bond number Bo and scaled capillary number Ca^* from (2.2), namely

$$\text{Bo} = \left(\frac{\hat{R}_0}{\hat{\ell}}\right)^2 \ll 1 \quad \text{and} \quad \text{Ca}^* = \frac{\text{Ca}}{\epsilon^3} = \frac{\hat{\mu}\hat{U}}{\epsilon^3\hat{\sigma}} \ll 1, \tag{3.1}$$

are small. We note that the capillary number Ca defined in (2.2) arises when the characteristic radial and vertical length scales of the droplet are the same and that a scaled capillary number Ca^* arises when we consider situations in which the radial and vertical length scales of the droplet are different.

The mean curvature of the free surface of the droplet is therefore spatially constant, and so at leading order in the limit $\epsilon \to 0$ its free-surface profile $\hat{h}$ satisfies

$$\frac{\partial}{\partial \hat{r}}\left(\frac{1}{\hat{r}}\frac{\partial}{\partial \hat{r}}\left(\hat{r}\frac{\partial \hat{h}}{\partial \hat{r}}\right)\right) = 0, \tag{3.2}$$

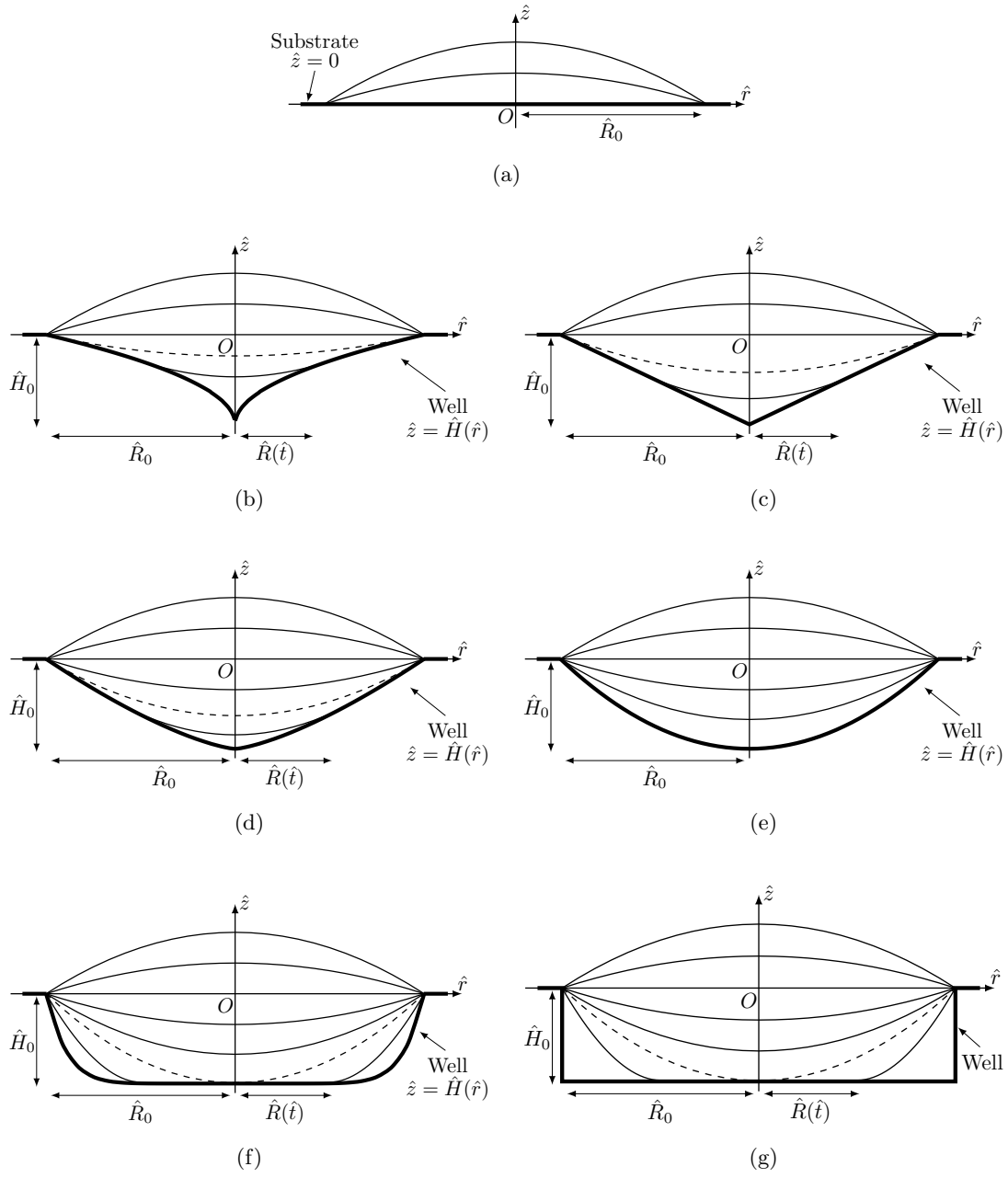

Figure 3.1: Sketch of snapshots of the free-surface profile $\hat{z} = \hat{h}(\hat{r}, \hat{t})$ of a thin droplet evaporating in a shallow axisymmetric well with profile $\hat{z} = \hat{H}(\hat{r}) = -\hat{H}_0(1 - (\hat{r}/\hat{R}_0)^n)$ in the otherwise dry, planar surface $\hat{z} = 0$ of a substrate, for (a) either $\hat{H}_0 = 0$ or $n = 0$ (*i.e.* a planar substrate with no well), (b) $0 < n < 1$, (c) $n = 1$ (*i.e.* a conical well), (d) $1 < n < 2$, (e) $n = 2$ (*i.e.* a paraboloidal well), (f) $2 < n < \infty$, and (g) in the limit $n \to \infty$ (*i.e.* a cylindrical well). In (b)–(g) the free-surface profile at $\hat{t} = \hat{t}_{\text{touchdown}}$ is indicated with a dashed curve. Note that the dashed curve is not visible in (e) as touchdown occurs everywhere simultaneously within the well in the special case $n = 2$.

and hence takes the general form

$$\hat{h} = c_1 \hat{r}^2 + c_2 \log \hat{r} + c_3, \tag{3.3}$$

where the $c_i = c_i(t)$ for $i = 1, 2, 3$ are yet to be determined.

We consider a shaped well with profile $\hat{z} = \hat{H}(\hat{r})$ (≤ 0), where

$$\hat{H} = -\hat{H}_0 \left(1 - \left(\frac{\hat{r}}{\hat{R}_0}\right)^n\right) \quad \text{for} \quad 0 \leq \hat{r} \leq \hat{R}_0, \tag{3.4}$$

in which the exponent n (≥ 0) is a constant. The volume of the well (*i.e.* its volume below the plane $\hat{z} = 0$) is given by

$$\hat{V}_{\text{well}} = \frac{\pi n \hat{H}_0 \hat{R}_0^2}{2+n}, \tag{3.5}$$

and any three of the four quantities $\hat{V}_{\text{well}}$, $\hat{R}_0$, $\hat{H}_0$ and n may be prescribed. Cases with either $\hat{H}_0 = 0$ or $n = 0$ in (3.4), sketched in Figure 3.1(a), correspond to the familiar case of a droplet on a planar substrate with no well, as described in Chapter 2. The cases $n = 1$, $n = 2$ and in the limit $n \to \infty$, also included in Figure 3.1, correspond respectively to a conical well, a paraboloidal well (which will turn out to be an important special case), and a cylindrical well with vertical side $\hat{r} = \hat{R}_0$ and flat bottom $\hat{z} = -\hat{H}_0$. The latter case, which, as discussed in Chapter 1, is of particular interest from a practical point of view, is the subject of the experimental investigation described in Section 3.5. At its lowest point located at $\hat{r} = 0$, $\hat{z} = -\hat{H}_0$ the profile of the well (3.4) has a cusp when $0 < n < 1$, has a corner when $n = 1$, and is flat when $n > 1$; also its curvature there is infinite when $0 < n < 2$, takes the value $4\hat{H}_0/\hat{R}_0^2$ when $n = 2$, and is zero when $n > 2$. The slope of the well at its lip is $n\hat{H}_0/\hat{R}_0$.

We assume that, at least in the first stage of the evolution, the contact line is pinned at the lip of the well located at $\hat{r} = \hat{R}_0$, $\hat{z} = 0$. The initial volume of the droplet, $\hat{V}_0$, could be greater than, equal to, or less than the volume of the well, $\hat{V}_{\text{well}}$, in which case the initial free surface of the droplet would be respectively above, at, or below the plane $\hat{z} = 0$. Although all of these cases could be analysed by the present approach, for

definiteness we take $\hat{V}_0$ to be greater than $\hat{V}_{\rm well}$, so that initially the well is completely filled and the free surface is above $\hat{z} = 0$.

At some time $\hat{t} = \hat{t}_{\rm touchdown}$ ($0 < \hat{t}_{\rm touchdown} \leq \hat{t}_{\rm lifetime}$) the free surface makes contact tangentially (*i.e.* at zero contact angle) with the surface of the well. As shown by the dashed curves in Figure 3.1, when $0 < n < 2$ touchdown occurs at the lip of the well, and when $n > 2$ it occurs at the centre of the well. In the special case $n = 2$ touchdown occurs everywhere simultaneously within the well, and so the dashed curve is not visible in Figure 3.1(e). Before touchdown the behaviour of the droplet is the same in all three cases, which may therefore be analysed together, but after touchdown the behaviour is different, and it is then convenient to consider the three cases separately.

In the special case $n = 2$ the droplet has completely evaporated at $\hat{t} = \hat{t}_{\rm touchdown}$, and so $\hat{t}_{\rm lifetime} = \hat{t}_{\rm touchdown}$. However, in the general case $n \neq 2$ the droplet has not completely evaporated at $t = \hat{t}_{\rm touchdown}$, and the nature of its subsequent evolution depends on whether $0 < n < 2$ or $n > 2$. When $0 < n < 2$ we assume that, as sketched in Figure 3.1(b)–(d), the contact line de-pins from the lip of the well, and thereafter the contact line recedes (*i.e.* moves inwards towards the centre of the well) with decreasing radius $\hat{R} = \hat{R}(\hat{t})$ until $\hat{R}(\hat{t}_{\rm lifetime}) = 0$, at which time the droplet has completely evaporated. On the other hand, when $n > 2$ we assume that, as sketched in Figure 3.1(f,g), a new inner contact line appears at the centre of the well (*i.e.* at the centre of the droplet, which then becomes annular), and thereafter the inner contact line recedes (*i.e.* moves outwards towards the lip of the well, where the outer contact line remains pinned) with increasing radius $\hat{R} = \hat{R}(\hat{t})$ until $\hat{R}(\hat{t}_{\rm lifetime}) = \hat{R}_0$, at which time the droplet has completely evaporated.

In the next two Sections we analyse the evolution of the droplet before and after touchdown, respectively.

3.3 Evolution before touchdown

We nondimensionalise and scale the variables according to (2.13) with $\hat{L} = \hat{R}_0$ for the droplet, and similarly for the atmosphere except that $\hat{z} = \hat{R}_0 z^{\rm a}$; in addition we

introduce the scalings

$$\hat{H} = \hat{\theta}_0 \hat{R}_0 H, \quad \hat{H}_0 = \hat{\theta}_0 \hat{R}_0 H_0, \tag{3.6}$$

for the well.

Before touchdown, *i.e.* for $0 \leq t \leq t_{\text{touchdown}}$, the contact line is pinned at the lip of the well, and so the free-surface profile given by (3.3) must satisfy $h(1,t) = 0$; in addition, h must be finite at $r = 0$, and is therefore of the familiar paraboloidal form

$$h = h_{\text{m}} \left(1 - r^2\right), \qquad h_{\text{m}} = \frac{\theta}{2}, \tag{3.7}$$

where $h_{\text{m}} = h_{\text{m}}(t) = h(0,t)$ is the height of the free surface at the centre of the well, and $\theta = \theta(t)$ is the angle that the free surface at the lip of the well makes with the plane $z^{\text{a}} = 0$, *i.e.* $\theta = -\partial h/\partial r$ at $r = 1$. We note that equation (3.7) corresponds to the familiar solution for a thin droplet on a planar substrate given by (2.17) in Chapter 2 when $R \equiv 1$. However, unlike for a droplet on a planar substrate for which both h_{m} and θ must be non-negative, for a droplet in a well they may be positive, zero or negative. The volume $V = V(t)$ of the droplet is related to V_{well}, H_0, n and θ by

$$V = V_{\text{well}} + \frac{\pi\theta}{4} = \frac{\pi n H_0}{2+n} + \frac{\pi\theta}{4}. \tag{3.8}$$

The problem for the (static) concentration $c = c(r, z^{\text{a}})$ of vapour in the atmosphere before touchdown is given by (2.20)–(2.25) when $R \equiv 1$, namely

$$\nabla^2 c = 0 \quad \text{in} \quad z^{\text{a}} > 0, \tag{3.9}$$

with

$$c = 1 \quad \text{on} \quad z^{\text{a}} = 0 \quad \text{for} \quad 0 \leq r \leq 1, \tag{3.10}$$

$$c \to 0 \quad \text{as} \quad r^2 + z^{\text{a}2} \to \infty, \tag{3.11}$$

$$\frac{\partial c}{\partial z^{\text{a}}} = 0 \quad \text{on} \quad z^{\text{a}} = 0 \quad \text{for} \quad r > 1, \tag{3.12}$$

$$J = -\frac{\partial c}{\partial z^{\mathrm{a}}} \quad \text{on} \quad z^{\mathrm{a}} = 0 \quad \text{for} \quad 0 \le r \le 1, \tag{3.13}$$

$$\frac{\mathrm{d}V}{\mathrm{d}t} = -2\pi \int_0^1 J\, r\, \mathrm{d}r. \tag{3.14}$$

The initial values of θ, h_{m}, and V are given by

$$\theta = 1, \quad h_{\mathrm{m}} = \frac{1}{2}, \quad V = \frac{\pi n H_0}{2+n} + \frac{\pi}{4} \quad \text{at} \quad t = 0. \tag{3.15}$$

The solution for the concentration c may be written in the form

$$c = \frac{2}{\pi} \sin^{-1} \frac{2}{\left[(1+r)^2 + z^{\mathrm{a}2}\right]^{1/2} + \left[(1-r)^2 + z^{\mathrm{a}2}\right]^{1/2}}, \tag{3.16}$$

which, using (3.13), leads to the solution for the local evaporative flux J, namely

$$J = \frac{2}{\pi(1-r^2)^{1/2}}, \tag{3.17}$$

which exhibits the familiar (integrable) square-root singularity at the contact line $r = 1$ even when the free surface is below the plane $z^{\mathrm{a}} = 0$. Equations (3.16) and (3.17) correspond to the familiar solutions for a thin droplet on a planar substrate given by (2.26) and (2.27) in Chapter 2 when $R \equiv 1$. We note that for $0 \le t \le t_{\mathrm{touchdown}}$ the concentration c and hence the local flux J are independent of t, whereas for $t_{\mathrm{touchdown}} < t \le t_{\mathrm{lifetime}}$ they depend on t via their dependence on $R = R(t)$.

Substituting the expression for V given in (3.8) and the expression for J given in (3.17) into (3.14) yields

$$\frac{\mathrm{d}V}{\mathrm{d}t} = \frac{\pi}{4}\frac{\mathrm{d}\theta}{\mathrm{d}t} = -4, \tag{3.18}$$

and so the evolution of the droplet before touchdown is given by

$$h = h_{\mathrm{m}}(1-r^2), \quad \theta = 1 - \frac{16t}{\pi}, \quad h_{\mathrm{m}} = \frac{1}{2} - \frac{8t}{\pi}, \quad V = \frac{\pi n H_0}{2+n} + \frac{\pi}{4} - 4t. \tag{3.19}$$

The free surface is instantaneously flat (*i.e.* $\theta = 0$, $h_{\mathrm{m}} = 0$ and $V = V_{\mathrm{well}}$) at some

time $t = t_{\text{flat}}$ given by

$$t_{\text{flat}} = \frac{\pi}{16} \simeq 0.1963. \tag{3.20}$$

As well as being of interest in its own right, the occurrence of a flat free surface is relatively easy to observe experimentally.

When $0 < n < 2$ touchdown occurs when $\theta = -H'(1) = -nH_0$, where a dash denotes differentiation with respect to argument, showing that

$$t = t_{\text{touchdown}} = \frac{\pi(1 + nH_0)}{16}, \quad h_{\text{m}} = -\frac{nH_0}{2}, \quad V = \frac{\pi n(2-n)H_0}{4(2+n)} \tag{3.21}$$

at touchdown. As we have already stated, in the special case $n = 2$ touchdown occurs everywhere simultaneously within the well, and so $t_{\text{lifetime}} = t_{\text{touchdown}} = \pi(1+2H_0)/16$. When $n > 2$ touchdown occurs when $h_{\text{m}} = -H_0$, showing that

$$t = t_{\text{touchdown}} = \frac{\pi(1 + 2H_0)}{16}, \quad \theta = -2H_0, \quad V = \frac{\pi(n-2)H_0}{2(n+2)} \tag{3.22}$$

at touchdown. When either $H_0 = 0$ or $n = 0$ equations (3.21) and (3.22) give $t_{\text{lifetime}} = t_{\text{touchdown}} = t_{\text{flat}} = \pi/16$, recovering the familiar expression for the lifetime of a pinned droplet on a planar substrate (see, for example, Stauber *et al.* [268, 270]).

3.4 Evolution after touchdown

3.4.1 $0 < n < 2$

When $0 < n < 2$ the free surface touches down at the lip of the well located at $r = 1$, $z = 0$ at $t = t_{\text{touchdown}}$, and after touchdown, *i.e.* for $t_{\text{touchdown}} < t \leq t_{\text{lifetime}}$, the non-annular droplet has a receding circular contact line of radius $R = R(t)$ which satisfies $R(t_{\text{touchdown}}) = 1$ and $R(t_{\text{lifetime}}) = 0$. We must specify a condition in addition to $h = H$ at the moving contact line. Since the (paraboloidal) free surface (3.19) for $0 \leq t \leq t_{\text{touchdown}}$ touches down with zero contact angle at $r = 1$, we make the modelling assumption that the contact angle at the receding contact line remains at the

value zero throughout the subsequent evolution. Thus we have the boundary conditions

$$h = H = -H_0(1 - R^n), \quad \frac{\partial h}{\partial r} = H' = nH_0R^{n-1} \quad \text{at} \quad r = R. \tag{3.23}$$

The solution (3.3) for h satisfying (3.23) with h finite at $r = 0$ takes the form

$$h = H(R) - \frac{nH_0R^{n-2}}{2}\left(R^2 - r^2\right), \tag{3.24}$$

or, equivalently,

$$h = h_{\mathrm{m}} + \frac{nH_0R^{n-2}r^2}{2}, \quad \text{where} \quad h_{\mathrm{m}} = -H_0 + \frac{(2-n)H_0R^n}{2}, \tag{3.25}$$

for $0 \le r \le R$, and V is given by

$$V = \frac{\pi n(2-n)H_0R^{2+n}}{4(2+n)}. \tag{3.26}$$

The (now quasi-static) concentration $c = c(r, z^{\mathrm{a}}, t)$ of vapour in the atmosphere still satisfies Laplace's equation (3.9) and the boundary condition (3.11), but conditions (3.10) and (3.12)–(3.15) must be replaced with

$$c = 1 \quad \text{on} \quad z^{\mathrm{a}} = 0 \quad \text{for} \quad 0 \le r \le R, \tag{3.27}$$

$$\frac{\partial c}{\partial z^{\mathrm{a}}} = 0 \quad \text{on} \quad z^{\mathrm{a}} = 0 \quad \text{for} \quad r > R, \tag{3.28}$$

$$J = -\frac{\partial c}{\partial z^{\mathrm{a}}} \quad \text{on} \quad z^{\mathrm{a}} = 0 \quad \text{for} \quad 0 \le r \le R, \tag{3.29}$$

$$\frac{\mathrm{d}V}{\mathrm{d}t} = -2\pi \int_0^R J\, r \,\mathrm{d}r, \tag{3.30}$$

$$R = 1, \quad V = \frac{\pi n(2-n)H_0}{4(2+n)} \quad \text{at} \quad t = t_{\text{touchdown}}, \tag{3.31}$$

respectively; in addition, we have

$$R = 0, \quad V = 0 \quad \text{at} \quad t = t_{\text{lifetime}}. \tag{3.32}$$

We note that the problem for the concentration c in this case corresponds to the familiar problem for a thin droplet on a planar substrate given by (2.20)–(2.25) in Chapter 2 since, just as (3.27) and (3.29) are applied on $z^{\mathrm{a}} = 0$ at leading order in $\hat{\theta}_0 \to 0$ rather than on the free surface for a thin droplet, as discussed in Chapter 2, similarly (3.28) for $R < r \leq 1$ is applied on $z^{\mathrm{a}} = 0$ rather than on the well for a shallow well. The solution for the concentration c of the problem defined by (3.9), (3.11), (3.27) and (3.28) is analogous to (3.16) and is given by

$$c = \frac{2}{\pi} \sin^{-1} \frac{2R}{\left[(R+r)^2 + z^{\mathrm{a}2}\right]^{1/2} + \left[(R-r)^2 + z^{\mathrm{a}2}\right]^{1/2}}, \tag{3.33}$$

which, using (3.29), leads to the solution for the flux J analogous to (3.17), namely

$$J = \frac{2}{\pi (R^2 - r^2)^{1/2}}. \tag{3.34}$$

Both (3.33) and (3.34) correspond to the solutions for a thin droplet on a planar substrate given by (2.26) and (2.27) in Chapter 2.

Substituting (3.26) and (3.34) into (3.30) yields

$$R^n \frac{\mathrm{d}R}{\mathrm{d}t} = -\frac{16}{\pi n(2-n) H_0}, \tag{3.35}$$

leading to an explicit solution for R after touchdown, namely

$$R = \left[\frac{1}{n(2-n)H_0} \left(1 + n + 3nH_0 - \frac{16(1+n)t}{\pi} \right) \right]^{1/(1+n)}, \tag{3.36}$$

with h given by (3.24) and V given by (3.26), *i.e.*

$$V = \frac{\pi}{4(2+n)\left[n(2-n)H_0\right]^{1/(1+n)}} \left(1 + n + 3nH_0 - \frac{16(1+n)t}{\pi} \right)^{(2+n)/(1+n)}. \tag{3.37}$$

Figure 3.2 shows the evolution of the free-surface profile h for $n = 1$ and $n = 2$ with $H_0 = 1$. Figure 3.3 shows plots of R and V as functions of t for a range of values of n, again with $H_0 = 1$. Note that $\mathrm{d}R/\mathrm{d}t \to \infty$ and (although not very easy to see in Figure 3.3(b)) $\mathrm{d}V/\mathrm{d}t \to 0^+$ in the limit $t \to t^-_{\mathrm{lifetime}}$.

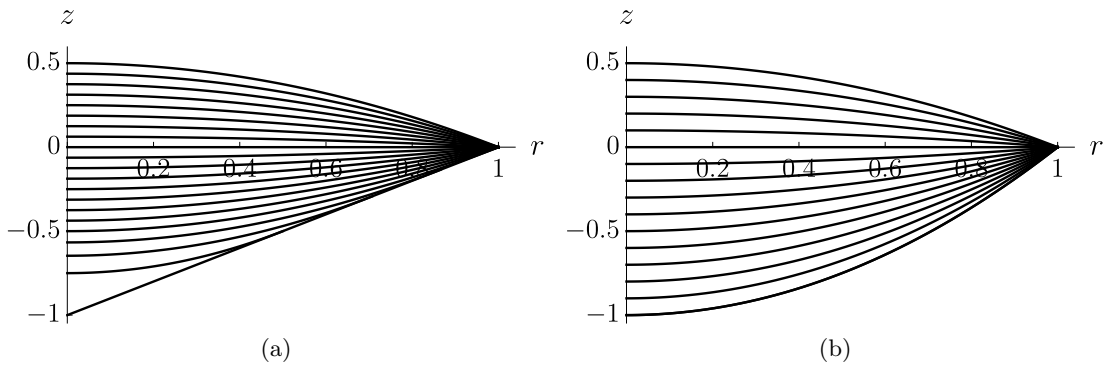

Figure 3.2: Evolution of the free-surface profile h given by (3.19) for $0 \leq t \leq t_{\text{touchdown}}$ and by (3.24) for $t_{\text{touchdown}} < t \leq t_{\text{lifetime}}$ for (a) a conical well with $n = 1$ and $H_0 = 1$, and (b) a paraboloidal well with $n = 2$ and $H_0 = 1$. In (a) the curves are drawn at intervals of $t_{\text{touchdown}}/16 = \pi/128 \simeq 0.0245$, and the lifetime is $t_{\text{lifetime}} = 5\pi/32 \simeq 0.4909$, while in (b) the curves are drawn at intervals of $t_{\text{touchdown}}/15 = \pi/80 \simeq 0.0393$, and the lifetime is $t_{\text{lifetime}} = t_{\text{touchdown}} = 3\pi/16 \simeq 0.5890$.

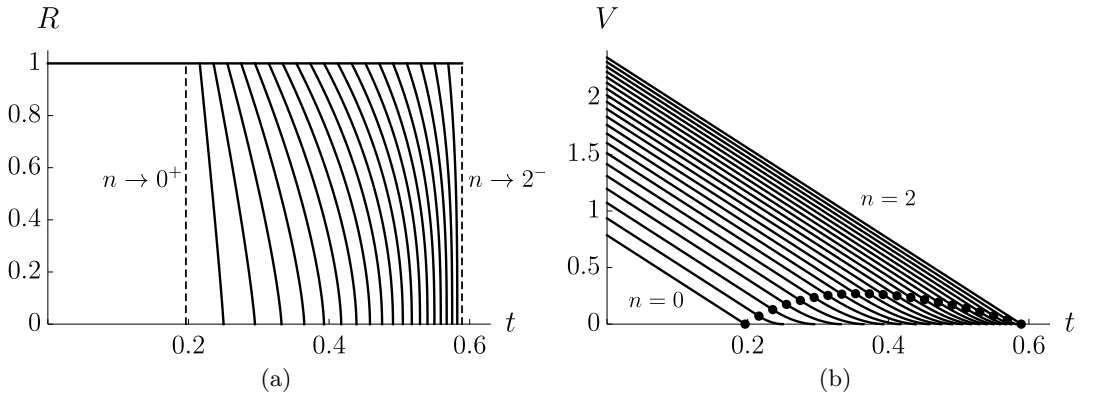

Figure 3.3: Plots of (a) the radius R of the receding contact line given by (3.36), and (b) the volume V of the droplet given by (3.19) for $0 \leq t \leq t_{\text{touchdown}}$ and by (3.37) for $t_{\text{touchdown}} < t \leq t_{\text{lifetime}}$ as functions of t for $n = 0$, $1/10$, $1/5$, $\ldots$, 2 in the case $H_0 = 1$. The vertical dashed lines in (a) correspond to the limits $n \to 0^+$ and $n \to 2^-$, and the dots in (b) correspond to touchdown (at the lip of the well) at $t = t_{\text{touchdown}} = \pi(1 + nH_0)/16$.

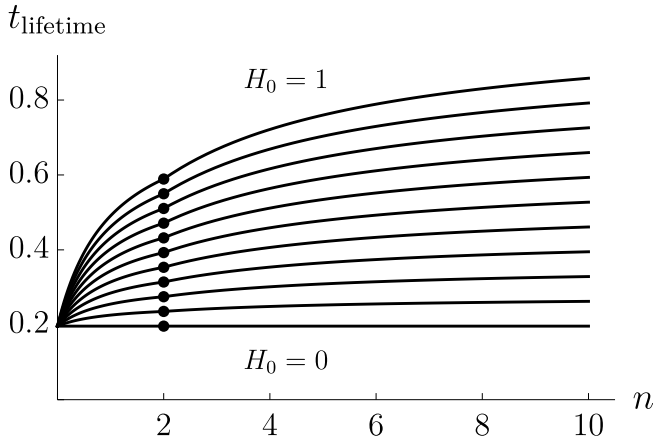

Figure 3.4: Plot of the lifetime of the droplet, t_{lifetime}, given by (3.38) for $0 \leq n \leq 2$ and by (3.50) for $n > 2$, as a function of n for $H_0 = 0$, 1/10, 1/5, ..., 1. The dots denote the values $t_{\text{lifetime}} = t_{\text{touchdown}} = \pi(1+2H_0)/16$ for $n = 2$. The curves approach the asymptotic values $t_{\text{lifetime}} = \pi[1 + 2(1 + 8\alpha_\infty)H_0]/16 \simeq 0.1963 + 0.8228H_0$ in the limit $n \to \infty$.

The lifetime of the droplet, t_{lifetime}, which corresponds to $R = 0$ and $V = 0$, is given by

$$t_{\text{lifetime}} = \frac{\pi(1 + n + 3nH_0)}{16(1 + n)}, \tag{3.38}$$

which is linear in H_0. Figure 3.4 includes a plot of t_{lifetime} given by (3.38) as a function of n for $0 \leq n \leq 2$ (*i.e.* to the left of the dots) for a range of values of H_0. For a given value of H_0, the shortest lifetime is $\pi/16$, corresponding to $n = 0$, and the longest lifetime is $\pi(1 + 2H_0)/16$, corresponding to $n = 2$; also the longest life after touchdown (*i.e.* the largest value of $t_{\text{lifetime}} - t_{\text{touchdown}}$) is $(2 - \sqrt{3})\pi H_0/8 \simeq 0.1052H_0$, corresponding to a well with $n = \sqrt{3} - 1 \simeq 0.7321$.

3.4.2 $n > 2$

When $n > 2$ the free surface touches down at the centre of the well located at $r = 0$, $z = -H_0$ at $t = t_{\text{touchdown}}$, and after touchdown, *i.e.* for $t_{\text{touchdown}} < t \leq t_{\text{lifetime}}$, the annular droplet has a pinned circular outer contact line $r = 1$ and a receding circular inner contact line of radius $R = R(t)$ which satisfies $R(t_{\text{touchdown}}) = 0$ and $R(t_{\text{lifetime}}) = 1$. We must again specify a condition in addition to $h = H$ at the moving contact line. Since the (paraboloidal) free surface (3.19) for $0 \leq t \leq t_{\text{touchdown}}$ touches

down with zero contact angle at $r = 0$, we again make the modelling assumption that the contact angle at the receding contact line remains at the value zero throughout the subsequent evolution, and so the boundary conditions (3.23) again hold. The solution (3.3) for h satisfying (3.23) and $h = 0$ at $r = 1$ takes the form

$$h = \frac{H_0\left[\left(-2R^2 + nR^n - (n-2)R^{n+2}\right)\log r - (1 - R^n + nR^n \log R)(1 - r^2)\right]}{1 - R^2 + 2R^2 \log R} \tag{3.39}$$

for $R \leq r \leq 1$, and V is given by

$$V = \pi H_0 f(R), \tag{3.40}$$

where we have defined the function $f = f(R)$ by

$$f = \frac{n\left[4 - (n+2)R^{n-2} + (n-2)R^{n+2}\right]}{4(n+2)} - \frac{\left(1 - R^2\right)^2\left[(n-2)R^n - nR^{n-2} + 2\right]}{4\left(1 - R^2 + 2R^2 \log R\right)}. \tag{3.41}$$

It is useful to note that $f \to (n-2)/[2(n+2)]$ in the limit $R \to 0^+$ (in agreement with the expression for V at touchdown given in (3.22)), and that $f \sim n^2(n-2)(1-R)^4/36 \to 0^+$ in the limit $R \to 1^-$.

The (again quasi-static) concentration c of vapour in the atmosphere still satisfies Laplace's equation (3.9) and the boundary condition (3.11), but in this case conditions (3.10) and (3.12)–(3.15) must be replaced with

$$c = 1 \quad \text{on} \quad z^{\mathrm{a}} = 0 \quad \text{for} \quad R \leq r \leq 1, \tag{3.42}$$

$$\frac{\partial c}{\partial z^{\mathrm{a}}} = 0 \quad \text{on} \quad z^{\mathrm{a}} = 0 \quad \text{for} \quad 0 \leq r < R \quad \text{and} \quad r > 1, \tag{3.43}$$

$$J = -\frac{\partial c}{\partial z^{\mathrm{a}}} \quad \text{on} \quad z^{\mathrm{a}} = 0 \quad \text{for} \quad R \leq r \leq 1. \tag{3.44}$$

$$\frac{\mathrm{d}V}{\mathrm{d}t} = -F(R), \quad \text{where} \quad F = 2\pi \int_R^1 J\, r\, \mathrm{d}r, \tag{3.45}$$

$$R = 0, \quad V = \frac{\pi(n-2)H_0}{2(n+2)} \quad \text{at} \quad t = t_{\text{touchdown}}, \tag{3.46}$$

respectively, where $F = F(R)$ denotes the total evaporative flux from the droplet; in

addition, we have

$$R = 1, \quad V = 0 \quad \text{at} \quad t = t_{\text{lifetime}}. \tag{3.47}$$

Perhaps surprisingly, no simple closed-form solution of the problem for c defined by (3.9), (3.11), (3.42) and (3.43) is available (see Section 10.1.1 of Popov *et al.* [219] for an overview of previous work on this problem in the context of contact mechanics). The problem was reformulated as equivalent integral equations by, for example, Cooke [51], Williams [300], and Fabrikant [83], and the last of these also gave an iteration-based infinite-series solution to their formulation. Since our primary concern is with the total flux F, we obtained this numerically in two independent ways, namely by solving the integral equation of Cooke [51] by means of Chebyshev–Gauss quadrature with typically 200 nodes, and by solving Laplace's equation for c using the finite-element package COMSOL Multiphysics 5.3a (COMSOL Inc.), from which J and hence F were obtained; the values of F obtained using these two different approaches were found to be in good agreement. In particular, the values of F agreed to within 0.3% for $0 < R < 0.9$ and to within 1% for $0.9 \leq R < 0.99$. For $0.99 < R < 1$ the mesh refinement in COMSOL must be altered due to the thinness of the annulus and so less confidence is placed in the values of F obtained using this method for these extreme values of R.

Figure 3.5 shows an example of contours of c in the r-z^{a} plane for an annular droplet obtained using COMSOL Multiphysics, Figure 3.6 shows a plot of the local flux J from an annular droplet as a function of r ($R \leq r \leq 1$) for a range of values of R, as well as that from a non-annular droplet, and Figure 3.7 shows the total flux F from an annular droplet as a function of R ($0 \leq R \leq 1$). Intriguingly, as Figure 3.6 shows, the local flux J from a non-annular droplet is smaller than that from an annular droplet with the same outer radius, though, of course, the former is effective over a larger area than the latter (*i.e.* over $0 \leq r \leq 1$ rather than $R \leq r \leq 1$), and so leads to a larger value of the total flux F. Figure 3.6 also shows that $J \to \infty$ as $r \to R^+$ and $r \to 1^-$, and a local analysis shows that J has square-root singularities at both contact lines (*i.e.* the same singularity as a non-annular droplet). This is true even in the limit $R \to 0^+$, showing that the local flux J due to an annular droplet with a vanishingly small hole

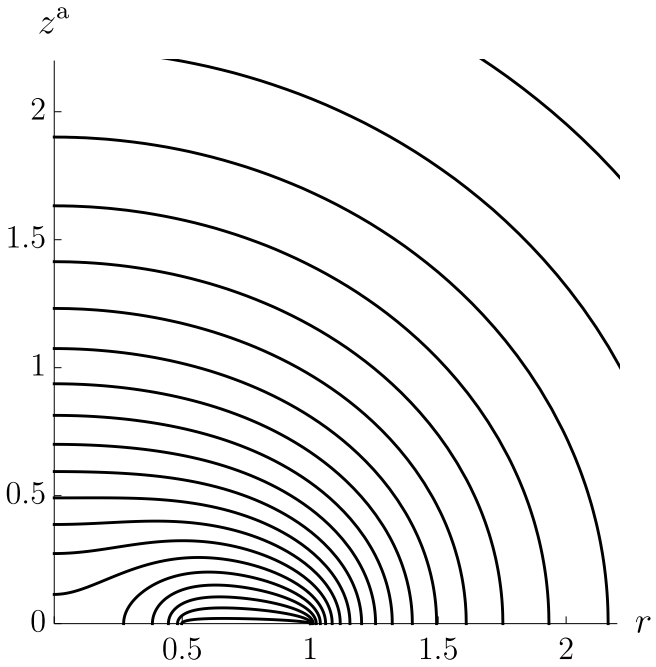

Figure 3.5: Plot of contours of the concentration c in the r-z^{a} plane for an annular droplet in the case $R = 1/2$. The contours are drawn at intervals of 0.04.

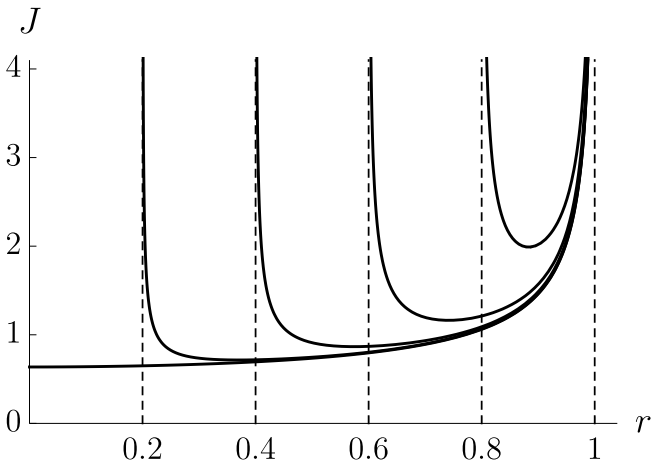

Figure 3.6: Plot of the local flux J from an annular droplet as a function of r ($R \leq r \leq 1$) in the cases $R = 0.2$, 0.4, 0.6 and 0.8, as well as that from a non-annular droplet given by (3.17).

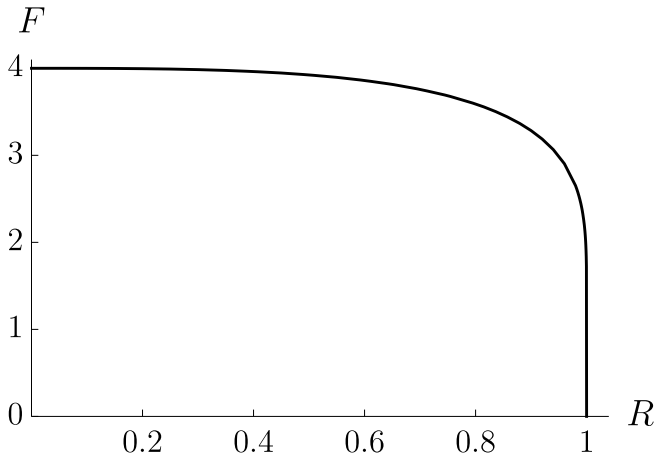

Figure 3.7: Plot of the total flux F from an annular droplet as a function of R ($0 \leq R \leq 1$).

at its centre is different from that due to a non-annular droplet (for which J given by (3.17) is well behaved at $r = 0$); the difference is, however, confined to a small region near to $r = R \to 0^+$ whose contribution to the total flux F is small, leading to $F \to 4^-$ as $R \to 0^+$, in agreement with the value $F = 4$ in the case of a non-annular droplet which appears in (3.18). Note that, as Figure 3.6 shows, J is asymmetric about the midpoint $(R+1)/2$ between the contact lines, and, as Figure 3.7 shows, $F \to 0^+$ as $R \to 1^-$, *i.e.* as the width of the annulus approaches zero.

As Figure 3.7 shows, the total flux F is nearly independent of R until R gets close to 1, showing that the increase of the perimeter $2\pi R$ of the receding inner contact line (where the local flux J is singular), which tends to increase the total flux, almost compensates for the decrease of the surface area $\pi(1-R^2)$ of the annular droplet, which tends to decrease the total flux, for most of the lifetime of the droplet. It is only near to the complete evaporation of the droplet, *i.e.* when R gets close to 1, that F rapidly decreases to zero.

With the total flux F now known, equations (3.40) and (3.45) give

$$\pi H_0 f'(R) \frac{\mathrm{d}R}{\mathrm{d}t} = -F(R), \tag{3.48}$$

where again a dash denotes differentiation with respect to argument, leading to an

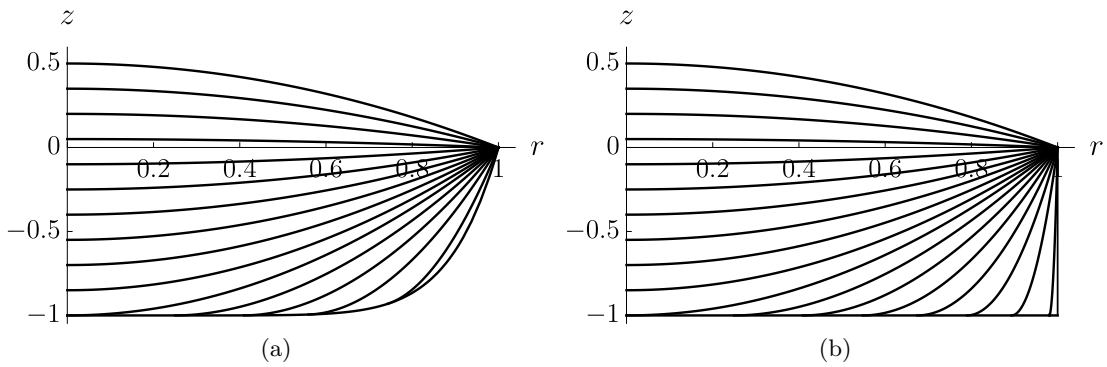

Figure 3.8: Evolution of the free-surface profile h given by (3.19) for $0 \leq t \leq t_{\text{touchdown}}$ and by (3.39) for $t_{\text{touchdown}} < t \leq t_{\text{lifetime}}$ for (a) a well with $n = 9$ and $H_0 = 1$, and (b) a cylindrical well (*i.e.* in the limit $n \to \infty$) with $H_0 = 1$. In (a) the curves are drawn at intervals of $t_{\text{touchdown}}/10 \simeq 0.0589$, and the lifetime is $t_{\text{lifetime}} \simeq 0.8454$, while in (b) the curves are drawn at intervals of $t_{\text{touchdown}}/10 \simeq 0.0589$, and the lifetime is $t_{\text{lifetime}} \simeq 1.0193$.

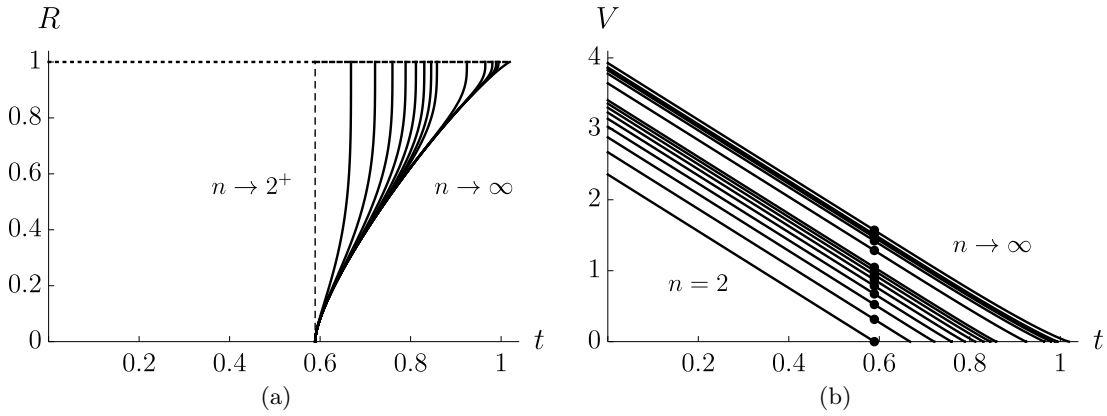

Figure 3.9: Plots of (a) the radius R of the receding inner contact line given by (3.49), and (b) the volume V of the droplet given by (3.19) for $0 \leq t \leq t_{\text{touchdown}}$ and by (3.40) for $t_{\text{touchdown}} < t \leq t_{\text{lifetime}}$ as functions of t for $n = 2$, 3, 4, ..., 10, 20, 40, 60, 80 and 100, and in the limit $n \to \infty$, in the case $H_0 = 1$. The vertical dashed line in (a) corresponds to the limit $n \to 2^+$, and the dots in (b) correspond to touchdown (at the centre of the well) at $t = t_{\text{touchdown}} = \pi(1 + 2H_0)/16 \simeq 0.5890$.

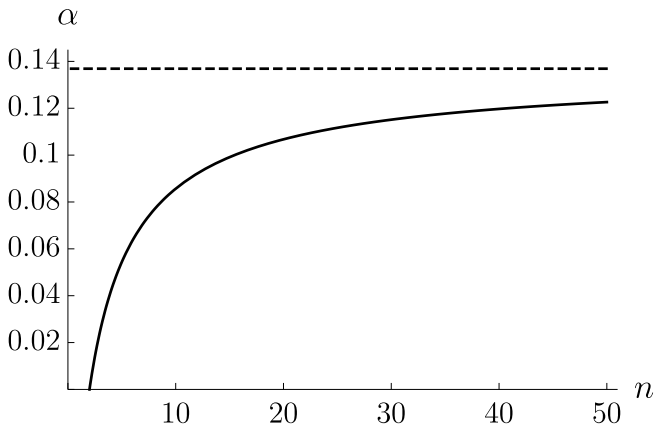

Figure 3.10: Plot of α given by (3.51) as a function of n for $n \geq 2$. The dashed line shows the asymptotic value $\alpha = \alpha_\infty \simeq 0.1369$ in the limit $n \to \infty$.

implicit solution for R after touchdown, namely

$$t = t_{\text{touchdown}} - \pi H_0 \int_0^R \frac{f'(\tilde{R})}{F(\tilde{R})}\,\mathrm{d}\tilde{R}, \tag{3.49}$$

with h given by (3.39) and V given by (3.40).

Figure 3.8(a) shows the evolution of the free-surface profile h for $n = 9$ with $H_0 = 1$. Figure 3.9 shows plots of R and V as functions of t for a range of values of n, again with $H_0 = 1$. The nearly linear dependence of V on t for $t_{\text{touchdown}} < t \leq t_{\text{lifetime}}$ evident in Figure 3.9(b) is a consequence of the fact that the total flux F is nearly independent of R until R gets close to 1, discussed above. Note that $\mathrm{d}R/\mathrm{d}t \to \infty$ and (although impossible to see in Figure 3.9(b)) $\mathrm{d}V/\mathrm{d}t \to 0^+$ in the limit $t \to t_{\text{lifetime}}^-$ (*i.e.* the same behaviour as when $0 < n < 2$).

The lifetime of the droplet, which corresponds to $R = 1$ and $V = 0$, is given by

$$t_{\text{lifetime}} = t_{\text{touchdown}} + \pi\alpha H_0 = \frac{\pi}{16}\left[1 + 2\left(1 + 8\alpha\right) H_0\right], \tag{3.50}$$

where the function $\alpha = \alpha(n)\,(\geq 0)$ is given by

$$\alpha = -\int_0^1 \frac{f'(R)}{F(R)}\,\mathrm{d}R, \tag{3.51}$$

which varies monotonically from $\alpha = 0$ when $n = 2$ to $\alpha = \alpha_\infty \simeq 0.1369$ in the limit

$n \to \infty$. Note that, like the corresponding expression for $0 < n < 2$ given by (3.38), t_{lifetime} given by (3.50) is linear in H_0. Figure 3.10 shows a plot of α as a function of n for $n \geq 2$, and Figure 3.4 includes a plot of t_{lifetime} given by (3.50) as a function of n for $n > 2$ (*i.e.* to the right of the dots) for a range of values of H_0.

3.4.3 The limit $n \to \infty$

In the limit $n \to \infty$, corresponding to a cylindrical well with vertical side $r = 1$ and flat bottom $z = -H_0$, after touchdown the annular droplet again has a pinned circular outer contact line $r = 1$ and a receding circular inner contact line $r = R$. The solution for h given by (3.39) reduces to

$$h = -\frac{H_0\left(1 - r^2 + 2R^2 \log r\right)}{1 - R^2 + 2R^2 \log R} \tag{3.52}$$

for $R \leq r \leq 1$, and V is again given by (3.40), where the function f reduces to

$$f = \frac{1 - R^4 + 4R^2 \log R}{2\left(1 - R^2 + 2R^2 \log R\right)}. \tag{3.53}$$

The evolution of the droplet in this limit is as described in Section 3.4.2, with, in particular, the lifetime of the droplet given by (3.50) with $\alpha = \alpha_\infty$, namely $t_{\text{lifetime}} = \pi[1 + 2(1 + 8\alpha_\infty)H_0]/16 \simeq 0.1963 + 0.8228H_0$. Figure 3.8(b) shows the evolution of the free-surface profile h in the limit $n \to \infty$ with $H_0 = 1$.

3.4.4 The critical times t_{flat}, $t_{\text{touchdown}}$ and t_{lifetime}

Figure 3.11 shows a plot of the critical times t_{flat}, given by (3.20), $t_{\text{touchdown}}$, given by (3.21) and (3.22), and t_{lifetime}, given by (3.38) and (3.50), as functions of n in the case $H_0 = 1$. In particular, Figure 3.11 illustrates that t_{flat} is independent of n, $t_{\text{touchdown}}$ increases linearly with n for $0 \leq n \leq 2$ but is independent of n for $n > 2$, t_{lifetime} increases non-linearly with n, $t_{\text{lifetime}} = t_{\text{touchdown}} = t_{\text{flat}} = \pi/16$ when $n = 0$, $t_{\text{lifetime}} = t_{\text{touchdown}} = \pi(1+2H_0)/16$ when $n = 2$, and $t_{\text{lifetime}} \to \pi[1+2(1+8\alpha_\infty)H_0]/16$ in the limit $n \to \infty$.

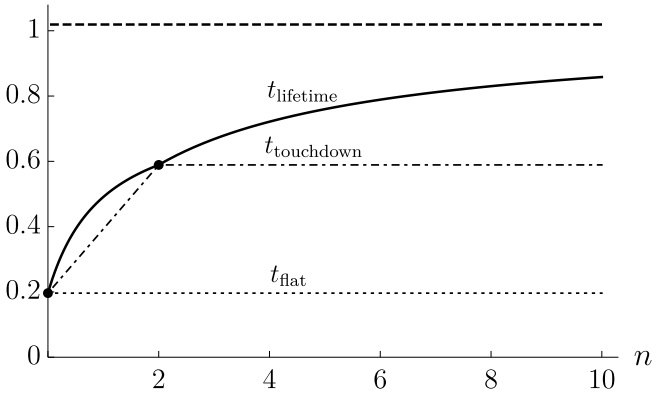

Figure 3.11: Plot of the critical times t_{flat}, given by (3.20) (dotted line), $t_{\text{touchdown}}$, given by (3.21) for $0 \leq n \leq 2$ and by (3.22) for $n > 2$ (dash-dotted line), and t_{lifetime}, given by (3.38) for $0 \leq n \leq 2$ and by (3.50) for $n > 2$ (solid line), as functions of n in the case $H_0 = 1$. The dashed line shows the asymptotic value $t_{\text{lifetime}} = \pi[1+2(1+8\alpha_\infty)H_0]/16 \simeq 1.0191$ in the limit $n \to \infty$.

3.5 Physical experiments

In this Section we give a brief summary of the physical experiments carried out by T. Colosimo, L. Yang, and C. D. Bain at Durham University for the special case of cylindrical wells. A complete account of the experimental procedure, including the well fabrication process and the image analysis, can be found in D'Ambrosio *et al.* [55].

3.5.1 Experimental procedure

The experimental procedure employed involved depositing single droplets of the volatile solvent methyl benzoate into shallow axisymmetric cylindrical wells and observing their behaviour as they evaporated. Methyl benzoate is sufficiently volatile that the experiments could be conducted within a reasonable time frame, and its physical properties are consistent with the assumptions of the mathematical model. A schematic diagram of the experimental set-up used is shown in Figure 3.12.

The experiments were carried out under ambient conditions with a relative humidity of methyl benzoate vapour of $\widehat{RH} = 0$ (and a relative humidity of water vapour of $\widehat{RH} = 0.34 \pm 0.10$). The atmospheric pressure was uncontrolled and the ambient temperature was controlled only to within 1°C of 22°C. The temperature of the substrate was

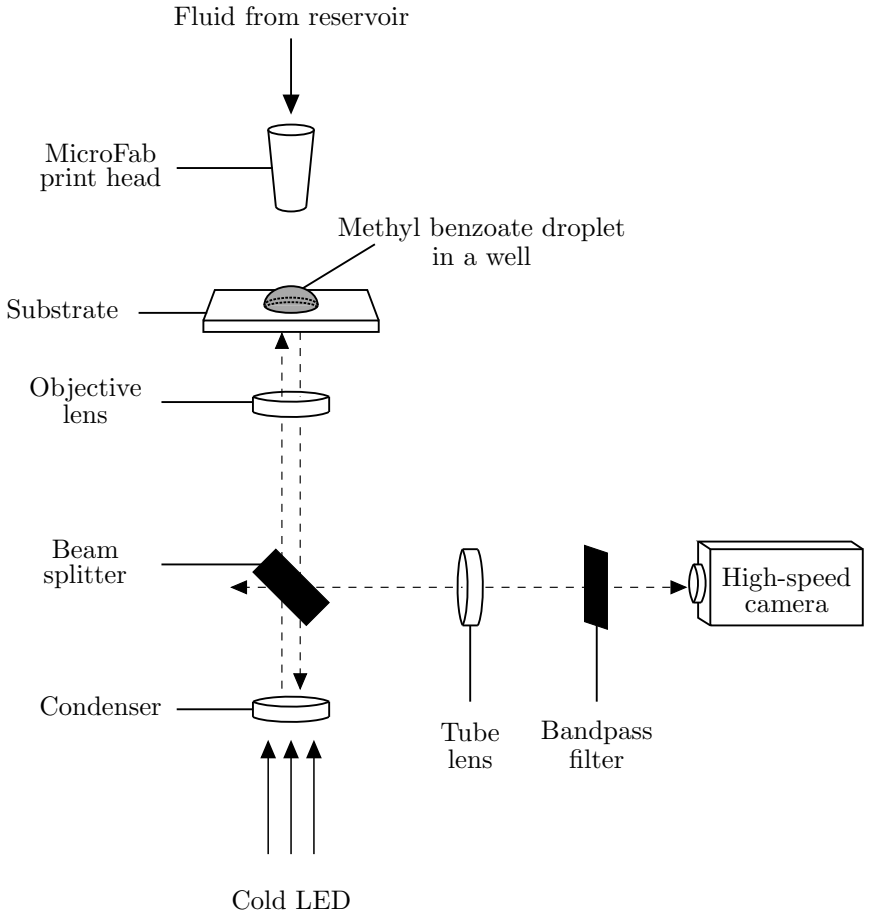

Figure 3.12: Schematic diagram of the experimental set-up used.

accurately maintained at 22°C by means of a Proportional-Integral-Derivative (PID) Peltier controller.

The experiments were performed using three shallow wells with radii 29 μm, 50 μm and 75 μm and depths 2.38 μm, 1.87 μm and 2.39 μm, respectively. The wells were fabricated in spin-cast films of photo-resist deposited onto glass substrates coated with indium tin oxide (ITO). Because of the nature of the manufacturing process, the sides of the wells are not perfectly vertical, but, given their small aspect ratios, it is reasonable to regard the wells as being cylindrical for the purpose of comparison with the theoretical predictions of the mathematical model described in Sections 3.2–3.4.

Picolitre droplets of methyl benzoate were ejected into the wells from a MicroFab print head (MJABP-01, Microfab Technologies Inc.) with a circular orifice of diameter 50 μm under a bipolar waveform generated by a MicroFab controller (JetDrive III CT-M3-02, Microfab Technologies Inc.). The droplet was illuminated from underneath by a cold LED at a wavelength of 470 nm (M470L3, Thorlabs Inc.). The reflected light from the sample was collected by a 50× objective lens (TU Plan ELWD, Nikon) with an image resolution of 0.4 μm/pixel, and captured through a bandpass filter (bandwidth 10 ± 2 nm, Thorlabs Inc.) with a high-speed camera (FASTCAM SA4, Photron). The experiments were performed six times for each well to verify the reproducibility of the results.

3.5.2 Experimental results

Thin-film interferometry was used to measure the evolution of the free surface of the droplet during its evaporation. Figure 3.13 shows a typical interferometric pattern observed during the present experiments. In particular, the high degree of axisymmetry shown in Figure 3.13 was found in all of the experiments. The initial time, $\hat{t} = 0$, was arbitrarily chosen to be a time at which well-resolved interference fringes were observed and the contact line of the droplet coincided with the lip of the well (taken to be at the boundary of the outermost bright fringe, as indicated by the circle in Figure 3.13), *i.e.* no fluid overflow.

Table 3.1 shows experimental values of the radius $\hat{R}_0$, the depth $\hat{H}_0$, and the aspect

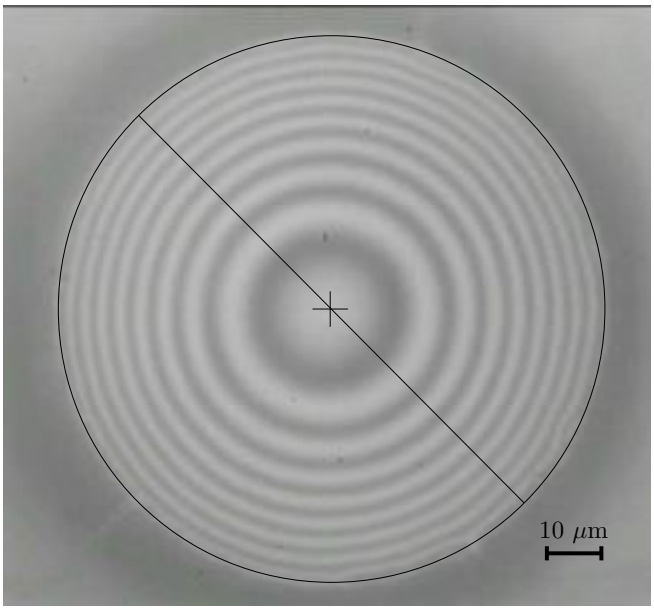

Figure 3.13: A typical interferometric pattern observed during the present experiments. The circle indicates the lip of the well, the cross the centre of the well, and the line the cross-section along which the fringes are analysed.

$\hat{R}_0$ (μm)	$\hat{H}_0$ (μm)	$\epsilon = \dfrac{\hat{H}_0}{\hat{R}_0}$	$\hat{\theta}_0$ (rad)	$\left.\dfrac{\mathrm{d}\hat{V}}{\mathrm{d}\hat{t}}\right\|_{\hat{t}=0}$ (pL s^{-1})	$\hat{t}_{\mathrm{flat}}$ (s)	$\hat{t}_{\mathrm{touchdown}}$ (s)	$\hat{t}_{\mathrm{lifetime}}$ (s)
29	2.38	0.083	5.59×10^{-3}	-1.58	0.060	1.888	3.976
50	1.87	0.037	6.73×10^{-3}	-2.86	0.210	2.838	5.438
75	2.39	0.032	5.78×10^{-3}	-4.38	0.408	5.056	10.392

Table 3.1: Experimental values of the radius $\hat{R}_0$, the depth $\hat{H}_0$, and the aspect ratio $\epsilon = \hat{H}_0/\hat{R}_0$ of the three wells investigated, together with values of the initial angle $\hat{\theta}_0$ and the initial evaporation rate $\left.\mathrm{d}\hat{V}/\mathrm{d}\hat{t}\right|_{\hat{t}=0}$, and the critical times $\hat{t}_{\mathrm{flat}}$, $\hat{t}_{\mathrm{touchdown}}$ and $\hat{t}_{\mathrm{lifetime}}$, for a representative droplet in each well.

ratio $\epsilon = \hat{H}_0/\hat{R}_0$ of the three wells investigated, together with values of the initial angle $\hat{\theta}_0$ and the initial evaporation rate $\mathrm{d}\hat{V}/\mathrm{d}\hat{t}\big|_{\hat{t}=0}$, and the critical times $\hat{t}_{\mathrm{flat}}$, $\hat{t}_{\mathrm{touchdown}}$ and $\hat{t}_{\mathrm{lifetime}}$, for a representative droplet in each well. Note that since the experimental values of the critical times depend on the arbitrarily chosen initial time, $\hat{t} = 0$, as well as on the values of the ambient temperature and the atmospheric pressure, representative (rather than average) results are given for each well. A parameter-free quantity involving the relative values of the critical times will be discussed in Section 3.6.

Figure 3.14 shows experimental results for the free-surface profile $\hat{h}$ of a droplet before touchdown and paraboloidal fits to these values as functions of $\hat{r}$ for all three wells at equally spaced times. All of the paraboloidal fits intersect to within $\Delta\hat{r} = \pm 1$ μm of the value of $\hat{R}_0$ and to within $\Delta\hat{h} = \pm 0.05$ μm of each other, indicating that the contact line of the droplet remains pinned at the lip of the well before touchdown. The depth $\hat{H}_0$ of each well was determined by the position of the average intersection point of the paraboloidal fits. The initial angle $\hat{\theta}_0$ of the droplet was calculated from the average of the derivatives of the paraboloidal fit to the initial free-surface profile at the lip of the well. The time at which the free surface is instantaneously flat, $\hat{t}_{\mathrm{flat}}$, was calculated from the average intersection point of the free-surface profile $\hat{h}$ for a range of values of $\hat{r}$. The uncertainty in the measurement of t_{flat} is ± 0.006 s[†].

Figure 3.15 shows experimental results for the normalised height of the free surface at the centre of the well, $\hat{h}_{\mathrm{m}}/\hat{H}_0$, and linear fits to these values as functions of $\hat{t}$ for all three wells. For each well, the time at which the free surface touches down at the centre of the well, $\hat{t}_{\mathrm{touchdown}}$, was calculated from the intersection point of the linear fit shown in Figure 3.15 with the bottom of the well. However, note that whereas for the 29 μm well the behaviour of $\hat{h}_{\mathrm{m}}$ is nearly linear until very close to touchdown, and hence the value of $\hat{t}_{\mathrm{touchdown}}$ calculated from the linear fit will be very close to the true value, for the 50 μm and 75 μm wells the behaviour of $\hat{h}_{\mathrm{m}}$ shows a pronounced slowing down as touchdown is approached, and so the values of $\hat{t}_{\mathrm{touchdown}}$ calculated from the linear fits will be underestimates of the true values.

After touchdown, the interference fringes become increasingly closely spaced, mak-

[†]C. D. Bain, personal communication

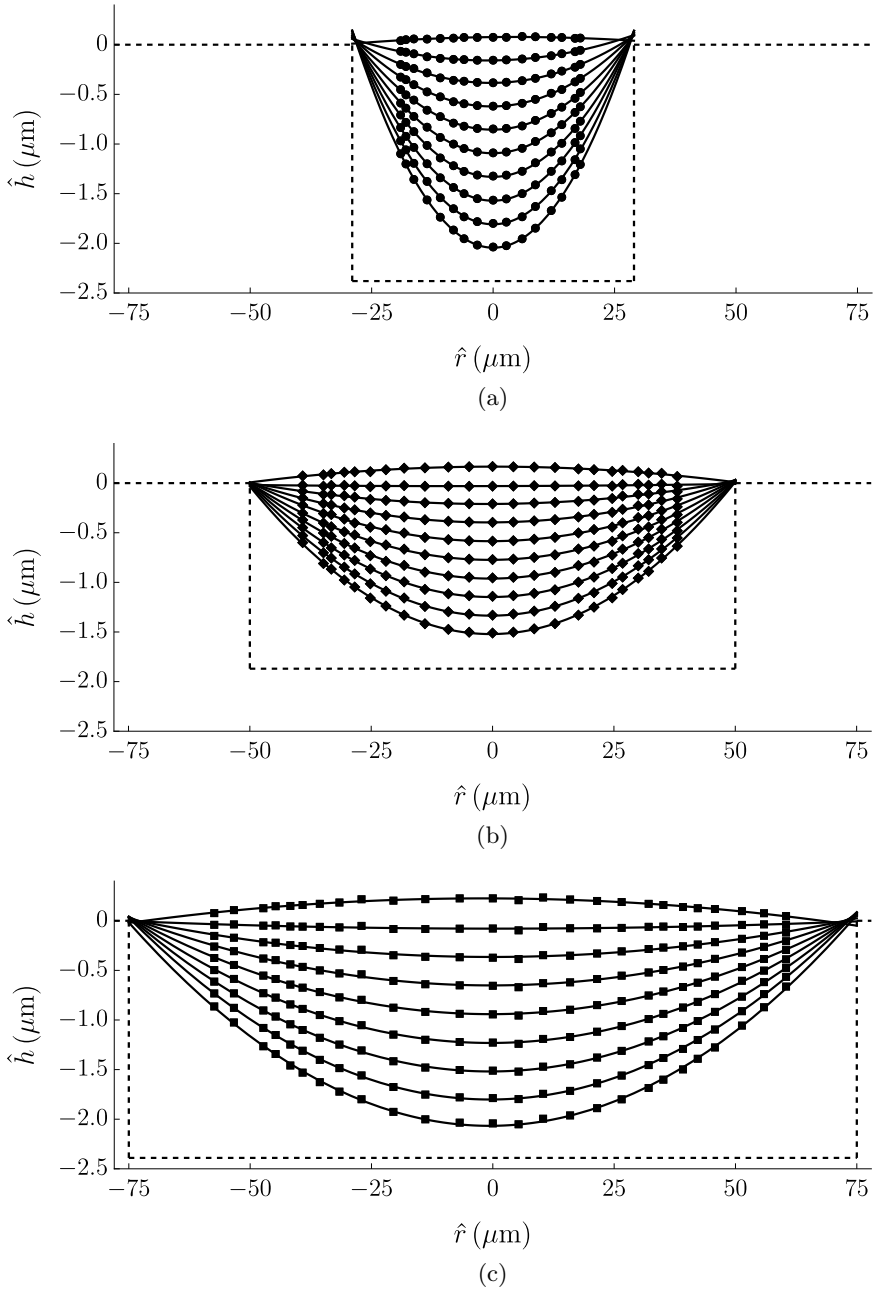

Figure 3.14: Experimental results for the free-surface profile $\hat{h}$ of a droplet before touchdown (symbols) and paraboloidal fits to these values (solid black lines) as functions of $\hat{r}$ for wells of radius (a) 29 μm at times $\hat{t} = 0, 0.18, \ldots, 1.62$ s, (b) 50 μm at times $\hat{t} = 0, 0.26, \ldots, 2.34$ s, and (c) 75 μm at times $\hat{t} = 0, 0.56, \ldots, 4.48$ s. The experimental values are denoted by circles, diamonds and squares for the 29 μm, 50 μm and 75 μm wells, respectively. The dashed lines correspond to the radius $\hat{R}_0$, the depth $\hat{H}_0$, and the position of the dry substrate for each well.

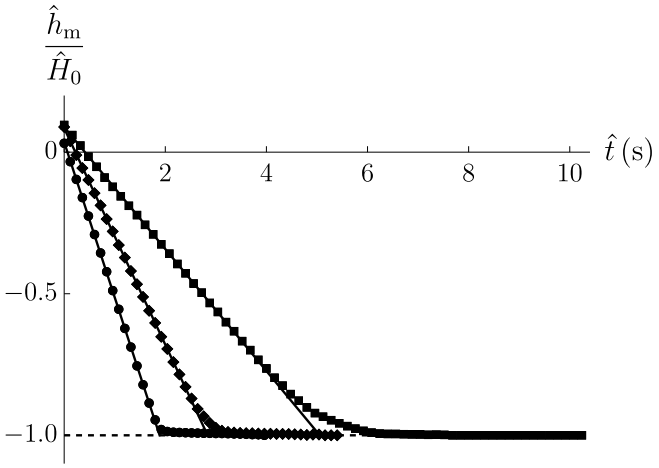

Figure 3.15: Experimental results for the normalised height of the free surface at the centre of the well, $\hat{h}_\mathrm{m}/\hat{H}_0$, (symbols) and linear fits to these values (solid black lines) as functions of $\hat{t}$ for wells of radius (a) 29 μm at times $\hat{t} = 0, 0.12, \ldots, 3.96$ s, (b) 50 μm at times $\hat{t} = 0, 0.12, \ldots, 5.40$ s, and (c) 75 μm at times $\hat{t} = 0, 0.16, \ldots, 10.24$ s. The experimental values are denoted by circles, diamonds and squares for the 29 μm, 50 μm and 75 μm wells, respectively. The dashed line corresponds to the normalised depth of the wells.

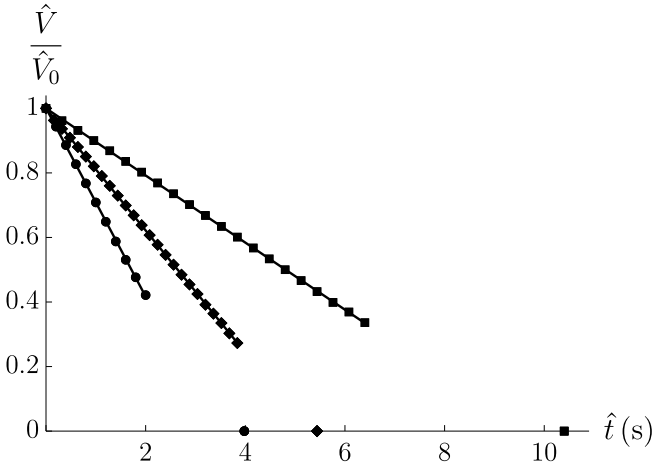

Figure 3.16: Experimental results for the normalised volume of a droplet, $\hat{V}/\hat{V}_0$, (symbols) and linear fits to these values (solid black lines) as functions of $\hat{t}$ for wells of radius 29 μm at times $\hat{t} = 0, 0.20, \ldots, 2.00$ s, 50 μm at times $\hat{t} = 0, 0.16, \ldots, 3.84$ s, and 75 μm at times $\hat{t} = 0, 0.32, \ldots, 6.40$ s. The experimental values are denoted by circles, diamonds and squares for the 29 μm, 50 μm and 75 μm wells, respectively. The symbols on the $\hat{t}$-axis correspond to $\hat{t} = \hat{t}_\mathrm{lifetime}$.

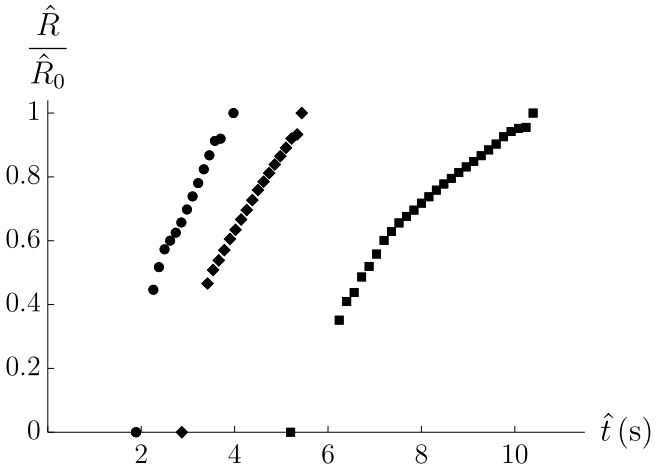

Figure 3.17: Experimental results for the normalised radius of the inner contact line, $\hat{R}/\hat{R}_0$, as functions of $\hat{t}$ for wells of radius 29 μm at times $\hat{t} = 2.32, 2.38, \ldots, 3.76$ s, 50 μm at times $\hat{t} = 3.38, 3.46, \ldots, 5.30$ s, and 75 μm at times $\hat{t} = 6.24, 6.40, \ldots, 10.24$ s. The experimental values are denoted by circles, diamonds and squares for the 29 μm, 50 μm and 75 μm wells, respectively. The symbols on the $\hat{t}$-axis correspond to $\hat{t} = \hat{t}_{\text{touchdown}}$, and those at $\hat{R}/\hat{R}_0 = 1$ to $\hat{t} = \hat{t}_{\text{lifetime}}$.

ing it increasingly difficult to resolve the free-surface profile near to the lip of the well. The resulting lack of experimental results means that the free surface cannot be accurately determined for very long after touchdown, and, in particular, that there is no certainty that the contact line remains pinned at the lip of the well after touchdown (as assumed in the mathematical model). However, given the good agreement between the experimental results and the theoretical predictions of the mathematical model which will be described in Section 3.6, we hypothesize that the effect of any de-pinning that does occur is minimal.

Figure 3.16 shows experimental results for the normalised volume of a droplet, $\hat{V}/\hat{V}_0$, obtained by calculating the volumes of the paraboloidal fits to the free-surface profiles, and linear fits to these values as functions of $\hat{t}$ for all three wells. Note that the difficulty of resolving the free-surface profile near to the lip of the well after touchdown means that the experimental values shown in Figure 3.16 stop shortly after $\hat{t} = \hat{t}_{\text{touchdown}}$ for each well. However, Figure 3.16 does show that the behaviour of $\hat{V}$ is nearly linear until shortly after touchdown.

Despite the interference fringes becoming increasingly closely spaced after touch-

down, the radius of the inner contact line can still be measured accurately by applying an appropriate threshold value to the intensity of the images of the droplets captured during the experiments. However, it should be noted that when the slope of the free surface is very small, this method is sensitive to the value of the threshold used and tends to overestimate the true value of $\hat{R}$. Figure 3.17 shows experimental values for the normalised radius of the inner contact line of a droplet, $\hat{R}/\hat{R}_0$, as functions of $\hat{t}$ for all three wells.

The lifetime of the droplet, $\hat{t}_{\text{lifetime}}$, was determined visually from the images of the droplet captured during the experiments as the time at which no further change is observed in the contrast at the contact line. The uncertainty in the measurement of t_{lifetime} is ± 0.02 s[††].

3.6 Comparison between theory and experiment

We now present comparisons between the theoretical predictions of the mathematical model described in Sections 3.2–3.4 in the case of a cylindrical well (*i.e.* in the limit $n \to \infty$) and the experimental results presented in Section 3.5. Specifically, we compare the evolution of the free-surface profile $\hat{h}$, the volume of the droplet $\hat{V}$, and the radius of the inner contact line $\hat{R}$, as well as the critical times $\hat{t}_{\text{flat}}$, $\hat{t}_{\text{touchdown}}$ and $\hat{t}_{\text{lifetime}}$. The theoretical predictions were calculated using the parameter values $\hat{\rho} = 1.087 \times 10^3$ kg m^{-3}, $\hat{c}_{\text{sat}} = 2.251 \times 10^{-3}$ kg m^{-3}, and $\hat{D} = 6.899 \times 10^{-6}$ m^2 s^{-1} for methyl benzoate at the temperature 22°C. The values of $\hat{\rho}$ and vapour pressure $\hat{p}_{\text{v}}$, the latter of which was used to obtain $\hat{c}_{\text{sat}}$, were calculated from Perry *et al.* [215] (Tables 2-30 and 2-6, respectively), and the value of the diffusion coefficient $\hat{D}$ was calculated from Fuller *et al.* [91] (Table 1). We note that there are no free parameters in the mathematical model, and no "tuning" of the parameter values has been performed in order to improve the agreement between the experimental results and the theoretical predictions.

As described in Section 3.2, the mathematical model is based on the assumptions that both the Bond number Bo and the scaled capillary number Ca* are small (so that the effect of gravity is negligible and the free surface of the droplet evolves

[††]C. D. Bain, personal communication

quasi-statically, respectively). Taking the radial velocity scale to be $\hat{U} = \hat{D}(\hat{c}_{\rm sat} - \hat{c}_\infty)/(\hat{\rho}\hat{\theta}_0\hat{R}_0)$, and using the values $\hat{\mu} = 1.851 \times 10^{-3}$ Pa s and $\hat{\sigma} = 3.720 \times 10^{-2}$ N m^{-1} for methyl benzoate at 25°C given by Sheu and Tu [252], confirms that the values of Bo and Ca* are indeed small for all of the experimental results presented in Section 3.5. Specifically, the values of Bo are approximately 10^{-4}, 10^{-3} and 10^{-3} for the 29 μm, 50 μm and 75 μm wells, respectively, and the values of Ca* are approximately 10^{-2} for all three wells.

Figure 3.18 shows a comparison between the experimental results and the theoretical predictions for the free-surface profile $\hat{h}$ of a droplet as functions of $\hat{r}$ for all three wells, while Figures 3.19 and 3.20 show comparisons between the experimental results and the theoretical predictions for the normalised volume of a droplet, $\hat{V}/\hat{V}_0$, and the normalised radius of the inner contact line, $\hat{R}/\hat{R}_0$, respectively, as functions of $\hat{t}$ for all three wells. In particular, Figures 3.18–3.20 show that, while the theoretical predictions are generally in good agreement with the experimental results (especially for the 50 μm well), the theoretical predictions lag slightly behind the experimental results for the 29 μm and 75 μm wells. We believe that this slight lag is due to the sensitivity of the theoretical predictions to the precise values of $\hat{c}_{\rm sat}$ and $\hat{D}$ used, as well as to the calculated values of $\hat{\theta}_0$. In particular, as already mentioned, the ambient temperature was controlled only to within 1°C and the value of $\hat{c}_{\rm sat}$ is rather sensitive to the precise value of the temperature at which it is evaluated; specifically, $\hat{c}_{\rm sat}$ changes by 6–8% for a 1°C change in temperature. Fitting the value(s) of $\hat{c}_{\rm sat}$, $\hat{D}$ and/or $\hat{\theta}_0$ would eliminate the lag between the theoretical predictions and the experimental results, especially given that the same values of $\hat{c}_{\rm sat}$ and $\hat{D}$ are currently used across all of the experiments, but we deliberately chose not to do this in order to provide a sterner test for the mathematical model.

In addition, we note that the mathematical model assumes that a new inner contact line appears at the centre of the well at touchdown, and so does not capture the very thin film left briefly on the bottom of the well in the experiments, which is most visible in the experimental results for the 75 μm well shown in Figure 3.18(c). However, the good agreement between the theoretical predictions and the experimental results

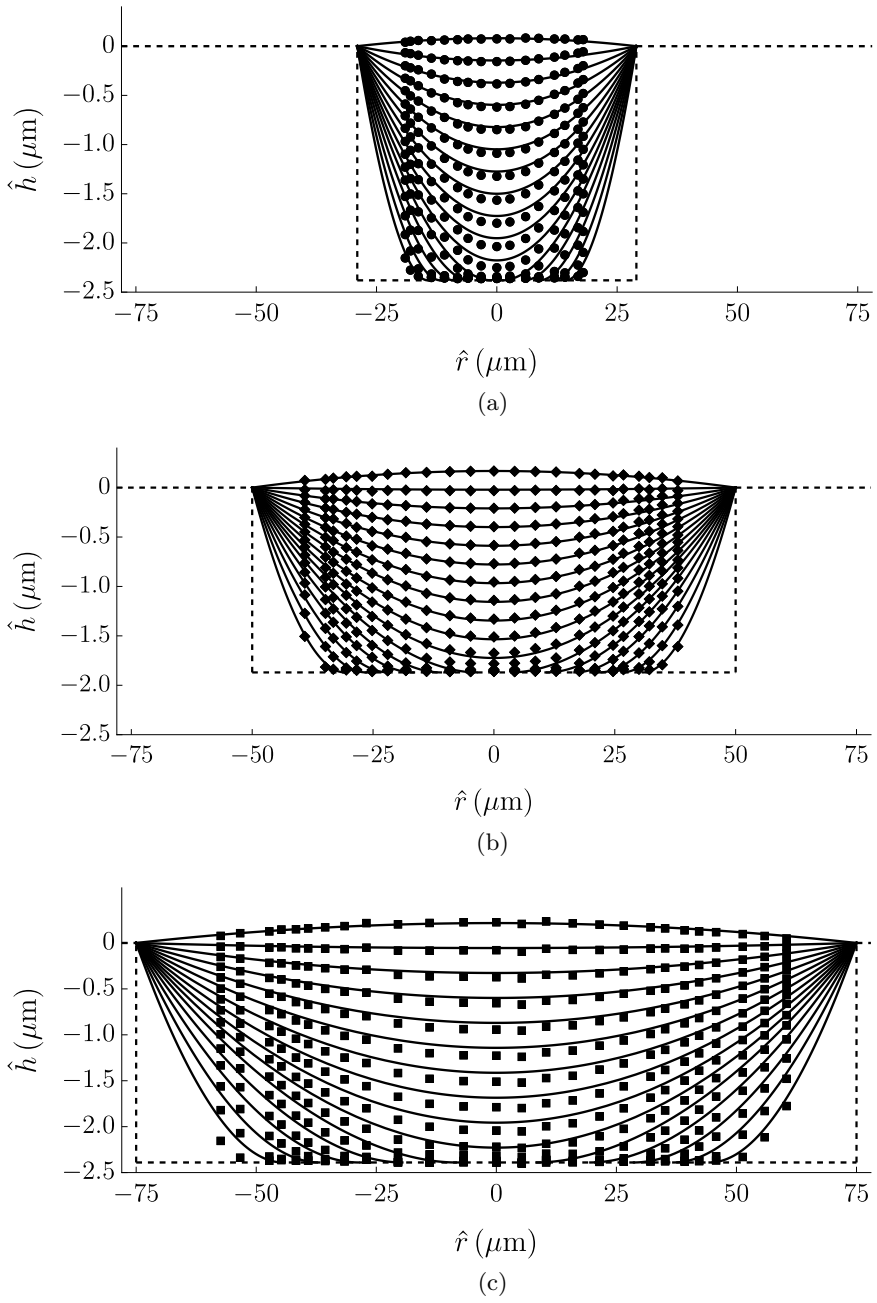

Figure 3.18: Comparison between the experimental results (symbols) and the theoretical predictions (solid black lines) for the free-surface profile $\hat{h}$ of a droplet as functions of $\hat{r}$ for wells of radius (a) 29 μm at times $\hat{t} = 0, 0.18, \ldots, 2.70$ s, (b) 50 μm at times $\hat{t} = 0, 0.26, \ldots, 4.16$ s, and (c) 75 μm at times $\hat{t} = 0, 0.56, \ldots, 7.84$ s. The experimental values are denoted by circles, diamonds and squares for the 29 μm, 50 μm and 75 μm wells, respectively. The dashed lines correspond to the radius $\hat{R}_0$, the depth $\hat{H}_0$, and the position of the dry substrate for each well.

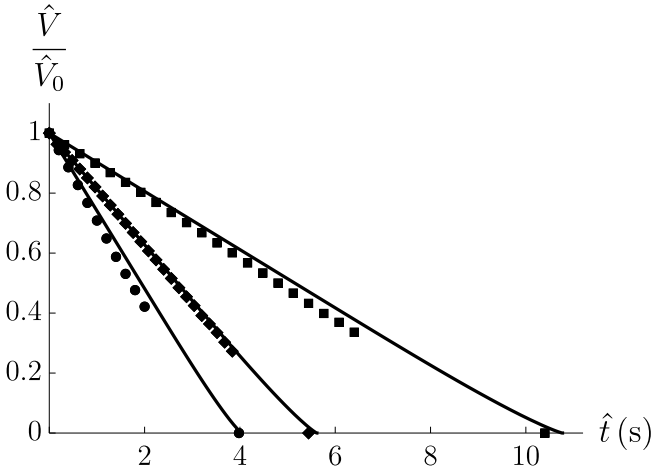

Figure 3.19: Comparison between the experimental results (symbols) shown in Figure 3.16 and the theoretical predictions (solid black lines) for the normalised volume of a droplet, $\hat{V}/\hat{V}_0$, as functions of $\hat{t}$ for all three wells. The experimental values are denoted by circles, diamonds and squares for the 29 μm, 50 μm and 75 μm wells, respectively.

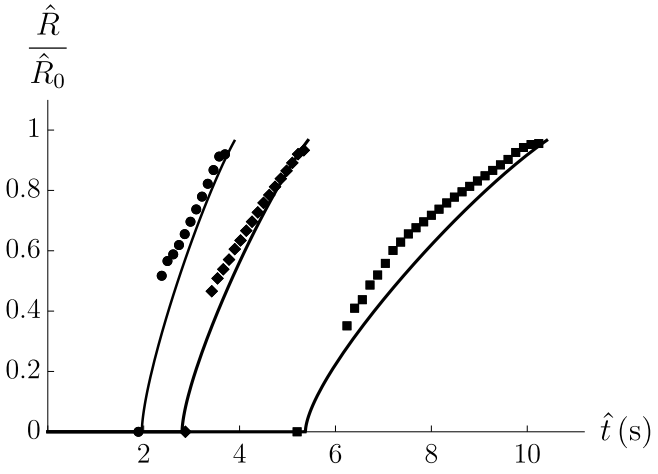

Figure 3.20: Comparison between the experimental results (symbols) shown in Figure 3.17 and the theoretical predictions (solid black lines) for the normalised radius of the inner contact line, $\hat{R}/\hat{R}_0$, as functions of $\hat{t}$ for all three wells. The experimental values are denoted by circles, diamonds and squares for the 29 μm, 50 μm and 75 μm wells, respectively.

$\hat{R}_0$ (μm)		$\hat{t}_{\text{flat}}$ (s)	$\hat{t}_{\text{touchdown}}$ (s)	$\hat{t}_{\text{lifetime}}$ (s)	$\mathcal{T}$
29	Experimental Values	0.060	1.888	3.976	2.142
	Theoretical Prediction	0.065	1.962	4.039	2.095
	Percentage Error	8%	3.9%	1.6%	−2.2%
50	Experimental Values	0.210	2.838	5.438	1.989
	Theoretical Prediction	0.231	2.801	5.615	2.095
	Percentage Error	10%	−1.3%	3.3%	5.3%
75	Experimental Values	0.408	5.056	10.392	2.148
	Theoretical Prediction	0.447	5.373	10.769	2.095
	Percentage Error	10%	6.3%	3.6%	−2.5%

Table 3.2: Comparison between the experimental values and the theoretical predictions for the critical times $\hat{t}_{\text{flat}}$, $\hat{t}_{\text{touchdown}}$ and $\hat{t}_{\text{lifetime}}$, and the parameter-free quantity $\mathcal{T}$ given by (3.54) for all three wells.

shown in Figures 3.18–3.20 indicates that the presence of this film has very little effect on the overall evolution of the droplet. At first sight, it might seem surprising that the most noticeable deviations from the quasi-static free-surface profiles predicted by the mathematical model occur for the shallowest well (*i.e.* for the well with the smallest value of ϵ). However, while, as already mentioned, the values of Ca^* are small for all three wells, the capillary number is inversely proportional to ϵ^3, and so larger values of Ca^*, and hence more significant deviations from quasi-static free-surface profiles, are to be expected for wells with smaller values of ϵ.

As previously noted in Section 3.5, the experimental values of the critical times depend on the arbitrarily chosen initial time, $\hat{t} = 0$, as well as on the values of the ambient temperature and the atmospheric pressure. Moreover, as also previously noted, the theoretical predictions for the critical times are sensitive to the precise values of $\hat{c}_{\text{sat}}$, $\hat{D}$ and $\hat{\theta}_0$. In order to remove all of these dependencies, we consider a parameter-free quantity involving the relative values of the critical times, namely

$$\mathcal{T} = \frac{\hat{t}_{\text{lifetime}} - \hat{t}_{\text{flat}}}{\hat{t}_{\text{touchdown}} - \hat{t}_{\text{flat}}}, \tag{3.54}$$

which, using the theoretical values of the critical times given by (3.20), (3.22) and (3.50) in the limit $n \to \infty$ takes the same (purely numerical) value, namely $\mathcal{T} = 1 + 8\alpha_\infty \simeq$

2.095, regardless of the values of the parameters. Table 3.2 shows a comparison between the experimental values and the theoretical predictions for $\hat{t}_{\text{flat}}$, $\hat{t}_{\text{touchdown}}$, $\hat{t}_{\text{lifetime}}$ and $\mathcal{T}$ for all three wells. Table 3.2 shows that the theoretical predictions are in good agreement with the experimental values, with average absolute errors of approximately 9%, 3.8%, 2.8% and 3.3% in $\hat{t}_{\text{flat}}$, $\hat{t}_{\text{touchdown}}$, $\hat{t}_{\text{lifetime}}$ and $\mathcal{T}$, respectively.

The comparisons presented in this Section show that, despite the inevitable experimental errors and uncertainties about the precise values of the parameters, the mathematical model captures the evolution of a thin droplet in a shallow cylindrical well rather well. The agreement is especially good given that, as already mentioned, there are no free parameters in the mathematical model, and no tuning of the parameter values has been performed in order to improve the agreement.

3.7 Comparison with previous experimental results

While the experimental results presented in Section 3.5 provide the most comprehensive test for the theoretical predictions of the mathematical model, it is also of interest to consider how well the present model is able to capture experimental results reported by previous authors. Making these comparisons is, unfortunately, hampered by a lack of complete information about the experiments.

Rieger *et al.* [226] studied the evaporation of ethylene glycol droplets in cylindrical nanoliter wells of various radii. In particular, they reported the evolution of the free-surface profile of a droplet before touchdown in a well with radius 100 μm and depth 6.13 μm, and concluded that it was a quasi-static spherical cap that was pinned at the lip of the well. Rieger *et al.* [226] gave the experimental values $\hat{t}_{\text{flat}} = 20$ s and $\hat{t}_{\text{touchdown}} = 160$ s, but not the experimental value of $\hat{t}_{\text{lifetime}}$, for this droplet, and so, unfortunately, we cannot calculate the experimental value of the parameter-free quantity $\mathcal{T}$ given by (3.54). The authors also did not give the value of the initial angle $\hat{\theta}_0$, but if we calculate it in exactly the same way as we did in Section 3.6, we obtain $\hat{\theta}_0 = 0.0144$. The value of the ambient temperature was also not reported, but if we assume that it was 20°C, then using the parameter values $\hat{\rho} = 1.114 \times 10^3$ kg m^{-3}, $\hat{c}_{\text{sat}} = 2.042 \times 10^{-4}$ kg m^{-3}, and $\hat{D} = 1.098 \times 10^{-5}$ m^2 s^{-1} calculated from Perry

et al. [215] (Tables 2-30 and 2-6, respectively) and Fuller *et al.* [91] (Table 1) in exactly the same way as we did in Section 3.6, the theoretical predictions are $\hat{t}_{\text{flat}} = 14.05$ s and $\hat{t}_{\text{touchdown}} = 133.7$ s, which are in error by 30% and 16%, respectively, compared to the experimental values. It should, however, be noted that, in addition to the uncertainties about the precise values of $\hat{c}_{\text{sat}}$, $\hat{D}$ and $\hat{\theta}_0$ already mentioned, some of this discrepancy may be due to the fact that ethylene glycol is hygroscopic, and so the droplet will absorb water vapour from the atmosphere, which will presumably lead to longer critical times than those predicted by the present mathematical model. Rieger *et al.* [226] did not investigate the evolution of the droplet after touchdown.

Subsequently, Chen *et al.* [45] studied the evaporation of water droplets in cylindrical nanoliter wells of various radii. The experiments were carried out in an atmosphere of air with relative humidity of water vapour of $\widehat{RH} = 0.60$ and an ambient temperature of 25°C. Chen *et al.* [45] reported quantitative data for the evolution of the radius of the inner contact line $\hat{R}$, but not for the evolution of the free-surface profile h or the volume of the droplet $\hat{V}$. Furthermore, they did not report the values of the initial angle $\hat{\theta}_0$. They did, however, give the critical times for a droplet in a well with radius 250 μm and depth 65 μm to be $\hat{t}_{\text{flat}} = 9 \pm 1$ s (estimated from their Figure 9), $\hat{t}_{\text{touchdown}} = 31$ s, and $\hat{t}_{\text{lifetime}} = 55$ s. In the absence of the value of $\hat{\theta}_0$, the only theoretical prediction that can be compared with these experimental results is that for $\mathcal{T}$ for the well with radius 250 μm, for which we find that the experimental value $\mathcal{T} = 2.09 \pm 0.05$ is in very good agreement with the theoretical value $\mathcal{T} = 2.095$.

3.8 Conclusions

Motivated by the industrial manufacture of OLED displays, in this Chapter we formulated and analysed a mathematical model for the evolution of a thin droplet in a shallow axisymmetric well with profile $\hat{z} = \hat{H}(\hat{r}) = -\hat{H}_0(1 - (\hat{r}/\hat{R}_0)^n)$ both before and after touchdown that accounts for the spatially non-uniform evaporation of the fluid, described physical experiments performed at Durham University using three cylindrical wells with different small aspect ratios, and validated the mathematical model by

comparing these experimental results with the corresponding theoretical predictions for a cylindrical well (*i.e.* in the limit $n \to \infty$).

The mathematical model describes how as the droplet evaporates its free surface becomes instantaneously flat at $t = t_{\text{flat}}$ and then touches down at $t = t_{\text{touchdown}}$ before the droplet completely evaporates at $t = t_{\text{lifetime}}$. In the special case $n = 2$ (*i.e.* a paraboloidal well) touchdown occurs everywhere simultaneously within the well, and so $t_{\text{lifetime}} = t_{\text{touchdown}} = \pi(1 + 2H_0)/16$. However, in the general case $n \neq 2$ the droplet has not completely evaporated at $t = t_{\text{touchdown}}$, and the nature of its subsequent evolution depends on the shape of the well. If the slope of the well at its lip is sufficiently small, specifically when $0 < n < 2$, then touchdown occurs at the lip of the well at $t = t_{\text{touchdown}}$ given by (3.21), at which instant the contact line de-pins from the lip of the well, and thereafter recedes towards the centre of the well, finally reaching it at $t = t_{\text{lifetime}}$ given by (3.38). On the other hand, if the slope of the well at its lip is sufficiently large, specifically when $n > 2$, then touchdown occurs at the centre of the well at $t = t_{\text{touchdown}}$ given by (3.22), at which instant a new inner contact line appears at the centre of the well, and thereafter recedes towards the lip of the well (where the outer contact line remains pinned), finally reaching it at $t = t_{\text{lifetime}}$ given by (3.50). In particular, we found that t_{flat} is independent of H_0 and n, $t_{\text{touchdown}}$ increases linearly with H_0 and with n for $0 \leq n \leq 2$ but is independent of n for $n > 2$, and t_{lifetime} also increases linearly with H_0 but non-linearly with n.

The physical experiments involved depositing single droplets of methyl benzoate in three cylindrical wells with different small aspect ratios and observing the evolution of the droplets as they evaporated. We found good agreement between the experimental results and the corresponding theoretical predictions for a cylindrical well. While the present mathematical model does not capture the very thin film left briefly on the bottom of the well in the experiments, the good agreement between the theoretical predictions and the experimental results indicates that the presence of this film has very little effect on the overall evolution of the droplet.

Chapter 4

The Effect of Gravity on the Shape, Evolution, and Lifetime of an Evaporating Droplet

4.1 Introduction

In this Chapter we study the effect of gravity on the shape, evolution, and lifetime of evaporating sessile and pendant droplets. Specifically, in Section 4.2 we formulate a mathematical model describing the evaporation of thin sessile and pendant droplets under the effect of gravity. In Section 4.3 we analyse the shape of sessile and pendant droplets of arbitrary volume and determine the limiting behaviours for small and large droplet volumes. In Section 4.4 we give theoretical predictions for the evolution, and hence the lifetime, of sessile and pendant droplets evaporating in the extreme modes of evaporation, namely in the CR and CA modes. In Sections 4.5 and 4.6 we extend the investigation of droplet evolution, and hence lifetime, to two mixed modes of evaporation, specifically to the SS and SJ modes, respectively.

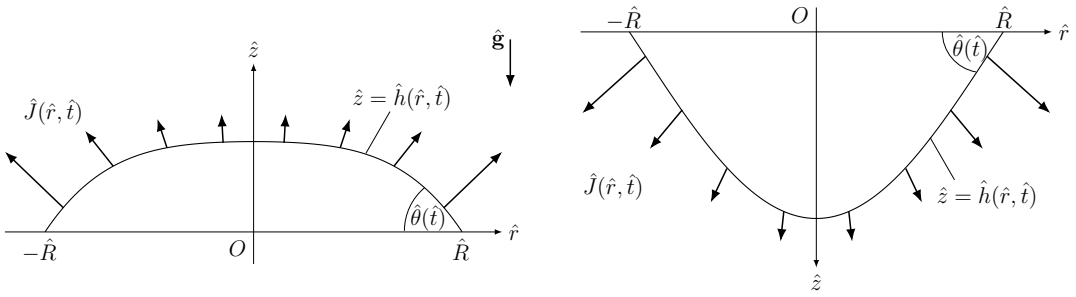

Figure 4.1: Sketch of a thin (a) sessile and (b) pendant droplet with contact radius $\hat{R}(\hat{t})$, contact angle $\hat{\theta}(\hat{t})$, and free surface $\hat{z}=\hat{h}(\hat{r},\hat{t})$ evaporating on a horizontal substrate under the effect of gravity $\hat{\mathbf{g}}$. The arrows indicate the local evaporative flux $\hat{J}(\hat{r},\hat{t})$.

4.2 Problem formulation

We consider an axisymmetric sessile or pendant droplet on a horizontal substrate undergoing quasi-static diffusion-limited evaporation in a quiescent atmosphere. As in Chapter 2, we refer the description to cylindrical polar coordinates $(\hat{r},\,\hat{\varphi},\,\hat{z})$, with $O\hat{z}$ along the axis of the droplet, perpendicular to the substrate at $\hat{z}=0$, pointing upwards or downwards for a sessile or a pendant droplet, respectively, as sketched in Figure 4.1. After the droplet is deposited at $\hat{t}=0$, its volume will decrease due to evaporation into the atmosphere. We denote the time at which the droplet has completely evaporated, *i.e.* the lifetimes of the droplet, by $\hat{t}_{\rm CR}$, $\hat{t}_{\rm CA}$, $\hat{t}_{\rm SS}$, and $\hat{t}_{\rm SJ}$ for a droplet evaporating in the CR, CA, SS, and SJ modes, respectively.

4.2.1 The droplet geometry

As in Chapter 2, we consider situations in which the droplet is thin and, in particular, in which the initial contact angle of the droplet, $\hat{\theta}_0 \ll 1$, is small. In the present Chapter, however, we consider situations in which the droplet is sufficiently large that the effect of gravity is not necessarily negligible, but in which surface tension is again sufficiently strong that the free surface of the droplet evolves quasi-statically. More specifically, we consider situations in which the the appropriately defined characteristic length scale of the droplet is $\hat{L}=\hat{\ell}$, and the appropriately defined Bond number Bo

and scaled capillary number Ca^* from (2.2), namely

$$\mathrm{Bo} = \left(\frac{\hat{L}}{\hat{\ell}}\right)^2 = 1 \quad \text{and} \quad \mathrm{Ca}^* = \frac{\mathrm{Ca}}{\hat{\theta}_0^3} = \frac{\hat{\mu}\hat{U}}{\hat{\theta}_0^3\hat{\sigma}} \ll 1, \tag{4.1}$$

are unity and small, respectively, where again $\hat{\ell} = \sqrt{\hat{\sigma}/\hat{\rho}\hat{g}}$ denotes the capillary length.

The pressure $\hat{p} = \hat{p}(\hat{r}, \hat{z}, \hat{t})$ within the droplet therefore satisfies

$$\hat{\nabla}\hat{p} = \mp\hat{\rho}\hat{g}\,\mathbf{e}_z, \tag{4.2}$$

where, here and throughout this Chapter, the upper and lower signs correspond to a sessile and a pendant droplet, respectively, and $\mathbf{e}_z$ denotes the unit vector in the z-direction. As in Chapter 2, the pressure $\hat{p}$ is subject to the Young–Laplace equation at the free surface, namely

$$\hat{p} - \hat{p}^{\mathrm{a}} = \hat{\sigma}\hat{\kappa} \quad \text{at} \quad \hat{z} = \hat{h}, \tag{4.3}$$

where, at leading order in the limit $\hat{\theta}_0 \to 0$, the mean curvature of the free surface of the droplet $\hat{\kappa}$ is given by

$$\hat{\kappa} = -\frac{1}{\hat{r}}\frac{\partial}{\partial\hat{r}}\left(\hat{r}\frac{\partial\hat{h}}{\partial\hat{r}}\right). \tag{4.4}$$

Solving (4.2) subject to (4.3) yields the governing equation for the free-surface profile $\hat{h}$:

$$\hat{\sigma}\frac{\partial}{\partial\hat{r}}\left(\frac{1}{\hat{r}}\frac{\partial}{\partial\hat{r}}\left(\hat{r}\frac{\partial\hat{h}}{\partial\hat{r}}\right)\right) \mp \hat{\rho}\hat{g}\frac{\partial\hat{h}}{\partial\hat{r}} = 0. \tag{4.5}$$

We note that in the absence of (or neglect of) gravitational effects, *i.e.* for $\hat{g} = 0$, (4.5) recovers the familiar governing equation for $\hat{h}$ for a small thin droplet given by (2.16) in Chapter 2 which, throughout this Chapter, will be referred to as the zero-gravity droplet.

4.2.2 The evaporative problem

We nondimensionalise and scale the variables according to (2.13) with $\hat{L} = \hat{\ell}$ for the droplet, and similarly for the atmosphere except that $\hat{z} = \hat{\ell}z^{\mathrm{a}}$. We note that, by using the capillary length $\hat{\ell}$ as the appropriate radial length scale for the droplet, the initial

value of the contact radius R_0 is not scaled to 1 as it was for the zero-gravity droplet, as presented in Chapters 2 and 3, but the initial value of the contact angle is still unity.

At leading order in the limit $\hat{\theta}_0 \to 0$ the problem for the concentration $c = c(r, z^{\rm a}, t)$ of vapour in the atmosphere is therefore given by (2.20)–(2.25), namely

$$\nabla^2 c = 0 \quad \text{for} \quad z^{\rm a} > 0, \tag{4.6}$$

with

$$c = 1 \quad \text{on} \quad z^{\rm a} = 0 \quad \text{for} \quad 0 \le r \le R, \tag{4.7}$$

$$c \to 0 \quad \text{as} \quad r^2 + z^{\rm a2} \to \infty, \tag{4.8}$$

$$\frac{\partial c}{\partial z^{\rm a}} = 0 \quad \text{on} \quad z^{\rm a} = 0 \quad \text{for} \quad r > R, \tag{4.9}$$

$$J = -\frac{\partial c}{\partial z^{\rm a}} \quad \text{on} \quad z^{\rm a} = 0 \quad \text{for} \quad 0 \le r \le R, \tag{4.10}$$

$$\frac{{\rm d}V}{{\rm d}t} = -F \quad \text{where} \quad F = 2\pi \int_0^R J\, r \, {\rm d}r. \tag{4.11}$$

The solution for the concentration c from (4.6)–(4.9) is given by

$$c = \frac{2}{\pi} \sin^{-1} \frac{2R}{\left[(R+r)^2 + z^{\rm a2}\right]^{1/2} + \left[(R-r)^2 + z^{\rm a2}\right]^{1/2}}, \tag{4.12}$$

which, using (4.10), leads to the solution for the local evaporative flux $J = J(r, t)$, namely

$$J = \frac{2}{\pi (R^2 - r^2)^{1/2}}. \tag{4.13}$$

Equations (4.12) and (4.13) correspond to the solution for the zero-gravity droplet given by (2.26) and (2.27) in Chapter 2. We note that, as in Chapters 2 and 3, the concentration c and hence the local flux J depend on t via their dependence on $R = R(t)$.

Substituting (4.13) into (4.11) and evaluating the integral yields the following equation describing the evolution of the droplet:

$$\frac{{\rm d}V}{{\rm d}t} = -4R. \tag{4.14}$$

4.3 The shape of the droplet

For both sessile and pendant droplets the free-surface profile obtained by solving (4.5) must satisfy the contact-line conditions

$$h = 0, \quad \frac{\partial h}{\partial r} = -\theta \quad \text{at} \quad r = R, \tag{4.15}$$

and the volume $V = V(t)$ of the droplet is given by

$$V = 2\pi \int_0^R h\, r \, \mathrm{d}r. \tag{4.16}$$

We will now derive the solutions for the shape of a sessile and a pendant droplet in turn.

4.3.1 A sessile droplet

For a sessile droplet, the solution for the free-surface profile $h = h(r, t)$ satisfying (4.5) subject to (4.15) and the condition that h is finite at $r = 0$ takes the form

$$h = \frac{\theta \left[I_0 \left(R \right) - I_0 \left(r \right) \right]}{I_1 \left(R \right)}, \tag{4.17}$$

where I_n denotes the modified Bessel function of the first kind of order n. In particular, the height at the middle of the droplet $h_\mathrm{m} = h_\mathrm{m}(t) = h(0, t)$ is given by

$$h_\mathrm{m} = \frac{\theta \left[I_0 \left(R \right) - 1 \right]}{I_1 \left(R \right)}. \tag{4.18}$$

From (4.16) the volume V of the droplet is

$$V = \frac{\pi \theta R^2 I_2 \left(R \right)}{I_1 \left(R \right)}. \tag{4.19}$$

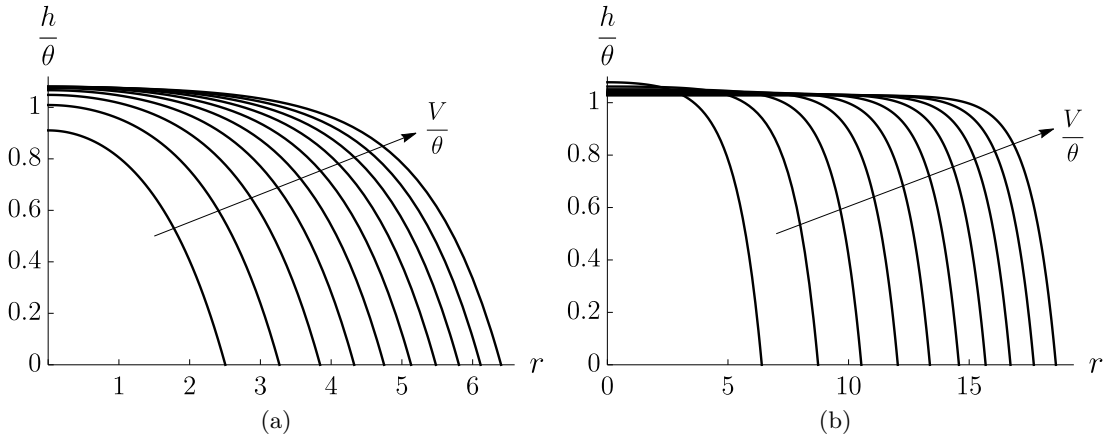

Figure 4.2: Plot of h/θ as a function of r for a sessile droplet when (a) $V/\theta = 10$, 20, ..., 100 and (b) $V/\theta = 100$, 200, ..., 1000. The arrows indicate the direction of increasing V/θ.

The initial values of θ, R, h_{m}, and V are given by

$$\theta = 1, \quad R = R_0, \quad h_{\mathrm{m}} = h_{\mathrm{m}_0} = \frac{I_0(R_0) - 1}{I_1(R_0)}, \quad V = V_0 = \frac{\pi R_0^2 I_2(R_0)}{I_1(R_0)} \quad \text{at} \quad t = 0. \tag{4.20}$$

Any one of the three initial values R_0, h_{m_0}, or V_0 may be prescribed, with the other two determined from (4.20). We note that, although we could compare sessile and pendant droplets of the same initial contact radius R_0 or initial height at the middle of the droplet h_{m_0}, we will compare sessile and pendant droplets of the same scaled volume V/θ or initial volume V_0 throughout this Chapter.

Figure 4.2 shows scaled droplet profiles h/θ for a range of values of the scaled volume V/θ. As the scaled volume of the droplet increases, the contact radius increases and the scaled free surface flattens. Figure 4.3 shows plots of the scaled height at the middle of the droplet h_{m}/θ and the contact radius R as functions of the scaled volume V/θ according to (4.18) and (4.19). In particular, as Figure 4.3(a) shows, h_{m}/θ is non-monotonic in V/θ, increasing from zero at $V/\theta = 0$ to a maximum value $h_{\mathrm{m}}/\theta = h_{\mathrm{m,max}}/\theta \simeq 1.081$ at $V/\theta \simeq 73.175$, corresponding to $R \simeq 5.586$, and subsequently decreasing to 1 as $V/\theta \to \infty$. This non-monotonic behaviour in h_{m} is in agreement with the numerical results of Padday [203] for the case of a non-thin sessile droplet, as

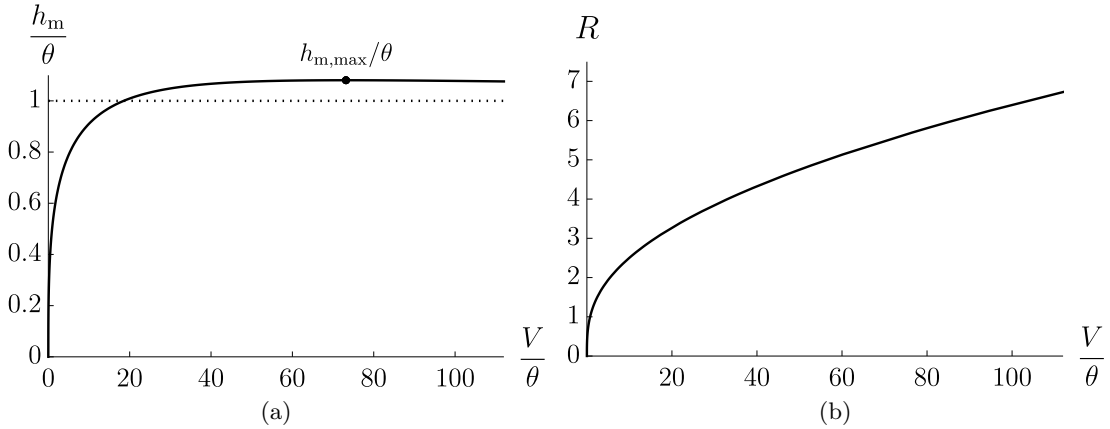

Figure 4.3: Plots of (a) h_m/θ and (b) R as functions of V/θ for a sessile droplet. The dot and the dashed line in (a) correspond to the maximum value $h_\mathrm{m}/\theta = h_{\mathrm{m,max}}/\theta \simeq 1.081$ at $V/\theta \simeq 73.175$ and the limiting value $h_\mathrm{m}/\theta \to 1$ as $V/\theta \to \infty$, respectively.

discussed in Chapter 1; in addition, this behaviour has been observed for the similar problem of liquid marbles (*i.e.* non-wetting droplets) by Aussillous and Quéré [17]. The contact radius R increases monotonically from zero at $V/\theta = 0$ to infinity as $V/\theta \to \infty$, as indicated in Figure 4.3(b).

In the limit of small contact radius ($R \to 0^+$), corresponding to the limit of small volume ($V \to 0^+$), surface-tension effects dominate over gravity and the sessile droplet becomes narrow and thin according to

$$\frac{h}{\theta} = \frac{1}{2R}\left(R^2 - r^2\right)\left[1 - \frac{\left(R^2 - r^2\right)}{16}\right] + O\left(R^2 - r^2\right)^3 \to 0^+, \tag{4.21}$$

$$\frac{h_\mathrm{m}}{\theta} = \frac{R}{2}\left(1 - \frac{R^2}{16}\right) + O\left(R^5\right) \to 0^+, \tag{4.22}$$

$$\frac{V}{\theta} = \frac{\pi R^3}{4}\left(1 - \frac{R^2}{24}\right) + O\left(R^7\right) \to 0^+. \tag{4.23}$$

In particular, at leading order in the limit $R \to 0^+$, (4.21)–(4.23) recover the familiar solutions for the zero-gravity droplet, given by (2.17)–(2.19) in Chapter 2, *i.e.* h is parabolic, h_m is linear in R, and V is proportional to the cube of the contact radius (*i.e.* to R^3).

In the limit of large contact radius ($R \to \infty$), corresponding to the limit of large

volume ($V \to \infty$), surface-tension effects are negligible away from the contact line, and the sessile droplet becomes wide and flat according to

$$\frac{h}{\theta} \sim \frac{h_{\mathrm{m}}}{\theta}, \tag{4.24}$$

$$\frac{h_{\mathrm{m}}}{\theta} = 1 + \frac{1}{2R} + \frac{3}{16R^2} + O\left(\frac{1}{R^3}\right) \to 1^+, \tag{4.25}$$

$$\frac{V}{\theta} = \pi R^2 \left(1 - \frac{3}{2R} + \frac{3}{8R^2}\right) + O\left(\frac{1}{R}\right) \to \infty. \tag{4.26}$$

In particular, at leading order in the limit $R \to \infty$, h has uniform thickness away from the contact line, h_{m} is finite, as indicated by the dashed line in Figure 4.3(a), and corresponds to the familiar solution for non-thin droplets in the small-angle limit (see, for example, Padday [203]), and V is proportional to the square of the contact radius (*i.e.* to R^2).

4.3.2 A pendant droplet

For a pendant droplet, the solution for the free-surface profile $h = h(r,t)$ satisfying (4.5) subject to (4.15) and the condition that h is finite at $r = 0$ takes the form

$$h = \frac{\theta\left[J_0\left(r\right) - J_0\left(R\right)\right]}{J_1\left(R\right)}, \tag{4.27}$$

where J_n denotes the Bessel function of the first kind of order n. There are infinitely many branches of solutions for h for a pendant droplet; however, only the lowest/first branch provides physically relevant solutions with $h \geq 0$ for $0 \leq r \leq R$. The height at the middle of the droplet h_{m} is given by

$$h_{\mathrm{m}} = \frac{\theta\left[1 - J_0\left(R\right)\right]}{J_1\left(R\right)}, \tag{4.28}$$

and the volume V from (4.16) is

$$V = \frac{\pi\theta R^2 J_2\left(R\right)}{J_1\left(R\right)}. \tag{4.29}$$

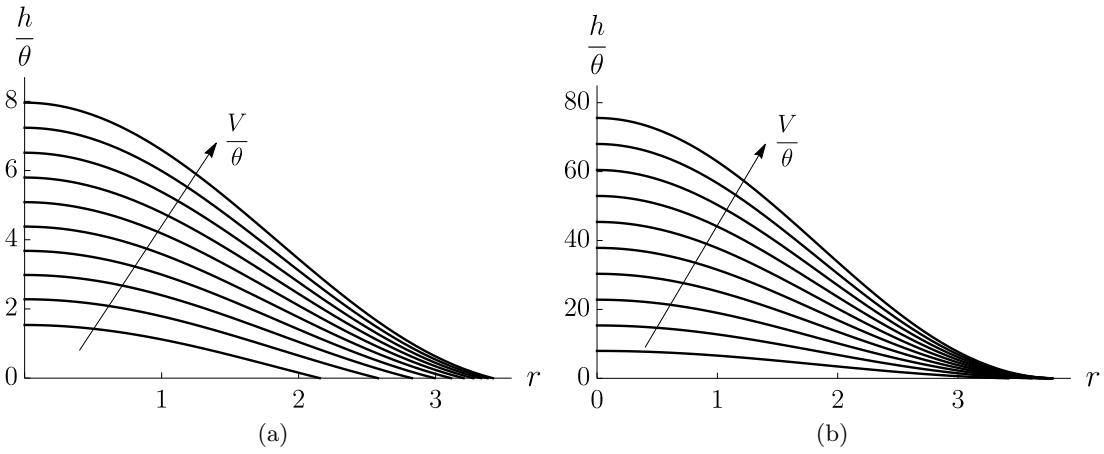

Figure 4.4: Plot of h/θ as a function of r for a pendant droplet when (a) $V/\theta = 10$, 20, ..., 100 and (b) $V/\theta = 100$, 200, ..., 1000. The arrows indicate the direction of increasing V/θ. We note that the vertical scales differ by an order of magnitude.

The initial values of θ and R are the same as those for a sessile droplet, with the initial values of h_{m} and V given by

$$h_{\mathrm{m}} = h_{\mathrm{m}_0} = \frac{1 - J_0(R_0)}{J_1(R_0)}, \quad V = V_0 = \frac{\pi R_0^2 J_2(R_0)}{J_1(R_0)} \quad \text{at} \quad t = 0. \tag{4.30}$$

Figure 4.4 shows scaled droplet profiles h/θ for a range of values of the scaled volume V/θ on the lowest branch of solutions. Figure 4.5 shows plots of the scaled height at the middle of the droplet h_{m}/θ and the contact radius R as functions of the scaled volume V/θ according to (4.28) and (4.29). In particular, h_{m}/θ increases monotonically from zero at $V/\theta = 0$ to infinity as $V/\theta \to \infty$, as indicated by Figure 4.5(a). As Figure 4.5(b) shows, the contact radius R increases monotonically from zero at $V/\theta = 0$ to a maximum value $R \to R_{\max} \simeq 3.832$, corresponding to the first zero of $J_1(R)$, as $V/\theta \to \infty$. Therefore, the contact radius R of a pendant droplet has a maximum value $R_{\max}$ and, in addition, we note that the contact radius R of a pendant droplet given by (4.29) is always smaller than that of a sessile droplet given by (4.19) for the same volume V which, as we shall see in Sections 4.4–4.6, is an important factor in the evolution, and hence the lifetimes, of evaporating sessile and pendant droplets.

In the limit of small contact radius ($R \to 0^+$), corresponding to the limit of small

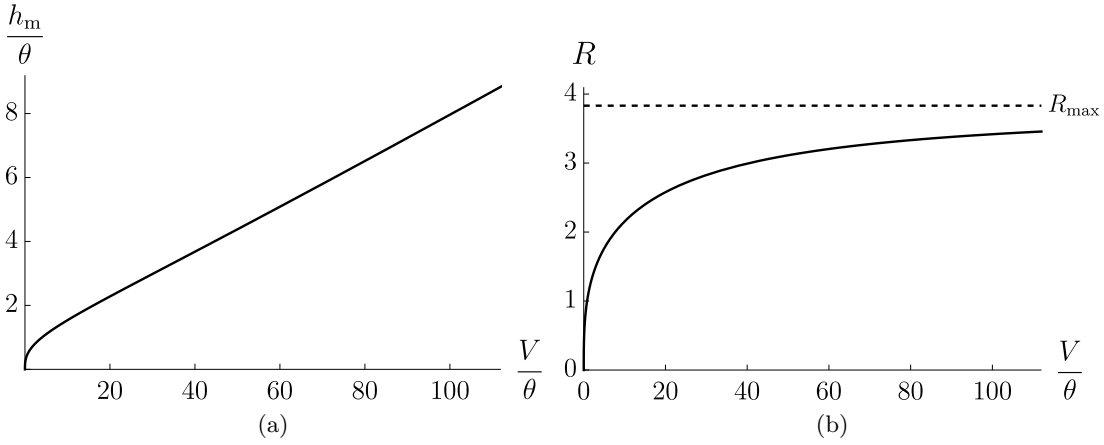

Figure 4.5: Plots of (a) h_m/θ and (b) R as functions of V/θ for a pendant droplet. The dashed line in (b) corresponds to the maximum value $R \to R_\mathrm{max} \simeq 3.832$ as $V/\theta \to \infty$.

volume ($V \to 0^+$), the pendant droplet becomes narrow and thin according to

$$\frac{h}{\theta} = \frac{1}{2R}\left(R^2 - r^2\right)\left[1 + \frac{\left(R^2 - r^2\right)}{16}\right] + O\left(R^2 - r^2\right)^3 \to 0^+, \tag{4.31}$$

$$\frac{h_\mathrm{m}}{\theta} = \frac{R}{2}\left(1 + \frac{R^2}{16}\right) + O\left(R^5\right) \to 0^+, \tag{4.32}$$

$$\frac{V}{\theta} = \frac{\pi R^3}{4}\left(1 + \frac{R^2}{24}\right) + O\left(R^7\right) \to 0^+, \tag{4.33}$$

which are analogous to the corresponding solutions for a sessile droplet (4.21)–(4.23) and are identical at leading order but differ at higher order. In particular, at leading order in the limit $R \to 0^+$, (4.31)–(4.33) recover the same solutions as that for a sessile droplet from (4.21)–(4.23), corresponding to the familiar solutions for the zero-gravity droplet, given by (2.17)–(2.19) in Chapter 2. Therefore, for sufficiently small droplets ($V \to 0$), or droplets in a low-gravity environment ($\hat{g} \to 0$), surface-tension effects dominate and the orientation of the droplet does not affect the shape at leading order.

In the limit of the maximum contact radius ($R \to R_\mathrm{max}^-$), corresponding to the limit of large volume ($V \to \infty$), the pendant droplet approaches a finite width and becomes deep according to

$$\frac{h}{\theta} \sim \frac{J_0\left(r\right) - J_0\left(R_\mathrm{max}\right)}{J_2\left(R_\mathrm{max}\right)\left(R_\mathrm{max} - R\right)}, \tag{4.34}$$

$$\frac{h_{\mathrm{m}}}{\theta} \sim \frac{1 - J_0\left(R_{\max}\right)}{J_2\left(R_{\max}\right)\left(R_{\max} - R\right)} \to \infty, \tag{4.35}$$

$$\frac{V}{\theta} \sim \frac{\pi R_{\max}^2}{R_{\max} - R} \to \infty. \tag{4.36}$$

In particular, h_{m} is unbounded and V is proportional to $1/\left(R_{\max} - R\right)$. As discussed in Chapter 1, the stability and existence of a pendant droplet has been studied extensively, and there is a volume at which the droplet becomes unstable and an upper bound on the volume of a pendant droplet, *i.e.* a detachment volume. However, analysing the stability of a pendant droplet is beyond the scope of this Chapter.

In the next three Sections we analyse the evolution of both sessile and pendant droplets evaporating in the extreme modes of evaporation, *i.e.* in the CR and CA modes, in the SS mode, and in the SJ mode, respectively.

4.4 Evaporating in the extreme modes

We consider the evolution of an evaporating droplet using the model described in Section 4.2. Specifically, the evolution, and hence the lifetime, of the evaporating droplet is governed by (4.14). As discussed in Chapter 1, the evolution of an evaporating droplet depends upon the mode in which it is evaporating. We will now describe the evolution of both sessile and pendant droplets under the effect of gravity evaporating in the CR and the CA mode, in turn.

4.4.1 Evolution of a droplet evaporating in the CR mode

For a droplet evaporating in the CR mode, *i.e.* with $R \equiv R_0$, $\theta = \theta(t)$, equation (4.14) becomes

$$\frac{\partial V}{\partial \theta}\frac{\mathrm{d}\theta}{\mathrm{d}t} = -4R_0. \tag{4.37}$$

Solving (4.37) yields the general (implicit) solution for the evolution of the droplet, namely

$$t = \frac{V(R_0, 1) - V(R_0, \theta)}{4R_0}. \tag{4.38}$$

where, here and throughout the rest of this Chapter, we express the volume $V = V(t) = V(R, \theta)$ as a function of the contact radius R and the contact angle θ of the droplet. Substituting the expression for V from (4.19) into (4.38) and re-arranging shows that the evolution of a sessile droplet is given explicitly by

$$\begin{aligned} R \equiv R_0, \quad \theta = 1 - \frac{4I_1(R_0)}{\pi R_0 I_2(R_0)} t, \quad h_{\mathrm{m}} = \frac{I_0(R_0) - 1}{I_1(R_0)} \left(1 - \frac{4I_1(R_0)}{\pi R_0 I_2(R_0)} t \right), \\ V = \frac{\pi R_0^2 I_2(R_0)}{I_1(R_0)} \left(1 - \frac{4I_1(R_0)}{\pi R_0 I_2(R_0)} t \right). \end{aligned} \tag{4.39}$$

In particular, this solution shows that the lifetime of a sessile droplet in the CR mode is given by

$$t_{\mathrm{CR}} = \frac{\pi R_0 I_2(R_0)}{4I_1(R_0)}. \tag{4.40}$$

The corresponding evolution of a pendant droplet is given by

$$\begin{aligned} R \equiv R_0, \quad \theta = 1 - \frac{4J_1(R_0)}{\pi R_0 J_2(R_0)} t, \quad h_{\mathrm{m}} = \frac{1 - J_0(R_0)}{J_1(R_0)} \left(1 - \frac{4J_1(R_0)}{\pi R_0 J_2(R_0)} t \right), \\ V = \frac{\pi R_0^2 J_2(R_0)}{J_1(R_0)} \left(1 - \frac{4J_1(R_0)}{\pi R_0 J_2(R_0)} t \right), \end{aligned} \tag{4.41}$$

and the lifetime of a pendant droplet in the CR mode is given by

$$t_{\mathrm{CR}} = \frac{\pi R_0 J_2(R_0)}{4J_1(R_0)}. \tag{4.42}$$

At leading-order in the limit $V_0 \to 0$ both (4.40) and (4.42) recover the expression for the lifetime of a zero-gravity droplet, namely $t_{\mathrm{CR}} = \pi R_0^2/16$ (see, for example, Wilson and Duffy [303]). Figure 4.6 shows t_{CR} plotted as a function of the initial volume V_0 for a sessile, zero-gravity, and pendant droplet. As Figure 4.6 shows, the lifetime of a pendant droplet is always greater than that of a zero-gravity droplet of the same initial volume, which is in turn greater than that of a sessile droplet. This is because the total evaporative flux from a droplet, F, is proportional to the contact radius R_0 from (4.37) and, as discussed in Subsection 4.3.2, the contact radius of a pendant droplet is always smaller than that of a sessile droplet of the same volume. Figure 4.7 shows the evolutions of R, θ, h_{m}, and V as functions of t for a sessile, zero-gravity, and pendant

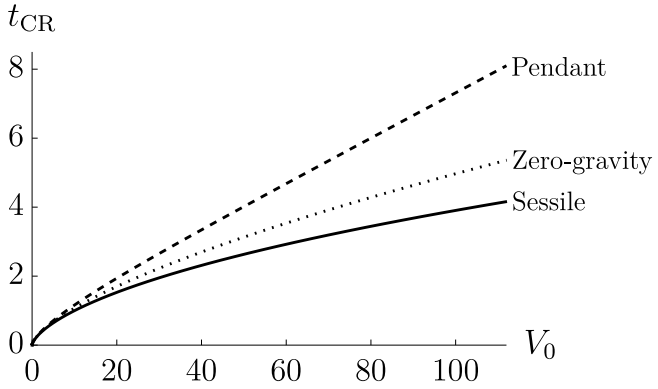

Figure 4.6: Plot of t_{CR} as a function of V_0 for a sessile (solid line), zero-gravity (dotted line) and pendant (dashed line) droplet.

droplet evaporating in the CR mode for an illustrative value of $V_0 = 10$. The contact radius R_0 of the droplet remains constant throughout the evaporation and θ, h_{m}, and V for a sessile and a pendant droplet, given by (4.39) and (4.41) respectively, are linear functions of t, as shown in Figures 4.7(b–d). In particular, Figure 4.7 confirms that for a zero-gravity droplet, the value of R_0 and the evolutions of θ, h_{m}, and V lie between those for a sessile and a pendant droplet of the same volume.

In the limit of an initially narrow droplet ($R_0 \to 0$), corresponding to a droplet with small initial volume ($V_0 \to 0$), the evolutions of θ, h_{m}, and V and the lifetime of a sessile and a pendant droplet, from (4.39) and (4.40) and from (4.41) and (4.42) respectively, are given by

$$\theta = 1 - \frac{16}{\pi R_0^2}\left(1 \pm \frac{R_0^2}{24}\right) t + O\left(R_0^4\right), \tag{4.43}$$

$$h_{\mathrm{m}} = \frac{R_0}{2}\left[1 \mp \frac{R_0^2}{16} - \frac{16}{\pi R_0^2}\left(1 \mp \frac{R_0^2}{48}\right) t\right] + O\left(R_0^5\right), \tag{4.44}$$

$$V = \frac{\pi R_0^3}{4}\left(1 \mp \frac{R_0^2}{24} - \frac{16}{\pi R_0^2} t\right) + O\left(R_0^7\right), \tag{4.45}$$

$$t_{\mathrm{CR}} = \frac{\pi R_0^2}{16}\left(1 - \frac{R_0^2}{24}\right) + O\left(R_0\right)^6, \tag{4.46}$$

where we note again that the upper and lower signs correspond to a sessile and a pendant droplet, respectively. In particular, at leading order in the limit $R_0 \to 0$,

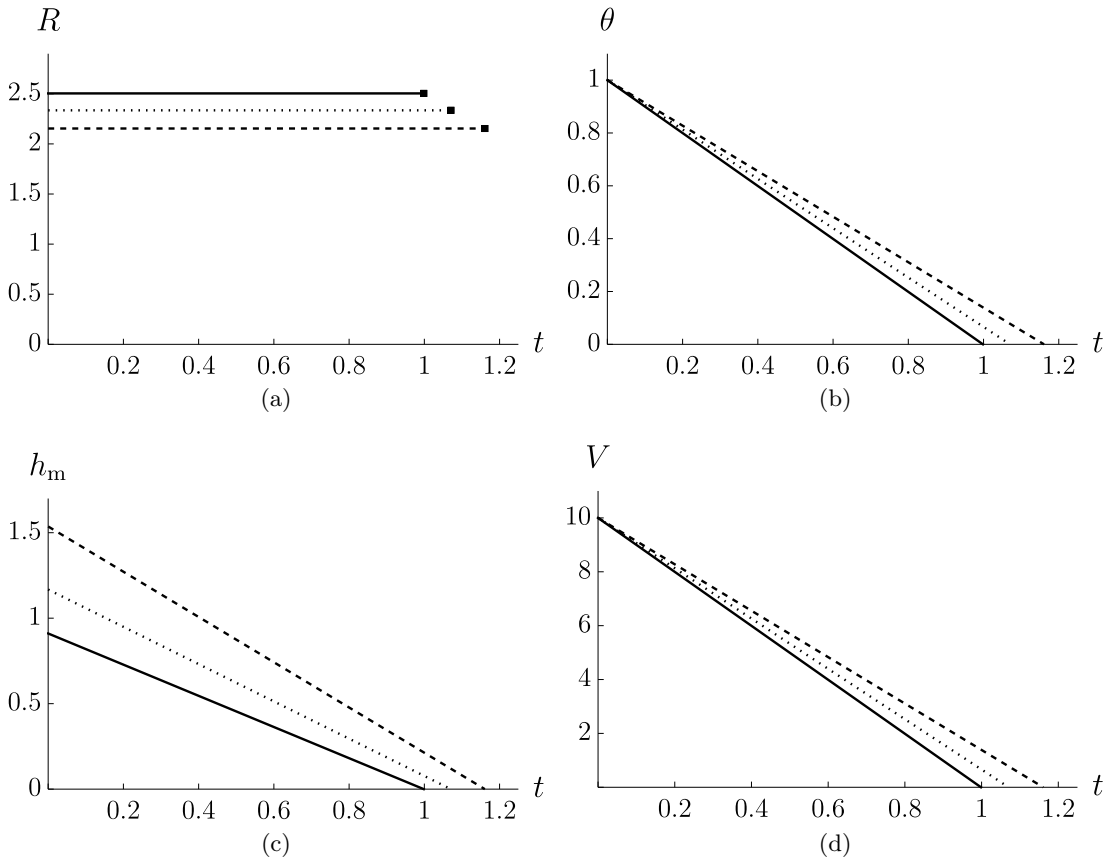

Figure 4.7: Evolutions of (a) R, (b) θ, (c) h_{m}, and (d) V as functions of t for a sessile (solid line), zero-gravity (dotted line), and pendant (dashed line) droplet evaporating in the CR mode for $V_0 = 10$. The squares in (a) correspond to t_{CR}.

(4.43)–(4.46) recover the familiar solutions for the zero-gravity droplet (see, for example, Wilson and Duffy [303]).

In the limit of an initially wide sessile droplet ($R_0 \to \infty$), corresponding to a sessile droplet with large initial volume ($V_0 \to \infty$), the leading-order evolutions (4.39) and the lifetime (4.40) are given by

$$\theta \sim 1 - \frac{4}{\pi R_0} t, \quad h_{\mathrm{m}} \sim 1 - \frac{4}{\pi R_0} t, \quad V \sim \pi R_0^2 \left(1 - \frac{4}{\pi R_0} t\right), \tag{4.47}$$

$$t_{\mathrm{CR}} \sim \frac{\pi R_0}{4}. \tag{4.48}$$

In the limit of a pendant droplet with an initial contact radius close to the maximum value ($R_0 \to R_{\max}$), corresponding to a pendant droplet with large initial volume ($V_0 \to \infty$), the leading-order evolutions (4.41) and the lifetime (4.42) are given by

$$\theta \sim 1 - \frac{4\left(R_{\max} - R_0\right)}{\pi R_{\max}} t, \tag{4.49}$$

$$h_{\mathrm{m}} \sim \frac{1 - J_0(R_{\max})}{J_2(R_{\max})\left(R_{\max} - R_0\right)} \left(1 - \frac{4\left(R_{\max} - R_0\right)}{\pi R_{\max}} t\right), \tag{4.50}$$

$$V \sim \frac{\pi R_{\max}^2}{R_{\max} - R_0} \left(1 - \frac{4\left(R_{\max} - R_0\right)}{\pi R_{\max}} t\right), \tag{4.51}$$

$$t_{\mathrm{CR}} \sim \frac{\pi R_{\max}}{4\left(R_{\max} - R_0\right)}. \tag{4.52}$$

4.4.2 Evolution of a droplet evaporating in the CA mode

For a droplet evaporating in the CA mode, *i.e.* with $R = R(t)$, $\theta \equiv 1$, equation (4.14) becomes

$$\frac{\partial V}{\partial R} \frac{\mathrm{d}R}{\mathrm{d}t} = -4R. \tag{4.53}$$

Solving (4.53) and using integration by parts yields the general (implicit) solution for the evolution of the droplet, namely

$$t = \frac{V(R_0, 1)}{4R_0} - \frac{V(R, 1)}{4R} + \int_R^{R_0} \frac{V(\tilde{R}, 1)}{4\tilde{R}^2} \, \mathrm{d}\tilde{R}. \tag{4.54}$$

Substituting the expression for V from (4.19) into (4.54) gives an implicit expression for the evolution of the contact radius $R = R(t)$ of a sessile droplet:

$$t = \frac{\pi}{4}\left(\frac{R_0 I_2(R_0)}{I_1(R_0)} - \frac{R I_2(R)}{I_1(R)} + \log\left[\frac{R I_1(R_0)}{R_0 I_1(R)}\right]\right), \tag{4.55}$$

with the evolution of h_m and V given by (4.18) and (4.19), respectively. The lifetime of a sessile droplet in the CA mode is then found by taking the limit of (4.55) as $R \to 0$ which gives

$$t_\mathrm{CA} = \frac{\pi}{4}\left(\frac{R_0 I_2(R_0)}{I_1(R_0)} + \log\left[\frac{2I_1(R_0)}{R_0}\right]\right). \tag{4.56}$$

Similarly, for a pendant droplet, substituting the expression for V from (4.29) into (4.53) gives an implicit expression for the evolution of the contact radius R and the lifetime of the droplet:

$$t = \frac{\pi}{4}\left(\frac{R_0 J_2(R_0)}{J_1(R_0)} - \frac{R J_2(R)}{J_1(R)} + \log\left[\frac{R_0 J_1(R)}{R J_1(R_0)}\right]\right), \tag{4.57}$$

$$t_\mathrm{CA} = \frac{\pi}{4}\left(\frac{R_0 J_2(R_0)}{J_1(R_0)} + \log\left[\frac{R_0}{2J_1(R_0)}\right]\right), \tag{4.58}$$

with the evolution of h_m and V given by (4.28) and (4.29), respectively. At leading-order in the limit $V_0 \to 0$ both (4.56) and (4.58) recover the expression for the lifetime of a zero-gravity droplet, namely $t_\mathrm{CA} = 3\pi R_0^2/32$ (see, for example, Wilson and Duffy [303]).

Figure 4.8 shows t_CA plotted as a function of the initial volume V_0 for a sessile, zero-gravity, and pendant droplet. In particular, Figure 4.8 confirms that the lifetime t_CA of a pendant droplet is always greater than that of a zero-gravity droplet of the same initial volume, which is in turn greater than that of a sessile droplet, as in the CR case discussed in the previous Subsection for droplets evaporating in the CR mode. In addition, we note that the lifetime of a sessile, zero-gravity, and pendant droplet in the CA mode is always greater than the corresponding lifetime in the CR mode, *i.e.* $t_\mathrm{CA} > t_\mathrm{CR}$ for each case. This is because the total evaporative flux from the droplet, F, remains constant at $4R_0$ for a droplet evaporating in the CR mode from (4.37), whereas, in the CA mode, it is a decreasing function of time $4R(t)$ from (4.53), and therefore a droplet evaporating in the CA mode will always take longer to evaporate in

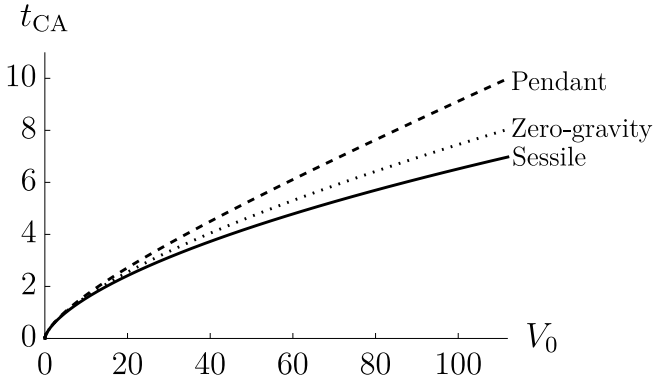

Figure 4.8: Plot of t_{CA} as a function of V_0 for a sessile (solid line), zero-gravity (dotted line), and pendant (dashed line) droplet.

this context. Figure 4.9 shows the evolutions of R, θ, h_{m}, and V as functions of t for a sessile, zero-gravity, and pendant droplet evaporating in the CA mode for an illustrative value of $V_0 = 10$. The contact angle of the droplet remains constant and equal to unity throughout the evaporation and R and V for a sessile and a pendant droplet, given by (4.55) and (4.19) and by (4.57) and (4.29) respectively, are monotonically decreasing functions of t, as shown in Figures 4.9(a), (b) and (d). We note that h_{m} is always a monotonically decreasing function of t for a pendant droplet given by (4.28); however, as discussed in Section 4.3, for a sessile droplet h_{m}/θ, given by (4.18), is non-monotonic in V/θ with a maximum value when $R \simeq 5.586$. Therefore, for a sessile droplet evaporating in the CA mode with initial contact radius $R_0 > 5.586$, corresponding to $V_0 > 73.175$, h_{m} is non-monotonic in t. Figure 4.10 shows the evolution of h_{m} as a function of t for a sessile droplet evaporating in the CA mode for a range of values of V_0 significantly greater than 73.175 showing the non-monotonic behaviour.

In the limit of an initially narrow droplet ($R_0 \to 0$), corresponding to a droplet with small initial volume ($V_0 \to 0$), the implicit evolutions of the contact radius R for a sessile and a pendant droplet, from (4.55) and (4.57) respectively, are given by

$$t = \frac{3\pi R_0^2}{32}\left[1 - \frac{R^2}{R_0^2} \mp \frac{5R_0^2}{144}\left(1 - \frac{R^4}{R_0^4}\right)\right] + O\left(R_0^6\right). \tag{4.59}$$

In particular, at leading order in the limit $R_0 \to 0$, (4.59) recovers the familiar solution for the zero-gravity droplet (see, for example, Wilson and Duffy [303]).

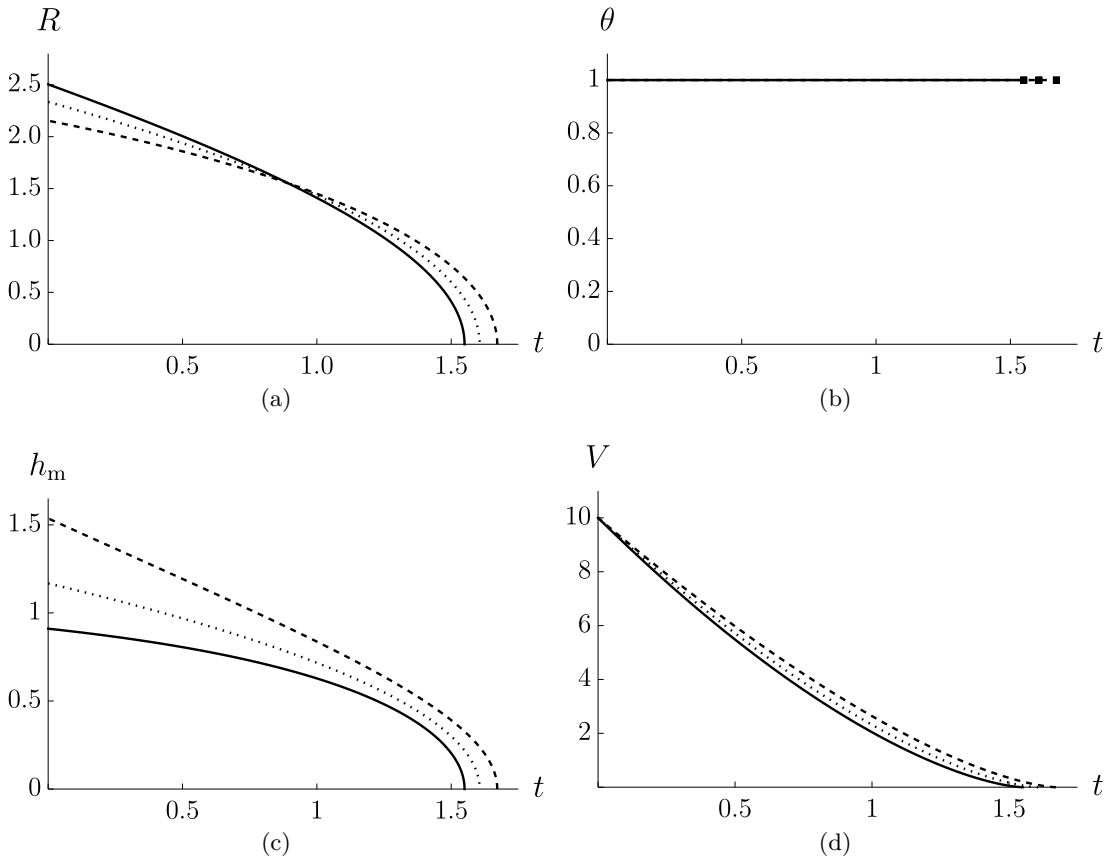

Figure 4.9: Evolutions of (a) R, (b) θ, (c) h_{m}, and (d) V as functions of t for a sessile (solid line), zero-gravity (dotted line), and pendant (dashed line) droplet evaporating in the CA mode for $V_0 = 10$. The squares in (b) correspond to t_{CA} for a sessile (left), zero-gravity (middle), and pendant (right) droplet.

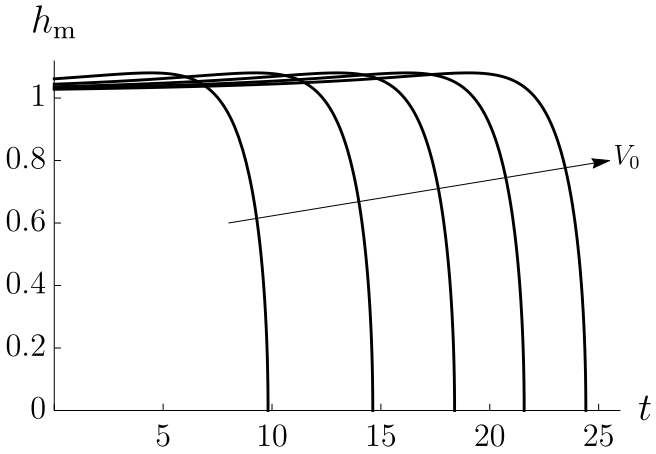

Figure 4.10: Evolution of h_{m} as a function of t for a sessile droplet evaporating in the CA mode when $V_0 = 200,\ 400,\ \ldots,\ 1000$. The arrow indicates the direction of increasing V_0.

In the limit of an initially wide sessile droplet ($R_0 \to \infty$), corresponding to a sessile droplet with large initial volume ($V_0 \to \infty$), the implicit evolution of R from (4.55) and the lifetime t_{CA} from (4.56) are given by

$$t \sim \frac{\pi}{4}\left(2R_0 - \frac{RI_2(R)}{I_1(R)} + \log\left[\frac{R}{(2\pi R_0^3)^{1/2} I_1(R)}\right]\right), \tag{4.60}$$

$$t_{\mathrm{CA}} \sim \frac{\pi}{4}\left(2R_0 + \frac{1}{2}\log\left[\frac{2}{\pi R_0^3}\right]\right). \tag{4.61}$$

We note that the contact radius R is close to its initial value R_0, and is therefore large, at the beginning of evaporation but will eventually become small as the droplet evaporates. The implicit evolution of R given by (4.60) therefore includes the behaviour of R throughout the evaporation. Moreover, away from $t = t_{\mathrm{CA}}$, *i.e.* for $R = O(R_0)$, the contact radius R is simply linear in t for a sessile droplet, and $t_{\mathrm{CA}} \sim \pi R_0/2 \sim 2t_{\mathrm{CR}}$ at leading order in this limit.

In the limit of a pendant droplet with initial contact radius close to the maximum value ($R_0 \to R_{\max}$), corresponding to a pendant droplet with large initial volume ($V_0 \to \infty$), the implicit evolution of R from (4.57) and the lifetime t_{CA} from (4.58) are

given by

$$t \sim \frac{\pi}{4}\left(\frac{R_0}{R_{\max}-R_0} - \frac{RJ_2(R)}{J_1(R)} + \log\left[\frac{R_{\max}J_1(R)}{R\left(R_{\max}-R_0\right)J_2(R_{\max})}\right]\right), \tag{4.62}$$

$$t_{\mathrm{CA}} \sim \frac{\pi}{4}\left(\frac{R_0}{R_{\max}-R_0} + \log\left[\frac{R_{\max}}{2\left(R_{\max}-R_0\right)J_2(R_{\max})}\right]\right). \tag{4.63}$$

We note that, as for the case of a sessile droplet, (4.62) includes the behaviour of R throughout the evaporation and that away from $t = t_{\mathrm{CA}}$, *i.e.* for $R = O(R_0)$, the contact radius R simply remains constant at its initial value R_0 for a pendant droplet, and $t_{\mathrm{CA}} \sim \pi R_0/(4(R_{\max}-R_0)) \sim t_{\mathrm{CR}}$ at leading-order in this limit. We also note that the lifetime of a pendant droplet evaporating in the CA mode in the limit of large initial volume is the same as that for the droplet evaporating in the CR mode at leading-order. Thus, it is necessary to include higher-order terms to distinguish between the lifetimes of a pendant droplet in the CA and the CR modes in the limit of large initial volume. As we shall see in subsequent Sections, this is also true for a pendant droplet evaporating in the mixed modes.

4.5 Evolution of a droplet evaporating in the SS mode

In the SS mode, the evolution of a droplet consists of a CR phase until a time $t = t^*$ at which the critical receding contact angle $\theta = \theta^*$ $(0 \leq \theta^* \leq 1)$ is reached, followed by a CA phase.

Solving (4.14) yields (4.38) for $0 \leq t \leq t^*$, and

$$t = \frac{V(R_0,1)}{4R_0} - \frac{V(R,\theta^*)}{4R} + \int_R^{R_0} \frac{V(\tilde{R},\theta^*)}{4\tilde{R}^2}\,\mathrm{d}\tilde{R}, \tag{4.64}$$

for $t^* < t \leq t_{\mathrm{SS}}$. The evolution of a sessile droplet for $0 \leq t \leq t^*$ is thus given by (4.39), where

$$t^* = \frac{\pi R_0 I_2(R_0)}{4I_1(R_0)}\left(1-\theta^*\right). \tag{4.65}$$

Substituting the expression for V from (4.19) into (4.64) gives an implicit expression for the evolution of the contact radius $R = R(t)$ of a sessile droplet for $t^* < t \leq t_{\mathrm{SS}}$,

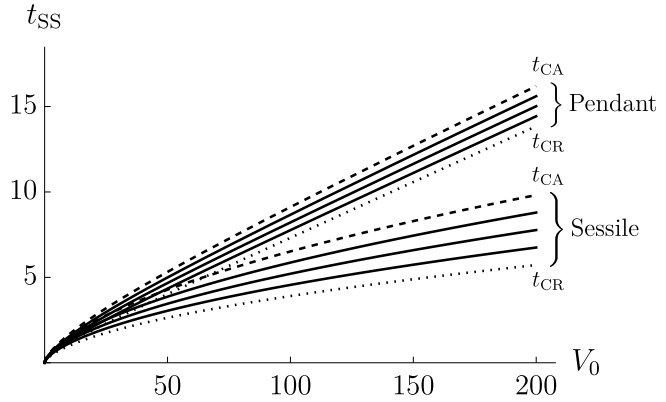

Figure 4.11: Plot of $t_{\rm SS}$ as a function of V_0 comparing a sessile and a pendant droplet when $\theta^* = 1/4, 1/2, 3/4$ (solid lines). The dotted and dashed lines correspond to $\theta^* = 0$ (CR mode) and $\theta^* = 1$ (CA mode), respectively.

namely

$$t = \frac{\pi}{4}\left(\frac{R_0 I_2(R_0)}{I_1(R_0)} + \theta^*\left\{\log\left[\frac{RI_1(R_0)}{R_0 I_1(R)}\right] - \frac{RI_2(R)}{I_1(R)}\right\}\right). \tag{4.66}$$

The lifetime of a sessile droplet in the SS mode is then found by taking the limit of (4.66) as $R \to 0$ to obtain

$$t_{\rm SS} = \frac{\pi}{4}\left(\frac{R_0 I_2(R_0)}{I_1(R_0)} + \theta^* \log\left[\frac{2I_1(R_0)}{R_0}\right]\right), \tag{4.67}$$

which satisfies $t_{\rm CR} \le t_{\rm SS} \le t_{\rm CA}$ for $0 \le \theta^* \le 1$. Figure 4.11 includes (as the lower set of curves) a plot of the lifetime $t_{\rm SS}$ as a function of V_0 for a sessile droplet for a range of values of θ^*. As Figure 4.11 shows, the lifetime of a sessile droplet in the SS mode is smallest when $\theta^* = 0$, *i.e.* in the CR mode, and is greatest when $\theta^* = 1$, *i.e.* in the CA mode. Figure 4.12 shows a plot of the free-surface profile h as a function of r at various times for an illustrative value of $V_0 = 10$, and the evolutions of R, θ, $h_{\rm m}$, and V as functions of t for a range of values of V_0 for a sessile droplet evaporating in the SS mode when $\theta^* = 1/2$. For $0 \le t \le t^*$, the contact radius is constant $R \equiv R_0$ and θ, $h_{\rm m}$, and V decrease linearly in t, and for $t^* < t \le t_{\rm SS}$ the contact angle is constant $\theta = \theta^* = 1/2$, R and V decrease monotonically in t, and $h_{\rm m}$ decreases monotonically in t for $0 < R_0 < 5.586$ (corresponding to $0 < V_0 < 73.175$) and is non-monotonic in t for $R_0 > 5.586$, as shown in Figure 4.12.

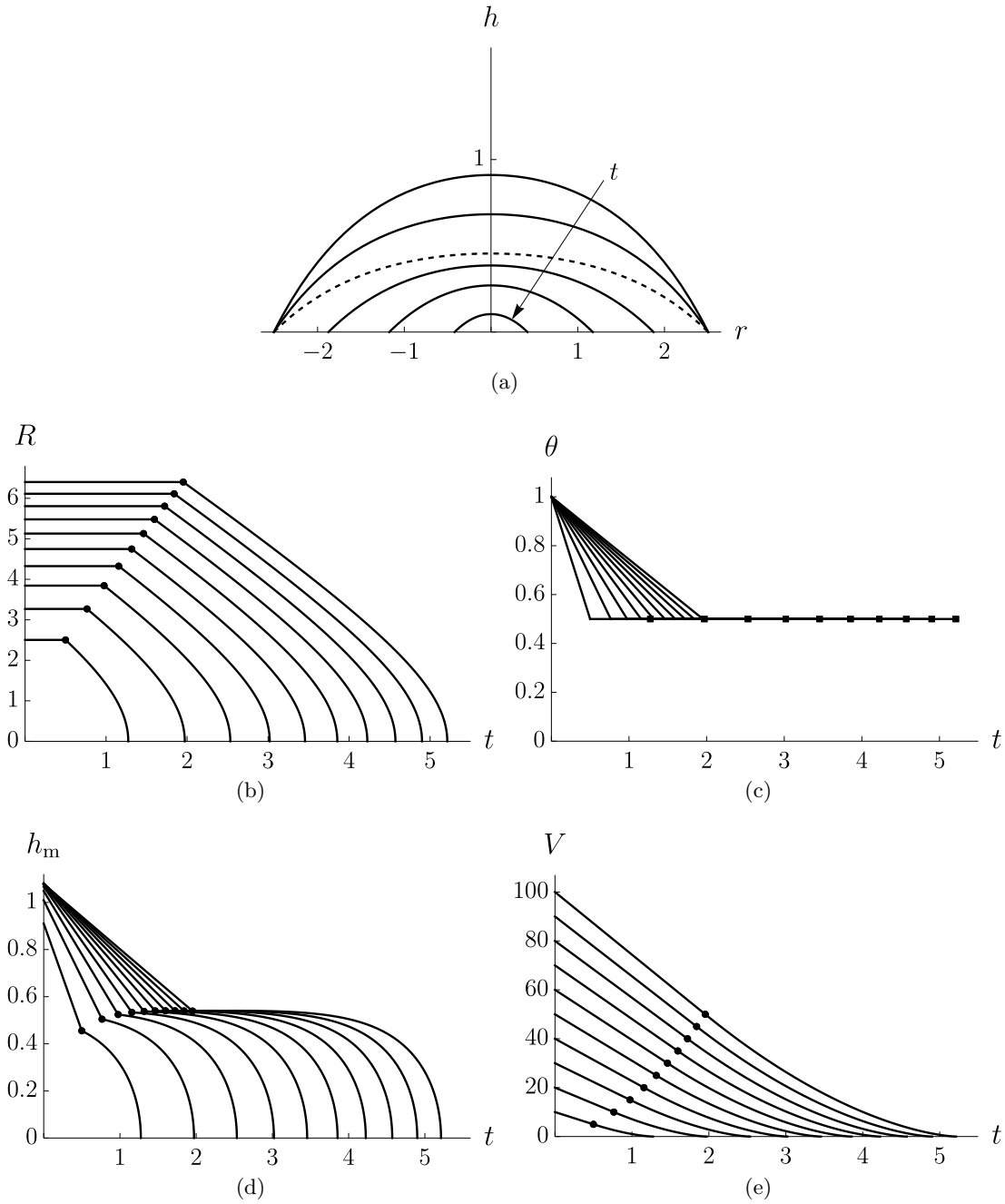

Figure 4.12: Plot of (a) the free-surface profile h as a function of r at times $t = 0$, $t^*/2$, t^*, $2(t_{\rm SS} - t^*)/5$, $3(t_{\rm SS} - t^*)/4$, $29(t_{\rm SS} - t^*)/30$ for $V_0 = 10$, and the evolutions of (b) R, (c) θ, (d) $h_{\rm m}$, and (e) V as functions of t for $V_0 = 10$, 20, ..., 100 for a sessile droplet evaporating in the SS mode when $\theta^* = 1/2$. The dashed line in (a) corresponds to h at $t = t^*$, and the symbols in (b)–(e) correspond to $t = t^*$ (circles) and $t = t_{\rm SS}$ (squares). The arrow in (a) indicates the direction of increasing t.

Similarly, for a pendant droplet the evolution for $0 \leq t \leq t^*$ is given by (4.41), where

$$t^* = \frac{\pi R_0 J_2(R_0)}{4 J_1(R_0)} (1 - \theta^*) . \tag{4.68}$$

Substituting the expression for V from (4.29) into (4.64) gives an implicit expression for the evolution of R of a pendant droplet for $t^* < t \leq t_{\mathrm{SS}}$, namely

$$t = \frac{\pi}{4} \left(\frac{R_0 J_2(R_0)}{J_1(R_0)} + \theta^* \left\{ \log \left[\frac{R_0 J_1(R)}{R J_1(R_0)} \right] - \frac{R J_2(R)}{J_1(R)} \right\} \right), \tag{4.69}$$

and the lifetime of a pendant droplet is given by

$$t_{\mathrm{SS}} = \frac{\pi}{4} \left(\frac{R_0 J_2(R_0)}{J_1(R_0)} + \theta^* \log \left[\frac{R_0}{2 J_1(R_0)} \right] \right), \tag{4.70}$$

which, as for a sessile droplet, satisfies $t_{\mathrm{CR}} \leq t_{\mathrm{SS}} \leq t_{\mathrm{CA}}$ for $0 \leq \theta^* \leq 1$. At leading-order in the limit $V_0 \to 0$ both (4.67) and (4.70) recover the expression for the lifetime of a zero-gravity droplet, namely $t_{\mathrm{SS}} = \pi R_0^2 (2 + \theta^*)/32$ (see, for example, Wilson and Duffy [303]). We also note that the time of contact-line de-pinning t^* and the lifetime t_{SS} of a pendant droplet in the SS mode are always greater than those of a zero-gravity droplet of the same initial volume V_0 and critical receding contact angle θ^*, which are in turn greater than those of a sessile droplet, for the reasons discussed in Section 4.4. However, unlike in Section 4.4, the evolutions and the lifetime for the zero-gravity droplet are not plotted in this Section for clarity in the Figures.

Figure 4.11 includes (as the upper set of curves) a plot of the lifetime t_{SS} as a function of V_0 for a pendant droplet for a range of values of θ^*. As for a sessile droplet, the lifetime of a pendant droplet in the SS mode is smallest when $\theta^* = 0$, *i.e.* in the CR mode, and is greatest when $\theta^* = 1$, *i.e.* in the CA mode, as shown in Figure 4.11. We also note that as V_0 increases, the change in the lifetime t_{SS} for each value of θ^* is greater for a sessile droplet than it is for a pendant droplet, as may be seen by comparing the lower and upper sets of curves in Figure 4.11. Therefore, the lifetime of a sessile droplet is more sensitive than a pendant droplet of the same volume to the mode in which it is evaporating. Figure 4.13 shows a plot of the free-surface profile h as

a function of r at various times for an illustrative value of $V_0 = 10$, and the evolutions of R, θ, h_{m}, and V as functions of t for a range of values of V_0 for a pendant droplet evaporating in the SS mode when $\theta^* = 1/2$. For $0 \leq t \leq t^*$, the contact radius is constant $R \equiv R_0$ and θ, h_{m}, and V decrease linearly in t, and for $t^* < t \leq t_{\mathrm{SS}}$ the contact angle is constant $\theta = \theta^* \equiv 1/2$, and R, h_{m}, and V decrease monotonically in t, as shown in Figure 4.12.

In the limit of an initially narrow droplet ($R_0 \to 0$), corresponding to a droplet with small initial volume ($V_0 \to 0$), the evolutions of θ, h_{m}, and V for a sessile and a pendant droplet evaporating in the SS mode for $0 \leq t \leq t^*$ are given by (4.43)–(4.45) with

$$t^* = \frac{\pi R_0^2}{16}\left(1-\theta^*\right)\left(1 \mp \frac{R_0^2}{24}\right) + O\left(R_0^6\right). \tag{4.71}$$

For $t^* < t \leq t_{\mathrm{SS}}$, the implicit evolutions of R for a sessile and a pendant droplet, from (4.66) and (4.69) respectively, are given by

$$t = \frac{\pi R_0^2}{32}\left[2 + \theta^* - \frac{3\theta^* R^2}{R_0^2} \mp \frac{R_0^2}{48}\left(4 + \theta^* - \frac{5\theta^* R^4}{R_0^4}\right)\right] + O\left(R_0^6\right). \tag{4.72}$$

In particular, at leading order in the limit $R_0 \to 0$, (4.72) recovers the familiar solution for the zero-gravity droplet (see, for example, Wilson and Duffy [303]).

In the limit of an initially wide sessile droplet ($R_0 \to \infty$) and a pendant droplet with initial contact radius close to the maximum value ($R_0 \to R_{\max}$), corresponding to a droplet with large initial volume ($V_0 \to \infty$), the leading-order evolutions of θ, h_{m}, and V for $0 \leq t \leq t^*$ are given by (4.47) and by (4.49)–(4.51), respectively. For $t^* < t \leq t_{\mathrm{SS}}$, the implicit evolution of R from (4.66) and the lifetime t_{SS} from (4.67) for a sessile droplet are given by

$$t \sim \frac{\pi}{4}\left(R_0\left(1+\theta^*\right) + \theta^*\left\{\log\left[\frac{R}{(2\pi R_0^3)^{1/2} I_1(R)}\right] - \frac{R I_2(R)}{I_1(R)}\right\}\right), \tag{4.73}$$

$$t_{\mathrm{SS}} \sim \frac{\pi}{4}\left(R_0\left(1+\theta^*\right) + \frac{\theta^*}{2}\log\left[\frac{2}{\pi R_0^3}\right]\right). \tag{4.74}$$

We note that, as in Subsection 4.4.2, (4.73) includes the behaviour of R throughout the evaporation and that away from $t = t_{\mathrm{SS}}$, *i.e.* for $R = O(R_0)$, the contact radius

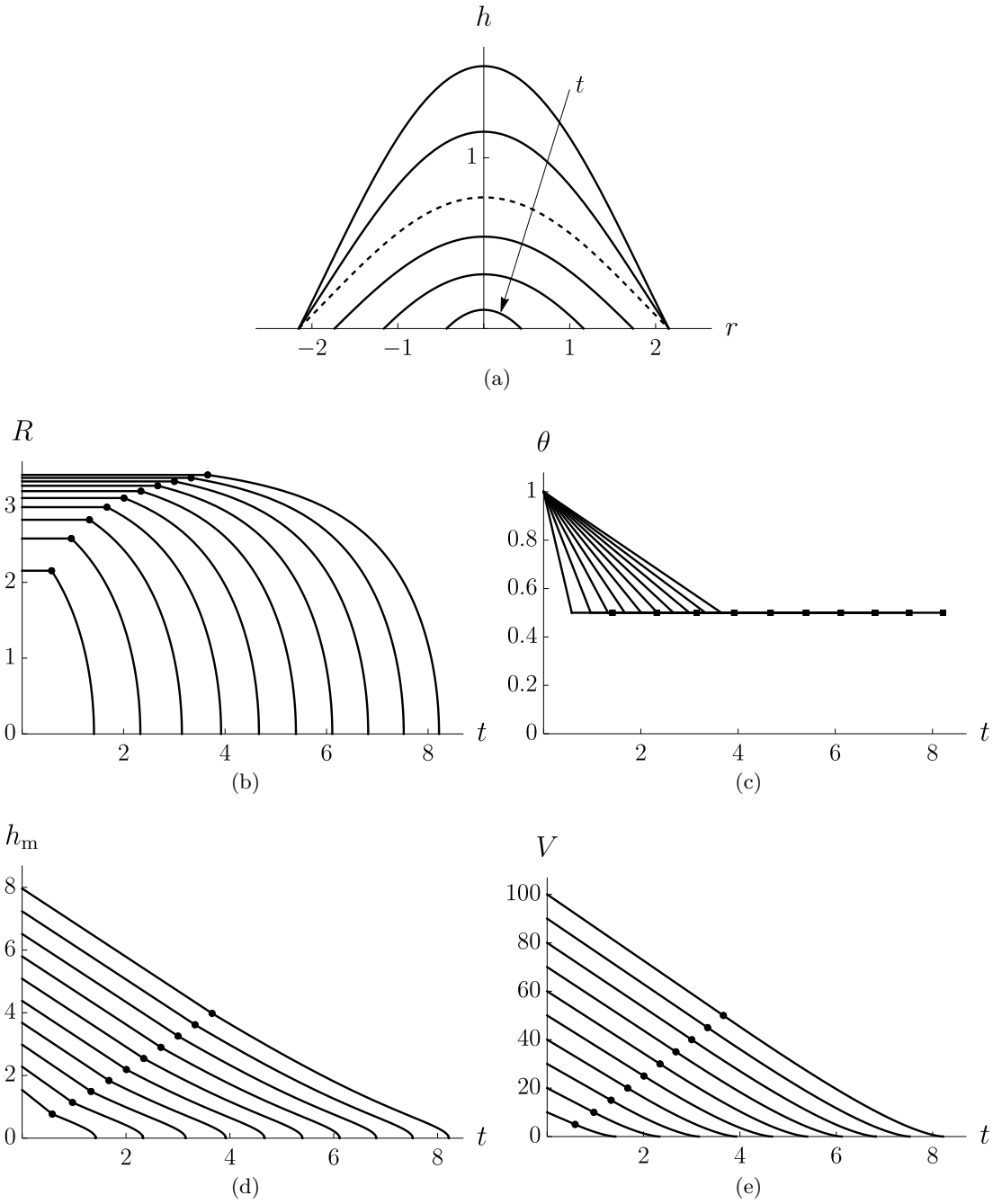

Figure 4.13: Plot of (a) the free-surface profile h as a function of r at times $t = 0$, $t^*/2$, t^*, $2(t_{SS} - t^*)/5$, $3(t_{SS} - t^*)/4$, $29(t_{SS} - t^*)/30$ for $V_0 = 10$, and the evolutions of (b) R, (c) θ, (d) h_m, and (e) V as functions of t for $V_0 = 10, 20, \ldots, 100$ for a pendant droplet evaporating in the SS mode when $\theta^* = 1/2$. The dashed line in (a) corresponds to h at $t = t^*$, and the symbols in (b)–(e) correspond to $t = t^*$ (circles) and $t = t_{SS}$ (squares). The arrow in (a) indicates the direction of increasing t.

is simply linear in t for $t^* < t \leq t_{\rm SS}$, and $t_{\rm SS} \sim \pi R_0(1+\theta^*)/4 \sim (1+\theta^*)t_{\rm CR}$ at leading-order in this limit.

For $t^* < t \leq t_{\rm SS}$, the implicit evolution of R from (4.69) and the lifetime $t_{\rm SS}$ from (4.70) of a pendant droplet are given by

$$t \sim \frac{\pi}{4}\left(\frac{R_0}{R_{\rm max}-R_0} + \theta^*\left\{\log\left[\frac{R_{\rm max}J_1(R)}{R\left(R_{\rm max}-R_0\right)J_2(R_{\rm max})}\right] - \frac{RJ_2(R)}{J_1(R)}\right\}\right), \tag{4.75}$$

$$t_{\rm SS} \sim \frac{\pi}{4}\left(\frac{R_0}{R_{\rm max}-R_0} + \theta^*\log\left[\frac{R_{\rm max}}{2\left(R_{\rm max}-R_0\right)J_2(R_{\rm max})}\right]\right). \tag{4.76}$$

As for the case of a sessile droplet, (4.75) includes the behaviour of R throughout the evaporation and away from $t_{\rm SS}$, *i.e.* for $R = O(R_0)$, the contact radius simply remains constant at its initial value for $t^* < t \leq t_{\rm SS}$, and $t_{\rm SS} \sim t_{\rm CA} \sim t_{\rm CR}$ at leading-order in this limit. Thus, as discussed in Subsection 4.4.2, it is necessary to include higher-order terms to distinguish between the lifetimes of a pendant droplet in the different modes of evaporation in the limit of large initial volume.

We note that setting either $\theta^* = 0$ or $\theta^* = 1$ in (4.74) or (4.76) recovers the lifetime of a sessile and a pendant droplet evaporating in the CR or the CA mode, respectively, as discussed in Section 4.4, in the limit of large initial volume ($V_0 \to \infty$).

4.6 Evolution of a droplet evaporating in the SJ mode

In the SJ mode, the evolution of a droplet consists of an infinite series of CR (stick) phases separated by an infinite series of jump phases in which the contact angle jumps instantaneously from $\theta_{\rm min}$ to $\theta_{\rm max}$, where $0 \leq \theta_{\rm min} \leq \theta_{\rm max} \leq 1$, with a corresponding jump decrease in the contact radius. We denote the constant value of the pinned contact radius during the $n^{\rm th}$ CR phase by R_n, which lasts from $t = t_{n-1}$ to $t = t_n$.

We assume that mass is conserved during the $n^{\rm th}$ jump, *i.e.* $V(R_n, \theta_{\rm min}) = V(R_{n+1}, \theta_{\rm max})$ at $t = t_n$. Therefore, from (4.19), the contact radius $R = R_n$ of a sessile droplet satisfies

$$R_{n+1}^2\frac{I_2(R_{n+1})}{I_1(R_{n+1})} = \left(\frac{\theta_{\rm min}}{\theta_{\rm max}}\right)R_n^2\frac{I_2(R_n)}{I_1(R_n)} = \left(\frac{\theta_{\rm min}}{\theta_{\rm max}}\right)^n R_0^2\frac{I_2(R_0)}{I_1(R_0)}. \tag{4.77}$$

Similarly, from (4.29), the contact radius $R = R_n$ of a pendant droplet satisfies

$$R_{n+1}^2 \frac{J_2(R_{n+1})}{J_1(R_{n+1})} = \left(\frac{\theta_{\min}}{\theta_{\max}}\right) R_n^2 \frac{J_2(R_n)}{J_1(R_n)} = \left(\frac{\theta_{\min}}{\theta_{\max}}\right)^n R_0^2 \frac{J_2(R_0)}{J_1(R_0)}. \tag{4.78}$$

During the first CR phase $R_1 = R_0$ from $t = t_0 = 0$ to $t = t_1$, with θ, h_{m}, and V given by (4.39) and (4.41) for a sessile and a pendant droplet, respectively. The time t_1 at which the droplet first jumps satisfies $\theta(t_1) = \theta_{\min}$ and for a sessile droplet is given by

$$t_1 = \frac{\pi R_0 I_2(R_0)}{4 I_1(R_0)} \left(1 - \theta_{\min}\right), \tag{4.79}$$

and for a pendant droplet by

$$t_1 = \frac{\pi R_0 J_2(R_0)}{4 J_1(R_0)} \left(1 - \theta_{\min}\right). \tag{4.80}$$

During the n^{th} CR phase, lasting from $t = t_{n-1}$ to $t = t_n$, the evolution of a sessile droplet is given by

$$R = R_n, \quad \theta = \theta_{\max} - \frac{4 I_1(R_n)}{\pi R_n I_2(R_n)} \left(t - t_{n-1}\right), \tag{4.81}$$

$$h_{\mathrm{m}} = \frac{I_0(R_n) - 1}{I_1(R_n)} \left(\theta_{\max} - \frac{4 I_1(R_n)}{\pi R_n I_2(R_n)} \left(t - t_{n-1}\right)\right), \tag{4.82}$$

$$V = \frac{\pi R_n^2 I_2(R_n)}{I_1(R_n)} \left(\theta_{\max} - \frac{4 I_1(R_n)}{\pi R_n I_2(R_n)} \left(t - t_{n-1}\right)\right), \tag{4.83}$$

where

$$\begin{aligned} t_n &= t_{n-1} + \left(\theta_{\max} - \theta_{\min}\right) \frac{\pi R_n I_2(R_n)}{4 I_1(R_n)} \\ &= \frac{\pi R_0 I_2(R_0)}{4 I_1(R_0)} \left(1 - \theta_{\min}\right) + \left(\theta_{\max} - \theta_{\min}\right) \sum_{k=2}^{n} \frac{\pi R_k I_2(R_k)}{4 I_1(R_k)}. \end{aligned} \tag{4.84}$$

The lifetime of a sessile droplet in the SJ mode is then found by taking the limit of

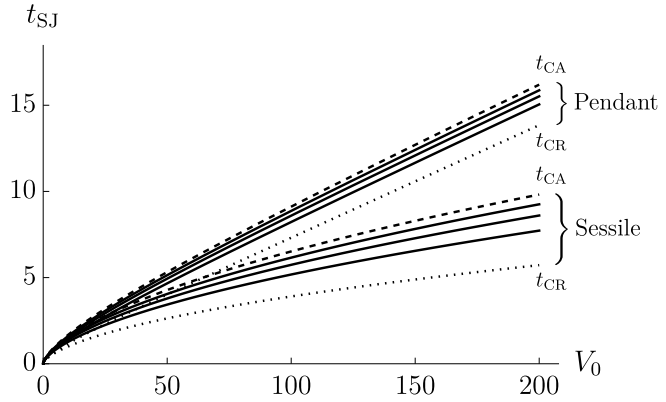

Figure 4.14: Plot of t_{SJ} as a function of V_0 comparing a sessile and a pendant droplet when $\theta_{\max} = 1$ and $\theta_{\min} = 1/4, 1/2, 3/4$ (solid lines). The dotted and dashed lines correspond to $\theta_{\min} = 0$ (CR mode) and $\theta_{\min} = \theta_{\max} = 1$ (CA mode), respectively.

(4.84) as $n \to \infty$, which gives

$$t_{\mathrm{SJ}} = \frac{\pi R_0 I_2(R_0)}{4 I_1(R_0)} (1 - \theta_{\min}) + (\theta_{\max} - \theta_{\min}) \sum_{k=2}^{\infty} \frac{\pi R_k I_2(R_k)}{4 I_1(R_k)}, \tag{4.85}$$

which satisfies $t_{\mathrm{CR}} \leq t_{\mathrm{SJ}} \leq t_{\mathrm{CA}}$ for $0 \leq \theta_{\min} \leq \theta_{\max} \leq 1$. Additionally, we note that $t_{\mathrm{SJ}} \to t_{\mathrm{SS}}$ when $\theta_{\max} \to \theta_{\min} = \theta^*$.

There are no explicit expressions for the sums involving the Bessel functions in equations (4.84) and (4.85) and so the evolution, and hence the lifetime, of a sessile droplet must be calculated numerically for this mode of evaporation. Additionally, to perform the numerical calculations for t_{SJ} from (4.85) we replace the infinite sum with a finite sum to N terms, where N is chosen to be sufficiently large that the answer does not change (to within some tolerance) for larger N. In practice, we imposed a relative tolerance of 10^{-3}, which corresponds to evaluating t_{SJ} from (4.85) with $N = 35$. Figure 4.14 includes (as the lower set of curves) a plot of the lifetime t_{SJ} as a function of V_0 for a sessile droplet for $\theta_{\max} = 1$ and a range of values of $\theta_{\min}$. As Figure 4.14 shows, the lifetime of a sessile droplet in the SJ mode is smallest when $\theta_{\min} = 0$, *i.e.* in the CR mode, and is greatest when $\theta_{\min} = \theta_{\max} = 1$, *i.e.* in the CA mode. Figure 4.15 shows a plot of the free-surface profile h as a function of r and the evolutions of R, θ, h_{m}, and V as functions of t for a sessile droplet evaporating in the SJ mode when $\theta_{\min} = 1/2$, $\theta_{\max} = 1$, and $V_0 = 10$ for $n = 35$ jump phases. For $t_{n-1} < t < t_n$, the contact radius

R_n is constant and θ, h_{m}, and V decrease linearly in t, and at $t = t_n$, R jumps to a lower value, θ and h_{m} jump to higher values, and V is conserved, as shown in Figure 4.15.

Similarly, the evolution of a pendant droplet during the n^{th} CR phase is given by

$$R = R_n, \quad \theta = \theta_{\max} - \frac{4J_1(R_n)}{\pi R_n J_2(R_n)}\,(t - t_{n-1})\,, \tag{4.86}$$

$$h_{\mathrm{m}} = \frac{1 - J_0(R_n)}{J_1(R_n)}\left(\theta_{\max} - \frac{4J_1(R_n)}{\pi R_n J_2(R_n)}\,(t - t_{n-1})\right), \tag{4.87}$$

$$V = \frac{\pi R_n^2 J_2(R_n)}{J_1(R_n)}\left(\theta_{\max} - \frac{4J_1(R_n)}{\pi R_n J_2(R_n)}\,(t - t_{n-1})\right), \tag{4.88}$$

where

$$\begin{aligned} t_n &= t_{n-1} + (\theta_{\max} - \theta_{\min})\,\frac{\pi R_n J_2(R_n)}{4I_J(R_n)} \\ &= \frac{\pi R_0 J_2(R_0)}{4J_1(R_0)}\,(1 - \theta_{\min}) + (\theta_{\max} - \theta_{\min})\sum_{k=2}^{n}\frac{\pi R_k J_2(R_k)}{4J_1(R_k)}. \end{aligned} \tag{4.89}$$

The lifetime of a pendant droplet in the SJ mode is then given by

$$t_{\mathrm{SJ}} = \frac{\pi R_0 J_2(R_0)}{4J_1(R_0)}\,(1 - \theta_{\min}) + (\theta_{\max} - \theta_{\min})\sum_{k=2}^{\infty}\frac{\pi R_k J_2(R_k)}{4J_1(R_k)}, \tag{4.90}$$

which, as for a sessile droplet, satisfies $t_{\mathrm{CR}} \leq t_{\mathrm{SJ}} \leq t_{\mathrm{CA}}$ for $0 \leq \theta_{\min} \leq \theta_{\max} \leq 1$ and $t_{\mathrm{SJ}} \to t_{\mathrm{SS}}$ as $\theta_{\max} \to \theta_{\min} = \theta^*$. At leading-order in the limit $V_0 \to 0^+$, both (4.85) and (4.90) recover the expression for the lifetime of a zero-gravity droplet, namely

$$t_{\mathrm{SJ}} = \frac{\pi R_0^2}{16}\left(1 - \theta_{\max} + (\theta_{\max} - \theta_{\min})\,\frac{\theta_{\max}^{2/3}}{\theta_{\max}^{2/3} - \theta_{\min}^{2/3}}\right), \tag{4.91}$$

(see, for example, Wilson and Duffy [303]). We also note that the time of the n^{th} jump t_n and the lifetime t_{SJ} of a pendant droplet in the SJ mode are always greater than those of a zero-gravity droplet of the same initial volume V_0 and critical angles $\theta_{\min}$ and $\theta_{\max}$, which are in turn greater that those of a sessile droplet, for the same reasons as those discussed in Section 4.4. However, unlike in Section 4.4, the evolutions and

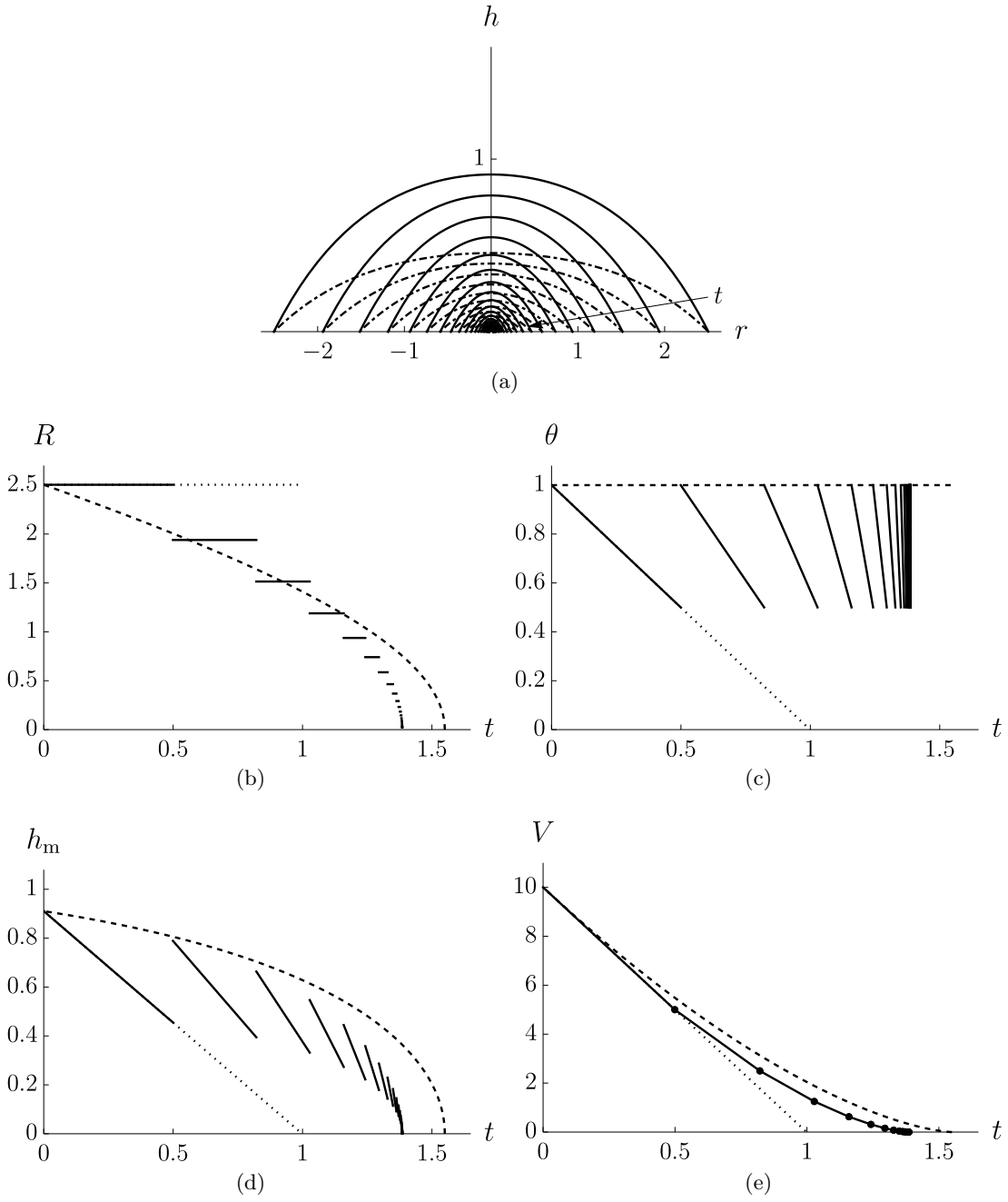

Figure 4.15: Plot of (a) the free-surface profile h as a function of r and the evolutions of (b) R, (c) θ, (d) h_m, and (e) V as functions of t for a sessile droplet evaporating in the SJ mode when $\theta_\mathrm{min} = 1/2$, $\theta_\mathrm{max} = 1$ and $V_0 = 10$ for $n = 35$ jump phases. The solid and dash-dotted lines in (a) correspond to h at $t = t_{n-1}$ when $\theta = \theta_\mathrm{max}$ and at $t = t_n$ when $\theta = \theta_\mathrm{min}$, respectively, the dotted and dashed lines in (b)–(e) correspond to $\theta_\mathrm{min} = 0$ (CR mode) and $\theta_\mathrm{min} = \theta_\mathrm{max} = 1$ (CA mode), respectively, and the dots in (e) correspond to $t = t_n$. The arrow in (a) indicates the direction of increasing t.

the lifetime for the zero-gravity droplet are not plotted in this Section for clarity in the Figures.

As for a sessile droplet, the evolution, and hence the lifetime, of a pendant droplet must be calculated numerically for this mode of evaporation, and we replace the infinite sum in (4.90) for t_{SJ} with a finite sum to $N = 35$ terms. Figure 4.14 includes (as the upper set of curves) a plot of the lifetime t_{SJ} as a function of V_0 for a pendant droplet for $\theta_{\max} = 1$ and a range of values of $\theta_{\min}$. As for a sessile droplet, the lifetime of a pendant droplet in the SJ mode is smallest when $\theta_{\min} = 0$, *i.e.* in the CR mode, and greatest when $\theta_{\min} = \theta_{\max} = 1$, *i.e.* in the CA mode, as shown in Figure 4.14. We also note that, as in Section 4.5, as V_0 increases, the change in the lifetime t_{SJ} for each value of $\theta_{\min}$ is greater for a sessile droplet than it is for a pendant droplet, as may be seen by comparing the lower and upper sets of curves in Figure 4.14. Figure 4.16 shows a plot of the free-surface profile h as a function of r and the evolutions of R, θ, h_{m}, and V as functions of t for a pendant droplet evaporating in the SJ mode when $\theta_{\min} = 1/2$, $\theta_{\max} = 1$ and $V_0 = 10$ for $n = 35$ jump phases. The evolutions of R, θ, h_{m}, and V for a pendant droplet in the SJ mode are qualitatively similar to the evolutions of a sessile droplet in the same mode.

In the limit of an initially narrow droplet ($R_0 \to 0$), corresponding to a droplet with small initial volume ($V_0 \to 0$), the leading-order solution for R_n and the evolutions of θ, h_{m}, and V for a sessile and a pendant droplet during the n^{th} CR phase, from (4.77), (4.81)–(4.83) and (4.78), (4.86)–(4.88) respectively, are given by

$$R_{n+1} \sim \left(\frac{\theta_{\min}}{\theta_{\max}}\right)^{n/3} R_0, \tag{4.92}$$

$$\theta \sim \theta_{\max} - \frac{16}{\pi R_n^2}\left(t - t_{n-1}\right), \tag{4.93}$$

$$h_{\mathrm{m}} \sim \frac{R_n}{2}\left[\theta_{\max} - \frac{16}{\pi R_n^2}\left(t - t_{n-1}\right)\right], \tag{4.94}$$

$$V \sim \frac{\pi R_n^3}{4}\left[\theta_{\max} - \frac{16}{\pi R_n^2}\left(t - t_{n-1}\right)\right], \tag{4.95}$$

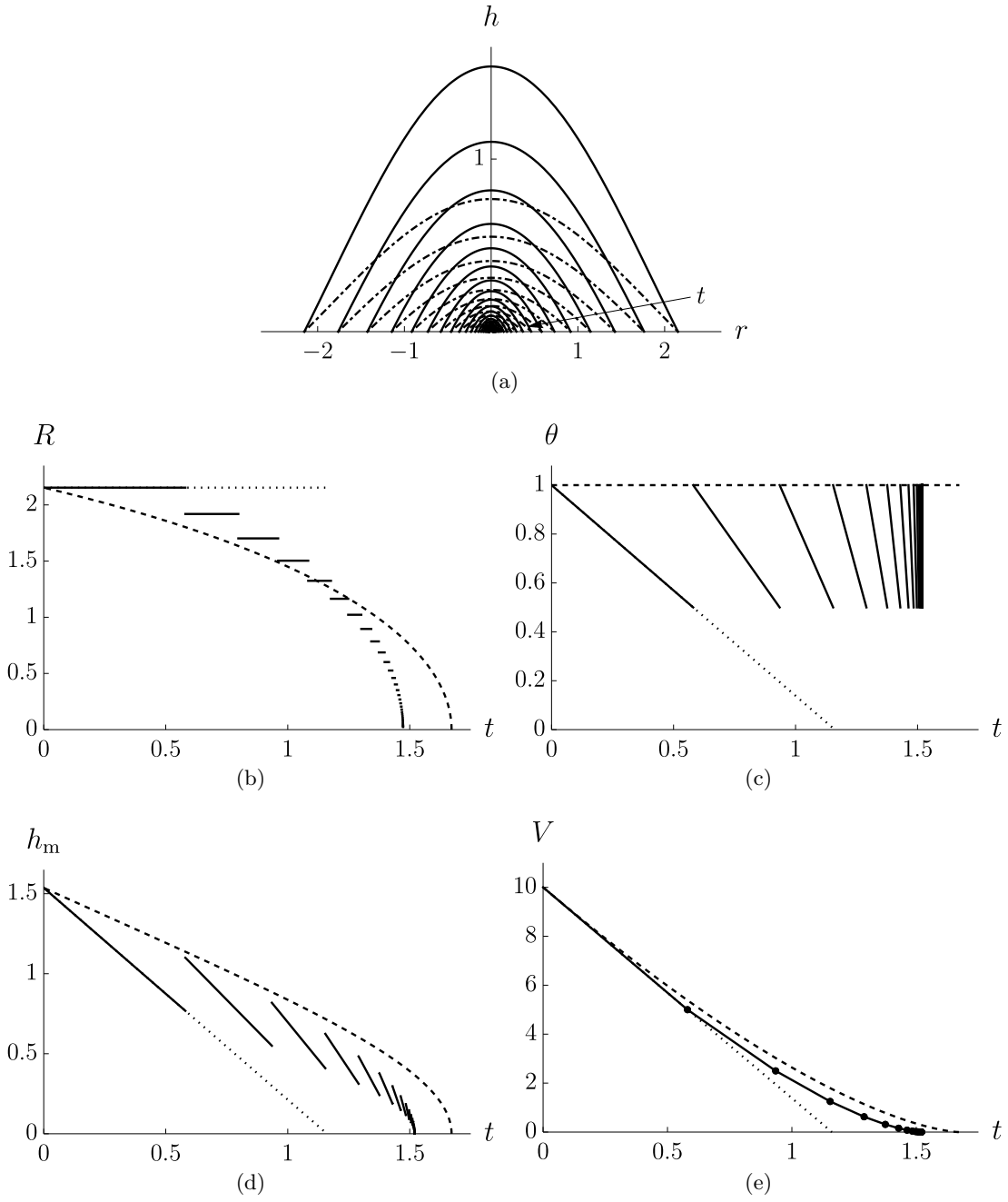

Figure 4.16: Plot of (a) the free-surface profile h as a function of r and the evolutions of (b) R, (c) θ, (d) h_{m}, and (e) V as functions of t for a pendant droplet evaporating in the SJ mode when $\theta_{\min} = 1/2$, $\theta_{\max} = 1$, and $V_0 = 10$ for $n = 35$ jump phases. The solid and dash-dotted lines in (a) correspond to h at $t = t_{n-1}$ when $\theta = \theta_{\max}$ and at $t = t_n$ when $\theta = \theta_{\min}$, respectively, the dotted and dashed lines in (b)–(e) correspond to $\theta_{\min} = 0$ (CR mode) and $\theta_{\min} = \theta_{\max} = 1$ (CA mode), respectively, and the dots in (e) correspond to $t = t_n$. The arrow in (a) indicates the direction of increasing t.

where

$$t_n \sim \frac{\pi R_0^2}{16}\left(1-\theta_{\max}+(\theta_{\max}-\theta_{\min})\frac{\left[1-\left(\frac{\theta_{\min}}{\theta_{\max}}\right)^{2n/3}\right]}{\left[1-\left(\frac{\theta_{\min}}{\theta_{\max}}\right)^{2/3}\right]}\right). \tag{4.96}$$

In particular, (4.92)–(4.96) correspond to the solutions for the zero-gravity droplet (see, for example, Wilson and Duffy [303]).

In the limit of an initially wide sessile droplet ($R_0 \to \infty$), corresponding to a sessile droplet with large initial volume ($V_0 \to \infty$), the leading-order solution for R_n from (4.77) and the evolutions of θ, h_{m}, and V from (4.81)–(4.83) during the n^{th} CR phase are given by

$$R_{n+1} \sim \left(\frac{\theta_{\min}}{\theta_{\max}}\right)^{n/2} R_0, \tag{4.97}$$

$$\theta \sim \theta_{\max} - \frac{4}{\pi R_n}\left(t - t_{n-1}\right), \tag{4.98}$$

$$h_{\mathrm{m}} \sim \theta_{\max} - \frac{4}{\pi R_n}\left(t - t_{n-1}\right), \tag{4.99}$$

$$V \sim \pi R_n^2\left(\theta_{\max} - \frac{4}{\pi R_n}\left(t - t_{n-1}\right)\right), \tag{4.100}$$

where

$$t_n \sim \frac{\pi R_0}{4}\left(1-\theta_{\max}+(\theta_{\max}-\theta_{\min})\frac{\left[1-\left(\frac{\theta_{\min}}{\theta_{\max}}\right)^{n/2}\right]}{\left[1-\left(\frac{\theta_{\min}}{\theta_{\max}}\right)^{1/2}\right]}\right). \tag{4.101}$$

The leading-order solution for the lifetime of a sessile droplet from (4.85) in this limit is then

$$t_{\mathrm{SJ}} \sim \frac{\pi R_0}{4}\left(1-\theta_{\max}+(\theta_{\max}-\theta_{\min})\frac{\theta_{\max}^{1/2}}{\theta_{\max}^{1/2}-\theta_{\min}^{1/2}}\right). \tag{4.102}$$

We note that, unlike for a droplet evaporating in the CA and SS modes discussed previously in which higher-order terms in this limit were considered, only leading-order solutions have been obtained for the SJ mode since the higher-order contributions would be unwieldy because of the dependence on Bessel functions.

In the limit of a pendant droplet with initial contact radius close to the maximum

value ($R_0 \to R_{\max}$), corresponding to a pendant droplet with large initial volume ($V_0 \to \infty$), the leading-order solution for R_n from (4.78) and evolutions of θ, h_{m}, and V from (4.86)–(4.88) during the n^{th} CR phase are given by

$$R_{n+1} \sim R_{\max} - \left(\frac{\theta_{\max}}{\theta_{\min}}\right)^n (R_{\max} - R_0)\,, \tag{4.103}$$

$$\theta \sim \theta_{\max} - \frac{4\,(R_{\max} - R_n)}{\pi R_{\max}}\,(t - t_{n-1})\,, \tag{4.104}$$

$$h_{\mathrm{m}} \sim \frac{1 - J_0(R_{\max})}{J_2(R_{\max})\,(R_{\max} - R_n)}\left(\theta_{\max} - \frac{4\,(R_{\max} - R_n)}{\pi R_{\max}}\,(t - t_{n-1})\right), \tag{4.105}$$

$$V \sim \frac{\pi R_{\max}^2}{R_{\max} - R_n}\left(\theta_{\max} - \frac{4\,(R_{\max} - R_n)}{\pi R_{\max}}\,(t - t_{n-1})\right), \tag{4.106}$$

where

$$t_n \sim \frac{\pi R_{\max}}{4\,(R_{\max} - R_0)}\left(1 - \theta_{\max} + (\theta_{\max} - \theta_{\min})\,\frac{\left[1 - \left(\dfrac{\theta_{\min}}{\theta_{\max}}\right)^n\right]}{\left[1 - \left(\dfrac{\theta_{\min}}{\theta_{\max}}\right)\right]}\right). \tag{4.107}$$

The leading-order solution for the lifetime of a pendant droplet from (4.90) in this limit is then

$$t_{\mathrm{SJ}} \sim \frac{\pi R_{\max}}{4\,(R_{\max} - R_0)}, \tag{4.108}$$

which is independent of $\theta_{\min}$ and $\theta_{\max}$. In particular, from (4.103), $R_{n+1} \to R_{\max}^-$ as $R_0 \to R_{\max}^-$ and so $t_{\mathrm{SJ}} \sim t_{\mathrm{SS}} \sim t_{\mathrm{CA}} \sim t_{\mathrm{CR}}$ at leading-order in this limit.

4.7 Conclusions

In this Chapter we have studied the effect of gravity on the shape, evolution, and lifetime of sessile and pendant droplets undergoing diffusion-limited evaporation. In particular, we formulated and analysed a mathematical model describing the dependence of the evaporation of a thin droplet on droplet volume, droplet orientation, and mode of evaporation.

The mathematical model describes how the shape of a droplet depends on its volume

and whether it is sessile or pendant. In particular, the model predicts that a sessile droplet will become wide and flat as the volume of the droplet increases, *i.e.* $R \to \infty$ and $h_{\mathrm{m}} \to 1^{+}$ as $V \to \infty$, whereas a pendant droplet will approach a finite width and become deep as the volume of the droplet increases, *i.e.* $R \to R_{\max}^{-}$ and $h_{\mathrm{m}} \to \infty$ as $V \to \infty$. In addition, h_{m} is non-monotonic in V for a sessile droplet, whereas h_{m} increases monotonically in V for a pendant droplet. Furthermore, the predicted contact radius R of a sessile droplet is always larger than that for a pendant droplet of the same volume and, as a consequence of this, so is the total evaporative flux from the droplet, F, namely $4R$ from (4.14).

The evolution and lifetime of evaporating sessile and pendant droplets were analysed for four different modes of evaporation, namely the CR, CA, SS, and SJ modes. In the CR mode, the contact radius $R \equiv R_0$ remains constant throughout the evaporation and the evolutions of θ, h_{m}, and V are linear functions of t for both sessile and pendant droplets. In the CA mode, the contact angle $\theta \equiv 1$ remains constant throughout the evaporation and R and V decrease monotonically in t for both sessile and pendant droplets. For a pendant droplet h_{m} is always a monotonically decreasing function of t; however, for a sessile droplet, h_{m} decreases monotonically in t for $R_0 < 5.586$, corresponding to $V_0 < 73.175$, and is non-monotonic in t for $R_0 > 5.586$. In addition, we have shown that the solutions for the evolution, and hence the lifetime, of a zero-gravity droplet always lie between those for a sessile and a pendant droplet. In the SS mode, the evolution of a droplet is as described by the CR and the CA mode in each phase. In the SJ mode, in each CR phase, *i.e.* for $t_{n-1} < t < t_n$, the contact radius R_n is constant and θ, h_{m}, and V decrease linearly in t, and at each instantaneous jump, *i.e.* at t_n, R jumps to a lower value, θ and h_{m} jump to higher values, and V is conserved for both sessile and pendant droplets. The predicted lifetimes of the droplets in each mode of evaporation, as well as the critical times t^* and t_n, are always greater for a pendant droplet than those for a zero-gravity droplet of the same initial volume and critical angles, which are in turn greater than those for a sessile droplet.

The solutions for the evolutions, and hence the lifetimes, of evaporating sessile and pendant droplets were also analysed for the limiting cases of initially small ($V_0 \to 0^{+}$)

and initially large ($V_0 \to \infty$) droplets. In particular, in the limit of a small droplet the leading-order behaviour corresponds to the solutions for a zero-gravity droplet and is independent of the orientation of the droplet, whereas, in the limit of a large droplet the behaviour depends on whether the droplet is sessile or pendant.

Chapter 5

The Effect of Spatial Variation in the Local Evaporative Flux on the Deposition from a Pinned Particle-Laden Sessile Droplet

5.1 Introduction

In this Chapter, motivated by the increasing interest in controlling the shape of the final deposit from an evaporating droplet, as discussed in Chapter 1, we consider the effect of spatial variation in the local evaporative flux on the deposition from a pinned particle-laden sessile droplet. Specifically, in Sections 5.2–5.5 we formulate and analyse a mathematical model for the evolution of, flow within, and transport of particles within, a thin sessile droplet with a general steady local evaporative-flux profile $\hat{J} = \hat{J}(\hat{r})$. In Section 5.6 we investigate a particular one-parameter family of spatially-varying local evaporative fluxes of the form $\hat{J} = \hat{J}(\hat{r}; n)$ that captures a wide range of qualitatively different behaviours and examine the asymptotic behaviour in three particular limits in detail in Section 5.7. In Section 5.8 we describe the behaviour of the particle paths when the transport of particles within the droplet is governed purely by advection.

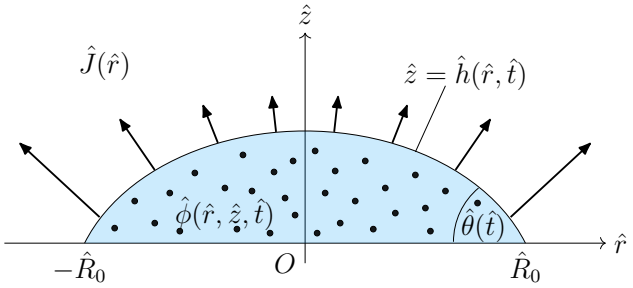

Figure 5.1: Sketch of a thin pinned sessile droplet with constant contact radius $\hat{R}_0$, contact angle $\hat{\theta}(\hat{t})$, and free surface $\hat{z} = \hat{h}(\hat{r}, \hat{t})$, containing a suspension of particles, evaporating on a planar substrate. The arrows indicate the local evaporative flux $\hat{J}(\hat{r})$, and the concentration of particles within the droplet is denoted by $\hat{\phi}(\hat{r}, \hat{z}, \hat{t})$.

5.2 Problem formulation

We consider the evaporation of an axisymmetric sessile droplet with a pinned contact line of constant radius $\hat{R}_0$ containing a suspension of particles on a planar substrate. As in Chapter 2, we refer the description to cylindrical polar coordinates $(\hat{r}, \hat{\varphi}, \hat{z})$ with $O\hat{z}$ along the axis of the droplet, perpendicular to the substrate at $\hat{z} = 0$, as sketched in Figure 5.1. After the droplet is deposited at $\hat{t} = 0$, its volume will decrease due to evaporation into the atmosphere until the time at which it has completely evaporated, *i.e.* the lifetime of the droplet, denoted by $\hat{t} = \hat{t}_{\text{lifetime}}$.

As in Chapter 2, we consider situations in which the droplet is thin, the droplet is sufficiently small that the effect of gravity is negligible, and the surface tension is sufficiently strong that the droplet evolves quasi-statically. More specifically, we consider situations in which the initial contact angle of the droplet, $\hat{\theta}_0 \ll 1$, is small, as are the appropriately defined Bond number Bo and scaled capillary number Ca^* from (2.2), namely

$$\text{Bo} = \left(\frac{\hat{R}_0}{\hat{\ell}}\right)^2 \ll 1 \quad \text{and} \quad \text{Ca}^* = \frac{\text{Ca}}{\hat{\theta}_0^3} = \frac{\hat{\mu}\hat{U}}{\hat{\theta}_0^3\hat{\sigma}} \ll 1. \tag{5.1}$$

The mean curvature of the free surface of the droplet is therefore spatially constant, and so at leading order in the limit $\hat{\theta}_0 \to 0$ its free surface profile $\hat{h}$ satisfies

$$\frac{\partial}{\partial \hat{r}}\left(\frac{1}{\hat{r}}\frac{\partial}{\partial \hat{r}}\left(\hat{r}\frac{\partial \hat{h}}{\partial \hat{r}}\right)\right) = 0. \tag{5.2}$$

As discussed in Chapter 1, the local evaporative flux $\hat{J}$ from the free surface of the droplet is dependent upon the process of evaporation and can take various forms depending on the physics of the problem. In this Chapter we shall assume that the droplet undergoes quasi-steady evaporation for which the local evaporative flux takes the general form $\hat{J} = \hat{J}(\hat{r})$, where $\hat{J}$ is a known function of $\hat{r}$. As we shall see in this Chapter, it is convenient to define the indefinite radial integral of the local evaporative flux, denoted by $\hat{I} = \hat{I}(\hat{r})$, as

$$\hat{I} = \int_0^{\hat{r}} \hat{J}(\tilde{r})\, \tilde{r}\, \mathrm{d}\tilde{r}. \tag{5.3}$$

As also discussed in Chapter 1, manipulation of the vapour field is often used as a way to control the deposition from an evaporating droplet, as this can enhance or suppress the local and total evaporative fluxes from the droplet. Motivated by this, in Section 5.6 we consider a particular one-parameter family of spatially-varying local evaporative fluxes of the form $\hat{J} = \hat{J}(\hat{r}; n)$ which captures a wide range of qualitatively different behaviours. In particular, this will include the spatially-uniform and diffusion-limited fluxes as special cases. In Appendix A we demonstrate that the analysis presented in this Chapter may be generalised to a separable time-dependent local evaporative flux of the form $\hat{J} = \hat{J}(\hat{r}, \hat{t}) = \hat{f}(\hat{r})\hat{g}(\hat{t})$, of the kind explored numerically by Fischer [84].

The evaporation induces a flow within the droplet that transports the particles within it. The goal of this Chapter is to determine the flow within the droplet, the resultant dynamics of the particles, the nature of the final deposit left behind on the substrate after the droplet has completely evaporated, and how each of these depend upon the spatial variation of the local evaporative flux. In the next three Sections we analyse the evolution of the droplet, solve the hydrodynamic problem for the fluid flow that is induced inside the droplet, and solve the problem for the motion of the particles within the droplet for a general $\hat{J} = \hat{J}(\hat{r})$.

5.3 Droplet evolution

We nondimensionalise and scale the variables according to (2.13) with $\hat{L} = \hat{R}_0$ for the droplet, and similarly for the atmosphere except that $\hat{z} = \hat{R}_0 z^{\mathrm{a}}$; in addition we introduce the scaling

$$\hat{I} = \hat{D}(\hat{c}_{\mathrm{sat}} - \hat{c}_{\infty})\hat{L}I. \tag{5.4}$$

We take the droplet to evaporate with a pinned contact line, *i.e.* in the CR mode, and so the free-surface profile given by (5.2) must satisfy $h(1,t) = 0$ and $\partial h/\partial r = -\theta$ at $r = 1$; in addition, h must be finite at $r = 0$, and is therefore of the familiar paraboloidal form

$$h = \frac{\theta(1-r^2)}{2}. \tag{5.5}$$

For the purpose of this Chapter, it is convenient to write h as a separable function of r and t, namely

$$h(r,t) = \theta(t)\eta(r) \quad \text{where} \quad \eta = \frac{1-r^2}{2}, \tag{5.6}$$

and to define the incomplete radial integral of η, denoted by $H = H(r)$, as

$$H = \int_0^r \eta(\tilde{r})\,\tilde{r}\,\mathrm{d}\tilde{r} = \frac{1-(1-r^2)^2}{8}, \tag{5.7}$$

and we note that $H(1) = 1/8$. The volume $V = V(t)$ of the droplet is given by

$$V = 2\pi \int_0^1 h\,r\,\mathrm{d}r = 2\pi\theta H(1) = \frac{\pi\theta}{4}. \tag{5.8}$$

We note that (5.5) and (5.8) correspond to the solutions given by (2.17) and (2.19) in Chapter 2 when $R \equiv 1$. The droplet evolves according to the global mass-conservation condition

$$\frac{\mathrm{d}V}{\mathrm{d}t} = -2\pi \int_0^1 J\,r\,\mathrm{d}r = -2\pi I(1), \tag{5.9}$$

so that, in particular, the (constant) total evaporative flux is given by

$$F = 2\pi I(1). \tag{5.10}$$

The initial values of θ and V are given by

$$\theta = 1, \quad V = V_0 = \frac{\pi}{4} \quad \text{at} \quad t = 0. \tag{5.11}$$

Substituting the expression for V given in (5.8) into (5.9) yields

$$\frac{\mathrm{d}V}{\mathrm{d}t} = 2\pi H(1)\frac{\mathrm{d}\theta}{\mathrm{d}t} = \frac{\pi}{4}\frac{\mathrm{d}\theta}{\mathrm{d}t} = -2\pi I(1), \tag{5.12}$$

and so the evolution of the droplet is given by

$$h = \theta\eta, \quad \theta = 1 - \frac{I(1)}{H(1)}t, \quad V = \frac{\pi}{4}\left(1 - \frac{I(1)}{H(1)}t\right). \tag{5.13}$$

The droplet has completely evaporated (*i.e.* $\theta = V = 0$) at $t = t_{\text{lifetime}}$ given by

$$t_{\text{lifetime}} = \frac{H(1)}{I(1)}. \tag{5.14}$$

5.4 The hydrodynamic problem

So far in this thesis we have considered only leading-order solutions in the limit $\mathrm{Ca}^* \to 0$. As discussed in Chapter 2, for $\mathrm{Bo} \ll 1$ and $\mathrm{Ca}^* \ll 1$ the Stokes equations reduce to the statement that the (scaled) leading-order pressure p satisfies $\nabla p = \mathbf{0}$. However, in order to determine the flow within the droplet, we must consider terms that are at first order in $\mathrm{Ca}^* \ll 1$. At leading order in $\hat{\theta}_0 \ll 1$ and $\mathrm{Bo} \ll 1$ and at first order in $\mathrm{Ca}^* \ll 1$, the Stokes equations reduce to the statement that the (scaled) leading-order velocity and first-order pressure within the droplet, denoted by $\mathbf{u} = (u(r,z,t), 0, w(r,z,t))$ and $p^{(1)} = p^{(1)}(r,z,t)$, respectively, satisfy (see, for example, Wray *et al.* [306])

$$\frac{\partial^2 u}{\partial z^2} = \frac{\partial p^{(1)}}{\partial r}, \quad \frac{\partial p^{(1)}}{\partial z} = 0, \tag{5.15}$$

in which the velocity $\hat{\mathbf{u}} = (\hat{u}, 0, \hat{w})$ of the fluid has been scaled according to

$$\hat{u} = \frac{\hat{D}(\hat{c}_{\text{sat}} - \hat{c}_\infty)}{\hat{\rho}\hat{\theta}_0\hat{R}_0}u, \quad \hat{w} = \frac{\hat{D}(\hat{c}_{\text{sat}} - \hat{c}_\infty)}{\hat{\rho}\hat{R}_0}w. \tag{5.16}$$

In particular, equation (5.15) shows that $p^{(1)}$ is independent of z, *i.e.* $p^{(1)} = p^{(1)}(r,t)$. As we shall see, $p^{(1)}$ is the only first-order term required to describe the leading-order problems for the hydrodynamic fluid flow and the transport of particles within the droplet. Therefore, we do not introduce superscripts "(0)" on the leading-order velocity components u and w for brevity.

The velocity $\mathbf{u}$ is subject to the usual mass-continuity condition, namely

$$\frac{1}{r}\frac{\partial(ru)}{\partial r} + \frac{\partial w}{\partial z} = 0, \tag{5.17}$$

as well as no-slip and no-penetration conditions on the substrate, *i.e.* $u(r,0,t) = w(r,0,t) = 0$. In addition, the governing equations (5.15) are subject to the interfacial stress-balance condition

$$\frac{\partial u}{\partial z} = 0 \quad \text{at} \quad z = h, \tag{5.18}$$

as well as the kinematic condition

$$\frac{\partial h}{\partial t} + \frac{1}{r}\frac{\partial(rQ)}{\partial r} = -J, \tag{5.19}$$

where $Q = Q(r,t)$, defined by

$$Q = \int_0^h u \, \mathrm{d}z, \tag{5.20}$$

is the local radial fluid flux. For the purpose of this Chapter, it is convenient to express Q in terms of I and H given by (5.3) and (5.7), respectively; integrating the kinematic condition (5.19) with respect to r and rearranging gives

$$Q = -\frac{1}{r}\int_0^r \left(J + \frac{\partial h}{\partial t}\right) \tilde{r} \, \mathrm{d}\tilde{r} = -\frac{1}{r}\left(\int_0^r J(\tilde{r}) \, \tilde{r} \, \mathrm{d}\tilde{r} + \frac{\mathrm{d}\theta}{\mathrm{d}t}\int_0^r \eta(\tilde{r}) \, \tilde{r} \, \mathrm{d}\tilde{r}\right), \tag{5.21}$$

and hence

$$Q = \frac{I(1)H(r) - H(1)I(r)}{rH(1)}. \tag{5.22}$$

The depth-averaged radial velocity, denoted by $\bar{u} = \bar{u}(r,t)$, is defined by

$$\bar{u} = \frac{1}{h}\int_0^h u \, \mathrm{d}z = \frac{Q}{h}. \tag{5.23}$$

Solving equations (5.15) and (5.17), subject to (5.18), and the no-slip and no-penetration conditions on the substrate, leads to (see, for example, Boulogne *et al.* [32])

$$u = \frac{1}{2}\frac{\partial p^{(1)}}{\partial r}\left(z^2 - 2hz\right), \quad w = \frac{z^2}{6r}\left[\frac{\partial p^{(1)}}{\partial r}\left(3r\frac{\partial h}{\partial r} + 3h - z\right) + r\frac{\partial^2 p^{(1)}}{\partial r^2}\left(3h - z\right)\right]. \tag{5.24}$$

Substituting the expression for u given in (5.24a) into (5.20) yields the solution for Q, namely

$$Q = -\frac{h^3}{3}\frac{\partial p^{(1)}}{\partial r}. \tag{5.25}$$

For a given local evaporative flux J, the evolution of the droplet may be calculated from (5.12). Then, the solution for Q is given by (5.22), the solution for $p^{(1)}$ is obtained by integrating (5.25), and u and w are given by (5.24).

5.5 The particle-transport problem

We will now derive the equations governing the transport of the particles within the droplet as it evaporates. Specifically, we investigate the transport of particles via the evolution of the concentration of particles and the evolution of the total mass of particles in the droplet.

5.5.1 Concentration of particles

The concentration of particles within the droplet, denoted by $\hat{\phi} = \hat{\phi}(\hat{r}, \hat{z}, \hat{t})$, satisfies the (scaled) advection-diffusion equation

$$\mathrm{Pe}_\mathrm{p}^*\left(\frac{\partial \phi}{\partial t} + u\frac{\partial \phi}{\partial r} + w\frac{\partial \phi}{\partial z}\right) = \hat{\theta}_0^2\left(\frac{1}{r}\frac{\partial}{\partial r}\left(r\frac{\partial \phi}{\partial r}\right)\right) + \frac{\partial^2 \phi}{\partial z^2}, \tag{5.26}$$

in which $\hat{\phi}$ has been nondimensionalised according to $\hat{\phi} = \bar{\phi}_0\phi$, where $\bar{\phi}_0$ is the volume-averaged initial concentration of particles within the droplet, and Pe_p^* is the appropri-

ately defined scaled particle Péclet number, namely

$$\mathrm{Pe}_\mathrm{p}^* = \hat{\theta}_0^2 \mathrm{Pe}_\mathrm{p} = \hat{\theta}_0^2 \frac{\hat{L}\hat{U}}{\hat{D}_\mathrm{p}} = \frac{\hat{\theta}_0 \hat{D}\,(\hat{c}_\mathrm{sat} - \hat{c}_\infty)}{\hat{\rho}\hat{D}_\mathrm{p}}, \tag{5.27}$$

where $\hat{D}_\mathrm{p}$ is the constant diffusivity of the particles in the fluid. We note that, similarly to the mass Péclet number in Chapter 2, the particle Péclet number Pe_p characterises the ratio of diffusive and advective particle transport.

The governing equation (5.26) is subject to conditions of no flux of particles at the substrate,

$$\frac{\partial \phi}{\partial z} = 0 \quad \text{on} \quad z = 0, \tag{5.28}$$

or through the free surface of the droplet,

$$\mathbf{n} \cdot \nabla \phi = \mathrm{Pe}_\mathrm{p}\, \phi J \quad \text{on} \quad z = h, \tag{5.29}$$

where $\mathbf{n}$ denotes the outward unit normal to the free surface of the droplet.

We consider situations in which the vertical diffusion of particles within the droplet is fast relative to evaporation. More specifically, we consider situations in which the scaled particle Péclet number satisfies

$$\hat{\theta}_0^2 \ll \mathrm{Pe}_\mathrm{p}^* \ll 1, \tag{5.30}$$

corresponding to a large (but not too large) particle Péclet number, *i.e.* $1 \ll \mathrm{Pe}_\mathrm{p} \ll \hat{\theta}_0^{-2}$ (see, for example, Wray *et al.* [306]). We therefore seek asymptotic solutions for ϕ of the form

$$\phi = \phi^{(0)} + \mathrm{Pe}_\mathrm{p}^* \phi^{(1)} + O\left(\mathrm{Pe}_\mathrm{p}^{*\,2}\right), \tag{5.31}$$

in the limit $\mathrm{Pe}_\mathrm{p}^* \to 0$. In Section 5.8 we will consider situations in which both the radial and vertical diffusion of particles within the droplet is slow relative to evaporation, corresponding to $\mathrm{Pe}_\mathrm{p} \gg \hat{\theta}_0^{-2}$ and $\mathrm{Pe}_\mathrm{p}^* \gg 1$.

In the limit $\hat{\theta}_0 \to 0$ and at leading-order in $\mathrm{Pe}_\mathrm{p}^* \ll 1$, (5.26), (5.28), and (5.29) give

$$\frac{\partial^2 \phi^{(0)}}{\partial z^2} = 0, \tag{5.32}$$

$$\frac{\partial \phi^{(0)}}{\partial z} = 0 \quad \text{on} \quad z = 0 \quad \text{and} \quad z = h, \tag{5.33}$$

which shows that $\phi^{(0)}$ is independent of z, specifically

$$\phi^{(0)} = \phi^{(0)}(r, t). \tag{5.34}$$

At first order in $\mathrm{Pe}_\mathrm{p}^* \ll 1$, (5.26), (5.28), and (5.29) give

$$\frac{\partial^2 \phi^{(1)}}{\partial z^2} = \frac{\partial \phi^{(0)}}{\partial t} + u \frac{\partial \phi^{(0)}}{\partial r}, \tag{5.35}$$

$$\frac{\partial \phi^{(1)}}{\partial z} = 0 \quad \text{on} \quad z = 0, \tag{5.36}$$

$$\frac{\partial \phi^{(1)}}{\partial z} = \phi^{(0)} J \quad \text{on} \quad z = h. \tag{5.37}$$

Integrating (5.35) with respect to z, subject to the boundary conditions (5.36) and (5.37), and dropping the superscript "(0)" on ϕ for clarity, yields the following governing equation for the leading-order concentration of particles ϕ (see, for example, Deegan *et al.* [64], Wray *et al.* [306]):

$$\frac{\partial \phi}{\partial t} + \bar{u} \frac{\partial \phi}{\partial r} = \frac{\phi J}{h}, \tag{5.38}$$

where $\bar{u}$ is given by (5.23). We note that determining the leading-order evolution of the concentration of particles from (5.38) does not require the solution for $\mathbf{u} = (u, 0, w)$.

Equation (5.38) may be solved via the method of characteristics:

$$\frac{\mathrm{d}\phi}{\mathrm{d}t} = \frac{\phi J}{h} \quad \text{on the characteristics determined by} \quad \frac{\mathrm{d}r}{\mathrm{d}t} = \bar{u}, \tag{5.39}$$

subject to a prescribed initial condition $\phi(r, 0) = \phi_0(r)$. Using the expressions for h

and $\mathrm{d}\theta/\mathrm{d}t$ given by (5.6) and (5.12), equations (5.39) can be expressed as

$$\frac{\mathrm{d}r}{\mathrm{d}\theta} = \frac{\mathrm{d}r/\mathrm{d}t}{\mathrm{d}\theta/\mathrm{d}t} = -\frac{H(1)Q(r)}{\theta I(1)\eta(r)}, \quad \frac{\mathrm{d}\phi}{\mathrm{d}r} = \frac{\mathrm{d}\phi/\mathrm{d}t}{\mathrm{d}r/\mathrm{d}t} = \frac{J(r)\phi}{Q(r)}. \tag{5.40}$$

Integration of (5.40) yields the implicit solution

$$\log\theta = -\int_{r_0}^{r} \frac{I(1)\eta(\tilde{r})}{H(1)Q(\tilde{r})}\,\mathrm{d}\tilde{r}, \qquad \log\frac{\phi}{\phi_0} = \int_{r_0}^{r} \frac{J(\tilde{r})}{Q(\tilde{r})}\,\mathrm{d}\tilde{r}, \tag{5.41}$$

where $r_0 = r_0(r,t)$ denotes the initial radial position of a particle at time $t = 0$ that subsequently travels to position r at time t, which is determined by solving (5.41a). To simplify the solution for ϕ, we note that adding the two equations in (5.41), and recalling that Q may be expressed in the form (5.22), yields

$$\begin{aligned}\log\theta + \log\frac{\phi}{\phi_0} &= -\int_{r_0}^{r} \frac{I(1)\eta(\tilde{r}) - H(1)J(\tilde{r})}{H(1)Q(\tilde{r})}\,\mathrm{d}\tilde{r} \\ &= -\int_{r_0}^{r} \frac{1}{\tilde{r}Q(\tilde{r})}\frac{\mathrm{d}\left(\tilde{r}Q(\tilde{r})\right)}{\mathrm{d}\tilde{r}}\,\mathrm{d}\tilde{r} \\ &= \log\frac{r_0 Q(r_0)}{rQ(r)},\end{aligned} \tag{5.42}$$

and hence the solution of the characteristic equations for the concentration of particles ϕ from (5.38) may be written in the form

$$\int_{r_0}^{r} \frac{I(1)\eta(\tilde{r})}{H(1)Q(\tilde{r})}\,\mathrm{d}\tilde{r} = -\log\theta, \qquad \frac{\phi}{\phi_0} = \frac{r_0 Q(r_0)}{\theta r Q(r)}. \tag{5.43}$$

Equations (5.43) will be used for calculating the concentration of particles ϕ in Section 5.6. The corresponding analysis for the case of a separable time-dependent local evaporative flux of the form $J = J(r,t) = f(r)g(t)$ is given in Appendix A.

5.5.2 Mass of particles

If a particle is advected by the flow to the contact line before the end of evaporation (*i.e.* for $0 < t < t_{\text{lifetime}}$) then the particle is deposited onto the substrate in a deposit ring at the contact line. If a particle is not advected to the contact line, then, in the absence of additional effects (such as particle adsorption onto the substrate) the

particle is deposited elsewhere on the substrate at the end of the evaporation (*i.e.* at $t = t_{\text{lifetime}}$). Therefore, depending on the nature of the flow, the total mass of particles within the bulk of the droplet may either be constant or a decreasing function of time.

The mass of particles in the bulk of the droplet at time $\hat{t}$, denoted by $\hat{M}_{\text{drop}} = \hat{M}_{\text{drop}}(\hat{t})$, satisfies

$$M_{\text{drop}} = 2\pi \int_0^1 \phi(r,t)\, h(r,t)\, r \, \mathrm{d}r, \tag{5.44}$$

where $\hat{M}_{\text{drop}}$ has been nondimensionalised according to $\hat{M}_{\text{drop}} = \bar{\phi}_0 \hat{\theta}_0 \hat{R}_0^3 M_{\text{drop}}$ and ϕh is the mass of particles per unit area within the footprint of the droplet. Alternatively, M_{drop} may be expressed as

$$M_{\text{drop}} = 2\pi \int_0^{r_0(1,t)} \phi_0(r)\, h(r,0)\, r \, \mathrm{d}r, \tag{5.45}$$

where $r_0(1,t)$ denotes the initial radial position of a particle that has subsequently travelled to the contact line at $r = 1$, where it has then been deposited at time t, determined by solving (5.43a).

The initial mass of particles in the droplet, defined by $M_{\text{drop}}(0) = M_0$, is given by

$$M_0 = 2\pi \int_0^1 \phi_0(r)\, h(r,0)\, r \, \mathrm{d}r. \tag{5.46}$$

The mass of particles in the deposit ring at time t, denoted by $M_{\text{ring}} = M_{\text{ring}}(t)$, is given by

$$M_{\text{ring}} = 2\pi \int_0^t \Big(\phi(r,\tilde{t})\, Q(r,\tilde{t})\, r \Big)\Big|_{r=1} \, \mathrm{d}\tilde{t}, \tag{5.47}$$

where $(\phi Q r)|_{r=1}$ is the flux of particles into the contact line $r = 1$ at time t. Alternatively, M_{ring} may be expressed as (see, for example, Deegan *et al.* [64])

$$M_{\text{ring}} = 2\pi \int_{r_0(1,t)}^1 \phi_0(r)\, h(r,0)\, r \, \mathrm{d}r. \tag{5.48}$$

Adding equations (5.45) and (5.48) confirms that the total mass of particles is conserved (*i.e.* $M_0 = M_{\text{drop}} + M_{\text{ring}}$).

For simplicity, throughout the remainder of this Chapter we will assume that the

initial concentration of particles within the droplet is spatially-uniform, which therefore takes the value $\phi_0 \equiv 1$, since ϕ is scaled by the volume-averaged initial concentration of particles $\bar{\phi}_0$. In this case the initial mass of particles in the droplet from (5.46) is

$$M_0 = 2\pi \int_0^1 h(r,0)\, r \, \mathrm{d}r = \frac{\pi}{4}. \tag{5.49}$$

5.6 A one-parameter family of spatially-varying local evaporative fluxes

In this Section we investigate the behaviour of the solutions described in Sections 5.2–5.5 for a general one-parameter family of prescribed spatially-varying local evaporative fluxes of the form $J = J(r;n)$. In particular, we will discuss the general qualitative behaviour of the solutions for the evolution of, flow within, and transport of particles within, an evaporating sessile droplet depending on the parameter n.

5.6.1 The prescribed local evaporative flux $J = J(r;n)$

We consider the one-parameter family of local evaporative fluxes of the form

$$J = J_0(n)(1-r^2)^n, \tag{5.50}$$

where the exponent n satisfies $n > -1$, so that the total evaporative flux from (5.10), namely $F = 2\pi I(1)$, is finite. The local evaporative flux (5.50) has been chosen because it captures a wide range of qualitatively different behaviours depending upon the choice of the parameter n. In particular, it includes diffusion-limited evaporation when $n = -1/2$, spatially-uniform evaporation when $n = 0$, evaporation that is proportional to the time derivative of the free-surface profile (where there is no resultant fluid flow, as explored experimentally by Deegan *et al.* [64]) when $n = 1$, and evaporation that is concentrated at the centre of the droplet, as observed, for example, through masking (see, for example, Vodolazskaya and Tarasevich [293]), in the limit $n \to \infty$.

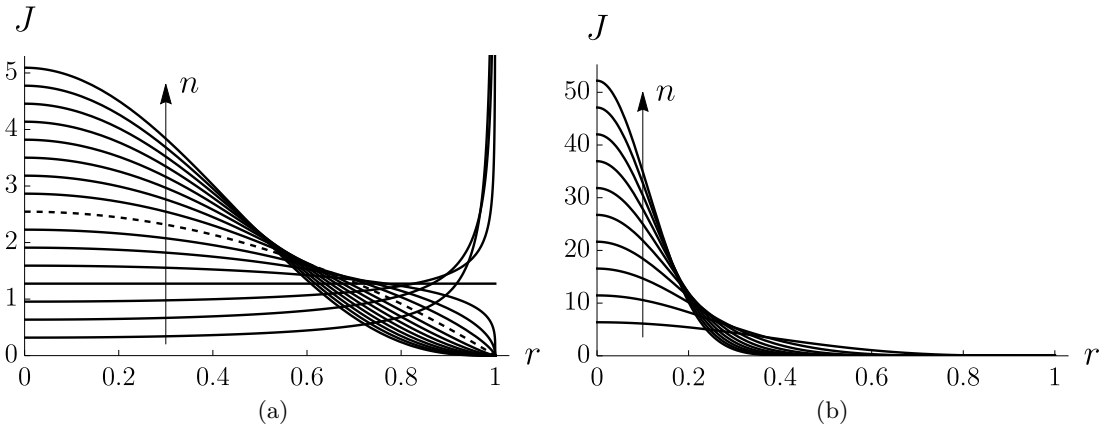

Figure 5.2: Plot of the local evaporative flux J given by (5.52) for (a) $n = -3/4, -1/2, \ldots, 3$ and (b) $n = 4, 8, \ldots, 40$. The arrows indicate the direction of increasing n and the dashed line in (a) corresponds to $n = 1$.

To facilitate comparisons for different values of n, we choose the pre-factor

$$J_0(n) = \frac{4(n+1)}{\pi}, \tag{5.51}$$

so that the total evaporative flux is equal to the value in the diffusion-limited case, corresponding to $F = 4$. In particular, as we shall see, this means that the lifetime of the droplet is the same for all $n > -1$.

The one-parameter family of local evaporative fluxes that we shall investigate in detail therefore takes the form

$$J = \frac{4(n+1)}{\pi}(1 - r^2)^n. \tag{5.52}$$

Figure 5.2 shows the behaviour of J for a range of values of $n > -1$. As Figure 5.2 shows, J increases monotonically with r from the centre of the droplet and diverges at the contact line for $-1 < n < 0$, is constant for $n = 0$, and decreases monotonically from the centre of the droplet to zero at the contact line for $n > 0$. In particular, at the centre of the droplet

$$J(0, n) = J_0(n) = \frac{4(n+1)}{\pi}, \tag{5.53}$$

which simply increases linearly with n, and near the contact line the behaviour of J

depends on the value of n as follows:

$$J = \frac{2^{2+n}(n+1)}{\pi}(1-r)^n + O(1-r)^{n+1} \to \left\{ \begin{array}{lll} \infty & \text{for} & -1 < n < 0 \\ \dfrac{4}{\pi} & \text{for} & n = 0 \\ 0^+ & \text{for} & n > 0 \end{array} \right\} \quad \text{as} \quad r \to 1^-. \tag{5.54}$$

In the limits $n \to -1^+$ and $n \to \infty$, the local evaporative flux J approaches zero everywhere except in regions near $r = 1$ and $r = 0$, respectively. We will explore the asymptotic behaviour of the evaporation in these particular limits in Section 5.7.

We also note the simple behaviour in the special case $n = 1$, in which $J = -\partial h/\partial t = 8(1-r^2)/\pi$. In this case there is no resultant flow within the droplet and hence no local radial fluid flux, *i.e.* $u \equiv w \equiv \bar{u} \equiv Q \equiv 0$. The concentration of particles ϕ from (5.43) therefore takes the simple form $\phi = 1/\theta$, remaining spatially uniform and increasing with t as the droplet evaporates. The distribution of the mass of particles per unit area within the footprint of the droplet $\phi h = h(r, 0) = (1 - r^2)/2$ is independent of t, the mass of particles within the bulk of the droplet from (5.44), $M_{\text{drop}} \equiv M_0$, remains constant at its initial value throughout the evaporation, and all of the particles are deposited onto the substrate at their initial radial position, forming a paraboloidal deposit that is proportional to the initial profile of the droplet.

We will now discuss the solutions for a general value of n (> -1). As we shall see, the solutions undergo a qualitative change in behaviour around the special case $n = 1$. We will explore the asymptotic behaviour of the evaporation in the limit $n \to 1^{\pm}$ in Section 5.7.

5.6.2 Droplet evolution

With (5.52), the radially-integrated flux I defined by (5.3) is

$$I = \int_0^r \frac{4(n+1)(1-\tilde{r})^n \tilde{r}}{\pi} \, \mathrm{d}\tilde{r} = \frac{2}{\pi}\left[1 - (1-r^2)^{n+1}\right], \tag{5.55}$$

and we note that $I(1) = 2/\pi$. Substituting the expression for $I(1)$ given in (5.55) and $H(1)$ given in (5.7) into (5.12) and (5.14) yields the evolution and lifetime of the droplet, namely

$$h = \theta\eta, \quad V = \frac{\pi}{4} - 4t, \quad \theta = 1 - \frac{16}{\pi}t, \tag{5.56}$$

$$t_{\text{lifetime}} = \frac{\pi}{16}. \tag{5.57}$$

In particular, due to the choice of the pre-factor $J_0(n)$ given in (5.51), V, θ, and t_{lifetime} are independent of the parameter n. In addition, (5.56) and (5.57) are simply the well-known solutions for a pinned droplet undergoing diffusion-limited evaporation (see, for example, Wilson and Duffy [303]).

5.6.3 The flow within the droplet

The solution (5.22) for the local radial fluid flux Q is

$$Q = \frac{2(1-r^2)}{\pi r}\Big[(1-r^2)^n - (1-r^2)\Big], \tag{5.58}$$

which, with (5.25), leads to the solution for the first-order pressure $p^{(1)}$, namely

$$p^{(1)} = -\frac{24}{\pi\theta^3}\Big[(2-n)r^2\,{}_3F_2\left(1,1,3-n;2,2;r^2\right) + \log\left(1-r^2\right)\Big], \tag{5.59}$$

where ${}_3F_2\left(a_1,a_2,a_3;b_1,b_2;x\right)$ is the generalised hypergeometric function defined by

$${}_3F_2\left(a_1,a_2,a_3;b_1,b_2;x\right) = \sum_{k=0}^{\infty}\frac{(a_1)_k\,(a_2)_k\,(a_3)_k}{(b_1)_k\,(b_2)_k}\frac{x^k}{k!} \quad \text{where} \quad (p)_k = \frac{\Gamma(p+k)}{\Gamma(p)}, \tag{5.60}$$

and $\Gamma(p)$ is the Gamma function defined by

$$\Gamma(p) = \int_0^{\infty} q^{p-1}\,\mathrm{e}^{-q}\,\mathrm{d}q. \tag{5.61}$$

Figure 5.3 shows the behaviour of Q for a range of values of $n > -1$.

Substituting the expressions for h given in (5.5) and $p^{(1)}$ given in (5.59) into the

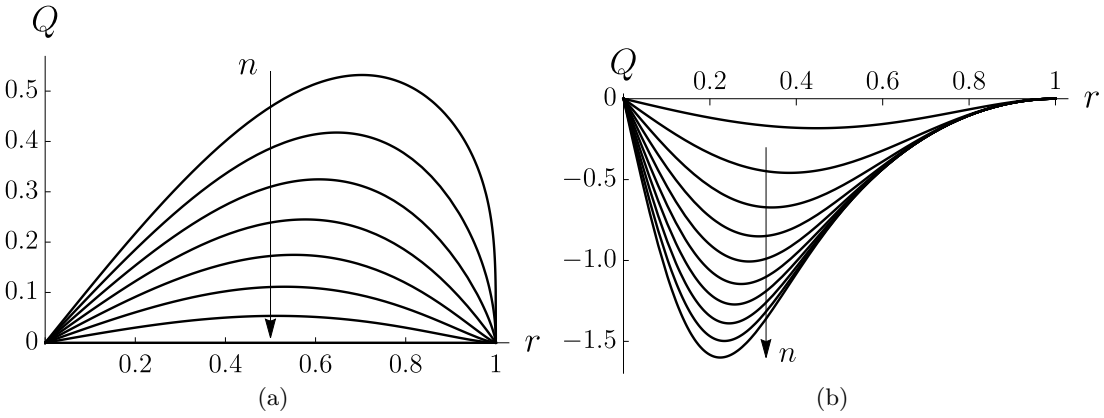

Figure 5.3: Plots of the local radial fluid flux Q given by (5.58) for (a) $n = -3/4, -1/2, \ldots, 1$ and (b) $n = 2, 4, \ldots, 20$. The arrows indicate the direction of increasing n.

expressions (5.24) leads to the solutions for u and w, namely

$$u = \frac{24}{\pi\theta^3(1-r^2)^2 r}\Big[(1-r^2)^n - (1-r^2)\Big]\Big[\theta(1-r^2)z - z^2\Big], \tag{5.62}$$

and

$$w = -\frac{8z^2}{\pi\theta^3(1-r^2)^3}\left[2(1-r^2)z + (1-r^2)^n\Big\{3\theta(1-n)(1-r^2) - 2(2-n)z\Big\}\right]. \tag{5.63}$$

It is straightforward to deduce from (5.62) that u is positive, corresponding to radially-outward flow, for $-1 < n < 1$, is zero, *i.e.* no flow, for $n = 1$, and is negative, corresponding to radially-inward flow, for $n > 1$, for all $0 < r < 1$ and $0 < t < t_{\text{lifetime}}$. It may also be shown from equation (5.63) that the flow in the z direction is downward for $-1 < n < 1$ and is zero for $n = 1$. For $n > 1$, the sign of w is dependent on the values of r, z, n, and t as follows:

$$w \begin{cases} > 0 & \text{for} \quad 0 < z < z_{\text{crit}}, \\ = 0 & \text{for} \quad z = z_{\text{crit}}, \\ < 0 & \text{for} \quad z_{\text{crit}} < z < h. \end{cases} \quad \text{where} \quad z_{\text{crit}} = \frac{3\theta(1-n)(1-r^2)}{2\left(2-n-(1-r^2)^{1-n}\right)}. \tag{5.64}$$

Figure 5.4 shows instantaneous streamlines of the flow within a droplet for (a) $n = -1/2$ and (b) $n = 2$ at an illustrative time $t = t_{\text{lifetime}}/2 = \pi/32$; these are typical values of n

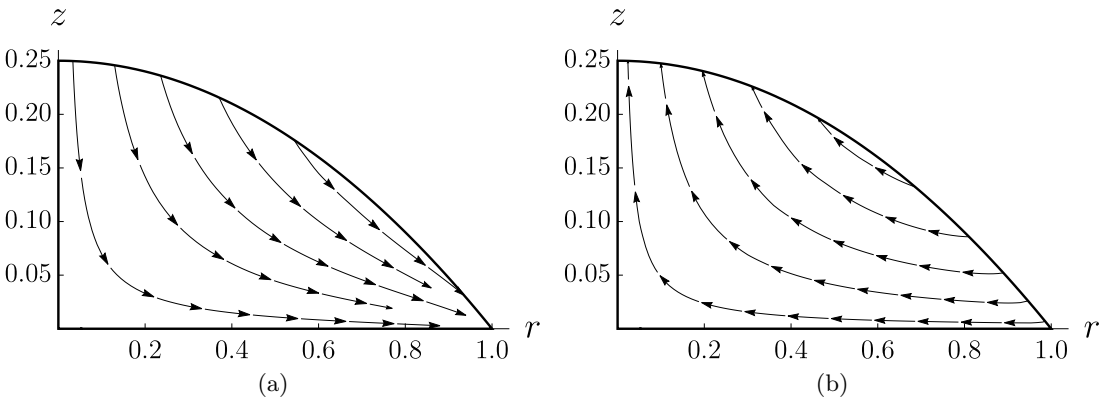

Figure 5.4: Instantaneous streamlines of the flow within a droplet for (a) $n = -1/2$ and (b) $n = 2$ at $t = \pi/32$.

which represent the qualitatively different behaviour for (a) $-1 < n < 1$ and (b) $n > 1$, respectively.

As we have already described in Section 5.5, the depth-averaged radial velocity $\bar{u}$ is sufficient to describe the evolution of the concentration of particles at leading-order, and hence the evolution of the total mass of particles in the droplet. Substituting the expressions for h given in (5.5) and Q given in (5.58) into the solution (5.23) for $\bar{u}$ yields

$$\bar{u} = \frac{4}{\pi\theta r}\Big[(1-r^2)^n - (1-r^2)\Big]. \tag{5.65}$$

Figure 5.5 shows the behaviour of $\bar{u}\theta$, which is independent of t, for a range of values of $n > -1$. Equation (5.65) shows that $\bar{u}$ is strictly positive for $-1 < n < 1$, as shown in Figure 5.5(a), is identically zero when $n = 1$, and is strictly negative for $n > 1$, as shown in Figure 5.5(b), for all $0 < r < 1$. In addition, (5.65) shows that $\bar{u}$ diverges with t as $t \to t^-_{\text{lifetime}}$ for $n > -1$ and $n \neq 1$. The local evaporative flux J and local radial fluid flux Q are constant in time t; however, as the droplet evaporates, the contact angle θ, and hence the free-surface profile h, of the droplet decrease and, in order to replenish the fluid to maintain a constant fluid flux, $\bar{u}$ must increase with t, eventually diverging as $h \to 0^+$. This divergence in the depth-averaged radial velocity towards the end of the lifetime of the droplet (sometimes referred to as the rush-hour effect) has been previously identified as a feature of evaporation-induced radially-outward

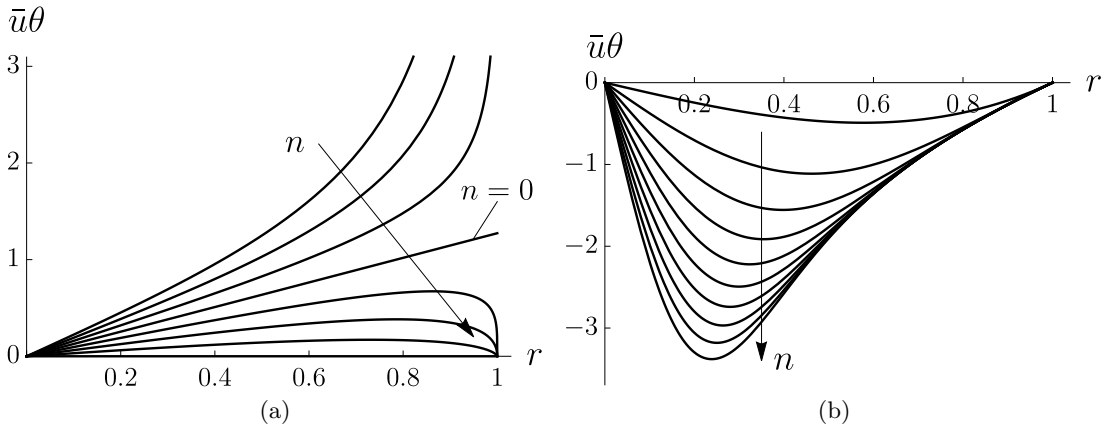

Figure 5.5: Plots of $\bar{u}\theta$ given by (5.65) for (a) $n = -3/4, -1/2, \ldots, 1$ and (b) $n = 2, 4, \ldots, 20$. The arrows indicate the direction of increasing n.

flow, for example, in the special case of diffusion-limited evaporation when $n = -1/2$, experimentally by Hamamoto *et al.* [105] and Marin *et al.* [178, 179], as discussed in Chapter 1, as well as analytically by Deegan *et al.* [64].

Near the centre of the droplet

$$\bar{u} = \frac{4r(1-n)}{\pi\theta} + O(r^3) \to \left\{ \begin{array}{lll} 0^+ & \text{for} & -1 < n < 1 \\ 0 & \text{for} & n = 1 \\ 0^- & \text{for} & n > 1 \end{array} \right\} \quad \text{as} \quad r \to 0^+. \tag{5.66}$$

Near the contact line the behaviour of $\bar{u}$ depends on the value of n as follows:

$$\bar{u} \to \left\{ \begin{array}{lll} \infty & \text{for} & -1 < n < 0 \\ \dfrac{4}{\pi\theta} & \text{for} & n = 0 \\ 0^+ & \text{for} & 0 < n < 1 \\ 0 & \text{for} & n = 1 \\ 0^- & \text{for} & n > 1 \end{array} \right\} \quad \text{as} \quad r \to 1^-. \tag{5.67}$$

Equation (5.67) shows that $\bar{u}$ exhibits three qualitatively different behaviours at the contact line; specifically, $\bar{u}$ is singular for $-1 < n < 0$, finite and non-zero for $n = 0$, and zero for $n > 0$, in line with the corresponding behaviour of J near the contact line.

5.6.4 The transport of particles within the droplet

For the chosen one-parameter family of fluxes (5.52), the integral in (5.43a) can be evaluated in closed form to give an implicit solution for the time $t = t(r_0, r)$ it takes for a particle at initial radial position r_0 to travel to the radial position r, namely

$$r_0(r,t) = \left[1 - \theta^{1/2}\left(\theta^{(n-1)/2} - 1 + (1-r^2)^{1-n}\right)^{1/(1-n)}\right]^{1/2}. \tag{5.68}$$

For the case of radially-outward flow when $-1 < n < 1$, the time at which a particle at initial radial position r_0 is deposited at the contact line, denoted by $t(r_0, 1) = t_{\text{CLdeposit}}(r_0)$, is obtained by evaluating equation (5.68) at $r = 1$ as follows:

$$r_0(1,t) = \left[1 - \left(1 - \theta^{(1-n)/2}\right)^{1/(1-n)}\right]^{1/2} \quad \text{for} \quad -1 < n < 1, \tag{5.69}$$

which recovers the solution for $t_{\text{CLdeposit}}$ obtained by Deegan *et al.* [64] and Boulogne *et al.* [32] for the special cases of diffusion-limited evaporation when $n = -1/2$ and spatially-uniform evaporation when $n = 0$, respectively. For the case of no radial flow when $n = 1$ only a particle that is initially at the contact line is deposited at the contact line at the end of evaporation, *i.e.* $t_{\text{CLdeposit}} = t_{\text{lifetime}}$ for $r_0 = 1$, and for the case of radially-inward flow when $n > 1$ no particles are deposited at the contact line. Figure 5.6 shows the behaviour of $t_{\text{CLdeposit}}/t_{\text{lifetime}}$ as a function of r_0 for a range of values of $-1 < n < 1$. For the case of radially-outward flow when $-1 < n < 1$, all of the particles are eventually transferred to the deposit ring at the contact line throughout the evaporation. In particular, as Figure 5.6 shows, particles that are initially close to the contact line are deposited first and particles that are initially close to the centre of the droplet are deposited towards the end of evaporation, *i.e.* $t_{\text{CLdeposit}}$ decreases monotonically from $t_{\text{CLdeposit}} = t_{\text{lifetime}}$ at $r_0 = 0$ to $t_{\text{CLdeposit}} = 0$ at $r_0 = 1$, as expected.

Substituting the expressions for Q given in (5.58) and r_0 given in (5.68) into (5.43b)

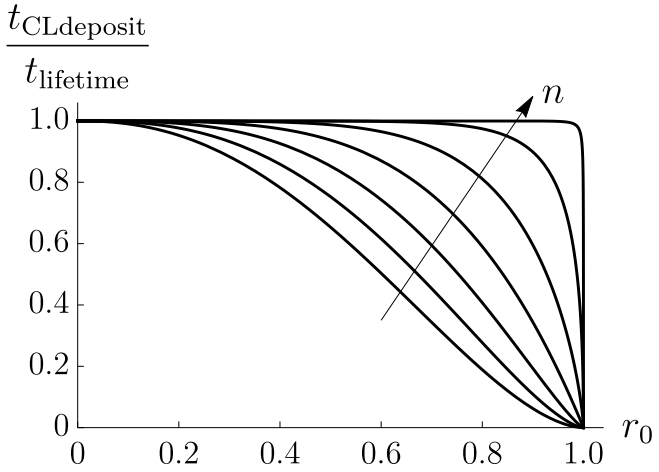

Figure 5.6: Plot of $t_{\text{CLdeposit}}/t_{\text{lifetime}}$ as a function of r_0 for $n = -3/4, -1/2, \ldots, 3/4$. The arrow indicates the direction of increasing n.

yields an explicit solution for the concentration of particles ϕ, namely

$$\phi = \left[1 + \frac{\theta^{(n-1)/2} - 1}{(1-r^2)^{1-n}}\right]^{(n+1)/(1-n)}, \tag{5.70}$$

which recovers the solutions obtained by Zheng [320] for the special cases of diffusion-limited evaporation when $n = -1/2$ and spatially-uniform evaporation when $n = 0$. Figure 5.7 shows the profile of ϕ at an illustrative time $t = t_{\text{lifetime}}/2 = \pi/32$ for a range of values of $n > -1$. The concentration of particles ϕ increases monotonically from the centre of the droplet to infinity at the contact line for $-1 < n < 1$, as shown in Figure 5.7(a), is spatially-uniform for $n = 1$, and decreases monotonically from the centre of the droplet to 1 at the contact line when $n > 1$, as shown in Figure 5.7(b), for all $0 < t < t_{\text{lifetime}}$. In particular, at the centre of the droplet

$$\phi(0,t) = \frac{1}{\theta^{(n+1)/2}}, \tag{5.71}$$

which increases monotonically with n, and throughout the evaporation, and near the

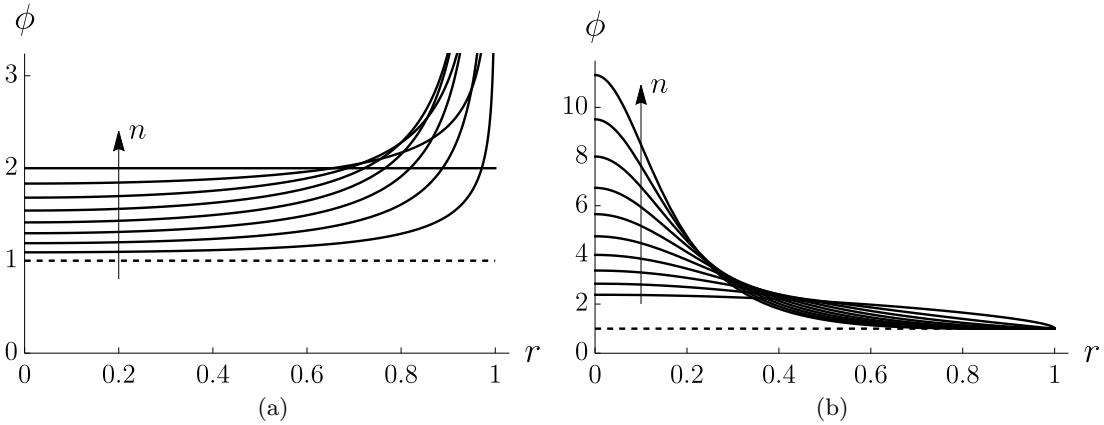

Figure 5.7: Profile of the concentration of particles ϕ given by (5.70) at $t = \pi/32$ plotted as a function of r for (a) $n = -3/4, -1/2, \ldots, 1$ and (b) $n = 3/2, 2, \ldots, 6$. The dashed lines indicate the initial concentration of particles at $t = 0$. The arrows indicate the direction of increasing n.

contact line the behaviour of ϕ depends on the value of n, as follows:

$$\phi \to \left\{ \begin{array}{lll} \infty & \text{for} & -1 < n < 1 \\ \dfrac{1}{\theta} & \text{for} & n = 1 \\ 1^+ & \text{for} & n > 1 \end{array} \right\} \quad \text{as} \quad r \to 1^-. \tag{5.72}$$

From (5.5) and (5.70), the distribution of the mass of particles per unit area within the droplet is given by

$$\phi h = \frac{\theta(1-r^2)}{2}\left[1 + \frac{\theta^{(n-1)/2} - 1}{(1-r^2)^{1-n}}\right]^{(n+1)/(1-n)}. \tag{5.73}$$

Figure 5.8 shows the evolution of ϕh throughout the evaporation for (a) $n = -1/2$, (b) $n = 0$, (c) $n = 1/2$, and (d) $n = 2$; these are typical values of n which represent the qualitatively different behaviour for (a) $-1 < n < 0$, (b) $n = 0$, (c) $0 < n < 1$, and (d) $n > 1$. As previously discussed, for the special case when $n = 1$, ϕh is independent of t and so is omitted because of its simplicity. Near the centre of the droplet

$$\phi(0,t)h(0,t) = \frac{\theta^{(1-n)/2}}{2}, \tag{5.74}$$

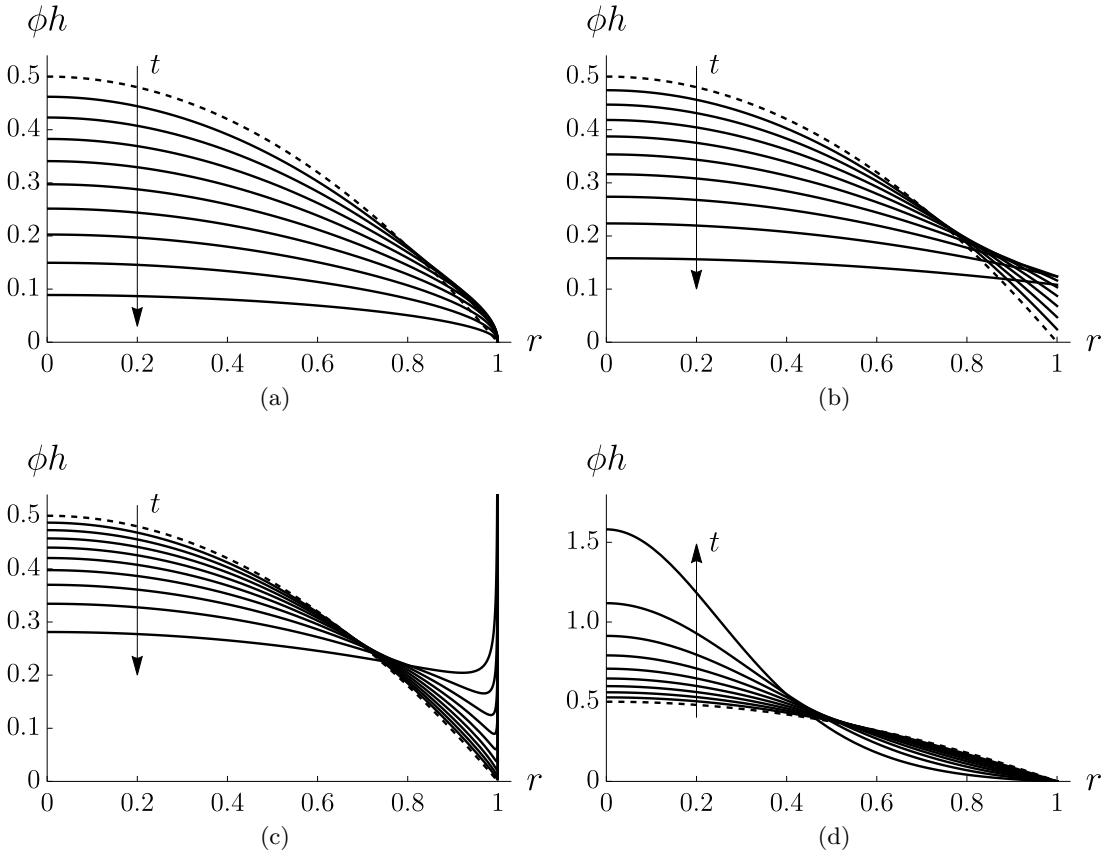

Figure 5.8: The distribution of the mass of particles ϕh at times $t = (0,\ 1/10,\ \ldots,\ 9/10) \times t_{\text{lifetime}}$ for (a) $n = -1/2$, (b) $n = 0$, (c) $n = 1/2$, and (d) $n = 2$. The dashed lines indicate the initial distribution of the mass of particles within the droplet at $t = 0$ given by $h(r, 0)$. The arrows indicate the direction of increasing t.

which decreases monotonically with t for $-1 < n < 1$ as particles are advected towards the contact line, as shown in Figures 5.8(a–c), is constant for $n = 1$, and increases monotonically for $n > 1$ as particles are advected towards the centre of the droplet, as shown in Figure 5.8(d). Near the contact line ϕh exhibits different behaviour depending on the value of n, as follows:

$$\phi h \to \left\{ \begin{array}{lll} 0 & \text{for} & -1 < n < 0 \\ \dfrac{\sqrt{\theta} - \theta}{2} & \text{for} & n = 0 \\ \infty & \text{for} & 0 < n < 1 \\ 0 & \text{for} & n \geq 1 \end{array} \right\} \quad \text{as} \quad r \to 1^{-}. \tag{5.75}$$

Equation (5.75) shows that $\phi h = 0$ at the contact line for $-1 < n < 0$ and $n \geq 1$. The result for $-1 < n < 0$ may seem counter-intuitive because of the radially-outward flow; however, in this case the rate at which particles are advected towards the contact line is balanced by the rate at which particles are transferred to the deposit ring. For $n = 0$, ϕh is a non-zero function of t at the contact line for all $0 < t < t_{\text{lifetime}}$, as shown in Figure 5.8(b), and for $0 < n < 1$, ϕh is singular at the contact line, as shown in Figure 5.8(c). In both of these cases, the rate at which particles are advected towards the contact line is greater than the rate at which particles are transferred to the deposit ring.

Substituting the solution for $r_0(1, t)$ given by (5.69) into the solutions for M_{drop} (5.45) and M_{ring} (5.48) yields

$$M_{\text{drop}} = M_0 \left\{ \begin{array}{lll} 1 - (1 - \theta^{(1-n)/2})^{2/(1-n)} & \text{for} & -1 < n < 1 \\ 1 & \text{for} & n \geq 1 \end{array} \right\}, \tag{5.76}$$

$$M_{\text{ring}} = M_0 \left\{ \begin{array}{lll} (1 - \theta^{(1-n)/2})^{2/(1-n)} & \text{for} & -1 < n < 1 \\ 0 & \text{for} & n \geq 1 \end{array} \right\}, \tag{5.77}$$

where we recall that $M_0 = \pi/4$ from (5.49). Figure 5.9 shows the evolutions of M_{drop}/M_0 and M_{ring}/M_0 as functions of t/t_{lifetime} for a range of values of n. In par-

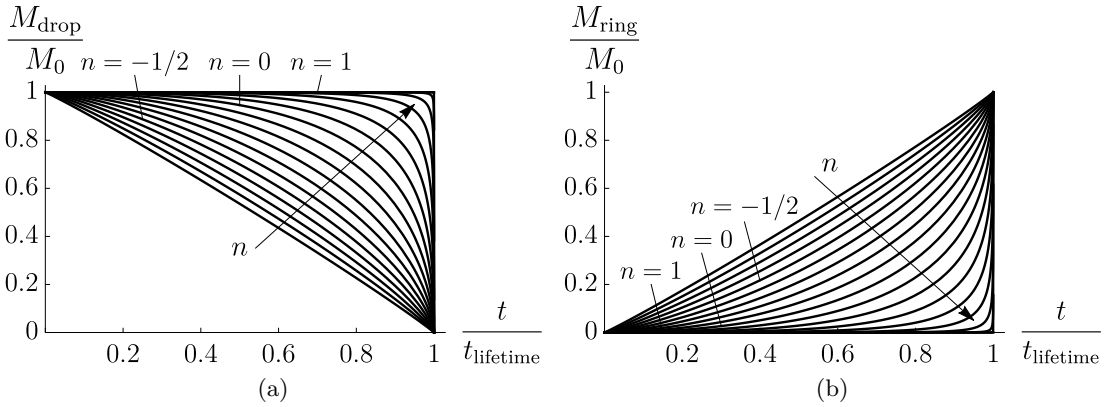

Figure 5.9: Evolution of (a) M_{drop}/M_0 from (5.76) and (b) M_{ring}/M_0 from (5.77) as functions of t/t_{lifetime} for $n = -9/10, -8/10, \ldots, 1$. The arrows indicate the direction of increasing n.

ticular, as Figure 5.9 shows, for $-1 < n < 1$, M_{drop} is a decreasing function of time, reaching zero at $t = t_{\text{lifetime}}$, *i.e.* all of the particles are eventually transferred to the deposit ring at the contact line, whereas for $n \geq 1$, M_{drop} remains constant at its initial value, *i.e.* all of the particles remain within the footprint of the droplet throughout the evaporation. From (5.76) and (5.77) the final distribution of the particles after the droplet has evaporated is given by $M_{\text{drop}} = 0$ and $M_{\text{ring}} = M_0$ when $-1 < n < 1$, and by $M_{\text{drop}} = M_0$ and $M_{\text{ring}} = 0$ when $n \geq 1$.

We note that for $-1 < n < 1$, the transfer of particles to the deposit ring, *i.e.* the growth of M_{ring}, becomes increasingly "rushed" towards the end of the lifetime of the droplet as n increases, approaching an instantaneous transfer at $t = t_{\text{lifetime}}$ as $n \to 1^-$, as shown in Figure 5.9. For $0 < n < 1$, J is zero at the contact line and the depth-averaged radially outward flow is positive for $0 < r < 1$ and is zero at the contact line. In this case, a particle is advected radially-outward towards the contact line; however, as it gets closer to the contact line, it slows down. Therefore, particles build up near the contact line which results in a non-zero value of ϕh locally. The divergence in $\bar{u}$ as $t \to t^-_{\text{lifetime}}$ causes the eventual "rushed" transfer of particles to the deposit ring.

5.7 Asymptotic behaviour in three particular limits

We will now examine the asymptotic behaviour of the evaporation for three particular limits in detail. Specifically, we shall describe the behaviour when the local evaporative flux J approaches zero everywhere except in a narrow region near the contact line, the time derivative of the free-surface profile $-\partial h/\partial t$, and zero everywhere except in a narrow region near the centre of the droplet, corresponding to the limits $n \to -1^+$, $n \to 1$, and $n \to \infty$, respectively.

5.7.1 The limit $n \to -1^+$

In the limit $n \to -1^+$ the local evaporative flux J given by (5.52) takes the form

$$J = \frac{4(n+1)}{\pi(1-r^2)} + \frac{4}{\pi(1-r^2)} \log(1-r^2)(n+1)^2 + O(n+1)^3 \to 0^+ \quad \text{as} \quad n \to -1^+. \tag{5.78}$$

In this limit J approaches zero everywhere except in a narrow boundary layer of thickness $O(n+1)$ near the contact line and is singular at $r = 1$. The corresponding behaviour of $\bar{u}$ given by (5.65) is

$$\bar{u} = \frac{4r(2-r^2)}{\pi\theta(1-r^2)} + \frac{4\log(1-r^2)}{\pi\theta r(1-r^2)}(n+1) + O(n+1)^2 \to \frac{4r(2-r^2)}{\pi\theta(1-r^2)}^- \quad \text{as} \quad n \to -1^+, \tag{5.79}$$

which is independent of n at leading order. At leading order, the evaporation from the boundary layer near $r = 1$ induces a flow within the droplet for which $\bar{u}$ is non-zero and monotonically increases from 0 at the centre of the droplet to infinity at the contact line. Figure 5.10 shows the behaviour of J and $\bar{u}\theta$ for $n = -9/10$, comparing the exact expressions with the leading-order asymptotic expressions in the limit $n \to -1^+$.

The behaviour of ϕ from (5.70) is

$$\phi = 1 + \frac{1}{2}\log\left[\frac{\theta^{-1} - 1 + (1-r^2)^2}{(1-r^2)^2}\right](n+1) + O(n+1)^2 \to 1^+ \quad \text{as} \quad n \to -1^+. \tag{5.80}$$

Away from $r = 1$, ϕ is spatially uniform and constant at leading order, but the expansion in (5.80) is non-uniform and ϕ diverges logarithmically at first order as $r \to 1^-$.

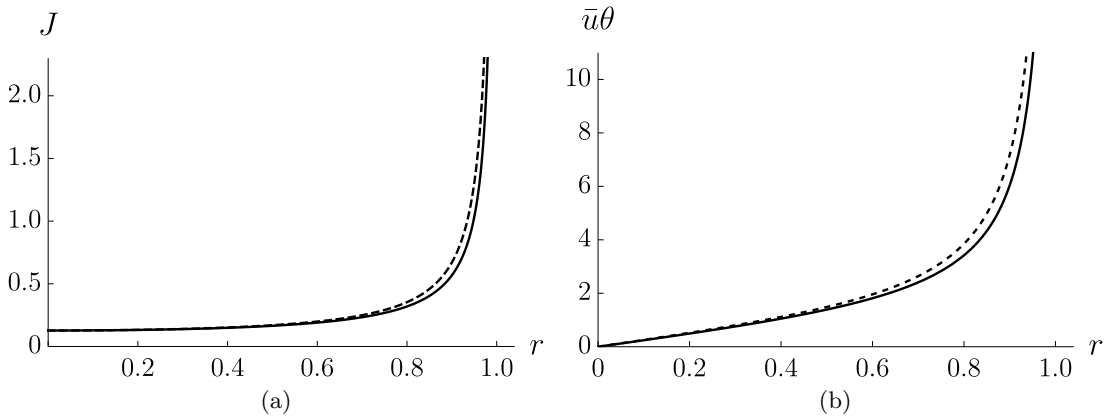

Figure 5.10: Plot of (a) J and (b) $\bar{u}\theta$ for $n = -9/10$, comparing the exact expressions from (5.52) and (5.65) (solid lines) with the leading-order asymptotic expressions in the limit $n \to -1^+$ from (5.78) and (5.79) (dashed lines).

Figure 5.11 shows the behaviour of ϕ for $n = -9/10$, comparing the exact expression with the asymptotic expression in the limit $n \to -1^+$ up to and including the $O(n+1)$ term. We note that, since the leading-order behaviour of ϕ is independent of n, we plot the asymptotic expression including the next order term. From (5.5) and (5.80), the leading-order term of $\phi h \sim h$ is simply equal to the free-surface profile of the droplet in this limit. Therefore, at leading order, the rate at which particles are being advected radially outward by the flow matches the rate at which particles are transferred to the deposit ring, as well as the rate at which the free-surface profile of the droplet decreases due to the evaporation.

The corresponding behaviours of M_{drop} and M_{ring}, from (5.76) and (5.77), respectively, are

$$M_{\text{drop}} = M_0\theta - \frac{M_0}{2}\Big[(1-\theta)\log(1-\theta) + \theta\log\theta\Big](n+1) + O(n+1)^2, \tag{5.81}$$

$$M_{\text{ring}} = M_0(1-\theta) + \frac{M_0}{2}\Big[(1-\theta)\log(1-\theta) + \theta\log\theta\Big](n+1) + O(n+1)^2, \tag{5.82}$$

and hence

$$M_{\text{drop}} \to M_0\theta^+ \quad \text{and} \quad M_{\text{ring}} \to M_0(1-\theta)^- \quad \text{as} \quad n \to -1^+, \tag{5.83}$$

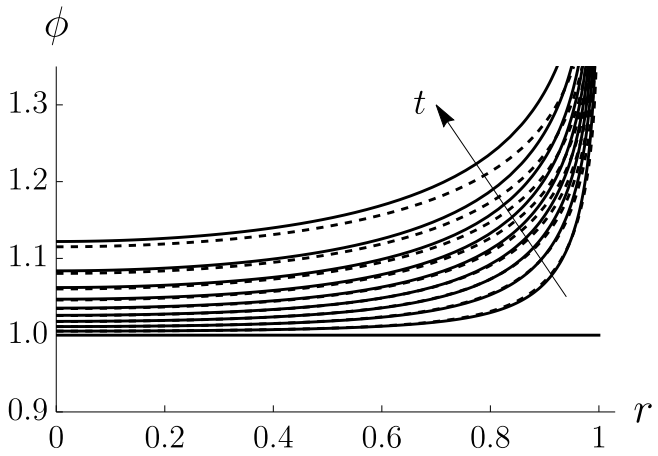

Figure 5.11: Plot of ϕ for $n = -9/10$, comparing the exact expression from (5.70) (solid lines) with the asymptotic expression in the limit $n \to -1^+$ up to and including the $O(n+1)$ term from (5.80) (dashed lines) for $t = (0,\ 1/10,\ \ldots,\ 9/10) \times t_{\text{lifetime}}$. The arrow indicates the direction of increasing t.

which are independent of n at leading order. Figure 5.12 shows the leading-order evolutions of M_{drop}/M_0 and M_{ring}/M_0 as functions of t/t_{lifetime}. At leading order, M_{drop} and M_{ring} vary linearly in t via their dependence on θ, as shown in Figure 5.12, and satisfy $M_{\text{drop}} \to 0^+$ and $M_{\text{ring}} \to M_0^-$ as $t \to t_{\text{lifetime}}^-$, *i.e.* all of the particles are transferred to the deposit ring at the contact line.

5.7.2 The limit $n \to 1$

As previously discussed, there is a qualitative change in the behaviour of the solutions described in Section 5.6 at the value $n = 1$. In the limit $n \to 1$, the local evaporative flux J from (5.52) takes the form

$$J = \frac{8(1-r^2)}{\pi} + \frac{4(1-r^2)}{\pi}\left[1 + 2\log\left(1-r^2\right)\right](n-1) + O(n-1)^2, \tag{5.84}$$

and hence

$$J \to \begin{cases} \dfrac{8(1-r^2)}{\pi}^{\pm} & \text{for} \quad 0 \le r < r_{\text{crit}} \\ \dfrac{8(1-r^2)}{\pi}^{\mp} & \text{for} \quad r_{\text{crit}} < r \le 1 \end{cases} \qquad \text{as} \quad n \to 1^{\pm}, \tag{5.85}$$

where

$$r_{\text{crit}} = (1 - \mathrm{e}^{-1/2})^{1/2} \simeq 0.6273 \tag{5.86}$$

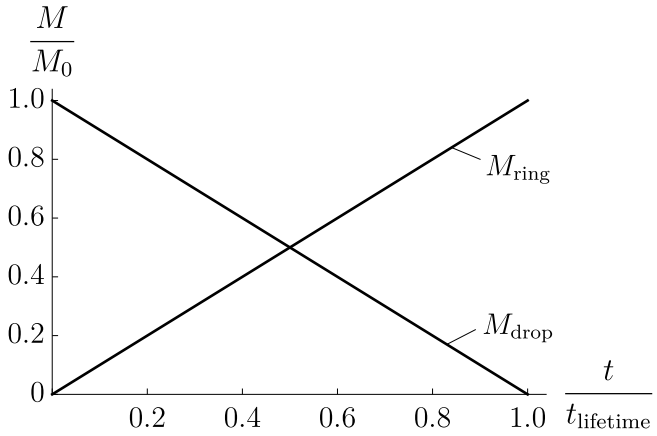

Figure 5.12: Leading-order evolutions of M_{drop}/M_0 and M_{ring}/M_0 as functions of t/t_{lifetime} in the limit $n \to -1^+$ from (5.83).

is the critical value of r at which the local evaporative flux J is equal to $-\partial h/\partial t$ at leading-order. The corresponding behaviour of $\bar{u}$ given by (5.65) is

$$\bar{u} = \frac{4(1-r^2)\log(1-r^2)}{\pi\theta r}(n-1) + O(n-1)^2 \to 0^{\mp} \quad \text{as} \quad n \to 1^{\pm}, \tag{5.87}$$

which changes sign depending upon the direction of approach to the value $n = 1$. Figure 5.13 shows the behaviour of J and $\bar{u}\theta$ for $n = 4/5$ and $6/5$, comparing the exact expressions with the asymptotic expressions in the limit $n \to 1^{\pm}$ up to and including the $O(n-1)$ terms. We note that, since J and $\bar{u}\theta$ are equal to the exact solution when $n = 1$ at leading-order, we plot the asymptotic expressions including the next order terms. We have chosen to evaluate the expressions at $n = 4/5$ and $n = 6/5$ to show a discernible difference between the asymptotic and exact expressions.

The behaviour of ϕ from (5.70) is

$$\phi = \frac{1}{\theta} + \frac{\log\theta}{2\theta}\left[1 + 2\log(1-r^2)\right](n-1) + O(n-1)^2, \tag{5.88}$$

and hence

$$\phi \to \begin{cases} \dfrac{1}{\theta}^{\pm} & \text{for} \quad 0 \le r < r_{\text{crit}} \\ \dfrac{1}{\theta}^{\mp} & \text{for} \quad r_{\text{crit}} < r < 1 \end{cases} \quad \text{as} \quad n \to 1^{\pm}. \tag{5.89}$$

Figure 5.14 shows the behaviour of ϕ for $n = 4/5$ and $n = 6/5$ at an illustrative

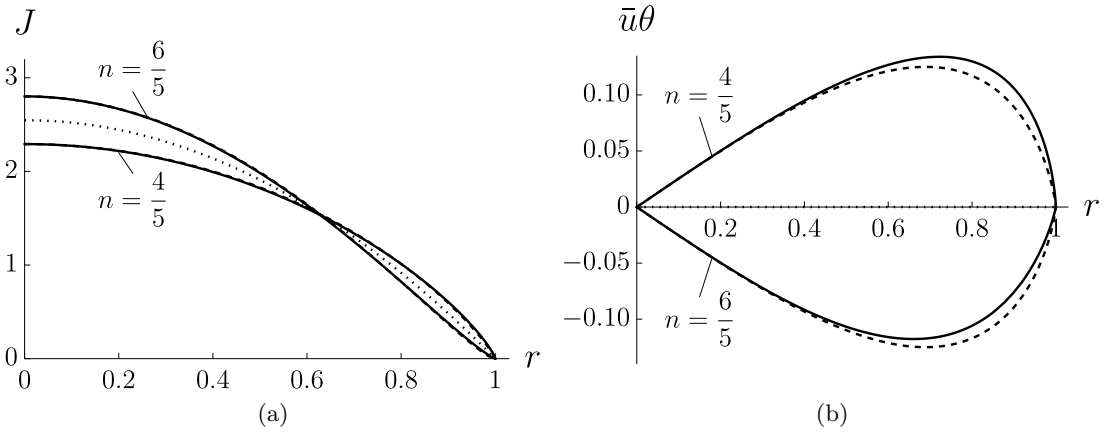

Figure 5.13: Plots of (a) J and (b) $\bar{u}\theta$ at $n = 4/5$ and $n = 6/5$ comparing the exact expressions from (5.52) and (5.65) (dashed lines) and the asymptotic expressions in the limit $n \to 1^{\pm}$ up to and including the $O(n-1)$ terms from (5.84) and (5.87) (dashed lines). The dotted lines correspond the exact solution when $n = 1$.

time $t = t_{\text{lifetime}}/2 = \pi/32$, comparing the exact expressions with the asymptotic expressions in the limit $n \to 1^{\pm}$ up to and including the $O(n-1)$ term. Again, since ϕ is equal to the exact solution when $n = 1$ at leading-order, we plot the asymptotic expression including the next order term. From (5.88), ϕ is spatially-uniform at leading order, increasing with t via the dependence on θ, but the expansion is non-uniform and diverges logarithmically near the contact line as $n \to 1^-$ and approaches the initial concentration 1 near the contact line as $n \to 1^+$, as shown in Figure 5.14. The change from positive $\bar{u}$ when $n \to 1^-$ to negative $\bar{u}$ when $n \to 1^+$ results in the qualitative change in behaviour of the concentration of particles within the droplet.

The corresponding behaviour for M_{drop} and M_{ring} from (5.76) and (5.77), respectively, is

$$M_{\text{drop}} = M_0 \left[1 - \theta^{1/2} \left(\frac{(n-1)}{2} \log\theta\right)^{2/(1-n)}\right] + O\left(n-1\right) \to M_0^- \quad \text{as} \quad n \to 1^-, \tag{5.90}$$

$$M_{\text{ring}} = M_0 \left[\theta^{1/2} \left(\frac{(n-1)}{2} \log\theta\right)^{2/(1-n)}\right] + O\left(n-1\right) \to 0^+ \quad \text{as} \quad n \to 1^-, \tag{5.91}$$

with $M_{\text{drop}} \equiv M_0$ and $M_{\text{ring}} \equiv 0$ for any $n \geq 1$. Figure 5.15 shows the evolutions of M_{drop}/M_0 and M_{ring}/M_0 for $n = 4/5$, comparing the exact expressions with the leading-

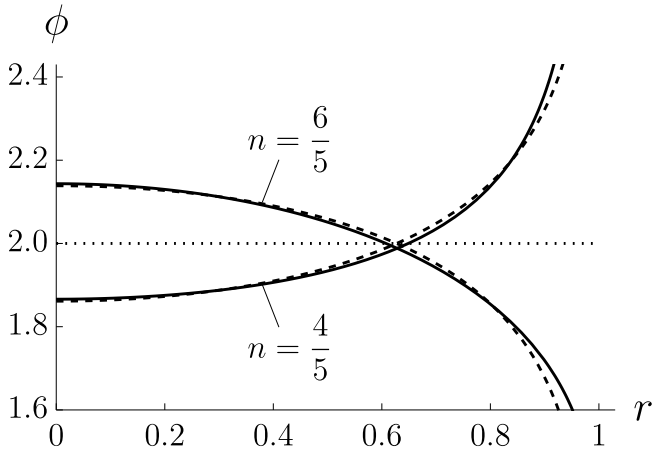

Figure 5.14: Plot of ϕ for $n = 4/5$ and $n = 6/5$ at $t = \pi/32$ comparing the exact expressions from (5.70) (dashed lines) with the the asymptotic expressions in the limit $n \to 1^{\pm}$ up to and including the $O(n-1)$ term from (5.88) (dashed lines). The dotted lines correspond the exact solution when $n = 1$.

order asymptotic expressions in the limit $n \to 1^-$, where the dotted lines correspond to the solution for any $n \geq 1$. At leading order, M_{drop} and M_{ring} approach M_0 and 0, respectively, as $n \to 1^-$. However, the expansions in (5.90) and (5.91) are non-uniform, and the mass of particles within the droplet decreases to zero as $t \to t^-_{\text{lifetime}}$, as shown in Figure 5.15(a).

5.7.3 The limit $n \to \infty$

We will now consider the limit $n \to \infty$, in which J approaches zero everywhere except in a narrow region near the centre of the droplet. The local evaporative flux J from (5.52) takes the form

$$J \sim \frac{4n}{\pi} \mathrm{e}^{-nr^2} \quad \text{as} \quad n \to \infty \tag{5.92}$$

at leading order, which shows that there is a narrow internal layer of width $r = O(1/\sqrt{n}) \ll 1$ near the centre of the droplet in which $J = O(n) \gg 1$ and outside of which J is exponentially small. The corresponding leading-order behaviour of $\bar{u}$ given by (5.65) is

$$\bar{u} \sim -\frac{4}{\pi\theta r}\left(1 - r^2 - \mathrm{e}^{-nr^2}\right) \quad \text{as} \quad n \to \infty, \tag{5.93}$$

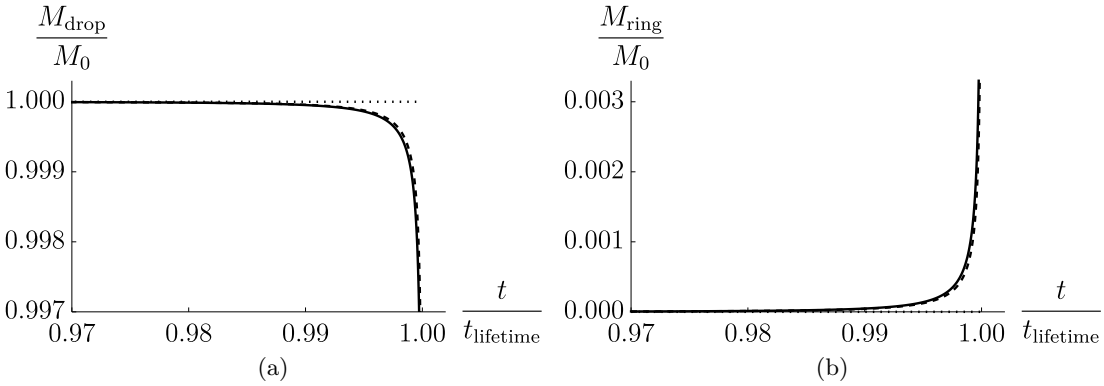

Figure 5.15: Evolutions of (a) M_{drop}/M_0 and (b) M_{ring}/M_0 as functions of t/t_{lifetime} for $n = 4/5$ comparing the exact expressions from (5.76) and (5.77) (solid lines) with the leading-order asymptotic expressions in the limit $n \to 1^-$ from (5.90) and (5.91) (dashed lines). The dotted lines correspond to the exact solution when $n = 1$, *i.e.* (a) $M_{\text{drop}} = M_0 = \pi/4$ and (b) $M_{\text{ring}} = 0$.

which shows that $\bar{u} = O(\sqrt{n}) \to -\infty$ in the narrow internal layer of width $r = O(1/\sqrt{n}) \ll 1$ near the centre of the droplet and $\bar{u} \sim -4(1 - r^2)/(\pi\theta r) = O(1)$ away from $r = 0$. Figure 5.16 shows the behaviour of J and $\bar{u}\theta$ for $n = 10$, comparing the exact expressions with the leading-order asymptotic expressions in the limit $n \to \infty$.

The leading-order behaviour of ϕ from (5.70) is

$$\phi \sim \left[1 - \mathrm{e}^{-nr^2}\left(1 - \theta^{(n-1)/2}\right)\right]^{-1-2/n} \quad \text{as} \quad n \to \infty, \tag{5.94}$$

which shows that ϕ increases monotonically with t via its dependence on θ in the narrow internal layer of width $r = O(1/\sqrt{n}) \ll 1$ near the centre of the droplet, and remains constant at the initial value of 1 away from $r = 0$. Figure 5.17 shows the behaviour of ϕ for $n = 10$, comparing the exact expression with the leading-order asymptotic expression in the limit $n \to \infty$. In accordance with the behaviour for all $n > 1$, $M_{\text{drop}}(t) \equiv M_0$ and $M_{\text{ring}}(t) \equiv 0$ in this limit.

5.8 Particle paths

So far in this Chapter we have considered the transport of particles within the droplet for situations in which the scaled particle Péclet number $\mathrm{Pe}_{\mathrm{p}}^*$ satisfies (5.30), correspond-

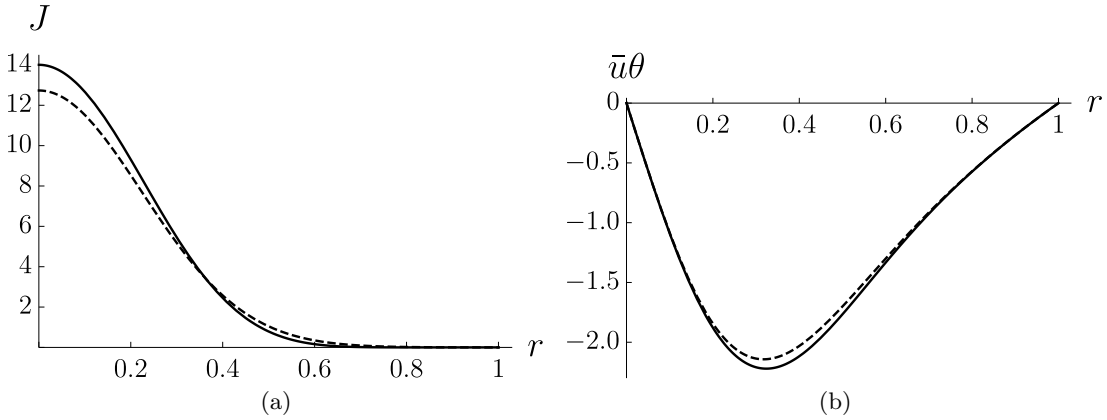

Figure 5.16: Plots of (a) J and (b) $\bar{u}\theta$ for $n = 10$ comparing the exact expressions from (5.52) and (5.65) (solid lines) with the leading-order asymptotic expressions in the limit $n \to \infty$ from (5.92) and (5.93) (dashed lines).

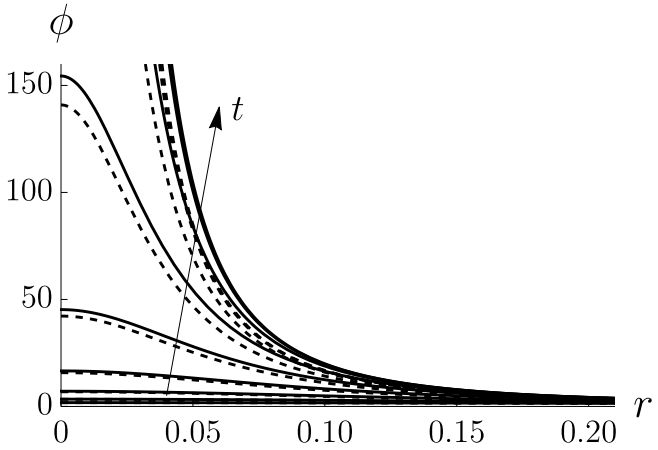

Figure 5.17: Plot of ϕ for $n = 10$, comparing the exact expression from (5.70) (solid lines) with the leading-order asymptotic approximation in the limit $n \to \infty$ from (5.94) (dashed lines) for $t = (0, 1/10, \ldots, 9/10) \times t_{\text{lifetime}}$. The arrow indicates the direction of increasing t.

ing to a particle Péclet number $\mathrm{Pe_p}$ that is large (but not too large), *i.e.* $1 \ll \mathrm{Pe_p} \ll \hat{\theta}_0^{-2}$. In this situation the vertical and radial transport of particles within the droplet are dominated by diffusion and advection, respectively, as described in Subsection 5.5.1. In this Section we will consider situations in which both the radial and vertical diffusion of particles within the droplet are slow relative to evaporation. More specifically, we consider situations in which the scaled particle Péclet number satisfies

$$\mathrm{Pe_p^*} \gg 1, \tag{5.95}$$

corresponding to a sufficiently large particle Péclet number, *i.e.* $\mathrm{Pe_p} \gg \hat{\theta}_0^{-2}$.

For $\mathrm{Pe_p^*} \gg 1$ and $\mathrm{Pe_p} \gg \hat{\theta}_0^{-2}$ the transport of particles within the droplet is governed purely by advection and we investigate the transport of particles via the paths of the particles. In particular, the path $(r, z) = (r(t), z(t))$ taken by a particle as it is advected by the flow within the droplet is governed by the ordinary differential equations (see, for example, Kang *et al.* [132]):

$$\frac{\mathrm{d}r}{\mathrm{d}t} = u, \quad \frac{\mathrm{d}z}{\mathrm{d}t} = w \quad \text{for} \quad 0 \leq z < h, \tag{5.96}$$

for $0 < r < 1$, subject to initial conditions of the form $(r(0), z(0)) = (r_0, z_0)$, where (r_0, z_0) is the initial position of a particle, and where u and w are given in (5.24). Motivated by experimental observations for the motion of spherical particles (see, for example, Yunker *et al.* [316]), we make the natural modelling assumption that if a particle reaches the free surface of the droplet, then it thereafter stays on (but moves along) the free surface, according to

$$\frac{\mathrm{d}r}{\mathrm{d}t} = u|_{z=h}, \quad \frac{\mathrm{d}z}{\mathrm{d}t} = (w - J)|_{z=h} = \frac{\partial h}{\partial t} + u|_{z=h}\frac{\partial h}{\partial r} \quad \text{on} \quad z = h, \tag{5.97}$$

without disturbing the shape of the droplet or the flow within. We shall hereafter refer to a particle reaching the free surface of the droplet as free-surface capture.

For the one-parameter family of spatially-varying local evaporative fluxes given by (5.52), the particle paths satisfy the governing equations (5.96), and (5.97) if the particle

reaches the free surface, where u and w are given by (5.62) and (5.63), respectively. The nature of the solutions for u and w means that the governing equations for the particle paths are coupled non-linear differential equations that must, in general, be solved numerically for all $n \neq 1$.

For the special case $n = 1$ there is no flow within the droplet, *i.e.* $u \equiv w \equiv 0$, and so particles remain at their initial positions (r_0, z_0). However, as the droplet evaporates the free surface moves downward, and a particle initially at $r = r_0$ and $z = z_0$ is captured by the free surface at time $t = t_{\text{capture}}$ given by

$$t_{\text{capture}} = \frac{\pi\left(1 - r_0^2 - 2z_0\right)}{16(1 - r_0^2)}. \tag{5.98}$$

Thereafter the particle moves vertically downwards on the descending free surface (*i.e.* with no lateral motion), and is deposited onto the substrate at the end of the evaporation at $r = r_0$ and $z = 0$. Therefore, as a consequence of the spatially-uniform initial concentration of particles within the paraboloidal droplet, the particles form a paraboloidal deposit at $t = t_{\text{lifetime}}$.

For the general case $-1 < n < 1$ and $n > 1$ the governing equations (5.96) and (5.97) were solved numerically. Figure 5.18 shows the path taken by a representative particle that starts at the initial position $(r_0, z_0) = (3/10, 3/10)$ for a range of values of $n > -1$, and Figure 5.19 shows an example of twelve representative particle paths for (a) $n = -1/2$ and (b) $n = 2$; these are typical values of n which represent the qualitatively different behaviour for (a) $-1 < n < 1$ and (b) $n > 1$. Figure 5.18 confirms that the particles end up at the contact line for $-1 < n < 1$ and at the centre of the droplet for $n > 1$. Figure 5.19 shows that all particles will be captured by the free surface of the droplet at time $t = t_{\text{capture}}$ (denoted by the squares) before they are deposited onto the substrate at time $t = t_{\text{deposit}}$, *i.e.* $t_{\text{capture}} < t_{\text{deposit}}$, for all $n > -1$. In particular, for $-1 < n < 1$ the particles are advected downward and outward by the flow, as illustrated in Figure 5.19(a); however, all of the particles are eventually captured by the descending free surface, and thereafter move downward and outward towards the contact line along the descending free surface. The same qualitative behaviour (*i.e.*

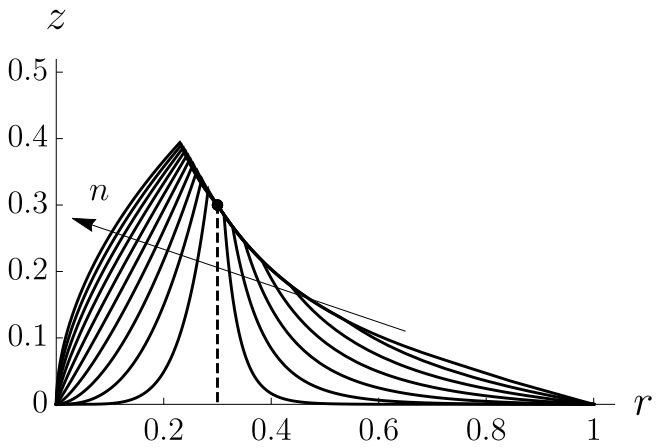

Figure 5.18: Paths taken by a representative particle that starts at the initial position $(r_0, z_0) = (3/10, 3/10)$ for $n = -3/4, -1/2, \ldots, 1, 3/2, \ldots, 6$. The vertical dashed line corresponds to the particle path for $n = 1$. The arrow indicates the direction of increasing n.

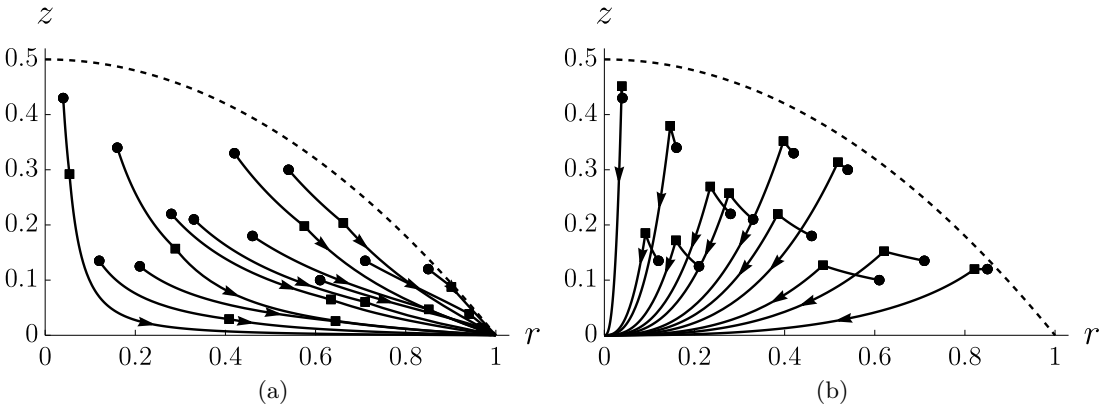

Figure 5.19: Twelve representative particle paths for (a) $n = -1/2$ and (b) $n = 2$. The dots and squares correspond to the initial position (r_0, z_0) of each particle at $t = 0$ and the time of free-surface capture at $t = t_{\text{capture}}$, respectively. The dashed lines correspond to the profile of the free surface of the droplet at $t = 0$.

all of the particles being captured by, and thereafter moving towards the contact line along, the descending free surface) is in agreement with the numerical study of non-thin droplets for the special case of diffusion-limited evaporation by Kang *et al.* [132]. In particular, Kang *et al.* [132] found that the cumulative number of particles being captured by the free surface is directly proportional to the volume lost from the droplet due to evaporation. The study also considered the concentration of particles within the bulk of the droplet and on the free surface of the droplet separately and found that the concentration of particles in the bulk of the droplet remains spatially-uniform and constant at its initial value, and that it is the flow at the free surface of the droplet that controls deposition. For $n > 1$, the particles are initially advected upward and inward by the flow, as illustrated in Figure 5.19(b). Analogously to the case $-1 < n < 1$, all of the particles are eventually captured by the descending free surface, and thereafter move downward and inward towards the centre of the droplet along the descending free surface. The particles are deposited onto the substrate at the end of evaporation at the centre of the droplet, *i.e.* $t_{\text{deposit}} = t_{\text{lifetime}}$.

5.9 Conclusions

In this Chapter we have studied the effect of spatial variation in the local evaporative flux on the deposition from a pinned particle-laden sessile droplet. In particular, we formulated and analysed a mathematical model describing the evolution of, flow within, and transport of particles within, a thin sessile droplet with a general steady local evaporative flux profile $J = J(r)$. Using this model we investigated the behaviour for a particular one-parameter family of spatially-varying local evaporative fluxes given by $J = 4(1+n)(1-r^2)^n/\pi$ and gave details of the qualitatively different behaviours depending upon the parameter n.

For the one-parameter family of spatially-varying local evaporative fluxes, the model describes how, as the droplet evaporates, the direction of the flow within the droplet, and hence the evolution of both the concentration of particles and the total mass of particles within the droplet, depend upon the parameter n, with a qualitative change in behaviour around the value $n = 1$. In particular, the model predicts that for $-1 < n <$

1 the evaporation induces a positive depth-averaged radial velocity $\bar{u}$ which advects particles towards the contact line of the droplet. The concentration of particles ϕ near the contact line therefore increases, and all of the particles are eventually transferred to the deposit ring at the contact line, *i.e.* $M_{\text{ring}}(t_{\text{lifetime}}) = M_0$. For the special case $n = 1$, there is no resultant flow within the droplet. Therefore, the concentration of particles ϕ remains spatially-uniform and increases with t, and all of the particles remain within the droplet where they are deposited at the end of evaporation, *i.e.* $M_{\text{ring}}(t_{\text{lifetime}}) = 0$ and $M_{\text{drop}}(t_{\text{lifetime}}) = M_0$. For $n > 1$ the evaporation induces a negative depth-averaged radial velocity $\bar{u}$ which advects particles towards the centre of the droplet. The concentration of particles ϕ near the centre of the droplet therefore increases, and all of the particles remain within the droplet where they are deposited at the end of evaporation, *i.e.* $M_{\text{ring}}(t_{\text{lifetime}}) = 0$ and $M_{\text{drop}}(t_{\text{lifetime}}) = M_0$. In particular, we have illustrated the sometimes overlooked result of Deegan *et al.* [64] that a singularity in the local evaporative flux at the contact line of the droplet is not required for a ring deposit to form. Specifically, the model predicts ring deposits even in the case of local evaporative fluxes that are zero at the contact line, *i.e.* for $0 < n < 1$. The asymptotic behaviour for the evaporation was also analysed for three particular limits, namely for $n \to 1^-$, $n \to 1^{\mp}$, and $n \to \infty$.

The particle paths within the droplet were determined numerically for the case when the transport of particles is governed purely by advection. It was found that all of the particles are eventually captured by, and thereafter move along, the descending free surface. In particular, when $n = 1$, the particles are motionless until some time when they are reached by the free surface, thereafter moving downwards to deposit onto the substrate, forming a paraboloidal deposit. In addition, for $-1 < n < 1$ and $n > 1$, particles move along the descending free surface towards the contact line to form a ring deposit and towards the centre of the droplet where they are then deposited, respectively.

Chapter 6

Conclusions and Future Work

6.1 Conclusions

In this thesis we have used a combination of analytical and numerical techniques to investigate the evolution of, and the deposition from, an evaporating sessile droplet.

In Chapters 1 and 2 we discussed relevant work by previous authors and formulated the diffusion-limited model of an evaporating sessile droplet, respectively.

In Chapter 3 we considered the evaporation of a thin droplet in a shallow axisymmetric well with profile $\hat{z} = \hat{H}(\hat{r}) = -\hat{H}_0(1-(\hat{r}/\hat{R}_0)^n)$ both before and after touchdown that accounts for the spatially non-uniform evaporation of the fluid, described physical experiments performed at Durham University using three cylindrical wells with different small aspect ratios, and validated the mathematical model by comparing these experimental results with the corresponding theoretical predictions for a cylindrical well (*i.e.* in the limit $n \to \infty$). We found that, depending on the shape of the well, touchdown can occur at the lip of the well for $0 < n < 2$, everywhere simultaneously for $n = 2$, or at the centre of the well for $n > 2$. We described the dependence of the predicted critical times on the shape of the well. In particular, we found that t_{flat} is independent of H_0 and n, $t_{\text{touchdown}}$ increases linearly with both H_0 and with n for $0 \leq n \leq 2$, but is independent of n for $n > 2$, and that t_{lifetime} also increases linearly with H_0 but non-linearly with n. We found good agreement between the experimental results and the corresponding theoretical predictions for the evolution, and hence the

critical times, of methyl benzoate droplets evaporating in cylindrical wells.

In Chapter 4 we considered the evaporation of thin sessile and pendant droplets under the effect of gravity evaporating in the CR, CA, SS, and SJ modes of evaporation. The mathematical model describes how the shape of a droplet depends on its volume and whether it is sessile or pendant. In particular, we found that for a sessile droplet the height at the middle of a droplet h_{m} is non-monotonic in V, with $R \to \infty$ and $h_{\mathrm{m}} \to 1$ as $V \to \infty$, whereas for a pendant droplet, h_{m} increases monotonically in V, with $h_{\mathrm{m}} \to \infty$ and $R \to R_{\max}$ as $V \to \infty$. Additionally, the mathematical model confirms that the contact radius R of a sessile droplet is always larger than that for a pendant droplet of the same volume and, as a consequence of this, so is the total evaporative flux from the droplet, namely $F = 4R$. Therefore, we found that the predicted lifetimes of the droplets in each mode of evaporation, as well as the critical times t^* and t_n, are always greater for a pendant droplet than those for a zero gravity droplet of the same initial volume and critical angles, which are in turn greater than those for a sessile droplet. The solutions for the evolutions, and hence the lifetimes, of evaporating sessile and pendant droplets were also analysed for the limiting cases of initially small ($V_0 \to 0$) and initially large ($V_0 \to \infty$) droplets. In particular, in the limit of initially small droplets, the leading-order behaviour corresponds to the solution for a zero-gravity droplet and is therefore independent of the orientation of the droplet, whereas in the limit of initially large droplets, the behaviour depends on whether the droplet is sessile or pendant.

In Chapter 5 we considered the effect of spatial variation in the local evaporative flux on the deposition of particles from an evaporating sessile droplet. We investigated the evaporation for a particular one-parameter family of spatially-varying local evaporative fluxes given by $J = 4(1+n)(1-r^2)^n/\pi$ and gave details of the qualitatively different behaviours depending upon the parameter n. In particular, the mathematical model predicts that for $-1 < n < 1$ the evaporation induces a positive depth-averaged radial velocity $\bar{u}$ which advects particles towards the contact line of the droplet, and all of the particles are eventually transferred to the deposit ring at the contact line, *i.e.* $M_{\mathrm{ring}}(t_{\mathrm{lifetime}}) = M_0$. For the special case $n = 1$, there is no flow within the

droplet, all of the particles remain within the droplet throughout evaporation, and are deposited onto the substrate at the end of evaporation to form a paraboloidal deposit, *i.e.* $M_{\text{ring}}(t_{\text{lifetime}}) = 0$ and $M_{\text{drop}}(t_{\text{lifetime}}) = M_0$. For $n > 1$ the evaporation induces a negative depth-averaged radial velocity $\bar{u}$ which advects particles towards the centre of the droplet, all of the particles remain within the droplet throughout evaporation, and are deposited at the centre of the droplet at the end of evaporation, *i.e.* $M_{\text{ring}}(t_{\text{lifetime}}) = 0$ and $M_{\text{drop}}(t_{\text{lifetime}}) = M_0$. We illustrated the sometimes overlooked result of Deegan *et al.* [64] that a singularity in the local evaporative flux at the contact line of the droplet is not required for a deposit ring to form at the contact line. Specifically, the mathematical model predicts ring deposits for local evaporative fluxes that are singular ($-1 < n < 0$), finite and non-zero ($n = 0$), and zero ($0 < n < 1$) at the contact line. The asymptotic behaviour for the evaporation was also analysed for three particular limiting cases, namely for $n \to -1^+$, $n \to 1^{\pm}$, and $n \to \infty$. In addition, the particle paths within the droplet were determined numerically for the case when the transport of particles is governed purely by advection. We found that all of the particles are eventually captured by, and thereafter move along, the descending free surface.

6.2 Future work

The work described in this thesis suggests many possible directions for future study. We will first briefly outline various possible extensions to the mathematical models presented in this thesis and then describe three specific avenues for future work in detail, namely, the evolution of, and the deposition from, an evaporating annular droplet, the effect of gravity on the flow within, and the deposition from, an evaporating droplet, and the effect of particle interactions on the deposition from an evaporating sessile droplet.

It should, of course, first be emphasised that the mathematical models for the evaporation of a droplet presented in this thesis are based on various assumptions which are particularly amenable to theoretical analysis and that future work could focus on relaxing some of these assumptions. For example, although many practical

situations involve thin droplets ($\hat{\theta}_0 \ll 1$) with strong surface tension ($\mathrm{Ca}^* \ll 1$), there are certainly applications in which the evaporation of droplets on hydrophobic and/or superhydrophobic substrates with $\hat{\theta}_0 = O(1)$ and the evaporation of more volatile fluids with $\mathrm{Ca}^* = O(1)$ are of interest, and capturing such behaviours will require generalisations of the mathematical models presented in this thesis. In addition, the mathematical model for the transport of particles presented in Chapter 5 is not able to quantify the shape of the final deposit, and to do so would require an extension to the present model by, for example, accounting for particle volume through particle packing or gelation (see, for example, Popov [220] and Zheng [320]).

Moreover, in industrial applications a variety of additional physical effects which are not included in the present mathematical models may be important. For example, as discussed in Chapter 1, in situations in which significant evaporative cooling occurs, temperature-dependent surface tension (see, for example, Hu and Larson [117] and Ristenpart *et al.* [227]) and/or temperature-dependent saturation concentration (see, for example, Dunn *et al.* [72], Schofield *et al.* [238], and Sefiane *et al.* [243]) effects can be important, while in other situations buoyancy effects within the atmosphere (see, for example, Carle *et al.* [37], Dunn *et al.* [72], and Shahidzadeh-Bonn *et al.* [247]) may play an important role.

6.2.1 The evolution of and the deposition from an evaporating annular droplet

For obvious reasons, the vast majority of previous work on evaporating droplets has focussed on the case of an axisymmetric droplet with a single circular contact line. However, as we discussed in Chapter 3, an annular droplet, *i.e.* an axisymmetric droplet with two circular contact lines, arises in the evaporation of a droplet in a well, which is of relevance to the manufacture of OLED displays. The evaporation of an annular droplet is of scientific interest in its own right, and arises in a number of other industrial contexts, such as in microfluidics, lab-on-chip devices, and electric conductors (see, for example, Chen and Hung [44], Jokinen *et al.* [124], and Schäfle *et al.* [237]), as well as in the study of bacterial colonies (see, for example, Si *et al.* [258]). Therefore, one

direction for future work is to investigate the evolution of, and the deposition from, an evaporating annular droplet.

We have carried out preliminary work in this direction using the numerical results for the spatially non-uniform local evaporative flux J obtained in Chapter 3 to describe the evolution of a thin annular droplet undergoing diffusion-limited evaporation in which both contact lines are pinned, as well as the masses of the deposit rings that form at both the inner and outer contact lines. The next step would be to explore the evolution of, flow within, and transport of particles within, an annular droplet for other modes of evaporation. We note that this inevitably becomes more complicated than for the typical case of an axisymmetric droplet with one circular contact line since there are two contact lines and two contact angles and hence more possible modes of evaporation.

6.2.2 The effect of gravity on the flow within and deposition from an evaporating droplet

In Chapter 4 we described the effect of gravity on the shape, evolution, and lifetime of an evaporating droplet, and so a natural direction for future work is to extend this study to investigate the flow within, and the deposition from, an evaporating droplet under the effect of gravity.

We have carried out preliminary work in this direction, obtaining analytical solutions for the depth-averaged radial velocity $\bar{u}$ and numerical solutions for the evolution of the mass of particles within thin sessile and pendant droplets undergoing diffusion-limited evaporation in the CR mode, as described by the evaporative model in Chapter 4. Figure 6.1 shows the behaviour of $\bar{u}\theta$ as a function of r/R_0 for a thin sessile, zero gravity, and pendant droplet for an illustrative value of $V_0 = 100$. In particular, $\bar{u}$ is quantitatively different, but qualitatively similar, for sessile and pendant droplets under the effect of gravity, in agreement with the results of Kolegov and Lobanov [143] for a sessile droplet evaporating with a modified diffusion-limited evaporative flux.

The next steps would be to explore the behaviour of the flow and the transport of particles within sessile and pendant droplets evaporating in the CR, CA, SS, and

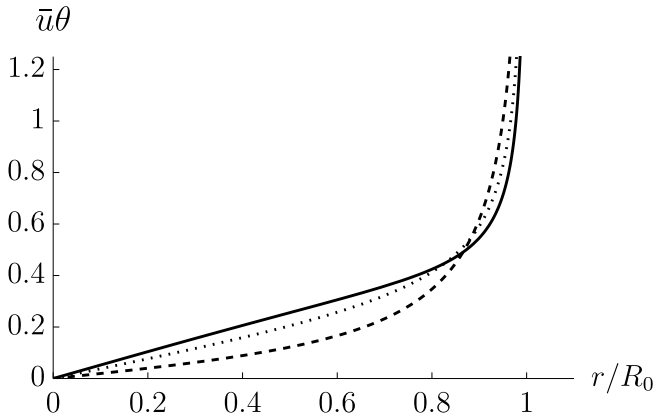

Figure 6.1: Plot of $\bar{u}\theta$ as a function of r/R_0 for a thin sessile (solid line), zero gravity (dotted line), and pendant (dashed line) droplet undergoing diffusion-limited evaporation in the CR mode for $V_0 = 100$.

SJ modes. However, we note that, in general, modelling the deposition from a droplet undergoing diffusion-limited evaporation in the CA, SS, and SJ modes is typically more complex than that for a droplet evaporating in the CR mode, even for the case of small droplets. Therefore, future work could investigate the deposition from a small droplet undergoing diffusion-limited evaporation in the different modes, or use a simpler model for J, such as a spatially-uniform evaporative flux, to gain insight on the deposition from a droplet under the effect of gravity.

6.2.3 The effect of particle interactions on the deposition from an evaporating droplet

Another direction for future work is to extend the mathematical model for the transport of particles within an evaporating droplet described in Chapter 5 to include one or more kinds of particle interactions. As discussed in Chapter 1, particle interactions, such as particle–free surface, particle–particle, and particle–substrate interactions, can play a key role in the deposition from an evaporating droplet and are often promoted to control the shape of the final deposit.

We have carried out preliminary work in this direction, investigating the effect of particle–substrate adsorption on the deposition from a thin sessile droplet evaporating in the CR mode with a general local evaporative flux profile $J = J(r)$. Figure 6.2

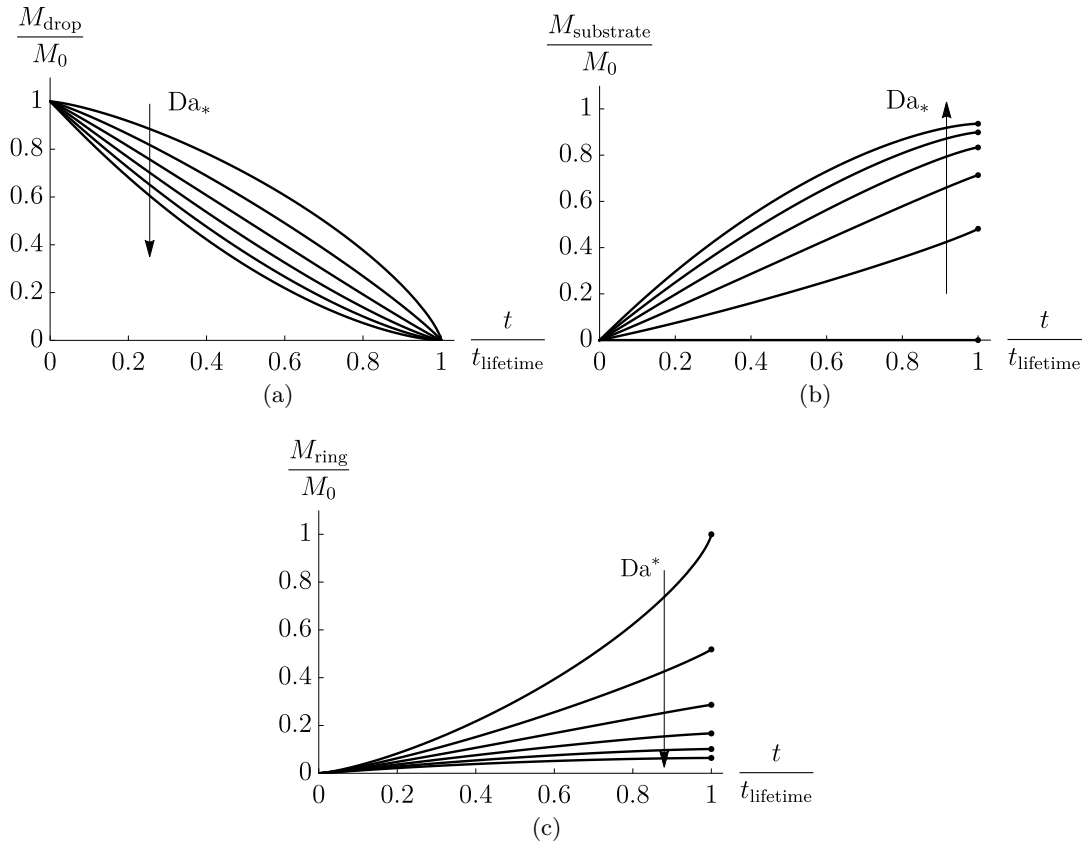

Figure 6.2: Evolution of (a) M_{drop}/M_0, (b) $M_{\text{substrate}}/M_0$, and (c) M_{ring}/M_0 as functions of t/t_{lifetime} for a thin sessile droplet undergoing diffusion-limited evaporation in the CR mode for $\text{Da}^* = 0, 0.4, \ldots, 2$.

shows an example of the evolutions of M_{drop}/M_0, the (scaled) mass adsorbed onto the substrate $M_{\text{substrate}}/M_0$, and M_{ring}/M_0 as functions of t/t_{lifetime} for a droplet undergoing diffusion-limited evaporation with different values of the (scaled) Damköhler number Da^*, which is a nondimensional measure of the particle–substrate adsorption rate. Unlike the mathematical model for the transport of particles presented in Chapter 5, in the presence of particle–substrate adsorption particles may be deposited onto the substrate throughout the evaporation. In particular, for diffusion-limited evaporation, for larger values of Da^*, more particles are deposited within the footprint of the droplet throughout evaporation, and fewer particles are transferred to the deposit ring at the contact line at the end of evaporation. Since, in this mathematical model, particles may be deposited onto the substrate throughout the evaporation, future work could

investigate the effect of the time dependence in the local evaporative flux profile on the deposition from an evaporating droplet. For example, the mathematical model provides the potential to study the effect of intermittent masking above the droplet, *e.g.* $J = J(r; n(t))$.

In conclusion, we believe that the results described in this thesis make a worthwhile contribution to the study of evaporating sessile droplets; however, as indicated here, there are several open questions and many interesting aspects of this problem which future work should seek to address.

Appendix A

The Deposition from an Evaporating Droplet: A Separable Time-Dependent Local Evaporative Flux

The purpose of this Appendix is to demonstrate that the analysis described in Sections 5.2–5.5 in Chapter 5 for the evolution of, flow within, and transport of particles within, a thin pinned sessile evaporating droplet for the case of a purely r-dependent evaporative flux $J = J(r)$ may be generalised to a separable time-dependent evaporative flux $J = J(r,t) = f(r)g(t)$, where f and g are prescribed functions of r and t respectively. In particular, we consider the same situation as that described in Sections 5.2–5.5 in Chapter 5, except that the local evaporative flux may be decomposed as $J = f(r)g(t)$.

The indefinite radial integral of the local evaporative flux, $I = I(r,t)$, is defined as

$$I = \mathcal{F}(r)g(t), \quad \text{where} \quad \mathcal{F}(r) = \int_0^r f(\tilde{r})\,\tilde{r}\,\mathrm{d}\tilde{r}. \tag{A.1}$$

The global mass-conservation condition may therefore be written as

$$\frac{\mathrm{d}V}{\mathrm{d}t} = -2\pi\mathcal{F}(1)g(t). \tag{A.2}$$

The evolution of the droplet is then given by

$$h = \theta\eta, \quad V = \frac{\pi}{4}\left(1 - \frac{K(t)}{H(1)}\right), \quad \theta = 1 - \frac{K(t)}{H(1)}, \tag{A.3}$$

where $K = K(t)$ is the indefinite time integral of the radially-integrated flux, namely

$$K(t) = \mathcal{F}(1)\mathcal{G}(t), \quad \mathcal{G}(t) = \int_0^t g(\tilde{t})\,\mathrm{d}\tilde{t}. \tag{A.4}$$

Unlike in the case in which J is independent of t, the evolutions of the h, V, and θ are no longer linear in t.

The local radial fluid flux $Q = Q(r,t)$ is found by integrating the kinematic condition (5.19) with respect to r and rearranging, which gives:

$$Q = q(r)g(t), \quad q(r) = \frac{\mathcal{F}(1)H(r) - H(1)\mathcal{F}(r)}{rH(1)}. \tag{A.5}$$

The expression for Q in (A.5) is separable in r and t and differs from the corresponding expression in the case when $J = J(r) = f(r)$ from (5.22) through a multiplying factor of $g(t)$.

As in Chapter 5, for a given local evaporative flux J, the evolution of the droplet may be calculated from (A.3). Then, the solution for Q is given by (A.5), the solution for $p^{(1)}$ is obtained by integrating (5.25), and u and w are given by (5.24).

The leading-order concentration of particles $\phi = \phi(r,t)$ satisfies (5.38), which may be solved via the characteristic equations (5.39). Using the expressions for h and $\mathrm{d}\theta/\mathrm{d}t$ given by (5.6) and (A.3), respectively, the characteristic equations can be expressed as

$$\frac{\mathrm{d}r}{\mathrm{d}\theta} = \frac{\mathrm{d}r/\mathrm{d}t}{\mathrm{d}\theta/\mathrm{d}t} = -\frac{H(1)q(r)}{\theta\mathcal{F}(1)\eta(r)}, \quad \frac{\mathrm{d}\phi}{\mathrm{d}r} = \frac{\mathrm{d}\phi/\mathrm{d}t}{\mathrm{d}r/\mathrm{d}t} = \frac{f(r)\phi}{q(r)}. \tag{A.6}$$

Integration of (A.6) yields the implicit solution

$$\log\theta = -\int_{r_0}^{r} \frac{\mathcal{F}(1)\eta(\tilde{r})}{H(1)q(\tilde{r})}\,\mathrm{d}\tilde{r}, \qquad \log\frac{\phi}{\phi_0} = \int_{r_0}^{r} \frac{f(\tilde{r})}{q(\tilde{r})}\,\mathrm{d}\tilde{r}, \tag{A.7}$$

where, as in Chapter 5, $r_0 = r_0(r,t)$ denotes the initial radial position of a particle at

$t = 0$ that has subsequently travelled to position r at time t, determined by solving (A.7a). As in Chapter 5, we simplify the solution for ϕ by adding the two equations in (A.7), and recalling that Q may be expressed in the form (A.5), to yield

$$\begin{aligned}\log\theta + \log\frac{\phi}{\phi_0} &= -\int_{r_0}^{r} \frac{\mathcal{F}(1)\eta(\hat{r}) - H(1)f(\hat{r})}{H(1)q(\hat{r})}\,\mathrm{d}\hat{r} \\ &= -\int_{r_0}^{r} \frac{1}{\hat{r}q(\hat{r})}\frac{\mathrm{d}\big(\hat{r}q(\hat{r})\big)}{\mathrm{d}\hat{r}}\,\mathrm{d}\hat{r} \\ &= \log\frac{r_0 q(r_0)}{rq(r)}. \end{aligned} \tag{A.8}$$

Hence the solution of the characteristic equations for the concentration of particles ϕ from (5.38) may be written in the form

$$\int_{r_0}^{r} \frac{F(1)\eta(\hat{r})}{H(1)q(\tilde{r})}\,\mathrm{d}\tilde{r} = -\log\theta, \qquad \frac{\phi}{\phi_0} = \frac{r_0 q(r_0)}{\theta r q(r)}, \tag{A.9}$$

where $\theta(t)$ is given by (A.3) and $q(r)$ is given by (A.5). Surprisingly, the function $g(t)$ does not appear in the final solution for ϕ. In addition, the solution for ϕ when $J = J(r,t) = f(r)g(t)$ differs from the solution when $J = J(r) = f(r)$ only through the time-dependence of θ which will in turn affect the solution for $r_0 = r_0(r,t)$. Therefore, the solution for ϕ for a separably time-dependent evaporative flux has similar behaviour to the solution found in Chapter 5 for a local evaporative flux that is solely a function of r, given that they have the same r-dependence.

The evolution of the mass of particles in the bulk of the droplet M_{drop} and in the deposit ring M_{ring} are then given by (5.45) and (5.48), respectively.

The solutions given in this Appendix for the evolution of the droplet, Q, and ϕ are consistent with those given in Chapter 5 for the case when $J = J(r) = f(r)$ for $g(t) \equiv 1$.

Bibliography

[1] E. Adachi, A. S. Dimitrov, and K. Nagayama. Stripe patterns formed on a glass surface during droplet evaporation. *Langmuir*, 11(4):1057–1060, 1995. doi: 10.1021/la00004a003.

[2] H. Ahn and G. Son. Numerical simulation of liquid film evaporation in circular and square microcavities. *Numerical Heat Transfer, Part A: Applications*, 67(9):934–951, 2015. doi: 10.1080/10407782.2014.949153.

[3] M. Ait Saada, S. Chikh, and L. Tadrist. Evaporation of a sessile drop with pinned or receding contact line on a substrate with different thermophysical properties. *International Journal of Heat and Mass Transfer*, 58(1-2):197–208, 2013. doi: 10.1016/j.ijheatmasstransfer.2012.11.026.

[4] V. S. Ajaev. Viscous flow of a volatile liquid on an inclined heated surface. *Journal of Colloid and Interface Science*, 280(1):165–173, 2004. doi: 10.1016/j.jcis.2004.07.026.

[5] V. S. Ajaev. Spreading of thin volatile liquid droplets on uniformly heated surfaces. *Journal of Fluid Mechanics*, 528:279–296, 2005. doi: 10.1017/S0022112005003320.

[6] K. N. Al-Milaji and H. Zhao. New perspective of mitigating the coffee-ring effect: Interfacial assembly. *The Journal of Physical Chemistry C*, 123(19):12029–12041, 2019. doi: 10.1021/acs.jpcc.9b00797.

[7] N. Anantharaju, M. Panchagnula, and S. Neti. Evaporating drops on patterned surfaces: Transition from pinned to moving triple line. *Journal of Colloid and Interface Science*, 337(1):176–182, 2009. doi: 10.1016/j.jcis.2009.04.095.

[8] D. M. Anderson and S. H. Davis. The spreading of volatile liquid droplets on heated surfaces. *Physics of Fluids*, 7(2):248–265, 1995. doi: 10.1063/1.868623.

[9] M. Anyfantakis and D. Baigl. Manipulating the coffee-ring effect: Interactions at work. *ChemPhysChem*, 16(13):2726–2734, 2015. doi: 10.1002/cphc.201500410.

[10] M. Anyfantakis, D. Baigl, and B. P. Binks. Evaporation of drops containing silica nanoparticles of varying hydrophobicities: Exploiting particle–particle interactions for additive-free tunable deposit morphology. *Langmuir*, 33(20):5025–5036, 2017. doi: 10.1021/acs.langmuir.7b00807.

[11] M. Anyfantakis, Z. Geng, M. Morel, S. Rudiuk, and D. Baigl. Modulation of the coffee-ring effect in particle/surfactant mixtures: the importance of particle–interface interactions. *Langmuir*, 31(14):4113–4120, 2015. doi: 10.1021/acs.langmuir.5b00453.

[12] S. Armstrong, G. McHale, R. Ledesma-Aguilar, and G. G. Wells. Pinning-free evaporation of sessile droplets of water from solid surfaces. *Langmuir*, 35(8):2989–2996, 2019. doi: 10.1021/acs.langmuir.8b03849.

[13] S. Armstrong, G. McHale, R. Ledesma-Aguilar, and G. G. Wells. Evaporation and electrowetting of sessile droplets on slippery liquid-like surfaces and slippery liquid-infused porous surfaces (SLIPS). *Langmuir*, 36(38):11332–11340, 2020. doi: 10.1021/acs.langmuir.0c02020.

[14] A. Askounis, D. Orejon, V. Koutsos, K. Sefiane, and M. E. R. Shanahan. Nanoparticle deposits near the contact line of pinned volatile droplets: size and shape revealed by atomic force microscopy. *Soft Matter*, 7(9):4152–4155, 2011. doi: 10.1039/C1SM05241A.

[15] A. Askounis, K. Sefiane, V. Koutsos, and M. E. R. Shanahan. Structural transitions in a ring stain created at the contact line of evaporating nanosuspension sessile drops. *Physical Review E*, 87(1):012301, 2013. doi: 10.1103/PhysRevE.87.012301.

[16] A. Askounis, K. Sefiane, V. Koutsos, and M. E. R. Shanahan. The effect of evaporation kinetics on nanoparticle structuring within contact line deposits of volatile drops. *Colloids and Surfaces A: Physicochemical and Engineering Aspects*, 441:855–866, 2014. doi: 10.1016/j.colsurfa.2012.10.017.

[17] P. Aussillous and D. Quéré. Properties of liquid marbles. *Proceedings of the Royal Society A: Mathematical, Physical and Engineering Sciences*, 462(2067):973–999, 2006. doi: 10.1098/rspa.2005.1581.

[18] L. Bansal, P. Seth, B. Murugappan, and S. Basu. Suppression of coffee ring: (Particle) size matters. *Applied Physics Letters*, 112(21):211605, 2018. doi: 10.1063/1.5034119.

[19] L. Yu. Barash, T. P. Bigioni, V. M. Vinokur, and L. N. Shchur. Evaporation and fluid dynamics of a sessile drop of capillary size. *Physical Review E*, 79(4):046301, 2009. doi: 10.1103/PhysRevE.79.046301.

[20] M. V. Bartashevich, V. V. Kuznetsov, and O. A. Kabov. Gravity effect on the axisymmetric drop spreading. *Microgravity Science and Technology*, 22(1):107–114, 2010. doi: 10.1007/s12217-009-9153-5.

[21] F. Bashforth and J. C. Adams. *An attempt to test the theories of capillary action by comparing the theoretical and measured forms of drops of fluid.* University Press, Cambridge, 1883.

[22] G. Berteloot, A. Hoang, A. Daerr, H. P. Kavehpour, F. Lequeux, and L. Limat. Evaporation of a sessile droplet: Inside the coffee stain. *Journal of Colloid and Interface Science*, 370(1):155–161, 2012. doi: 10.1016/j.jcis.2011.10.053.

[23] R. Bhardwaj, X. Fang, P. Somasundaran, and D. Attinger. Self-assembly of colloidal particles from evaporating droplets: role of DLVO interactions and proposition of a phase diagram. *Langmuir*, 26(11):7833–7842, 2010. doi: 10.1021/la9047227.

[24] K. S. Birdi, D. T. Vu, and A. Winter. A study of the evaporation rates of small water drops placed on a solid surface. *The Journal of Physical Chemistry*, 93(9):3702–3703, 1989. doi: 10.1021/j100346a065.

[25] S. Biswas, S. Gawande, V. Bromberg, and Y. Sun. Effects of particle size and substrate surface properties on deposition dynamics of inkjet-printed colloidal drops for printable photovoltaics fabrication. *Journal of Solar Energy Engineering*, 132(2):021010, 2010. doi: 10.1115/1.4001470.

[26] H. Bodiguel, F. Doumenc, and B. Guerrier. Stick-slip patterning at low capillary numbers for an evaporating colloidal suspension. *Langmuir*, 26(13):10758–10763, 2010. doi: 10.1021/la100547j.

[27] E. Bonaccurso, H.-J. Butt, B. Hankeln, B. Niesenhaus, and K. Graf. Fabrication of microvessels and microlenses from polymers by solvent droplets. *Applied Physics Letters*, 86(12):124101, 2005. doi: 10.1063/1.1886263.

[28] E. Bormashenko, A. Musin, and M. Zinigrad. Evaporation of droplets on strongly and weakly pinning surfaces and dynamics of the triple line. *Colloids and Surfaces A: Physicochemical and Engineering Aspects*, 385(1-3):235–240, 2011. doi: 10.1016/j.colsurfa.2011.06.016.

[29] W. Bou Zeid and D. Brutin. Influence of relative humidity on spreading, pattern formation and adhesion of a drying drop of whole blood. *Colloids and Surfaces A: Physicochemical and Engineering Aspects*, 430:1–7, 2013. doi: 10.1016/j.colsurfa.2013.03.019.

[30] E. A. Boucher and M. J. B. Evans. Pendent drop profiles and related capillary phenomena. *Proceedings of the Royal Society of London. A. Mathematical and Physical Sciences*, 346(1646):349–374, 1975. doi: 10.1098/rspa.1975.0180.

[31] E. A. Boucher, M. J. B. Evans, and H. J. Kent. Capillary phenomena. II. Equilibrium and stability of rotationally symmetric fluid bodies. *Proceedings of the Royal Society of London. A. Mathematical and Physical Sciences*, 349(1656):81–100, 1976. doi: 10.1098/rspa.1976.0061.

[32] F. Boulogne, F. Ingremeau, and H. A. Stone. Coffee-stain growth dynamics on dry and wet surfaces. *Journal of Physics: Condensed Matter*, 29(7):074001, 2017. doi: 10.1088/1361-648x/aa5160.

[33] C. Bourgès-Monnier and M. E. R. Shanahan. Influence of evaporation on contact angle. *Langmuir*, 11(7):2820–2829, 1995. doi: 10.1021/la00007a076.

[34] F. Brochard-Wyart, H. Hervet, C. Redon, and F. Rondelez. Spreading of "heavy" droplets: I. Theory. *Journal of Colloid and Interface Science*, 142(2):518–527, 1991. doi: 10.1016/0021-9797(91)90082-J.

[35] D. Brutin and V. Starov. Recent advances in droplet wetting and evaporation. *Chemical Society Reviews*, 47(2):558–585, 2018. doi: 10.1039/C6CS00902F.

[36] J. P. Burelbach, S. G. Bankoff, and S. H. Davis. Nonlinear stability of evaporating/condensing liquid films. *Journal of Fluid Mechanics*, 195:463–494, 1988. doi: 10.1017/S0022112088002484.

[37] F. Carle, B. Sobac, and D. Brutin. Experimental evidence of the atmospheric convective transport contribution to sessile droplet evaporation. *Applied Physics Letters*, 102(6):061603, 2013. doi: 10.1063/1.4792058.

[38] H. S. Carslaw and J. C. Jaeger. The flow of heat in regions bounded by surfaces of the cylindrical coordinate system. In *Conduction of Heat in Solids*, pages 214–229. Clarendon Press, Oxford, 1959.

[39] P. Cavadini, J. Erz, D. Sachsenheimer, A. Kowalczyk, N. Willenbacher, P. Scharfer, and W. Schabel. Investigation of the flow field in thin polymer films due to inhomogeneous drying. *Journal of Coatings Technology and Research*, 12(5):921–926, 2015. doi: 10.1007/s11998-015-9725-9.

[40] A.-M. Cazabat and G. Guéna. Evaporation of macroscopic sessile droplets. *Soft Matter*, 6(12):2591–2612, 2010. doi: 10.1039/B924477H.

[41] V. Charitatos and S. Kumar. Droplet evaporation on soft solid substrates. *Soft Matter*, 17(41):9339–9352, 2021. doi: 10.1039/D1SM00828E.

[42] S. Chatterjee, M. Kumar, J. S. Murallidharan, and R. Bhardwaj. Evaporation of initially heated sessile droplets and the resultant dried colloidal deposits on substrates held at ambient temperature. *Langmuir*, 36(29):8407–8421, 2020. doi: 10.1021/acs.langmuir.0c00756.

[43] C.-T. Chen, C.-C. Chieng, and F.-G. Tseng. Uniform solute deposition of evaporable droplet in nanoliter wells. *Journal of Microelectromechanical Systems*, 16(5):1209–1218, 2007. doi: 10.1109/JMEMS.2007.904327.

[44] C.-T. Chen and T.-Y. Hung. Morphology and deposit of picoliter droplet tracks generated by inkjet printing. *Journal of Micromechanics and Microengineering*, 26(11):115005, 2016. doi: 10.1088/0960-1317/26/11/115005.

[45] C.-T. Chen, F.-G. Tseng, and C.-C. Chieng. Evaporation evolution of volatile liquid droplets in nanoliter wells. *Sensors and Actuators A: Physical*, 130–131:12–19, 2006. doi: 10.1016/j.sna.2005.09.010.

[46] X. Chen, R. Ma, J. Li, C. Hao, W. Guo, B. L. Luk, S. C. Li, S. Yao, and Z. Wang. Evaporation of droplets on superhydrophobic surfaces: Surface roughness and small droplet size effects. *Physical Review Letters*, 109(11):116101, 2012. doi: 10.1103/PhysRevLett.109.116101.

[47] Y. Chen, F. Hong, and P. Cheng. Transient flow patterns in an evaporating sessile drop: A numerical study on the effect of volatility and contact angle. *International Communications in Heat and Mass Transfer*, 112:104493, 2020. doi: 10.1016/j.icheatmasstransfer.2020.104493.

[48] V. H. Chhasatia, A. S. Joshi, and Y. Sun. Effect of relative humidity on contact angle and particle deposition morphology of an evaporating colloidal drop. *Applied Physics Letters*, 97(23):231909, 2010. doi: 10.1063/1.3525167.

[49] V. H. Chhasatia and Y. Sun. Interaction of bi-dispersed particles with contact line in an evaporating colloidal drop. *Soft Matter*, 7(21):10135–10143, 2011. doi: 10.1039/C1SM06393F.

[50] H. Cho, S.-m. Kim, H. Liang, and S. Kim. Electric-potential-induced uniformity in graphene oxide deposition on porous alumina substrates. *Ceramics International*, 46(10):14828–14839, 2020. doi: 10.1016/j.ceramint.2020.03.008.

[51] J. C. Cooke. Triple integral equations. *The Quarterly Journal of Mechanics and Applied Mathematics*, 16(2):193–203, 1963. doi: 10.1093/qjmam/16.2.193.

[52] R. V. Craster and O. K. Matar. Dynamics and stability of thin liquid films. *Reviews of Modern Physics*, 81(3):1131–1198, 2009. doi: 10.1103/RevModPhys.81.1131.

[53] A. Crivoi and F. Duan. Elimination of the coffee-ring effect by promoting particle adsorption and long-range interaction. *Langmuir*, 29(39):12067–12074, 2013. doi: 10.1021/la402544x.

[54] A. Crivoi, X. Zhong, and F. Duan. Crossover from the coffee-ring effect to the uniform deposit caused by irreversible cluster-cluster aggregation. *Physical Review E*, 92(3):032302, 2015. doi: 10.1103/PhysRevE.92.032302.

[55] H.-M. D'Ambrosio, T. Colosimo, B. R. Duffy, S. K. Wilson, L. Yang, C. D. Bain, and D. E. Walker. Evaporation of a thin droplet in a shallow well: theory and experiment. *Journal of Fluid Mechanics*, 927:A43, 2021. doi: 10.1017/jfm.2021.772.

[56] S. Das, A. Dey, G. Reddy, and D. D. Sarma. Suppression of the coffee-ring effect and evaporation-driven disorder to order transition in colloidal droplets. *The Journal of Physical Chemistry Letters*, 8(19):4704–4709, 2017. doi: 10.1021/acs.jpclett.7b01814.

[57] S. Dash and S. V. Garimella. Droplet evaporation dynamics on a superhydrophobic surface with negligible hysteresis. *Langmuir*, 29(34):10785–10795, 2013. doi: 10.1021/la402784c.

[58] S. Dash, N. Kumari, and S. V. Garimella. Characterization of ultrahydrophobic hierarchical surfaces fabricated using a single-step fabrication methodology. *Journal of Micromechanics and Microengineering*, 21(10):105012, 2011. doi: 10.1088/0960-1317/21/10/105012.

[59] S. David, K. Sefiane, and L. Tadrist. Experimental investigation of the effect of thermal properties of the substrate in the wetting and evaporation of sessile drops. *Colloids and Surfaces A: Physicochemical and Engineering Aspects*, 298(1-2):108–114, 2007. doi: 10.1016/j.colsurfa.2006.12.018.

[60] P. G. de Gennes. Wetting: statics and dynamics. *Reviews of Modern Physics*, 57(3):827–863, 1985. doi: 10.1103/RevModPhys.57.827.

[61] D. Debuisson, A. Merlen, V. Senez, and S. Arscott. Stick–jump (SJ) evaporation of strongly pinned nanoliter volume sessile water droplets on quick drying, micropatterned surfaces. *Langmuir*, 32(11):2679–2686, 2016. doi: 10.1021/acs.langmuir.6b00070.

[62] R. D. Deegan. Pattern formation in drying drops. *Physical Review E*, 61(1):475–485, 2000. doi: 10.1103/PhysRevE.61.475.

[63] R. D. Deegan, O. Bakajin, T. F. Dupont, G. Huber, S. R. Nagel, and T. A. Witten. Capillary flow as the cause of ring stains from dried liquid drops. *Nature*, 389(6653):827–829, 1997. doi: 10.1038/39827.

[64] R. D. Deegan, O. Bakajin, T. F. Dupont, G. Huber, S. R. Nagel, and T. A. Witten. Contact line deposits in an evaporating drop. *Physical Review E*, 62(1):756–765, 2000. doi: 10.1103/PhysRevE.62.756.

[65] S. Devineau, M. Anyfantakis, L. Marichal, L. Kiger, M. Morel, S. Rudiuk, and D. Baigl. Protein adsorption and reorganization on nanoparticles probed

by the coffee-ring effect: application to single point mutation detection. *Journal of the American Chemical Society*, 138(36):11623–11632, 2016. doi: 10.1021/jacs.6b04833.

[66] N. R. Devlin, K. Loehr, and M. T. Harris. The importance of gravity in droplet evaporation: A comparison of pendant and sessile drop evaporation with particles. *AIChE Journal*, 62(3):947–955, 2016. doi: 10.1002/aic.15120.

[67] E. Dietrich, E. S. Kooij, X. Zhang, H. J. W. Zandvliet, and D. Lohse. Stick-jump mode in surface droplet dissolution. *Langmuir*, 31(16):4696–4703, 2015. doi: 10.1021/acs.langmuir.5b00653.

[68] J. Drelich, E. Chibowski, D. D. Meng, and K. Terpilowski. Hydrophilic and superhydrophilic surfaces and materials. *Soft Matter*, 7(21):9804–9828, 2011. doi: 10.1039/C1SM05849E.

[69] V. Dugas, J. Broutin, and E. Souteyrand. Droplet evaporation study applied to DNA chip manufacturing. *Langmuir*, 21(20):9130–9136, 2005. doi: 10.1021/la050764y.

[70] V. R. Dugyala and M. G. Basavaraj. Control over coffee-ring formation in evaporating liquid drops containing ellipsoids. *Langmuir*, 30(29):8680–8686, 2014. doi: 10.1021/la500803h.

[71] G. J. Dunn, S. K. Wilson, B. R. Duffy, S. David, and K. Sefiane. A mathematical model for the evaporation of a thin sessile liquid droplet: Comparison between experiment and theory. *Colloids and Surfaces A: Physicochemical and Engineering Aspects*, 323(1–3):50–55, 2008. doi: 10.1016/j.colsurfa.2007.09.031.

[72] G. J. Dunn, S. K. Wilson, B. R. Duffy, S. David, and K. Sefiane. The strong influence of substrate conductivity on droplet evaporation. *Journal of Fluid Mechanics*, 623:329–351, 2009. doi: 10.1017/S0022112008005004.

[73] G. J. Dunn, S. K. Wilson, B. R. Duffy, and K. Sefiane. Evaporation of a thin droplet on a thin substrate with a high thermal resistance. *Physics of Fluids*, 21(5):052101, 2009. doi: 10.1063/1.3121214.

[74] A. D. Eales, N. Dartnell, S. Goddard, and A. F. Routh. The impact of trough geometry on film shape. A theoretical study of droplets containing polymer, for P-OLED display applications. *Journal of Colloid and Interface Science*, 458:53–61, 2015. doi: 10.1016/j.jcis.2015.07.036.

[75] A. M. J. Edwards, P. S. Atkinson, C. S. Cheung, H. Liang, D. J. Fairhurst, and F. F. Ouali. Density-driven flows in evaporating binary liquid droplets. *Physical Review Letters*, 121(18):184501, 2018. doi: 10.1103/PhysRevLett.121.184501.

[76] B. El Fil, G. Kini, and S. Garimella. A review of dropwise condensation: Theory, modeling, experiments, and applications. *International Journal of Heat and Mass Transfer*, 160:120172, 2020. doi: 10.1016/j.ijheatmasstransfer.2020.120172.

[77] H. B. Eral, D. M. Augustine, M. H. G. Duits, and F. Mugele. Suppressing the coffee stain effect: how to control colloidal self-assembly in evaporating drops using electrowetting. *Soft Matter*, 7(10):4954–4958, 2011. doi: 10.1039/C1SM05183K.

[78] H. B. Eral, D. J. C. M. 't Mannetje, and J. M. Oh. Contact angle hysteresis: a review of fundamentals and applications. *Colloid and Polymer Science*, 291(2):247–260, 2013. doi: 10.1007/s00396-012-2796-6.

[79] H. Y. Erbil. Evaporation of pure liquid sessile and spherical suspended drops: A review. *Advances in Colloid and Interface Science*, 170(1-2):67–86, 2012. doi: 10.1016/j.cis.2011.12.006.

[80] H. Y. Erbil, G. McHale, and M. I. Newton. Drop evaporation on solid surfaces: constant contact angle mode. *Langmuir*, 18(7):2636–2641, 2002. doi: 10.1021/la011470p.

[81] H. Y. Erbil, G. McHale, S. M. Rowan, and M. I. Newton. Determination of the receding contact angle of sessile drops on polymer surfaces by evaporation. *Langmuir*, 15(21):7378–7385, 1999. doi: 10.1021/la9900831.

[82] L. Espín and S. Kumar. Sagging of evaporating droplets of colloidal suspensions on inclined substrates. *Langmuir*, 30(40):11966–11974, 2014. doi: 10.1021/la503229z.

[83] V. I. Fabrikant. Dirichlet problem for an annular disk. *Zeitschrift für angewandte Mathematik und Physik*, 44(2):333–347, 1993. doi: 10.1007/BF00914289.

[84] B. J. Fischer. Particle convection in an evaporating colloidal droplet. *Langmuir*, 18(1):60–67, 2002. doi: 10.1021/la015518a.

[85] S. Fordham. On the calculation of surface tension from measurements of pendant drops. *Proceedings of the Royal Society of London. Series A. Mathematical and Physical Sciences*, 194(1036):1–16, 1948. doi: 10.1098/rspa.1948.0063.

[86] L. Fraštia, A. J. Archer, and U. Thiele. Dynamical model for the formation of patterned deposits at receding contact lines. *Physical Review Letters*, 106(7):077801, 2011. doi: 10.1103/PhysRevLett.106.077801.

[87] L. Fraštia, A. J. Archer, and U. Thiele. Modelling the formation of structured deposits at receding contact lines of evaporating solutions and suspensions. *Soft Matter*, 8(44):11363–11386, 2012. doi: 10.1039/C2SM26574E.

[88] J. Freed-Brown. Evaporative deposition in receding drops. *Soft Matter*, 10(47):9506–9510, 2014. doi: 10.1039/C4SM02133A.

[89] R. French. AMOLED comparison. `https://imgur.com/a/Y7xJN`, accessed on 28th October 2021.

[90] J. Fukai, H. Ishizuka, Y. Sakai, M. Kaneda, M. Morita, and A. Takahara. Effects of droplet size and solute concentration on drying process

of polymer solution droplets deposited on homogeneous surfaces. *International Journal of Heat and Mass Transfer*, 49(19-20):3561–3567, 2006. doi: 10.1016/j.ijheatmasstransfer.2006.02.049.

[91] E. N. Fuller, P. D. Schettler, and J. C. Giddings. New method for prediction of binary gas-phase diffusion coefficients. *Industrial & Engineering Chemistry*, 58(5):18–27, 1966. doi: 10.1021/ie50677a007.

[92] A. Gao, J. Liu, L. Ye, C. Schönecker, M. Kappl, H.-J. Butt, and W. Steffen. Control of droplet evaporation on oil-coated surfaces for the synthesis of asymmetric supraparticles. *Langmuir*, 35(43):14042–14048, 2019. doi: 10.1021/acs.langmuir.9b02464.

[93] M. Gao, P. Kong, L.-X. Zhang, and J.-N. Liu. An experimental investigation of sessile droplets evaporation on hydrophilic and hydrophobic heating surface with constant heat flux. *International Communications in Heat and Mass Transfer*, 88:262–268, 2017. doi: 10.1016/j.icheatmasstransfer.2017.09.010.

[94] J. L. Garcia-Cordero and Z. H. Fan. Sessile droplets for chemical and biological assays. *Lab on a Chip*, 17(13):2150–2166, 2017. doi: 10.1039/C7LC00366H.

[95] E. Y. Gatapova, A. A. Semenov, D. V. Zaitsev, and O. A. Kabov. Evaporation of a sessile water drop on a heated surface with controlled wettability. *Colloids and Surfaces A: Physicochemical and Engineering Aspects*, 441:776–785, 2014. doi: 10.1016/j.colsurfa.2013.05.046.

[96] E. Y. Gatapova, A. M. Shonina, A. I. Safonov, V. S. Sulyaeva, and O. A. Kabov. Evaporation dynamics of a sessile droplet on glass surfaces with fluoropolymer coatings: focusing on the final stage of thin droplet evaporation. *Soft Matter*, 14(10):1811–1821, 2018. doi: 10.1039/C7SM02192E.

[97] J. Gathany. Sneeze. `https://commons.wikimedia.org/wiki/File:Sneeze.JPG`, accessed on 15th October 2021.

[98] H. Gelderblom, A. G. Marin, H. Nair, A. van Houselt, L. Lefferts, J. H. Snoeijer, and D. Lohse. How water droplets evaporate on a superhydrophobic substrate. *Physical Review E*, 83(2):026306, 2011. doi: 10.1103/PhysRevE.83.026306.

[99] A. Georgiadis, F. N. Muhamad, A. Utgenannt, and J. L. Keddie. Aesthetically textured, hard latex coatings by fast IR-assisted evaporative lithography. *Progress in Organic Coatings*, 76(12):1786–1791, 2013. doi: 10.1016/j.porgcoat.2013.05.017.

[100] A. Georgiadis, A. F. Routh, M. W. Murray, and J. L. Keddie. Bespoke periodic topography in hard polymer films by infrared radiation-assisted evaporative lithography. *Soft Matter*, 7(23):11098–11102, 2011. doi: 10.1039/C1SM06527K.

[101] F. Giorgiutti-Dauphiné and L. Pauchard. Drying drops. *European Physical Journal E*, 41(3):32, 2018. doi: 10.1140/epje/i2018-11639-2.

[102] K. Gleason and S. A. Putnam. Microdroplet evaporation with a forced pinned contact line. *Langmuir*, 30(34):10548–10555, 2014. doi: 10.1021/la501770g.

[103] J. H. Guan, G. G. Wells, B. Xu, G. McHale, D. Wood, J. Martin, and S. Stuart-Cole. Evaporation of sessile droplets on slippery liquid-infused porous surfaces (SLIPS). *Langmuir*, 31(43):11781–11789, 2015. doi: 10.1021/acs.langmuir.5b03240.

[104] J. Halls. Ink-jet printing of PLED displays. *Information Display*, 21(2):10–15, 2005.

[105] Y. Hamamoto, J. R. E. Christy, and K. Sefiane. Order-of-magnitude increase in flow velocity driven by mass conservation during the evaporation of sessile drops. *Physical Review E*, 83(5):051602, 2011. doi: 10.1103/PhysRevE.83.051602.

[106] M. A. Hampton, T. A. H. Nguyen, A. V. Nguyen, Z. P. Xu, L. Huang, and V. Rudolph. Influence of surface orientation on the organization of nanoparticles in drying nanofluid droplets. *Journal of Colloid and Interface Science*, 377(1):456–462, 2012. doi: 10.1016/j.jcis.2012.03.024.

[107] S. Hardt and G. McHale. Flow and drop transport along liquid-infused surfaces. *Annual Review of Fluid Mechanics*, 54:83–104, 2022. doi: 10.1146/annurev-fluid-030121-113156.

[108] D. J. Harris, J. C. Conrad, and J. A. Lewis. Evaporative lithographic patterning of binary colloidal films. *Philosophical Transactions of the Royal Society A: Mathematical, Physical and Engineering Sciences*, 367(1909):5157–5165, 2009. doi: 10.1098/rsta.2009.0157.

[109] D. J. Harris, H. Hu, J. C. Conrad, and J. A. Lewis. Patterning colloidal films via evaporative lithography. *Physical Review Letters*, 98(14):148301, 2007. doi: 10.1103/PhysRevLett.98.148301.

[110] D. J. Harris and J. A. Lewis. Marangoni effects on evaporative lithographic patterning of colloidal films. *Langmuir*, 24(8):3681–3685, 2008. doi: 10.1021/la8000637.

[111] B. Haut and P. Colinet. Surface-tension-driven instabilities of a pure liquid layer evaporating into an inert gas. *Journal of Colloid and Interface Science*, 285(1):296–305, 2005. doi: 10.1016/j.jcis.2004.07.041.

[112] M. He, D. Liao, and H. Qiu. Multicomponent droplet evaporation on chemical micro-patterned surfaces. *Scientific Reports*, 7(1):41897, 2017. doi: 10.1038/srep41897.

[113] O. Hegde, A. Chattopadhyay, and S. Basu. Universal spatio-topological control of crystallization in sessile droplets using non-intrusive vapor mediation. *Physics of Fluids*, 33(1):012101, 2021. doi: 10.1063/5.0037120.

[114] S. D. Hoath. *Fundamentals of Inkjet Printing: The Science of Inkjet and Droplets*. John Wiley & Sons, 2016.

[115] S. W. Hong, J. Xu, and Z. Lin. Template-assisted formation of gradient concentric gold rings. *Nano Letters*, 6(12):2949–2954, 2006. doi: 10.1021/nl0624061.

[116] H. Hu and R. G. Larson. Evaporation of a sessile droplet on a substrate. *The Journal of Physical Chemistry B*, 106(6):1334–1344, 2002. doi: 10.1021/jp0118322.

[117] H. Hu and R. G. Larson. Analysis of the effects of Marangoni stresses on the microflow in an evaporating sessile droplet. *Langmuir*, 21(9):3972–3980, 2005. doi: 10.1021/la0475270.

[118] H. Hu and R. G. Larson. Analysis of the microfluid flow in an evaporating sessile droplet. *Langmuir*, 21(9):3963–3971, 2005. doi: 10.1021/la047528s.

[119] H. Hu and R. G. Larson. Marangoni effect reverses coffee-ring depositions. *The Journal of Physical Chemistry B*, 110(14):7090–7094, 2006. doi: 10.1021/jp0609232.

[120] S. Hu, Y. Wang, X. Man, and M. Doi. Deposition patterns of two neighboring droplets: Onsager variational principle studies. *Langmuir*, 33(23):5965–5972, 2017. doi: 10.1021/acs.langmuir.7b01354.

[121] I. G. Hwang, J. Y. Kim, and B. M. Weon. Droplet evaporation with complexity of evaporation modes. *Applied Physics Letters*, 110(3):031602, 2017. doi: 10.1063/1.4974292.

[122] R. J. Jackman, D. C. Duffy, E. Ostuni, N. D. Willmore, and G. M. Whitesides. Fabricating large arrays of microwells with arbitrary dimensions and filling them using discontinuous dewetting. *Analytical Chemistry*, 70(11):2280–2287, 1998. doi: 10.1021/ac971295a.

[123] M. Jayaweera, H. Perera, B. Gunawardana, and J. Manatunge. Transmission of COVID-19 virus by droplets and aerosols: A critical review on the unresolved dichotomy. *Environmental Research*, 188:109819, 2020. doi: 10.1016/j.envres.2020.109819.

[124] V. Jokinen, L. Sainiemi, and S. Franssila. Complex droplets on chemically modified silicon nanograss. *Advanced Materials*, 20(18):3453–3456, 2008. doi: 10.1002/adma.200800160.

[125] J.-Y. Jung, Y. W. Kim, and J. Y. Yoo. Behavior of particles in an evaporating didisperse colloid droplet on a hydrophilic surface. *Analytical Chemistry*, 81(19):8256–8259, 2009. doi: 10.1021/ac901247c.

[126] Y. Jung, T. Kajiya, T. Yamaue, and M. Doi. Film formation kinetics in the drying process of polymer solution enclosed by bank. *Japanese Journal of Applied Physics*, 48(3R):031502, 2009. doi: 10.1143/jjap.48.031502.

[127] M. A. Kadhim, N. Kapur, J. L. Summers, and H. Thompson. Experimental and theoretical investigation of droplet evaporation on heated hydrophilic and hydrophobic surfaces. *Langmuir*, 35(19):6256–6266, 2019. doi: 10.1021/acs.langmuir.8b03601.

[128] T. Kajiya, D. Kaneko, and M. Doi. Dynamical visualization of "coffee stain phenomenon" in droplets of polymer solution via fluorescent microscopy. *Langmuir*, 24(21):12369–12374, 2008. doi: 10.1021/la8017858.

[129] T. Kajiya, W. Kobayashi, T. Okuzono, and M. Doi. Controlling the drying and film formation processes of polymer solution droplets with addition of small amount of surfactants. *The Journal of Physical Chemistry B*, 113(47):15460–15466, 2009. doi: 10.1021/jp9077757.

[130] Kallerna. Water drops on car roof. `https://commons.wikimedia.org/wiki/File:Water_drops_on_car_roof.jpg`, accessed on 15th October 2021.

[131] J. Kamp, J. Villwock, and M. Kraume. Drop coalescence in technical liquid/liquid applications: a review on experimental techniques and modeling approaches. *Reviews in Chemical Engineering*, 33(1):1–47, 2017. doi: 10.1515/revce-2015-0071.

[132] S. J. Kang, V. Vandadi, J. D. Felske, and H. Masoud. Alternative mechanism for coffee-ring deposition based on active role of free surface. *Physical Review E*, 94(6):063104, 2016. doi: 10.1103/PhysRevE.94.063104.

[133] P. Kant, A. L. Hazel, M. Dowling, A. B. Thompson, and A. Juel. Controlling droplet spreading with topography. *Physical Review Fluids*, 2(9):094002, 2017. doi: 10.1103/PhysRevFluids.2.094002.

[134] P. Kant, A. L. Hazel, M. Dowling, A. B. Thompson, and A. Juel. Sequential deposition of microdroplets on patterned surfaces. *Soft Matter*, 14(43):8709–8716, 2018. doi: 10.1039/C8SM01373J.

[135] C. N. Kaplan and L. Mahadevan. Evaporation-driven ring and film deposition from colloidal droplets. *Journal of Fluid Mechanics*, 781:R2, 2015. doi: 10.1017/jfm.2015.496.

[136] M. M. Karim. Flower reflections in raindrop. `https://commons.wikimedia.org/wiki/File:Flower_reflections_in_raindrop.jpg`, accessed on 15th October 2021.

[137] D. Khojasteh, M. Kazerooni, S. Salarian, and R. Kamali. Droplet impact on superhydrophobic surfaces: A review of recent developments. *Journal of Industrial and Engineering Chemistry*, 42:1–14, 2016. doi: 10.1016/j.jiec.2016.07.027.

[138] D. Y. Kim and A. J. Steckl. Electrowetting on paper for electronic paper display. *ACS Applied Materials & Interfaces*, 2(11):3318–3323, 2010. doi: 10.1021/am100757g.

[139] H. Kim, F. Boulogne, E. Um, I. Jacobi, E. Button, and H. A. Stone. Controlled uniform coating from the interplay of Marangoni flows and surface-adsorbed macromolecules. *Physical Review Letters*, 116(12):124501, 2016. doi: 10.1103/PhysRevLett.116.124501.

[140] J.-H. Kim, S. I. Ahn, J. H. Kim, and W.-C. Zin. Evaporation of water droplets on polymer surfaces. *Langmuir*, 23(11):6163–6169, 2007. doi: 10.1021/la0636309.

[141] K. S. Kolegov. Simulation of patterned glass film formation in the evaporating colloidal liquid under IR heating. *Microgravity Science and Technology*, 30:113–120, 2018. doi: 10.1007/s12217-017-9587-0.

[142] K. S. Kolegov and L. Yu. Barash. Applying droplets and films in evaporative lithography. *Advances in Colloid and Interface Science*, 285:102271, 2020. doi: 10.1016/j.cis.2020.102271.

[143] K. S. Kolegov and A. I. Lobanov. Mathematical modeling of fluid dynamics in evaporating drop with taking into account capillary and gravitational forces. *Discrete and Continuous Models and Applied Computational Science*, 2014(2):375–380, 2014.

[144] N. M. Kovalchuk, A. Trybala, and V. M. Starov. Evaporation of sessile droplets. *Current Opinion in Colloid & Interface Science*, 19(4):336–342, 2014. doi: 10.1016/j.cocis.2014.07.005.

[145] M. Kuang, J. Wang, B. Bao, F. Li, L. Wang, L. Jiang, and Y. Song. Inkjet printing patterned photonic crystal domes for wide viewing-angle displays by controlling the sliding three phase contact line. *Advanced Optical Materials*, 2(1):34–38, 2014. doi: 10.1002/adom.201300369.

[146] M. Kuang, L. Wang, and Y. Song. Controllable printing droplets for high-resolution patterns. *Advanced Materials*, 26(40):6950–6958, 2014. doi: 10.1002/adma.201305416.

[147] O. Kudina, B. Eral, and F. Mugele. e-MALDI: An electrowetting-enhanced drop drying method for MALDI mass spectrometry. *Analytical Chemistry*, 88(9):4669–4675, 2016. doi: 10.1021/acs.analchem.5b04283.

[148] H. Kusumaatmaja and J. M. Yeomans. Modeling contact angle hysteresis on chemically patterned and superhydrophobic surfaces. *Langmuir*, 23(11):6019–6032, 2007. doi: 10.1021/la063218t.

[149] D. Kwak, J. A. Lim, B. Kang, W. H. Lee, and K. Cho. Self-organization of inkjet-printed organic semiconductor films prepared in inkjet-etched microwells. *Advanced Functional Materials*, 23(42):5224–5231, 2013. doi: 10.1002/adfm.201300936.

[150] R. G. Larson. Transport and deposition patterns in drying sessile droplets. *AIChE Journal*, 60(5):1538–1571, 2014. doi: 10.1002/aic.14338.

[151] M. Layani, M. Gruchko, O. Milo, I. Balberg, D. Azulay, and S. Magdassi. Transparent conductive coatings by printing coffee ring arrays obtained at room temperature. *ACS Nano*, 3(11):3537–3542, 2009. doi: 10.1021/nn901239z.

[152] C. Y. Lee, B. J. Zhang, J. Park, and K. J. Kim. Water droplet evaporation on Cu-based hydrophobic surfaces with nano-and micro-structures. *International Journal of Heat and Mass Transfer*, 55(7-8):2151–2159, 2012. doi: 10.1016/j.ijheatmasstransfer.2011.12.019.

[153] H. H. Lee, S. C. Fu, C. Y. Tso, and C. Y. H. Chao. Study of residue patterns of aqueous nanofluid droplets with different particle sizes and concentrations on different substrates. *International Journal of Heat and Mass Transfer*, 105:230–236, 2017. doi: 10.1016/j.ijheatmasstransfer.2016.09.093.

[154] P. Levermore, T. Schenk, H.-R. Tseng, H.-J. Wang, H. Heil, A. Jatsch, H. Buchholz, and E. Böhm. Ink-jet-printed OLEDs for display applications. *SID Symposium Digest of Technical Papers*, 47:484–486, 2016. doi: 10.1002/sdtp.10714.

[155] H. Li, N. Fowler, C. Struck, and S. Sivasankar. Flow triggered by instabilities at the contact line of a drop containing nanoparticles. *Soft Matter*, 7(11):5116–5119, 2011. doi: 10.1039/C1SM05097D.

[156] W. Li, W. Ji, H. Sun, D. Lan, and Y. Wang. Pattern formation in drying sessile and pendant droplet: Interactions of gravity settling, interface shrinkage, and capillary flow. *Langmuir*, 35(1):113–119, 2018. doi: 10.1021/acs.langmuir.8b02659.

[157] Y. Li, C. Diddens, P. Lv, H. Wijshoff, M. Versluis, and D. Lohse. Gravitational effect in evaporating binary microdroplets. *Physical Review Letters*, 122(11):114501, 2019. doi: 10.1103/PhysRevLett.122.114501.

[158] Y. Li, C. Diddens, T. Segers, H. Wijshoff, M. Versluis, and D. Lohse. Evaporating droplets on oil-wetted surfaces: Suppression of the coffee-stain effect. *Pro-*

ceedings of the National Academy of Sciences, 117(29):16756–16763, 2020. doi: 10.1073/pnas.2006153117.

[159] Y. Li, C. Lv, Z. Li, D. Quéré, and Q. Zheng. From coffee rings to coffee eyes. *Soft Matter*, 11(23):4669–4673, 2015. doi: 10.1039/C5SM00654F.

[160] Y.-F. Li, Y.-J. Sheng, and H.-K. Tsao. Evaporation stains: suppressing the coffee-ring effect by contact angle hysteresis. *Langmuir*, 29(25):7802–7811, 2013. doi: 10.1021/la400948e.

[161] Y.-F. Li, Y.-J. Sheng, and H.-K. Tsao. Solute concentration-dependent contact angle hysteresis and evaporation stains. *Langmuir*, 30(26):7716–7723, 2014. doi: 10.1021/la501438k.

[162] J. A. Lim, W. H. Lee, H. S. Lee, J. H. Lee, Y. D. Park, and K. Cho. Self-organization of ink-jet-printed triisopropylsilylethynyl pentacene via evaporation-induced flows in a drying droplet. *Advanced Functional Materials*, 18(2):229–234, 2008. doi: 10.1002/adfm.200700859.

[163] T. Lim, J. Yang, S. Lee, J. Chung, and D. Hong. Deposit pattern of inkjet printed pico-liter droplet. *International Journal of Precision Engineering and Manufacturing*, 13(6):827–833, 2012. doi: 10.1007/s12541-012-0108-1.

[164] T.-M. Liou, C.-Y. Chan, C.-C. Fu, and K.-C. Shih. Effects of impact inertia and surface characteristics on deposited polymer droplets in microcavities. *Journal of Microelectromechanical Systems*, 17(2):278–287, 2008. doi: 10.1109/JMEMS.2008.918385.

[165] T.-M. Liou, C.-Y. Chan, and K.-C. Shih. Study of the characteristics of polymer droplet deposition in fabricated rectangular microcavities. *Journal of Micromechanics and Microengineering*, 19(6):065028, 2009. doi: 10.1088/0960-1317/19/6/065028.

[166] D. Lohse and X. Zhang. Surface nanobubbles and nanodroplets. *Reviews of Modern Physics*, 87(3):981–1035, 2015. doi: 10.1103/RevModPhys.87.981.

[167] M. C. Lopes and E. Bonaccurso. Evaporation control of sessile water drops by soft viscoelastic surfaces. *Soft Matter*, 8(30):7875–7881, 2012. doi: 10.1039/C2SM25958C.

[168] M. C. Lopes, E. Bonaccurso, T. Gambaryan-Roisman, and P. Stephan. Influence of the substrate thermal properties on sessile droplet evaporation: Effect of transient heat transport. *Colloids and Surfaces A: Physicochemical and Engineering Aspects*, 432:64–70, 2013. doi: 10.1016/j.colsurfa.2013.04.017.

[169] V. A. Lubarda and K. A. Talke. Analysis of the equilibrium droplet shape based on an ellipsoidal droplet model. *Langmuir*, 27(17):10705–10713, 2011. doi: doi.org/10.1021/la202077w.

[170] C. F. Madigan, C. R. Hauf, L. D. Barkley, N. Harjee, E. Vronsky, and S. A. Van Slyke. Advancements in inkjet printing for OLED mass production. *SID Symposium Digest of Technical Papers*, 45:399–402, 2014. doi: 10.1002/j.2168-0159.2014.tb00108.x.

[171] S. Maheshwari, L. Zhang, Y. Zhu, and H.-C. Chang. Coupling between precipitation and contact-line dynamics: Multiring stains and stick-slip motion. *Physical Review Letters*, 100(4):044503, 2008. doi: 10.1103/PhysRevLett.100.044503.

[172] M. Majumder, C. S. Rendall, J. A. Eukel, J. Y. L. Wang, N. Behabtu, C. L. Pint, T.-Y. Liu, A. W. Orbaek, F. Mirri, J. Nam, et al. Overcoming the "coffee-stain" effect by compositional Marangoni-flow-assisted drop-drying. *The Journal of Physical Chemistry B*, 116(22):6536–6542, 2012. doi: 10.1021/jp3009628.

[173] R. Malinowski, G. Volpe, I. P. Parkin, and G. Volpe. Dynamic control of particle deposition in evaporating droplets by an external point source of vapor. *The Journal of Physical Chemistry Letters*, 9(3):659–664, 2018. doi: 10.1021/acs.jpclett.7b02831.

[174] L. K. Malla, R. Bhardwaj, and A. Neild. Analysis of profile and morphology of colloidal deposits obtained from evaporating sessile droplets. *Colloids and*

Surfaces A: Physicochemical and Engineering Aspects, 567:150–160, 2019. doi: 10.1016/j.colsurfa.2019.01.028.

[175] L. K. Malla, R. Bhardwaj, and A. Neild. Colloidal deposit of an evaporating sessile droplet on a non-uniformly heated substrate. *Colloids and Surfaces A: Physicochemical and Engineering Aspects*, 584:124009, 2020. doi: 10.1016/j.colsurfa.2019.124009.

[176] D. Mampallil and H. B. Eral. A review on suppression and utilization of the coffee-ring effect. *Advances in Colloid and Interface Science*, 252:38–54, 2018. doi: 10.1016/j.cis.2017.12.008.

[177] X. Man and M. Doi. Ring to mountain transition in deposition pattern of drying droplets. *Physical Review Letters*, 116(6):066101, 2016. doi: 10.1103/PhysRevLett.116.066101.

[178] Á. G. Marín, H. Gelderblom, D. Lohse, and J. H. Snoeijer. Order-to-disorder transition in ring-shaped colloidal stains. *Physical Review Letters*, 107(8):085502, 2011. doi: 10.1103/PhysRevLett.107.085502.

[179] Á. G. Marín, H. Gelderblom, D. Lohse, and J. H. Snoeijer. Rush-hour in evaporating coffee drops. *Physics of Fluids*, 23(9):091111, 2011. doi: 10.1063/1.3640018.

[180] P. Marizza, S. S. Keller, and A. Boisen. Inkjet printing as a technique for filling of micro-wells with biocompatible polymers. *Microelectronic Engineering*, 111:391–395, 2013. doi: 10.1016/j.mee.2013.03.168.

[181] H. Masoud and J. D. Felske. Analytical solution for Stokes flow inside an evaporating sessile drop: Spherical and cylindrical cap shapes. *Physics of Fluids*, 21(4):042102, 2009. doi: 10.1063/1.3112002.

[182] H. Masoud, P. D. Howell, and H. A. Stone. Evaporation of multiple droplets. *Journal of Fluid Mechanics*, 927:R4, 2021. doi: 10.1017/jfm.2021.785.

[183] S. Masoudi and H. C. Kuhlmann. Axisymmetric buoyant–thermocapillary flow in sessile and hanging droplets. *Journal of Fluid Mechanics*, 826:1066–1095, 2017. doi: 10.1017/jfm.2017.479.

[184] G. McHale, S. Aqil, N. J. Shirtcliffe, M. I. Newton, and H. Y. Erbil. Analysis of droplet evaporation on a superhydrophobic surface. *Langmuir*, 21(24):11053–11060, 2005. doi: 10.1021/la0518795.

[185] G. McHale, S. M. Rowan, M. I. Newton, and M. K. Banerjee. Evaporation and the wetting of a low-energy solid surface. *The Journal of Physical Chemistry B*, 102(11):1964–1967, 1998. doi: 10.1021/jp972552i.

[186] S. Middleman. The transfer of a drop from a capillary to an impermeable surface. In *Modeling Axisymmetric Flows: Dynamics of Films, Jets, and Drops*, pages 161–193. Academic Press, 1995.

[187] A. Mistry and K. Muralidhar. Spreading of a pendant liquid drop underneath a textured substrate. *Physics of Fluids*, 30(4):042104, 2018. doi: 10.1063/1.5012921.

[188] J. R. Moffat, K. Sefiane, and M. E. R. Shanahan. Effect of TiO_2 nanoparticles on contact line stick-slip behavior of volatile drops. *The Journal of Physical Chemistry B*, 113(26):8860–8866, 2009. doi: 10.1021/jp902062z.

[189] J. R. Moffat, K. Sefiane, and M. E. R. Shanahan. Nanofluid droplet evaporation kinetics and wetting dynamics on flat substrates. *Journal of Nano Research*, 7:75–80, 2009. doi: 10.4028/www.scientific.net/JNanoR.7.75.

[190] R. Mollaret, K. Sefiane, J. R. E. Christy, and D. Veyret. Experimental and numerical investigation of the evaporation into air of a drop on a heated surface. *Chemical Engineering Research and Design*, 82(4):471–480, 2004. doi: 10.1205/026387604323050182.

[191] M. Moore, A. Amirfazli, and S. F. Chini. Sessile and pendant micro-liter drops evaporate at different rates: an experimental approach. *Journal of Computational Applied Mechanics*, 47(1):109–119, 2016. doi: 10.22059/jcamech.2016.59260.

[192] M. R. Moore, D. Vella, and J. M. Oliver. The nascent coffee ring: how solute diffusion counters advection. *Journal of Fluid Mechanics*, 920:A54, 2021. doi: 10.1017/jfm.2021.463.

[193] N. Murisic and L. Kondic. On evaporation of sessile drops with moving contact lines. *Journal of Fluid Mechanics*, 679:219–246, 2011. doi: 10.1017/jfm.2011.133.

[194] T. A. H. Nguyen, S. R. Biggs, and A. V. Nguyen. Analytical model for diffusive evaporation of sessile droplets coupled with interfacial cooling effect. *Langmuir*, 34(23):6955–6962, 2018. doi: 10.1021/acs.langmuir.7b03862.

[195] T. A. H. Nguyen and A. V. Nguyen. Increased evaporation kinetics of sessile droplets by using nanoparticles. *Langmuir*, 28(49):16725–16728, 2012. doi: 10.1021/la303293w.

[196] T. A. H. Nguyen and A. V. Nguyen. On the lifetime of evaporating sessile droplets. *Langmuir*, 28(3):1924–1930, 2012. doi: 10.1021/la2036955.

[197] T. A. H. Nguyen, A. V. Nguyen, M. A. Hampton, Z. P. Xu, L. Huang, and V. Rudolph. Theoretical and experimental analysis of droplet evaporation on solid surfaces. *Chemical Engineering Science*, 69(1):522–529, 2012. doi: 10.1016/j.ces.2011.11.009.

[198] M. Oksuz and H. Y. Erbil. Comments on the energy barrier calculations during "stick–slip" behavior of evaporating droplets containing nanoparticles. *The Journal of Physical Chemistry C*, 118(17):9228–9238, 2014. doi: 10.1021/jp5010083.

[199] T. Okuzono, M. Kobayashi, and M. Doi. Final shape of a drying thin film. *Physical Review E*, 80(2):021603, 2009. doi: 10.1103/PhysRevE.80.021603.

[200] D. Orejon, K. Sefiane, and M. E. R. Shanahan. Stick–slip of evaporating droplets: substrate hydrophobicity and nanoparticle concentration. *Langmuir*, 27(21):12834–12843, 2011. doi: 10.1021/la2026736.

[201] D. Orejon, K. Sefiane, and M. E. R. Shanahan. Evaporation of nanofluid droplets with applied DC potential. *Journal of Colloid and Interface Science*, 407:29–38, 2013. doi: 10.1016/j.jcis.2013.05.079.

[202] J. F. Padday. The profiles of axially symmetric menisci. *Philosophical Transactions of the Royal Society of London. Series A, Mathematical and Physical Sciences*, 269(1197):265–293, 1971. doi: 10.1098/rsta.1971.0031.

[203] J. F. Padday. Sessile drop profiles: corrected methods for surface tension and spreading coefficients. *Proceedings of the Royal Society of London. A. Mathematical and Physical Sciences*, 330(1583):561–572, 1972. doi: 10.1098/rspa.1972.0159.

[204] J. F. Padday and A. R. Pitt. The stability of axisymmetric menisci. *Philosophical Transactions of the Royal Society of London. Series A, Mathematical and Physical Sciences*, 275(1253):489–528, 1973. doi: 10.1098/rsta.1973.0113.

[205] Z. Pan, S. Dash, J. A. Weibel, and S. V. Garimella. Assessment of water droplet evaporation mechanisms on hydrophobic and superhydrophobic substrates. *Langmuir*, 29(51):15831–15841, 2013. doi: 10.1021/la4045286.

[206] Z. Pan, J. A. Weibel, and S. V. Garimella. Influence of surface wettability on transport mechanisms governing water droplet evaporation. *Langmuir*, 30(32):9726–9730, 2014. doi: 10.1021/la501931x.

[207] Z. Pan, J. A. Weibel, and S. V. Garimella. Transport mechanisms during water droplet evaporation on heated substrates of different wettability. *International Journal of Heat and Mass Transfer*, 152:119524, 2020. doi: 10.1016/j.ijheatmasstransfer.2020.119524.

[208] A. K. Panwar, S. K. Barthwal, and S. Ray. Effect of evaporation on the contact angle of a sessile drop on solid substrates. *Journal of Adhesion Science and Technology*, 17(10):1321–1329, 2003. doi: 10.1163/156856103769172760.

[209] J. Park and J. Moon. Control of colloidal particle deposit patterns within picoliter droplets ejected by ink-jet printing. *Langmuir*, 22(8):3506–3513, 2006. doi: 10.1021/la053450j.

[210] C. Parneix, P. Vandoolaeghe, V. S. Nikolayev, D. Quéré, J. Li, and B. Cabane. Dips and rims in dried colloidal films. *Physical Review Letters*, 105(26):266103, 2010. doi: 10.1103/PhysRevLett.105.266103.

[211] M. Parsa, R. Boubaker, S. Harmand, K. Sefiane, M. Bigerelle, and R. Deltombe. Patterns from dried water-butanol binary-based nanofluid drops. *Journal of Nanoparticle Research*, 19(8):268, 2017. doi: 10.1007/s11051-017-3951-2.

[212] M. Parsa, S. Harmand, and K. Sefiane. Mechanisms of pattern formation from dried sessile drops. *Advances in Colloid and Interface Science*, 254:22–47, 2018. doi: 10.1016/j.cis.2018.03.007.

[213] M. Parsa, S. Harmand, K. Sefiane, M. Bigerelle, and R. Deltombe. Effect of substrate temperature on pattern formation of nanoparticles from volatile drops. *Langmuir*, 31(11):3354–3367, 2015. doi: 10.1021/acs.langmuir.5b00362.

[214] N. D. Patil, P. G. Bange, R. Bhardwaj, and A. Sharma. Effects of substrate heating and wettability on evaporation dynamics and deposition patterns for a sessile water droplet containing colloidal particles. *Langmuir*, 32(45):11958–11972, 2016. doi: 10.1021/acs.langmuir.6b02769.

[215] R. H. Perry, D. W. Green, and J. O. Maloney. *Perry's Chemical Engineers' Handbook, 7th edition.* McGraw–Hill, 1997.

[216] T. Pham and S. Kumar. Imbibition and evaporation of droplets of colloidal suspensions on permeable substrates. *Physical Review Fluids*, 4(3):034004, 2019. doi: 10.1103/PhysRevFluids.4.034004.

[217] R. G. Picknett and R. Bexon. The evaporation of sessile or pendant drops in still air. *Journal of Colloid and Interface Science*, 61(2):336–350, 1977. doi: 10.1016/0021-9797(77)90396-4.

[218] P. G. Pittoni, C.-C. Chang, T.-S. Yu, and S.-Y. Lin. Evaporation of water drops on polymer surfaces: Pinning, depinning and dynamics of the triple line. *Colloids and Surfaces A: Physicochemical and Engineering Aspects*, 432:89–98, 2013. doi: 10.1016/j.colsurfa.2013.04.045.

[219] V. L. Popov, M. Heß, and E. Willert. *Handbook of Contact Mechanics: Exact Solutions of Axisymmetric Contact Problems*. Springer Nature, 2019. doi: 10.1007/978-3-662-58709-6.

[220] Y. O. Popov. Evaporative deposition patterns: spatial dimensions of the deposit. *Physical Review E*, 71(3):036313, 2005. doi: 10.1103/PhysRevE.71.036313.

[221] T. K. Pradhan and P. K. Panigrahi. Evaporation induced natural convection inside a droplet of aqueous solution placed on a superhydrophobic surface. *Colloids and Surfaces A: Physicochemical and Engineering Aspects*, 530:1–12, 2017. doi: 10.1016/j.colsurfa.2017.07.034.

[222] Z. Pu, J. Tu, R. Han, X. Zhang, J. Wu, C. Fang, H. Wu, X. Zhang, H. Yu, and D. Li. A flexible enzyme-electrode sensor with cylindrical working electrode modified with a 3D nanostructure for implantable continuous glucose monitoring. *Lab on a Chip*, 18(23):3570–3577, 2018. doi: 10.1039/C8LC00908B.

[223] Z. Pu, X. Zhang, H. Wu, J. Wu, H. Yu, and D. Li. Cylindrical electrochemical sensor fabricated by rotated inkjet printing on flexible substrate for glucose monitoring. In *19th International Conference on Solid-State Sensors, Actuators and Microsystems (TRANSDUCERS)*, pages 1241–1244. IEEE, 2017. doi: 10.1109/TRANSDUCERS.2017.7994280.

[224] S. A. Putnam, A. M. Briones, L. W. Byrd, J. S. Ervin, M. S. Hanchak, A. White, and J. G. Jones. Microdroplet evaporation on superheated surfaces. *Inter-*

national Journal of Heat and Mass Transfer, 55(21-22):5793–5807, 2012. doi: 10.1016/j.ijheatmasstransfer.2012.05.076.

[225] J. Ren, A. Crivoi, and F. Duan. Disk-ring deposition in drying a sessile nanofluid droplet with enhanced Marangoni effect and particle surface adsorption. *Langmuir*, 36(49):15064–15074, 2020. doi: 10.1021/acs.langmuir.0c02607.

[226] B. Rieger, L. R. van den Doel, and L. J. van Vliet. Ring formation in nanoliter cups: Quantitative measurements of flow in micromachined wells. *Physical Review E*, 68(3):036312, 2003. doi: 10.1103/PhysRevE.68.036312.

[227] W. D. Ristenpart, P. G. Kim, C. Domingues, J. Wan, and H. A. Stone. Influence of substrate conductivity on circulation reversal in evaporating drops. *Physical Review Letters*, 99(23):234502, 2007. doi: 10.1103/PhysRevLett.99.234502.

[228] P. Roach, N. J. Shirtcliffe, and M. I. Newton. Progess in superhydrophobic surface development. *Soft Matter*, 4(2):224–240, 2008. doi: 10.1039/B712575P.

[229] A. F. Routh. Drying of thin colloidal films. *Reports on Progress in Physics*, 76(4):046603, 2013. doi: 10.1088/0034-4885/76/4/046603.

[230] A. F. Routh and W. B. Russel. Horizontal drying fronts during solvent evaporation from latex films. *AIChE Journal*, 44(9):2088–2098, 1998. doi: 10.1002/aic.690440916.

[231] S.-a. Ryu, J. Y. Kim, S. Y. Kim, and B. M. Weon. Drying-mediated patterns in colloid-polymer suspensions. *Scientific Reports*, 7:1079, 2017. doi: 10.1038/s41598-017-00932-z.

[232] P. J. Sáenz, A. W. Wray, Z. Che, O. K. Matar, P. Valluri, J. Kim, and K. Sefiane. Dynamics and universal scaling law in geometrically-controlled sessile drop evaporation. *Nature Communications*, 8:14783, 2017. doi: 10.1038/ncomms14783.

[233] I. Sandu, M. Dumitru, C. T. Fleaca, and F. Dumitrache. Hanging colloidal drop: A new photonic crystal synthesis route. *Photonics and Nanostructures – Fundamentals and Applications*, 29:42–48, 2018. doi: 10.1016/j.photonics.2018.02.001.

[234] I. Sandu and C. T. Fleaca. The influence of gravity on the distribution of the deposit formed onto a substrate by sessile, hanging, and sandwiched hanging drop evaporation. *Journal of Colloid and Interface Science*, 358(2):621–625, 2011. doi: 10.1016/j.jcis.2011.03.052.

[235] I. Sandu, I. Iordache, C. T. Fleaca, F. Dumitrache, and A. M. Niculescu. The influence of gravity on single crystallization in large volume drops. *Journal of Crystallization Process and Technology*, 4:206–211, 2014. doi: 10.4236/jcpt.2014.44025.

[236] N. Savva and S. Kalliadasis. Influence of gravity on the spreading of two-dimensional droplets over topographical substrates. *Journal of Engineering Mathematics*, 73(1):3–16, 2012. doi: 10.1007/s10665-010-9426-4.

[237] C. Schäfle, M. Brinkmann, C. Bechinger, P. Leiderer, and R. Lipowsky. Morphological wetting transitions at ring-shaped surface domains. *Langmuir*, 26(14):11878–11885, 2010. doi: 10.1021/la1011023.

[238] F. G. H. Schofield, D. Pritchard, S. K. Wilson, and K. Sefiane. The lifetimes of evaporating sessile droplets of water can be strongly influenced by thermal effects. *Fluids*, 6(4):141, 2021. doi: 10.3390/fluids6040141.

[239] F. G. H. Schofield, S. K. Wilson, D. Pritchard, and K. Sefiane. The lifetimes of evaporating sessile droplets are significantly extended by strong thermal effects. *Journal of Fluid Mechanics*, 851:231–244, 2018. doi: 10.1017/jfm.2018.496.

[240] F. G. H. Schofield, A. W. Wray, D. Pritchard, and S. K. Wilson. The shielding effect extends the lifetimes of two-dimensional sessile droplets. *Journal of Engineering Mathematics*, 120(1):89–110, 2020. doi: 10.1007/s10665-019-10033-7.

[241] K. Sefiane. On the formation of regular patterns from drying droplets and their potential use for bio-medical applications. *Journal of Bionic Engineering*, 7(4):S82–S93, 2010. doi: 10.1016/S1672-6529(09)60221-3.

[242] K. Sefiane. Patterns from drying drops. *Advances in Colloid and Interface Science*, 206:372–381, 2014. doi: 10.1016/j.cis.2013.05.002.

[243] K. Sefiane, S. K. Wilson, S. David, G. J. Dunn, and B. R. Duffy. On the effect of the atmosphere on the evaporation of sessile droplets of water. *Physics of Fluids*, 21(6):062101, 2009. doi: 10.1063/1.3131062.

[244] S. Semenov, V. M. Starov, R. G. Rubio, H. Agogo, and M. G. Velarde. Evaporation of sessile water droplets: Universal behaviour in presence of contact angle hysteresis. *Colloids and Surfaces A: Physicochemical and Engineering Aspects*, 391(1-3):135–144, 2011. doi: 10.1016/j.colsurfa.2011.07.013.

[245] S. Semenov, A. Trybala, H. Agogo, N. Kovalchuk, F. Ortega, R. G. Rubio, V. M. Starov, and M. G. Velarde. Evaporation of droplets of surfactant solutions. *Langmuir*, 29(32):10028–10036, 2013. doi: 10.1021/la401578v.

[246] C. Seo, D. Jang, J. Chae, and S. Shin. Altering the coffee-ring effect by adding a surfactant-like viscous polymer solution. *Scientific Reports*, 7:500, 2017. doi: 10.1038/s41598-017-00497-x.

[247] N. Shahidzadeh-Bonn, S. Rafaï, A. Azouni, and D. Bonn. Evaporating droplets. *Journal of Fluid Mechanics*, 549:307–313, 2006. doi: 10.1017/S0022112005008190.

[248] M. E. R. Shanahan. Simple theory of "stick-slip" wetting hysteresis. *Langmuir*, 11(3):1041–1043, 1995. doi: 10.1021/la00003a057.

[249] M. E. R. Shanahan and K. Sefiane. Kinetics of triple line motion during evaporation. In *Contact Angle, Wettability and Adhesion*, volume 6, pages 19–31. Koninklijke Brill NV Leiden, 2009.

[250] M. E. R. Shanahan, K. Sefiane, and J. R. Moffat. Dependence of volatile droplet lifetime on the hydrophobicity of the substrate. *Langmuir*, 27(8):4572–4577, 2011. doi: 10.1021/la200437s.

[251] X. Shao, F. Duan, Y. Hou, and X. Zhong. Role of surfactant in controlling the deposition pattern of a particle-laden droplet: Fundamentals and strategies. *Advances in Colloid and Interface Science*, 275:102049, 2020. doi: 10.1016/j.cis.2019.102049.

[252] Y.-W. Sheu and C.-H. Tu. Densities, viscosities, refractive indices, and surface tensions for 12 flavor esters from T = 288.15 K to T = 358.15 K. *Journal of Chemical & Engineering Data*, 50(5):1706–1710, 2005. doi: 10.1021/je050170x.

[253] T. Shimoda, K. Morii, S. Seki, and H. Kiguchi. Inkjet printing of light-emitting polymer displays. *Materials Research Society Bulletin*, 28(11):821–827, 2003. doi: 10.1557/mrs2003.231.

[254] D. H. Shin, S. H. Lee, C. K. Choi, and S. Retterer. The evaporation and wetting dynamics of sessile water droplets on submicron-scale patterned silicon hydrophobic surfaces. *Journal of Micromechanics and Microengineering*, 20(5):055021, 2010. doi: 10.1088/0960-1317/20/5/055021.

[255] D. H. Shin, S. H. Lee, J.-Y. Jung, and J. Y. Yoo. Evaporating characteristics of sessile droplet on hydrophobic and hydrophilic surfaces. *Microelectronic Engineering*, 86(4-6):1350–1353, 2009. doi: 10.1016/j.mee.2009.01.026.

[256] N. J. Shirtcliffe, G. McHale, S. Atherton, and M. I. Newton. An introduction to superhydrophobicity. *Advances in Colloid and Interface Science*, 161(1-2):124–138, 2010. doi: 10.1016/j.cis.2009.11.001.

[257] L. Shmuylovich, A. Q. Shen, and H. A. Stone. Surface morphology of drying latex films: Multiple ring formation. *Langmuir*, 18(9):3441–3445, 2002. doi: 10.1021/la011484v.

[258] T. Si, Z. Ma, and J. X. Tang. Capillary flow and mechanical buckling in a growing annular bacterial colony. *Soft Matter*, 14(2):301–311, 2018. doi: 10.1039/C7SM01452J.

[259] M. Singh, H. M. Haverinen, P. Dhagat, and G. E. Jabbour. Inkjet printing—process and its applications. *Advanced Materials*, 22(6):673–685, 2010. doi: 10.1002/adma.200901141.

[260] D. P. Siregar, J. G. M. Kuerten, and C. W. M. van der Geld. Numerical simulation of the drying of inkjet-printed droplets. *Journal of Colloid and Interface Science*, 392:388–395, 2013. doi: 10.1016/j.jcis.2012.09.063.

[261] B. Sobac and D. Brutin. Triple-line behavior and wettability controlled by nanocoated substrates: influence on sessile drop evaporation. *Langmuir*, 27(24):14999–15007, 2011. doi: 10.1021/la203681j.

[262] B. Sobac and D. Brutin. Thermal effects of the substrate on water droplet evaporation. *Physical Review E*, 86(2):021602, 2012. doi: 10.1103/PhysRevE.86.021602.

[263] C. Sodtke, V. S. Ajaev, and P. Stephan. Evaporation of thin liquid droplets on heated surfaces. *Heat and Mass Transfer*, 43(7):649–657, 2007. doi: 10.1007/s00231-006-0126-6.

[264] C. Sodtke, V. S. Ajaev, and P. Stephan. Dynamics of volatile liquid droplets on heated surfaces: theory versus experiment. *Journal of Fluid Mechanics*, 610:343–362, 2008. doi: 10.1017/S0022112008002759.

[265] A. P. Sommer. Limits of the impact of gravity on self-organizing nanospheres. *The Journal of Physical Chemistry B*, 108(24):8096–8098, 2004. doi: 10.1021/jp0487049.

[266] D. M. Soolaman and H.-Z. Yu. Water microdroplets on molecularly tailored surfaces: correlation between wetting hysteresis and evaporation mode switching. *The Journal of Physical Chemistry B*, 109(38):17967–17973, 2005. doi: 10.1021/jp051182s.

[267] J. M. Stauber. *On the evaporation of sessile droplets.* PhD thesis, University of Strathclyde, 2015. doi: 10.48730/b37k-0223.

[268] J. M. Stauber, S. K. Wilson, B. R. Duffy, and K. Sefiane. On the lifetimes of evaporating droplets. *Journal of Fluid Mechanics*, 744:R2, 2014. doi: 10.1017/jfm.2014.94.

[269] J. M. Stauber, S. K. Wilson, B. R. Duffy, and K. Sefiane. Evaporation of droplets on strongly hydrophobic substrates. *Langmuir*, 31(12):3653–3660, 2015. doi: 10.1021/acs.langmuir.5b00286.

[270] J. M. Stauber, S. K. Wilson, B. R. Duffy, and K. Sefiane. On the lifetimes of evaporating droplets with related initial and receding contact angles. *Physics of Fluids*, 27(12):122101, 2015. doi: 10.1063/1.4935232.

[271] T. Still, P. J. Yunker, and A. G. Yodh. Surfactant-induced Marangoni eddies alter the coffee-rings of evaporating colloidal drops. *Langmuir*, 28(11):4984–4988, 2012. doi: 10.1021/la204928m.

[272] H. J. Subramani, T. Al-Housseiny, A. U. Chen, M. Li, and O. A. Basaran. Dynamics of drop impact on a rectangular slot. *Industrial & Engineering Chemistry Research*, 46(19):6105–6112, 2007. doi: 10.1021/ie070290t.

[273] E. Sultan, A. Boudaoud, and M. B. Amar. Evaporation of a thin film: diffusion of the vapour and Marangoni instabilities. *Journal of Fluid Mechanics*, 543:183–202, 2005. doi: 10.1017/S0022112005006348.

[274] S. Sun, J. Li, and J. Han. How human thermal plume influences near-human transport of respiratory droplets and airborne particles: a review. *Environmental Chemistry Letters*, 19:1971–1982, 2021. doi: 10.1007/s10311-020-01178-4.

[275] P.-F. Sung, L. Wang, and M. T. Harris. Deposition of colloidal particles during the evaporation of sessile drops: Dilute colloidal dispersions. *International Journal of Chemical Engineering*, 2019:7954965, 2019. doi: 10.1155/2019/7954965.

[276] M. Szakáll, S. K. Mitra, K. Diehl, and S. Borrmann. Shapes and oscillations of falling raindrops — A review. *Atmospheric Research*, 97(4):416–425, 2010. doi: 10.1016/j.atmosres.2010.03.024.

[277] V. D. Ta, R. M. Carter, E. Esenturk, C. Connaughton, T. J. Wasley, J. Li, R. W. Kay, J. Stringer, P. J. Smith, and J. D. Shephard. Dynamically controlled deposition of colloidal nanoparticle suspension in evaporating drops using laser radiation. *Soft Matter*, 12(20):4530–4536, 2016. doi: 10.1039/C6SM00465B.

[278] R. Tadmor. Approaches in wetting phenomena. *Soft Matter*, 7(5):1577–1580, 2011. doi: 10.1039/C0SM00775G.

[279] R. Tadmor. Open problems in wetting phenomena: pinning retention forces. *Langmuir*, 37(21):6357–6372, 2021. doi: 10.1021/acs.langmuir.0c02768.

[280] E. Talbot, C. Bain, R. De Dier, W. Sempels, and J. Vermant. Droplets drying on surfaces. In S. D. Hoath, editor, *Fundamentals of Inkjet Printing*, chapter 10, pages 251–279. Wiley–VCH Verlag, 2017.

[281] E. L. Talbot, A. Berson, P. S. Brown, and C. D. Bain. Evaporation of picoliter droplets on surfaces with a range of wettabilities and thermal conductivities. *Physical Review E*, 85(6):061604, 2012. doi: 10.1103/PhysRevE.85.061604.

[282] E. L. Talbot, H. N. Yow, L. Yang, A. Berson, S. R. Biggs, and C. D. Bain. Printing small dots from large drops. *ACS Applied Materials & Interfaces*, 7(6):3782–3790, 2015. doi: 10.1021/am5087177.

[283] Y. Yu. Tarasevich, I. V. Vodolazskaya, and O. P. Isakova. Desiccating colloidal sessile drop: dynamics of shape and concentration. *Colloid and Polymer Science*, 289(9):1015–1023, 2011. doi: 10.1007/s00396-011-2418-8.

[284] Y. Yu. Tarasevich, I. V. Vodolazskaya, and L. V. Sakharova. Mathematical modeling of pattern formation caused by drying of colloidal film under a mask. *The European Physical Journal E*, 39(2):26, 2016. doi: 10.1140/epje/i2016-16026-5.

[285] P. Taylor. The wetting of leaf surfaces. *Current Opinion in Colloid & Interface Science*, 16(4):326–334, 2011. doi: 10.1016/j.cocis.2010.12.003.

[286] T. Traianou. A tiny world in a fallen drop. `https://commons.wikimedia.org/wiki/File:A_tiny_world_in_a_fallen_drop.jpg`, accessed on 15th October 2021.

[287] J. R. Trantum, D. W. Wright, and F. R. Haselton. Biomarker-mediated disruption of coffee-ring formation as a low resource diagnostic indicator. *Langmuir*, 28(4):2187–2193, 2012. doi: 10.1021/la203903a.

[288] E. C. Tredenick, W. A. Forster, R. Pethiyagoda, R. M. van Leeuwen, and S. W. McCue. Evaporating droplets on inclined plant leaves and synthetic surfaces: Experiments and mathematical models. *Journal of Colloid and Interface Science*, 592:329–341, 2021. doi: 10.1016/j.jcis.2021.01.070.

[289] A. Trybala, A. Okoye, S. Semenov, H. Agogo, R. G. Rubio, F. Ortega, and V. M. Starov. Evaporation kinetics of sessile droplets of aqueous suspensions of inorganic nanoparticles. *Journal of Colloid and Interface Science*, 403:49–57, 2013. doi: 10.1016/j.jcis.2013.04.017.

[290] L. R. van den Doel and L. J. van Vliet. Temporal phase-unwrapping algorithm for dynamic interference pattern analysis in interference-contrast microscopy. *Applied Optics*, 40(25):4487–4500, 2001. doi: 10.1364/AO.40.004487.

[291] V. K. Vlasko-Vlasov, M. Sulwer, E. V. Shevchenko, J. Parker, and W. K. Kwok. Ring patterns generated by an expanding colloidal meniscus. *Physical Review E*, 102(5):052608, 2020. doi: 10.1103/PhysRevE.102.052608.

[292] I. V. Vodolazskaya and Yu. Yu. Tarasevich. The model of drying sessile drop of colloidal solution. *Modern Physics Letters B*, 25(15):1303–1310, 2011. doi: 10.1142/S0217984911026280.

[293] I. V. Vodolazskaya and Yu. Yu. Tarasevich. Modeling of mass transfer in a film of solution evaporating under the mask with holes. *The European Physical Journal E*, 40(10):83, 2017. doi: 10.1140/epje/i2017-11574-8.

[294] D. Walker, H. Leith, L. Duff, L. W. Tan, H.-R. Tseng, T. Schenk, and P. Levermore. High resolution ink-jet printed OLED for display applications. *NIP & Digital Fabrication Conference, Printing for Fabrication 2016 (NIP32)*, pages 469–471, 2016.

[295] J. Wang and J. Fukai. Evaporation rate profiles from a liquid in a cylindrical hole. *Journal of Chemical Engineering of Japan*, 51(1):49–52, 2018. doi: 10.1252/jcej.17we221.

[296] H. M. J. M. Wedershoven, K. R. M. Deuss, C. Fantin, J. C. H. Zeegers, and A. A. Darhuber. Active control of evaporative solution deposition by means of modulated gas phase convection. *International Journal of Heat and Mass Transfer*, 117:303–312, 2018. doi: 10.1016/j.ijheatmasstransfer.2017.09.123.

[297] H. Wente. The stability of the axially symmetric pendent drop. *Pacific Journal of Mathematics*, 88(2):421–470, 1980. doi: 10.2140/pjm.1980.88.421.

[298] E. Widjaja and M. T. Harris. Particle deposition study during sessile drop evaporation. *AIChE Journal*, 54(9):2250–2260, 2008. doi: 10.1002/aic.11558.

[299] H. Wijshoff. Drop dynamics in the inkjet printing process. *Current Opinion in Colloid & Interface Science*, 36:20–27, 2018. doi: 10.1016/j.cocis.2017.11.004.

[300] W. E. Williams. Note on the electrostatic problem for a circular annulus. *The Quarterly Journal of Mechanics and Applied Mathematics*, 16(2):205–207, 1963. doi: 10.1093/qjmam/16.2.205.

[301] D. Willmer, K. A. Baldwin, C. Kwartnik, and D. J. Fairhurst. Growth of solid conical structures during multistage drying of sessile poly(ethylene oxide) droplets. *Physical Chemistry Chemical Physics*, 12(16):3998–4004, 2010. doi: 10.1039/B922727J.

[302] S. K. Wilson and H.-M. D'Ambrosio. Evaporation of sessile droplets. *Annual Review of Fluid Mechanics*. to appear.

[303] S. K. Wilson and B. R. Duffy. Mathematical models for the evaporation of sessile droplets. In *Drying of Complex Fluid Drops*. Royal Society of Chemistry, 2021.

[304] A. M. Worthington. II. On pendent drops. *Proceedings of the Royal Society of London*, 32(212-215):362–377, 1881. doi: 10.1098/rspl.1881.0032.

[305] A. W. Wray, B. R. Duffy, and S. K. Wilson. Competitive evaporation of multiple sessile droplets. *Journal of Fluid Mechanics*, 884:A45, 2020. doi: 10.1017/jfm.2019.919.

[306] A. W. Wray, P. S. Wray, B. R. Duffy, and S. K. Wilson. Contact-line deposits from multiple evaporating droplets. *Physical Review Fluids*, 6(7):073604, 2021. doi: 10.1103/PhysRevFluids.6.073604.

[307] L. Xu, Z. Li, and S. Yao. Directional motion of evaporating droplets on gradient surfaces. *Applied Physics Letters*, 101(6):064101, 2012. doi: 10.1063/1.4742860.

[308] W. Xu, R. Leeladhar, Y. T. Kang, and C.-H. Choi. Evaporation kinetics of sessile water droplets on micropillared superhydrophobic surfaces. *Langmuir*, 29(20):6032–6041, 2013. doi: 10.1021/la400452e.

[309] A.-S. Yang, M.-T. Yang, and M.-C. Hong. Numerical study for the impact of liquid droplets on solid surfaces. *Proceedings of the Institution of Mechanical Engineers, Part C: Journal of Mechanical Engineering Science*, 221(3):293–301, 2007. doi: 10.1243/0954406JMES488.

[310] Q. Yang, Y. Gao, F. He, and P. Hao. Patterning in colloidal droplets by forced airflow. *Journal of Applied Physics*, 129(2):024701, 2021. doi: 10.1063/5.0026182.

[311] X. Yang, Z. Jiang, P. Lyu, Z. Ding, and X. Man. Deposition pattern of drying droplets. *Communications in Theoretical Physics*, 73(4):047601, 2021. doi: 10.1088/1572-9494/abda21.

[312] X. Yang, C. Y. Li, and Y. Sun. From multi-ring to spider web and radial spoke: competition between the receding contact line and particle deposition in a drying colloidal drop. *Soft Matter*, 10(25):4458–4463, 2014. doi: 10.1039/C4SM00497C.

[313] T. M. Yen, X. Fu, T. Wei, R. U. Nayak, Y. Shi, and Y.-H. Lo. Reversing coffee-ring effect by laser-induced differential evaporation. *Scientific Reports*, 8:3157, 2018. doi: 10.1038/s41598-018-20581-0.

[314] T. Young. III. An essay on the cohesion of fluids. *Philosophical Transactions of the Royal Society of London*, 95:65–87, 1805. doi: 10.1098/rstl.1805.0005.

[315] P. J. Yunker, M. A. Lohr, T. Still, A. Borodin, D. J. Durian, and A. G. Yodh. Effects of particle shape on growth dynamics at edges of evaporating drops of colloidal suspensions. *Physical Review Letters*, 110(3):035501, 2013. doi: 10.1103/PhysRevLett.110.035501.

[316] P. J. Yunker, T. Still, M. A. Lohr, and A. G. Yodh. Suppression of the coffee-ring effect by shape-dependent capillary interactions. *Nature*, 476(7360):308–311, 2011. doi: 10.1038/nature10344.

[317] D. Zang, S. Tarafdar, Y. Yu. Tarasevich, M. D. Choudhury, and T. Dutta. Evaporation of a droplet: From physics to applications. *Physics Reports*, 804:1–56, 2019. doi: 10.1016/j.physrep.2019.01.008.

[318] L. Zhang, T. Ku, X. Cheng, Y. Song, and D. Zhang. Inkjet droplet deposition dynamics into square microcavities for OLEDs manufacturing. *Microfluidics and Nanofluidics*, 22(4):47, 2018. doi: 10.1007/s10404-018-2068-y.

[319] Y. Zhao, Q. Guo, T. Lin, and P. Cheng. A review of recent literature on icing phenomena: Transport mechanisms, their modulations and controls. *International Journal of Heat and Mass Transfer*, 159:120074, 2020. doi: 10.1016/j.ijheatmasstransfer.2020.120074.

[320] R. Zheng. A study of the evaporative deposition process: pipes and truncated transport dynamics. *The European Physical Journal E*, 29(2):205–218, 2009. doi: 10.1140/epje/i2009-10469-7.

[321] X. Zhong, A. Crivoi, and F. Duan. Sessile nanofluid droplet drying. *Advances in Colloid and Interface Science*, 217:13–30, 2015. doi: 10.1016/j.cis.2014.12.003.

[322] X. Zhong and F. Duan. Disk to dual ring deposition transformation in evaporating nanofluid droplets from substrate cooling to heating. *Physical Chemistry Chemical Physics*, 18(30):20664–20671, 2016. doi: 10.1039/C6CP03231A.

[323] X. Zhong and F. Duan. Flow regime and deposition pattern of evaporating binary mixture droplet suspended with particles. *The European Physical Journal E*, 39(2):18, 2016. doi: 10.1140/epje/i2016-16018-5.

[324] A. Zigelman and O. Manor. A model for pattern deposition from an evaporating solution subject to contact angle hysteresis and finite solubility. *Soft Matter*, 12(26):5693–5707, 2016. doi: 10.1039/C6SM00579A.

[325] A. Zigelman and O. Manor. The deposition of colloidal particles from a sessile drop of a volatile suspension subject to particle adsorption and coagulation. *Journal of Colloid and Interface Science*, 509:195–208, 2018. doi: 10.1016/j.jcis.2017.08.088.

[326] A. Zigelman and O. Manor. Simulations of the dynamic deposition of colloidal particles from a volatile sessile drop. *Journal of Colloid and Interface Science*, 525:282–290, 2018. doi: 10.1016/j.jcis.2018.04.054.